ISSN 1580-2949
UDK 669+666+678+53 MTAEC9, 46(3)191–315(2012)

MATER. TEHNOL.	LETNIK VOLUME 46	ŠTEV. NO. 3	STR. P. 191–315	LJUBLJANA SLOVENIJA	MAY–JUNE 2012

VSEBINA – CONTENTS

IZVIRNI ZNANSTVENI ČLANKI – ORIGINAL SCIENTIFIC ARTICLES

STROKOVNI ČLANKI – PROFESSIONAL ARTICLES

UDK 621.746.27
Original scientific article/Izvirni znanstveni članek

ISSN 1580-2949
MTAEC9, 46(3)193(2012)

AUTOMATED FRACTAL ANALYSIS OF A NETWORK OF THERMAL FATIGUE CRACKS

AVTOMATIČNA FRAKTALNA ANALIZA MREŽE RAZPOK ZARADI TERMIČNE UTRUJENOSTI

Pavlo Maruschak

Ternopil Ivan Pul'uj National Technical University, Ternopil, Ukraine
maruschak.tu.edu@gmail.com

Prejem rokopisa – received: 2011-06-08; sprejem za objavo – accepted for publication: 2012-02-03

We have studied continuous-casting machine rolls' surface thermal cracking images. On the fundamentals of fractals a thermal cracking procedure analysis was proposed. The achieved results show that the thermal cracks have a strong self-similarity, according to the fractal laws, and the values of the fractal dimensions range from 1.0 to 2.0. The relationship between the fractal dimensions and the distribution values of the cracks' lengths is established. A new method of diagnostics and certain ideas for the analysis of the thermal cracking of a continuous casting machine roll with fractals theory is proposed.

Keywords: multiple cracks, thermal fatigue, fractal, damage, diagnostics, surface

Raziskana je površina valjev naprave za kontinuirano litje s toplotnimi razpokami. Uporabljena je procedura fraktalne analize razpok. Dobljeni rezultati kažejo, da so po fraktalnih zakonih toplotne razpoke med seboj podobne in imajo fraktalno dimenzijo v območju 1,0 do 2,0. Opredeljena je odvisnost med fraktalno dimenzijo in porazdelitvijo dolžine razpok. Na podlagi fraktalne teorije je predlagana nova diagnostična metoda in nove ideje za analizo toplotnega razpokanja na napravi za kontinuirano litje.

Ključne besede: številne razpoke, toplotna utrujenost, fraktali, poškodbe, diagnostika, površine

1 INTRODUCTION

The timing and safety of steel pouring on a continuous billet casting machine (CCM) depend on the properties and condition of the surface of the rollers, which are the main load-bearing structures and transportation means for moving the slab[1]. Significant thermomechanical loads cause a degradation of the surface properties and the occurrence of "crazing"[1–3].

There are a number of approaches to diagnose the multiple cracking by means of processing the digital images of the analyzed surface; however, they are not widely adopted in metallurgical practice due to the underdevelopment of the theoretical and methodological background[4–6].

Some works are dedicated to the formulation of the main requirements and the assessment criteria for multiple cracking; however, they need to be further improved[7–11]. The overall and rapid assessment of the geometry of the network of cracks is possible by using fractal geometry, which allows a determination of the configuration of cracks and the self-similarity of the fractured structures[8,11].

The purpose of this work is to improve the rapid diagnosis of the degradation of the CCM roller surface affected by a network of thermal fatigue cracks.

2 RESEARCH TECHNIQUE

The algorithm for the identification of the crack position consists of the following main steps: binarisation of the original grayscale image, its filtering, and repeated binarisation of the obtained image. The complete methods for the multiple-cracks digitalization are not described in this paper, but a few articles have been published on this subject[8,9,11]. In order to establish the crack position relative to each pixel it was necessary to determine whether the pixels belong to the crack surface or the background. This task was performed using binarisation. In a binary image the white pixels corresponded to the background and the black ones to the object. The analysis of the cracked surface images was performed using the "Fractalys" software developed by Gilles Vuidel[12], which was preliminarily tested on the model image of the Sierpinsky Carpet.

The fractal dimension was determined by the cellular method[7]. In addition, each element of the image was surrounded by a frame with a square shape in order to determine the number of pixels in a limited area.

Using the progressive approximation method we magnified the analyzed window with a view to determining the number of black pixels in frames with different sizes. As a result of the image processing a series of points (empirical curve) was obtained, where the abscise axis corresponds to the size of the lateral face of the frame and the ordinate axis represents the number N (1) of elementary particles of the image (pixels) surrounded by a frame of a certain size[7]:

$$N = \varepsilon^{-D+} c \tag{1}$$

where N is the number of black pixels in the window; ε is the size of the elementary square; D is the fractal

dimension; c is the parameter that allows a correct adjustment of the empirical curve.

For multiple defects the damage is distributed in a highly irregular way in reality. But it is experimentally established that multiple cracking is a fractal process in a finite range of scales[4,6]. This means that one could use a fractal dimension as a diagnosis parameter for a multiple cracking network geometry. General remarks about fractals and fractal dimensions may be found in[4–6] and particular precisions were given in[7]. The adequacy of determining the fractal dimension of the fractured structures by the cellular method was additionally checked by the net method[10].

The obtained curve was reconstructed on a logarithmic scale by means of an approximation to the exponential equation[7]:

$$\lg(N(\varepsilon)) = -D\lg(\varepsilon) + c \quad (2)$$

Since the real image is not an ideal fractal (it is not a continuous function), the approximation of the obtained pixel array was performed, which was followed by a determination of the correlation coefficient.

3 RESULTS AND DISCUSSION OF THE FRACTAL ANALYSIS OF THE FRACTURED SURFACE

The D values testify to the ordered state of the structure for which the morphology of the fractured structure is preserved. Within certain sections of the image the D values below 1.0 were found, which are typical of the individual fractured fragments. However, with an expansion of the area of analysis the D values always exceeded 1.0. It was observed that the analyzed image contains several independent morphological sets (sections of cracks), which propagated independently, (**Figure 1a**). For the case investigated D = 1.4 ... 1.3, which testifies to a well-bound, multi-scale network of cracks with numerous free intervals of different sizes, some of which are comparable to the crack size.

The external surface of the analyzed template was milled with a step h = 0.4 mm, and a change in the numerical readings for cracking was determined at various depths relative to the external surface of the template. A local increase in D was detected at a depth of 0.8 mm, which is connected with an "increase" in the area of cracking due to the incomplete removal of the oxidized external sections of the material. Later on the D value decreases monotonously (**Figure 1b**). With an increase in the number of identified cracks the fractal dimension increases, which is typical of the adjacent

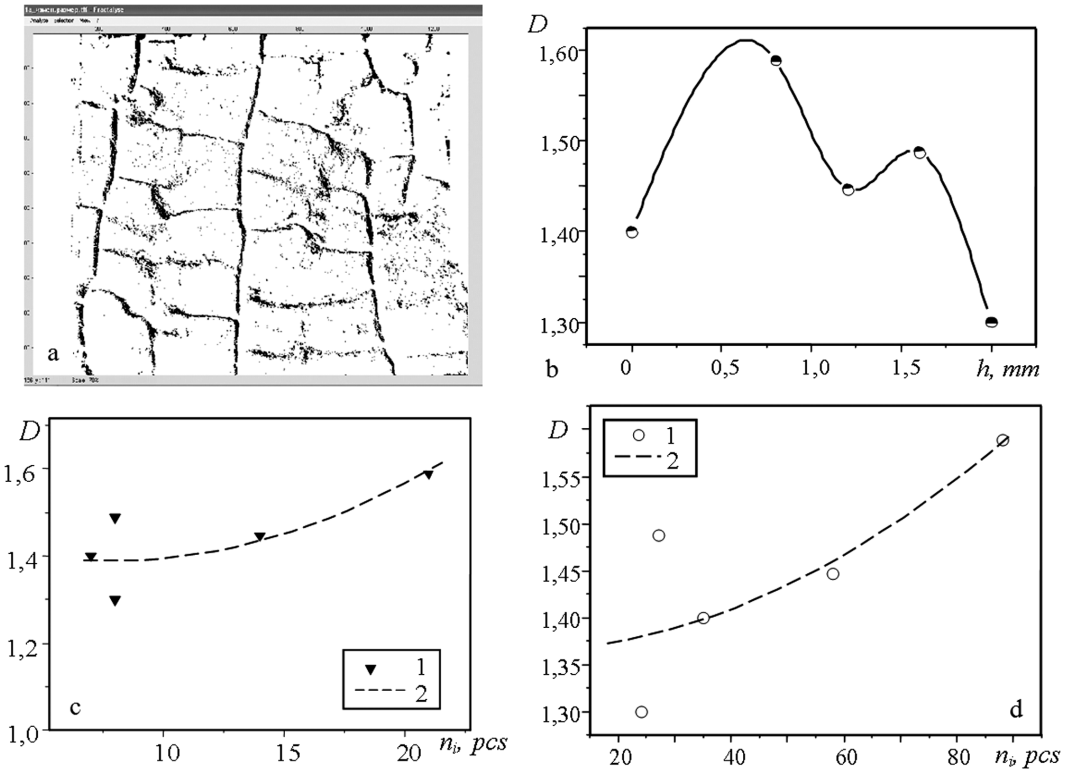

Figure 1: Analysis of the multiple cracking surface: a) image of surface; b) change a fractal dimension on the depth of analyzable area; c) dependence of fractal dimension on the quantity of identified coalesced cracks and d) individual cracks; 1 – experimental data; 2 – approximation

Slika 1: Analiza površine z mnogimi razpokami: a) slika površine, b) sprememba fraktalne dimenzije v globini analizirane površine, c) odvisnost fraktalne dimenzije od količine identificiranih koalesciranih razpok, d) posamične razpoke, 1 – eksperimentalni podatki, 2 – aproksimacija

cracks and the "joint" cracks that appeared due to the coalescence (**Figure 1c, d**).

The quality of the fractal dimension evaluation was controlled with reference to the value of the correlation coefficient, which was not below 0.99.

4 NORMALIZATION OF DEFECTIVENESS USING THE FRACTAL DIMENSION

The measurement of the in-service defectiveness is important as a parameter for digital diagnostics. It was performed by the fractal dimension, taking into account possible limit states[13]. The allowable fractal dimension [D] under a thermomechanical loading typical for the metallurgical equipment must be lower than the critical value $D_{cr} = f(\sigma, T)$:

$$[D] \leq \frac{D_{cr}}{n_1}$$

where n_1 is the fractal stock coefficient.

The fractal dimension allows a description of the spatial cracking structure, taking into account the off-orientation degree of the network of cracks. The evaluation of the fractal dimension effectively supplements the existing methods for the diagnostics of theCCM rollers[1,8–11]. Using the methods of fractal geometry we analyzed the geometrical model of the multiple cracking. Their spatial dimensions correspond to the dimensions of the statistical massifs of binary images showing real fractured structures. The value D_{cr} must be within the range 0.0–2.0, provided that the image $D_{cr} < 1.0$ contains the non-joint (separate) elements. At $1.0 < D_{cr} < 2.0$, the image is composed of the mixed elements and contains both small and large clusters with separate isolated elements.

5 CONCLUSIONS

Approaches are proposed that allow the integral assessment of the multiple cracking network geometry by means of the fractal dimension. It characterizes the anisotropy of the topological properties of fractured structures. An increase in the fractal dimension testifies to the accumulation of damage on the analyzed surface. The obtained D values testify to the ordered state of the structure, at which the morphology of individual elements of the network of cracks is preserved. The dependence of the fractal dimension on the number of identified single and joint cracks is established.

6 REFERENCES

[1] P. Yasniy, P. Maruschak, V. Hlado, T. Vuherer, V. Gliha, Journal for Welding and Applied Techniques, 52 (**2009**), 5–10

[2] A. P. Kravchenko, L. K. Leshchinskii, L. S. Lepikhov, et al., Metallurgist, 28 (**1984**), 137

[3] P. Yasniy, P. Maruschak, I. Konovalenko, V. Gliha, T. Vuherer, R. Bishchak, Multiple cracks on continuous caster rolls surface: A three-dimensional view, Proc. of the 4th Int. conf. Processing and Structure of Materials (May 27–29), Palić, Serbia, 2010, 7–12

[4] J. Yang, Y. Zhang, Y. Zhu, Mech. Syst. and Signal Proces, 21 (**2007**), 2012

[5] A. Carpinteri, S. A. Puzzi, Engineering Fract. Mech., 73 (**2006**), 2110

[6] C. Y. Lu, Y. W. Mai, Y. Bai, Philosophical Magazine Letter, 85 (**2005**), 67

[7] B. B. Mandelbrot, The Fractal Geometry of Nature, WH Freeman & Co., New York, 1982

[8] P. V. Yasnii, P. O. Marushchak, I. V. Konovalenko, R. T. Bishchak, Materials Science, 46 (**2008**), 833

[9] P. V. Yasnii, P. O. Marushchak, I. V. Konovalenko, R. T. Bishchak, Materials Science, 47 (**2009**), 798

[10] P. Yasniy, P. Maruschak, R. Bishchak, I. Konovalenko, Metallurgija, 3 (**2010**), 228

[11] I. V. Konovalenko, P. O. Marushchak, Optoelectronics, Instrumentation and Data Processing, 47 (**2011**), 360

[12] http://www.fractalyse.org/en-paper.html

[13] P. Yasniy, P. Maruschak, I. Konovalenko, R. Bishchak, Mechanika, 17 (**2011**) 3, 251

UDK 539.37:519.61/.64
Original scientific article/Izvirni znanstveni članek

ISSN 1580-2949
MTAEC9, 46(3)197(2012)

COMPUTER SIMULATION OF FATIGUE, CREEP AND THERMAL-FATIGUE CRACKS PROPAGATION IN GAS-TURBINE BLADES

RAČUNALNIŠKA SIMULACIJA NAPREDOVANJA UTRUJENOSTNIH RAZPOK, RAZPOK PRI LEZENJU IN TERMIČNO-UTRUJENOSTNIH RAZPOK V LOPATICAH PLINSKIH TURBIN

Artem Semenov[1], Sergey Semenov[1], Anatoly Nazarenko[1], Leonid Getsov[2]

[1]St. Petersburg State Polytechnical University, St. Petersburg, Russia
[2]NPO CKTI, St. Petersburg, Russia
guetsov@yahoo.com

Prejem rokopisa – received: 2011-07-06; sprejem za objavo – accepted for publication: 2012-03-01

Methods and computational algorithms for determining the growth rate of fatigue creep and thermal-fatigue cracks are considered. The rate of crack growth is dependent on the stress-intensity factor (or J-integral) for fatigue, on the C*-integral for creep and on the stress-intensity factor (or J-integral) and C*-integral for thermal fatigue. Simulations of the crack propagation under fatigue, creep and thermal fatigue at the edge of the blade of a gas turbine are carried out and discussed.

Keywords: fatigue, creep, thermal fatigue, crack, C*-integral, turbine blades, finite element simulation

Članek obravnava metode in računske algoritme za določanje hitrosti rasti utrujenostnih in toplotno utrujenostnih razpok pri lezenju. Hitrost rasti razpoke je odvisna od intenzitete napetostnega faktorja (ali J- integrala) pri utrujenosti, od C*-integrala pri lezenju in od intenzitete napetostnega faktorja (ali J-integrala) in od C*-integrala pri toplotni utrujenosti. Predstavljene in komentirane so simulacije širjenja razpoke po robovih lopatic plinske turbine pri utrujenosti, lezenju in toplotnem utrujanju.

Ključne besede: utrujenost, lezenje, toplotna utrujenost, razpoka, *C**-integral, turbinske lopatice, metoda končnih elementov

1 INTRODUCTION

Blades of a gas-turbine engine (GTE) are subjected to extreme non-steady operating conditions which can give rise to cracking. With the non-destructive testing of the turbine blades after operation, cracks of various sizes, configuration and locations could be detected. Fractographic studies allow us to identify the nature of the detected cracks. Usually, the cracks are[1] because of:

- fatigue (**Figure 1a**),
- creep fracture (**Figure 1b**),
- thermal fatigue (**Figure 1c**).

For an accurate assessment of the durability and life prediction of blades, it is expected during calculations to take into account not only the stage of the crack initiation, but also the stage of the crack propagation and consider the differentiation of specific types of cracks and their growth patterns. To estimate the remaining life of individual blades with a known configuration of crack, the most reliable prediction is based on calculations in the context of a three-dimensional analysis, which includes the kinetics of the crack growth and takes into account changes of the shape of the crack front and of its growth direction.

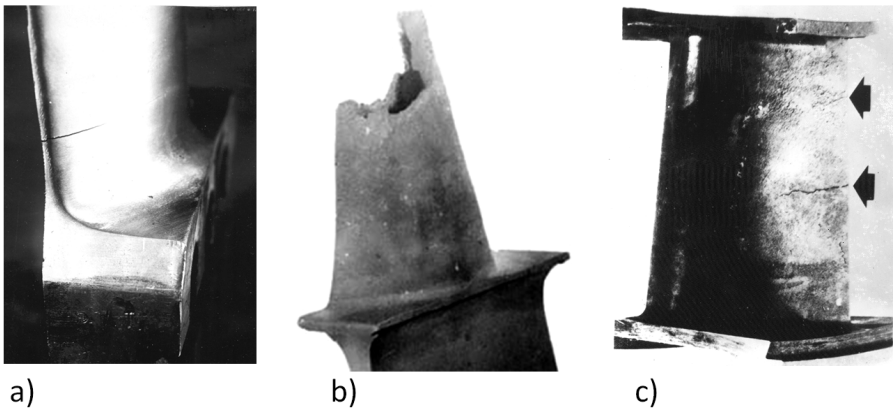

Figure 1: Cracks of different nature in gas-turbine blades: a) fatigue crack; b) creep crack; c) thermal fatigue cracks
Slika 1: Razpoke različne narave v turbinskih lopaticah: a) utrujenostna razpoka; b) razpoka zaradi lezenja, c) razpoke zaradi termične utrujenosti

The accumulation of experimental data on the rate of the propagation of cracks of different natures, the development of improved phenomenological models of inelastic deformation, improvement of methods of computational mechanics and computer technology advances make it possible to implement solutions to complex, non-linear, boundary value problems arising with the modelling of crack propagation in turbine blades. In some cases, a direct mathematical modelling of crack growth eliminates costly and time-consuming experiments to confirm the state of the blades.

The aim of this work was to develop and implement methods for the resource calculation of the blades in which cracks were detected during the control. The approach is based on a direct-step simulation of the crack propagation using the finite-element method (FEM) and experimental data on the dependence of the crack growth rate from the stress-intensity factor (SIF) amplitude ΔK and the C^*-integral obtained for the blade material. The main steps of the practical implementation techniques are discussed below:

- determination of the size and the crack location in the blade based on the results of an inspection (or analysis of statistical data on failures) and the identification of the nature of the defects identified with fractographic methods;
- identification of the alleged operation modes GTE, which caused the formation of the cracks;
- solving problems of heat conduction and aerodynamics in order to determine the distribution of the temperature fields in the bulk of the blade and the distribution of the gas pressure on the surface of the blade, as well as their dependence on time;
- solution to the problems of thermo-elasticity, thermo-elasto-plasticity and creep to determine the stress-strain state of the blades in the presence of growing cracks;
- computational-experimental determination of the rate of growth of cracks in different modes (based on the diagrams ΔK – da/dN, C^* – da/dt at different operating temperatures);
- identification of the critical state of the blade that causes its destruction (or maximum values of permissible stress that could be reached according to the strength standards and material characteristics);
- wording of the requirements for the minimum time before the next audit.

2 COMPUTATIONAL METHOD FOR THE CRACK GROWTH PREDICTION IN TURBINE BLADES

This methodology is used to determine the kinetics of crack propagation, estimate the number of cycles (or time) to reach a critical crack length (or to determine its length for a given number of load cycles or duration of operation). The initial distribution of defects is accepted as surface cracks of a given length and the calculations are made according to actual and (or) predictive models of operation (modes of loading, the load levels).

2.1 Models for the crack propagation rate

To determine the growth rate of fatigue cracks the following Paris power-type approximation was used:

$$\frac{\mathrm{d}a}{\mathrm{d}N} = B(\Delta K_{eff})^m \tag{1}$$

where B and m are material constants, $\Delta K_{eff} = K_{\max} - K_{op} \leq \Delta K = K_{\max} - K_{\min}$ are the effective scope of the SIF, which in the simplest model that takes into account only the stage of steady growth and simply reflects the effect of the crack closure, defined by the relations:

$$\Delta K_{eff} = \begin{cases} K_{\max} - K_{\min}, R = \dfrac{K_{\min}}{K_{\max}} \geq 0, \\ K_{\max}, \qquad R = \dfrac{K_{\min}}{K_{\max}} < 0, \end{cases} \tag{2}$$

In the presence of additional experimental information on the form of the kinetic diagrams of fatigue fracture (KDFF), more complicated equations than (1) may be used. The effect of cycle asymmetry and the presence of transient regions in the KDFF can be taken into account, for example, by using the equations:

Forman[2]

$$\frac{\mathrm{d}a}{\mathrm{d}N} = \frac{B(\Delta K)^m}{(1-R)K_c - \Delta K} \tag{3}$$

Walker[3]

$$\frac{\mathrm{d}a}{\mathrm{d}N} = B[(1-R)^n \Delta K]^m \tag{4}$$

or other, more complex, equations[4–8].

While analyzing the growth of short cracks in modes of loading, corresponding to the threshold region SIF, it is necessary to take into account the specific nature of KDFF and, for instance, explicitly use the terms da/dN = 0 when $\Delta K \leq \Delta K_{\mathrm{th}}$ and da/d$N \neq 0$ under $\Delta K > \Delta K_{\mathrm{th}}$ – the threshold range of SIF, which depends on the material, on the cycle asymmetry and on the aggressive environment.

To determine the creep crack growth rate, the following expression is used:

$$\frac{\mathrm{d}a}{\mathrm{d}t} = A(C^*)^q \tag{5}$$

where A and q are the material characteristics depending, in general, on the temperature and C^*-integral[9], which is invariant when considering the steady creep stage. In general, the three-dimensional case for an arbitrarily oriented crack with a curved edge, uses a vector-integral defined by:

$$C_k^* = \int_S \left(W^* n_k - n_i \sigma_{ij} \frac{\partial \dot{u}_j}{\partial x_k} \right) \mathrm{d}S \quad (6)$$

where S is the surface, covering the front of the crack and n_k – k^{th}-vector component normal to the surface.

The parameters of growth of a thermal fatigue crack (low-cycle fatigue) for an arbitrary cycle form were defined using the expression:

$$\frac{\mathrm{d}a}{\mathrm{d}N} = B(\Delta K_{eff})^m + \int_0^{\tau_c} A(C^*(\tau))^q \, \mathrm{d}\tau \quad (7)$$

where the values of the material parameters B, m, A and q are the same as in equations (1) and (5). The integration is performed within one cycle (from 0 to τ_c). The first term in (7) characterizes the growth of thermal fatigue cracks due to thermoelastic stresses during starting and stopping of GTE and the second, the growth of cracks in operating conditions between starts. It should be noted, however, the following features of ΔK_{eff} value in low-cycle (thermal) fatigue: during thermocycling the cycle of stress tends to a symmetry[1] and during the half cycle of compression the crack closes. For irregular regimes of thermal cycling under conditions of frequent and abrupt changes of level and duration of exposure, instead of (7) the following expression should be used:

$$\mathrm{d}a = B(\Delta K_{eff})^m \, \mathrm{d}N + A(C^*(\tau))^q \, \mathrm{d}\tau \quad (8)$$

2.2 Calculation of fatigue crack growth kinetics

The problem is solved in a linear-elastic formulation under the assumption of small strains. The external exposure is considered as the action of centrifugal forces, gas pressure and vibration loads. If necessary, the influence of the temperature fields can be accounted, also. In the FE model of the blade fracture, the crack is defined geometrically by introducing at different banks nodes with identical coordinates but with different numbers. When meshing the region with finite elements, it is desirable to use a focused mesh around the crack's front line and use hexahedral finite elements.

The whole operation period is divided into intervals (with a given number of cycles ΔN), each interval for a typical cycle and two elastic problems are solved in the presence of cracks. First, the maximum value of SIF $K_{\max}$ is determined, corresponding to the positive direction of the application of vibration loads. Then the minimum value of SIF $K_{\min}$ is determined, corresponding to the opposite direction of application of vibration loads. The values of $K_{\max}$ and $K_{\min}$ are defined for each node at the front of the crack.

During the determination of the maximum SIF in the case of the conditions $K_{\mathrm{I}} >> K_{\mathrm{II}}$ and $K_{\mathrm{I}} >> K_{\mathrm{III}}$, the direction of crack growth is preserved (crack of normal separation, I mode). When these inequalities violate the correction of the crack-growth direction $\Delta\theta$ should be accounted for by determining the angle of deviation from the original direction of growth based on the criterion of maximum tensile stress $K_{\mathrm{I}} \sin\Delta\theta + K_{\mathrm{II}} (3 \cos\Delta\theta - 1) = 0$. Hence, we have:

$$\Delta\theta = 2\mathrm{arctg}\left[\frac{1 - \sqrt{1 + 8(K_{\mathrm{II}} / K_{\mathrm{I}})^2}}{4(K_{\mathrm{II}} / K_{\mathrm{I}})} \right]$$

The increment of crack length is determined by the relations:

$$\Delta a = \begin{cases} B(\Delta K_{\mathrm{eff}})^m \, \Delta N, & \Delta K_{\mathrm{eff}} > \Delta K_{\mathrm{th}} \\ 0 & \Delta K_{\mathrm{eff}} \le \Delta K_{\mathrm{th}} \end{cases} \quad (9)$$

Based on the values of crack increment, the crack length for the next iteration,

$$a_{i+1} = a_i + \Delta a \quad (10)$$

is determined, the FE mesh is modified and the previous steps of the calculation are repeated until the critical crack length is reached.

When using the Paris law in order to minimize the computational cost, the increment of crack length is determined for the most loaded point of the front using the expression:

$$\Delta a = A(C^*)^q \, \Delta t \quad (11)$$

The calculation of the SIF K_{I}, K_{II}, K_{III} is based on an analysis of the distribution of crack displacement fields in the vicinity of its tip. Except for the extreme points of the crack front, the asymptotic behaviour of stresses in the region near the crack tip is assumed to be flat deformable. When using the FE software ANSYS version 12 and above, the SIF can be considered automatically.

2.3 Calculation of creep crack growth kinetics

In solving the boundary problems in a FE analysis a nonlinear viscoelastic material model with a steady-state creep law for stage II is used (the Norton's law).

The whole operation period is divided into time steps Δt and the stress-strain state of the blade is determined at each interval. Based on the obtained values, the C^*-integral is calculated for each node at the crack front. The increment of crack length is determined by the integration of equation (5). Using the explicit Euler method, we obtain the expression:

$$\Delta a = \Delta a_{\max} \left(\frac{K_{\mathrm{I}}}{K_{\mathrm{Imax}}} \right)^m \quad (12)$$

Based on the values of the crack increment, the crack length for the next iteration is determined with (10), for which the FE mesh is modified and the previous steps of the calculation are repeated until the critical crack length is reached.

The order of the calculation is as follows:

- Creation of a FE model with a crack.
- Setting the properties of the material.

- Evaluation of C^*-integral.
- Determination of crack-length increment.

The calculations of C^*-integral can be made automatically using the FE software package ABAQUS version 6.10 and above.

2.4 Calculation of thermal fatigue crack growth kinetics

When the loading conditions consist of relatively short start/stop periods versus the exposure time at elevated temperature, the solution may be simplified to a formulation based on a separate consideration of the exposure time using the creep model and the elasto-plastic model for periods of start/stop. A further simplification is possible while analyzing the start/stop period when the stresses, remote from the crack tip, do not exceed the yield stress and the elastic material model may be used for the calculations.

The whole operation period is divided into intervals (with a given number of cycles ΔN, the duration of each cycle τ_c). At each interval and for a typical cycle in the presence of a crack in the blade, two boundary problems are solved: the analysis of the creep processes within the cycle and the analysis of the fatigue in the thermo-elastic formulation to solve the problem when the engine is stopped (cooling). During start-up (heating) the surface cracks tend to be closed. The increment of crack length is determined by integrating (7) and for one typical cycle (block of cycles with similar values of ΔK_{eff} and C^*) we have:

$$\Delta a = \left[B(\Delta K_{\text{eff}})^m + \int_0^{\tau_c} A(C^*(\tau))^q \, \mathrm{d}\tau \right] \Delta N \qquad (13)$$

Based on the values of crack increment, the crack length for the next iteration is determined with (10), for which the FE mesh is modified and the previous steps of the calculation are repeated until the critical crack length is reached. The calculation of the parameters characterizing the fatigue-crack growth may be performed using the FE software packages ANSYS or ABAQUS, and the parameters related to creep, with the help of ABAQUS.

3 SIMULATION OF CRACK GROWTH IN A TURBINE BLADE

Let us consider the results of calculations made for the blade in **Figure 2**. In these calculations we assumed that the crack (idealized defect) is located at the output edge in the plane orthogonal to the blade and has an initial length of 1 mm. The fatigue, creep and thermal fatigue crack are located, respectively, at a height of (15, 50 and 80) mm (1/3 height of the blade) from the root section of the blade.

The blade was fixed in the direction of its axis over all nodes on the lower grounds and also three degrees of freedom in the plane of ground are fixed for the elimination of rigid body translations in this plane and rotation around its axis. The calculations used a model of linear elastic isotropic material (for the fatigue cracks), Norton's model (for the crack creep) and the model thermo-visco-elastic-plastic (for the thermal fatigue cracks). The problems were solved under the assumption of small strains. The material parameters were determined on the basis of references (for operating temperature at 850 °C)[10,11].

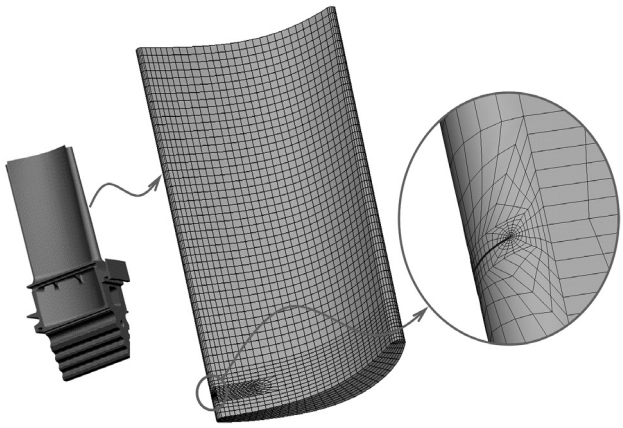

Figure 2: FE model of the blade with the crack (1 mm initial length) located at a height of 15 mm from the root section

Slika 2: FE-model lopatice z razpoko (1 mm začetna dolžina) na razdalji 15 mm od korenskega dela

3.1 Simulation of the fatigue crack growth

The FE model of the blade with the crack of initial length is shown in **Figure 3**. The FE mesh in the cracks plane of blades consists of quadratic isoparametric 20-node elements. The parameters of the FE models with an initial fatigue crack are given in **Table 1**.

Table 1: Parameters of FE model for the blade with a crack

Tabela 1: Parametri FE-modela za lopatico z razpoko

For the initial crack length		For a crack length of 1.7 mm	
Number of nodes	73 197	Number of nodes	65 021
Number of elements	16 382	Number of elements	14 476
Number of degrees of freedom	219 591	Number of degrees of freedom	195 063

In this problem the load was been taken as follows: action of centrifugal forces (ω = 3000 rpm), gas pressure on the lateral surface (p (x, y, z),), vibration loads (± F_x, ± F_y). The distribution of the stress intensity fields for the case of a positive direction of the application of vibration loads is shown in **Figure 4**.

The SIF values, computed for the case of positive direction of application of vibration loads (the definition of K_{max}), are presented in **Table 2** for all the corner nodes lying on the front of the crack.

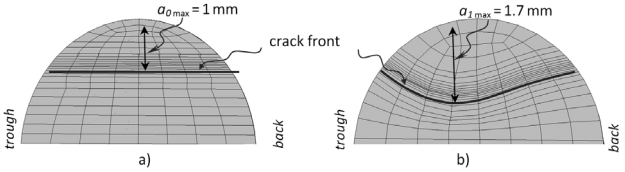

Figure 3: Edge of the blade and fatigue crack front (in the plane of propagation): a) initial configuration, b) crack after 10^7 cycles
Slika 3: Rob lopatice in čelo razpoke (v ravnini propagacije): a) začetna konfiguracija in b) razpoka po 10^7 ciklih

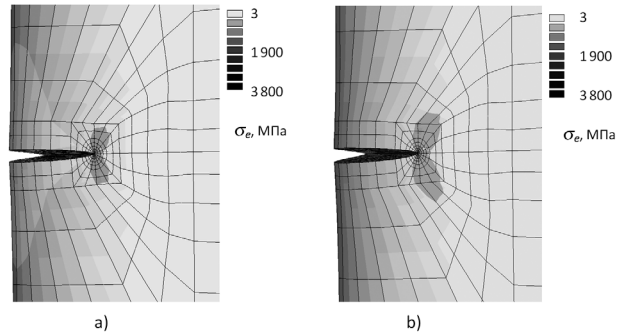

Figure 4: Field distribution of von Mises stress intensity in the blade with: a) fatigue-crack length of 1 mm and b) 1.7 mm after 10^7 cycles
Slika 4: Polje razdelitve von Misesove intenzitete napetosti v lopatici z utrujenostno razpoko z: a) dolžino 1 mm in b) 1,7 mm po 10^7 ciklih

Table 2: SIF values for the case of a positive direction of the application of vibration loads (definition of K_{max}) for a fatigue-crack length of 1 mm. The distance is measured along the crack front (from the back through).
Tabela 2: SIF-vrednosti za primer pozitivne smeri obremenitve zaradi vibracij (definicija K_{max}) za dolžino razpoke 1 mm. Dolžina je merjena vzdolž čela razpoke (od hrbta skozi).

Distance (mm)	K_I/ (MPa/m$^{0.5}$)	K_{II}/ (MPa/m$^{0.5}$)	K_{III}/ (MPa/m$^{0.5}$)
0	4.20	0.27	0.02
0.56	8.92	0.51	0.05
1.11	10.76	0.66	0.04
1.67	12.17	0.76	0.03
2.22	12.92	0.82	0.06
2.78	13.12	0.85	0.07
3.33	12.54	0.84	0.06
3.89	11.15	0.83	0.06
4.44	5.66	0.60	0.05

The change of position of the crack front with the increase in the number of cycles is shown in **Figure 5**. Originally, a straight edge is close to semi-elliptical for $N = 10^7$ and with a further increase to $N = 2 \cdot 10^7$ a progressive development of cracks in the region adjacent to the back is observed.

3.2 Simulation of creep crack growth

As a model problem, a blade with a crack 1 mm long, located on the edge of the output at 80 mm from the root section was chosen. The crack was identified as described above.

The creep-crack growth was investigated for a time of 100 000 h, which roughly corresponds to 11 years. In

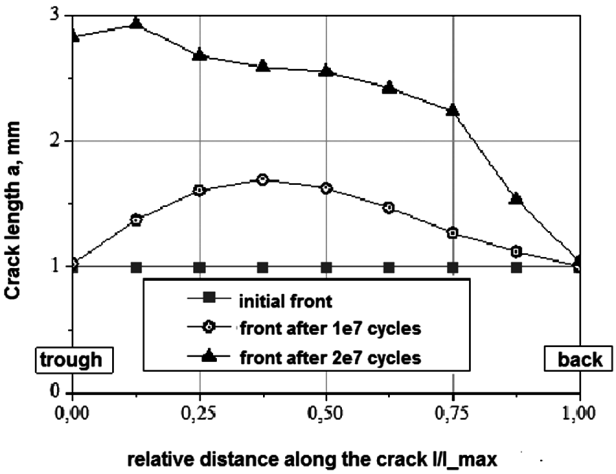

Figure 5: Evolution of fatigue-crack front with an increasing number of cycles
Slika 5: Evolucija čela utrujnostne razpoke pri povečanju števila ciklov

the FE solution of the nonlinear boundary value problem for the stress, a step-incremental iterative procedure was used. The value of the initial size of the time step was assumed to be equal to 10^{-10} s. In the process of the boundary solution, the step size was adaptively changed and increased, gradually. The precision of the creep strain was assumed to be of 10^{-6}, which corresponds to an error in the calculation of stresses 0.12 MPa and the corresponding integrals of the asymptotic values of C^*-integrals were determined based on the resulting FE solutions of the nonlinear boundary problem for the stress fields and displacements (and velocities). The time dependence of changes for the five characteristic points on the front of the crack, as shown in **Figure 6**. The crack growth during the year is shown in **Figure 7**.

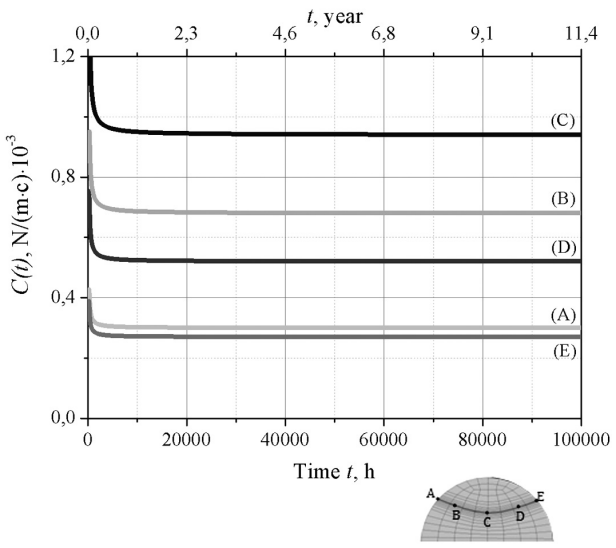

Figure 6: Dependence of $C(t)$-integral on the time for the characteristic points on the front of the crack
Slika 6: Odvisnost $C(t)$-integrala za karakteristične točke čela razpoke

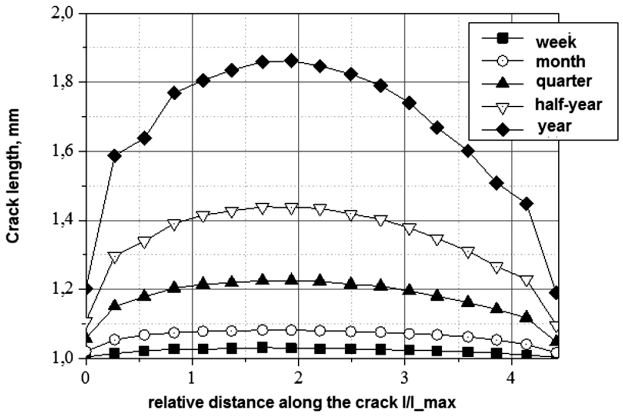

Figure 7: Evolution of the crack front
Slika 7: Evolucija čela razpoke

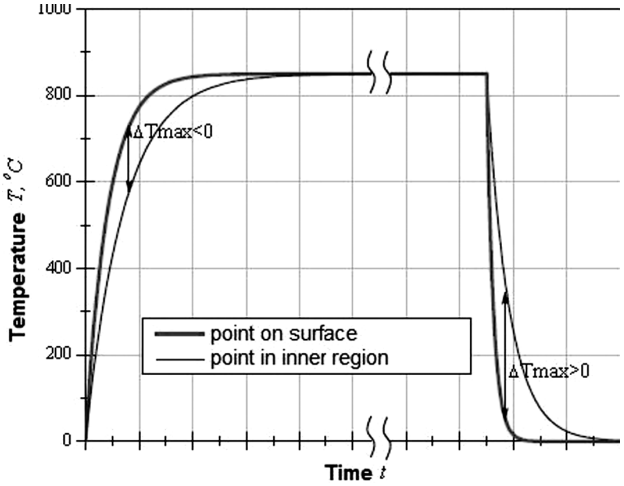

Figure 8: Schematic representation of the effect of the inhomogeneity of the temperature field in the blade during starting up and shutting down the turbine
Slika 8: Shematična predstavitev vpliva nehomogenosti temperaturnega polja v lopatici pri zagonu in zaustavitvi turbine

3.3 Simulation of thermal fatigue crack growth

Schematic representation of the effect of inhomogeneity of temperature field, observed at the start and stop of GTE, was set in accordance with **Figure 8**.

The determined values of the scale SIF at the first stage of the modelling process of the growth for all the nodes lying on the front of the crack are shown in **Table 3**. It should be noted that the condition of fatigue-crack propagation $\Delta K > \Delta K_{th}$ is satisfied for all nodes on the crack front. Table 3 shows the crack-growth rate calculated in accordance with (7), as well as separate components of the crack rate caused by fatigue and creep.

It should be noted that in this case the component due to creep dominates. In **Table 3**, also the values of the increment of crack length after $1.5 \cdot 10^4$ cycles, calculated using equation (5), are shown. The increment of the crack length Δa (based on $1.5 \cdot 10^4$ cycles) from the *arc* coordinate, is calculated in this case along the crack front (for different front sites). Based on the values of crack increment, the crack length for the next iteration is determined with (10), for which the FE mesh is modified and the previous steps of the calculation are repeated until the critical crack length is reached.

4 CONCLUSIONS

1. The methods and computational algorithms for the simulation of propagation process of fatigue, creep and thermal fatigue cracks in the blades were developed and verified for an uncooled stationary GTE turbine blade. Finite-element calculations were performed using the ANSYS and ABAQUS FE software.
2. It was established that the shape of front of cracks of different nature varies significantly with the accumulation of the number of cycles and the operating time.
3. It is shown that for the considered blade geometry and the assumed initial crack configurations, the values of K_I are dominating on K_{II} and K_{III}.
4. During the thermal cycling, the maximum SIF scale determining the components of fatigue-crack growth are observed at the stop of GTE.

Table 3: SIF ΔK_I, contributions from fatigue, creep, and the total value of thermal fatigue crack growth rate $\Delta a/\Delta N$, as well as the increment of crack length Δa for $1.5 \cdot 10^4$ cycles in the first step of modelling the growth (for crack length of 1 mm)
Tabela 3: SIF ΔK_1, deleži utrujenosti, lezenja in skupna velikost hitrosti rasti utrujenostne razpoke $\Delta a/\Delta N$ in prirastek povečanja dolžine razpoke Δa za $1{,}5 \cdot 10^4$ cikle v prvi stopnji modeliranja rasti razpoke (za razpoko z dolžino 1 mm)

Distance along the crack front from the back through (mm)	ΔK_I/ (MPa m$^{0.5}$)	$\Delta a_{fat}/\Delta N$/ mm per cycle	$\Delta a_{creep}/\Delta N$/ mm per cycle	$\Delta a/\Delta N$/ mm per cycle	Δa (based on $1.5 \cdot 10^4$ cycle), mm
0	12.22	$5.53 \cdot 10^{-8}$	0	$5.53 \cdot 10^{-8}$	0.0008
0.56	26.22	$1.10 \cdot 10^{-6}$	$3.50 \cdot 10^{-6}$	$4.60 \cdot 10^{-6}$	0.0690
1.11	30.41	$1.97 \cdot 10^{-6}$	$1.79 \cdot 10^{-5}$	$1.99 \cdot 10^{-5}$	0.2980
1.67	32.93	$2.69 \cdot 10^{-6}$	$2.97 \cdot 10^{-5}$	$3.24 \cdot 10^{-5}$	0.4860
2.22	33.61	$2.92 \cdot 10^{-6}$	$3.07 \cdot 10^{-5}$	$3.36 \cdot 10^{-5}$	0.5040
2.78	32.78	$2.65 \cdot 10^{-6}$	$2.38 \cdot 10^{-5}$	$2.65 \cdot 10^{-5}$	0.3970
3.33	30.17	$1.91 \cdot 10^{-6}$	$1.04 \cdot 10^{-5}$	$1.23 \cdot 10^{-5}$	0.1850
3.89	25.85	$1.04 \cdot 10^{-6}$	$1.58 \cdot 10^{-7}$	$1.20 \cdot 10^{-6}$	0.0180
4.44	11.97	$5.11 \cdot 10^{-8}$	0	$5.11 \cdot 10^{-8}$	0.0008

5. The areas of possible practical applications of the developed techniques are suggested.
6. The practical implementation of the calculations of the blade crack requires the systematic accumulation of experimental data for the blade material for the construction of diagrams ΔK – da/dN, C^* – da/dτ under different operating temperatures.

5 REFERENCES

[1] L. B. Getsov, Materials and durability of parts for gas turbines. Fourth edition in two volumes. Rybinsk. Ed. House gas turbine technology, 2010

[2] R. G. Forman, V. E. Kearney, R. M. Engle, Numerical Analysis of Crack Propagation in a Cyclic-Loaded Structure, Journal of Basic Engineering, Transactions of the ASME, 1967

[3] K. Walker, The Effect of Stress Ratio During Crack Propagation and Fatigue for 2024-T3 and 7075-T6 Aluminum. In: Effects of Environment and Complex Load History on Fatigue Life, ASTM STP 462 1970, 1–14

[4] F. Erdogan, M. Ratwani, Fatigue and fracture of cylindrical shells containing a circumferential crack, International Journal of Fracture Mechanics, 6 (**1970**), 379–392

[5] Jr. Newman, A crack closure model for predicting fatigue crack growth under aircraft spectrum loading. In Methods and Models for predicting Fatigue Crack Growth under Random Loading. ASTM STP 748 American Society for Testing and Materials, Philadelphia, PA., 1981, 53–84

[6] V. S. Balin, G. G. Madyakshas, Strength, durability and crack resistance of structures with long-term cyclic loading. St. Petersburg: Polytechnics, 1994, 204C

[7] A. V. Prokopenko, V. N. Trade, L. B. Getsov et al., Influence of the loading regime on the growth rate of fatigue cracks in stainless steels in air and sea salt solution, Strength of Materials, (**1983**) 12, 41–45

[8] A. V. Prokopenko, Method of determining the stress intensity factor in spades GTE, Strength of Materials, (**1984**) 4, 21–24

[9] J. D. Landes, J. A. Begley, A fracture mechanics approach to creep crack growth. In: Mechanics of Crack Growth, ASTM STP 590. Am. Soc. Testing Mat. 1976, 128–148

[10] Y. A. Nozhnitsky, E. R. Golubovsky, On the Strength Reliability of single-crystal turbine blades of high prospective GTE. In the book. Strength of materials and resource elements of power equipment, Proceedings of CKTI vyp.296, St. Petersburg, 2009, 74–82

[11] M. Tabuchi, K. Kubo, K. Yagi, A. T. Yokobori, A. Fuji, Results of Japanese round robin on creep crack growth evaluation methods for Ni-base superalloys, Engineering Fracture Mechanics, 62 (**1999**), 47–60

UDK 621.937
Original scientific article/Izvirni znanstveni članek

ISSN 1580-2949
MTAEC9, 46(3)205(2012)

MINIMIZATION OF THE SURFACE ROUGHNESS AND FORM ERROR ON THE MILLING OF FREE-FORM SURFACES USING A GREY RELATIONAL ANALYSIS

MINIMIZACIJA HRAPAVOSTI POVRŠINE IN OBLIKOVNE NAPAKE PRI OBDELAVI PROSTIH POVRŠIN Z UPORABO GREY ODVISNOSTNE ANALIZE

Mustafa Kurt[1], Selim Hartomacıoğlu[1], Bilçen Mutlu[1], Uğur Köklü[2]

[1]Technical Education Faculty, Marmara University, 34722, Kadikoy, Istanbul, Turkey
[2]Department of Mechanical Education, Technical Education Faculty, Dumlupinar University, Simav-Kütahya, Turkey
mustafakurt0406@gmail.com

Prejem rokopisa – received: 2011-07-25; sprejem za objavo – accepted for publication: 2012-01-23

The aim of this paper is to assess an experimental analysis of different tool-path strategies with respect to their influences on surface roughness and dimensional machining errors during free-form surface machining using experimental works. For this purpose, the machining of Al7075-T651 material, which is used in the production of free-form surfaces for the die-sinking sector, in particular, was examined using a ball-end mill in a 3-axis CNC machine. The effects of the tool diameters and of the rough and finished machining strategies on the presence and character of form errors and surface roughness were investigated and the results were optimized using a Grey Relational Analysis.
The results obtained from these experiments clearly indicate the influence of tool-path strategies and tool diameters on form errors, as well as the importance of the appropriate strategies for reducing the surface roughness.

Keywords: milling, free-form surface, form error, surface roughness

Namen tega dela je bil ovrednotenje analize različnih strategij orodja s stališča vpliva na hrapavost površine in dimenzijsko napako pri prosto oblikovni obdelavi na podlagi preskusov. S tem namenom je bila raziskana zlitina Al7075-T651, ki se uporablja pri izdelavi prosto oblikovanih površin, predvsem pri poglabljanju utorov, z orodjem s kroglasto glavo na tri osnem CNC stroju. Vplivi strategij premera glave orodja, grobe in končne obdelave na prisotnost in naravo napak in hrapavost površine so bili raziskani in rezultati optimizirani z uporabo Grey odvisnostne analize.
Rezultati preskusov jasno kažejo vpliv strategije poti in premera orodja na napako oblike in pomen strategij, primernih za zmanjšanje hrapavosti površine.

Ključne besede: obdelava, prosto oblikovana površina, napaka oblike, hrapavost površine

1 INTRODUCTION

Many products are designed with free-form surfaces to improve their aesthetics, which is important for customer satisfaction, particularly in the electronic and automotive industries. Furthermore, these products can have complicated surfaces to meet functional requirements, which necessitate specific aerodynamic, optical, medical, structural and processing characteristics.

The machining of free-form surfaces is a process that is both time-consuming and costly. There are more than 10,000 tool movements observed in a typical example of free-form surface machining. For this reason, the manufacture of free-form surfaces is defined as an "*error-prone*" process[1]. Consequently, selecting and controlling the cutting conditions, the cutting tools used and the strategies employed, each of which has an effect on product quality, is particularly important in order to minimize errors in the machining of free-form surfaces. Some examples of free-form surfaces and their machining are shown in **Figure 1**.

An algorithm for generating product-sensitivity-based tool paths designed for free-form surfaces was developed in the study conducted by Y-K. Choi et al.[2] The experiments were carried out under various machining conditions and the machined surfaces and designed surfaces were compared by scanning the machined parts. It was determined that the developed model and the experimental results matched.

Figure 1: Free-form surface and its machining[1]
Slika 1: Prosto oblikovana površina in njena obdelava[1]

The effects of the cutting diameter and the machining direction on the cutting force and the form error in the milling of curved surfaces were investigated in the study performed by K.K. Desai and P.V.M. Rao[3]. A theoretical model for the evaluation of the forces in the ball-end milling of curved surfaces was presented by B.W. Ikua et al.[4] Kim et al.[5] calculated the cutting force in the ball-end milling of free-form surfaces. In their study, the cutter contact area was determined from the z-map of the surface geometry and the current cutter location. It was shown that the proposed method predicted the cutting force effectively for any geometry, including sculptured surfaces with cusp marks and a hole.

Kaymakci and Lazoglu[6] have developed a new model that can be utilized as a tool incorporated with CAM software to predict 3D surface topographies, allowing the appropriate selection of the tool paths in free-form surfaces. V.G. Dhokia et al.[7] provided a predictive model using a design-of-experiments strategy to obtain optimized machining parameters for a specific surface roughness in the ball-end machining of polypropylene. This study reports on the use of new manufacturing knowledge to machine polypropylene using ball-end tooling in order to generate personalized sculptured surface products.

Antoniadis et al.[8] proposed a system for the prediction of surface topomorphy and roughness in ball-end milling for aerospace components and mould manufacture with a prediction system developed.

The literature research revealed that a large number of studies were carried out related to the machining of free-form surfaces, and these studies are still being conducted.

The majority of these studies focus on tool-path generation and the detection of and compensation for dimensional machining errors. The most important dimensional machining errors are described as the deviation from the actual geometry. A comparison method is used for the detection of the form error. This comparison method can provide a numerically designated indication of the differences between the designed surface and a scan of the machined surface[9].

2 MACHINING OF FREE-FORM SURFACES

Before a surface's final form is approached, the bulk of the unecessary material must be cut away. In preparation for this process, a standard operation called a roughing cut is employed first. Afterwards, an operation called semi-roughing is carried out in order to leave a uniform amount of chip for the finishing operation. An attempt to achieve the designed surface is made by applying the finishing operation. Afterwards, any chips remaining (particularly in the curved areas and the places where the cutting tools cannot reach) are removed with a clean-up process. Finally, the areas that cannot be machined by cutting tools are worked to designated tolerances by an EDM machine[10]. These common stages in free-form surface machining are presented in **Figure 2**.

Form error is one of the most significant machining errors in free-form surface machining. Form error is defined as the deviation from an ideal geometric shape. In general, the form error varies with respect to the cutting-tool geometry, the machining strategies and the condition of the machined surface. Essentially, form error is the result of cutting forces and the displacement that these forces bring about in the cutting tool. Another critical error in terms of product quality is the surface

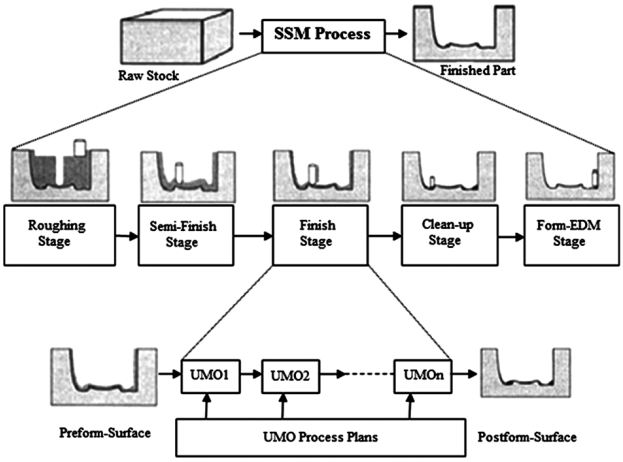

Figure 2: Stages in free-form surface machining[10]
Slika 2: Stopnje pri obdelavi prosto oblikovanih površin[10]

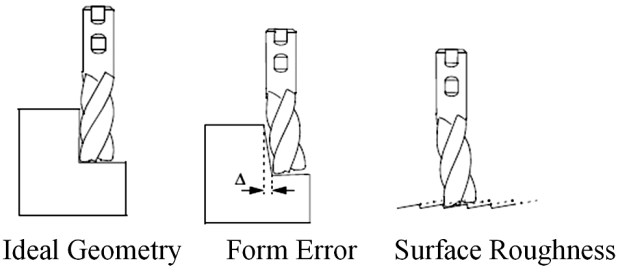

Figure 3: Effect of tool deflection on the form error and the surface roughness[11]
Slika 3: Vpliv upogiba orodja na napako oblike in hrapavost površine[11]

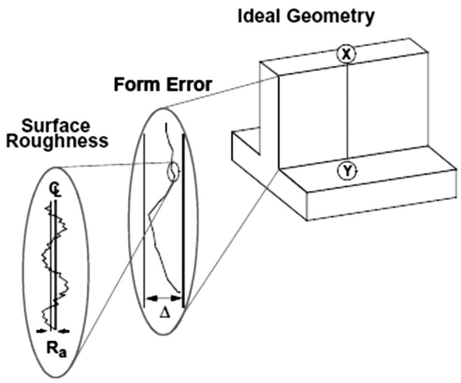

Figure 4: Deviations in form and surface quality[11]
Slika 4: Odstopanja oblike in kakovosti površine[11]

Table 1: Chemical composition and mechanical properties of the Al 7075-T6 material
Tabela 1: Kemična sestava in mehanske lastnosti zlitine Al 7075-T6

Chemical composition *w*/%	Si	Fe	Cu	Mn	Mg	Cr	Ni	Zn	Ti	Sn	V	Al
	0.393	0.260	1.26	0.044	1.94	0.288	0.027	5.92	0.086	0.0035	0.0087	89
	Ag	B	Be	Bi	Ca	Co	Li	Na	Pb	Sr	Zr	Cd
	0.0067	0.005	0.0028	0.001	0.048	0.032	0.347	0.015	0.0058	0.211	0.0014	0.0001
Mechanical properties	Tensile strength (MPa)			Yield strength (MPa)		Elongation (%)		Shear modulus (MPa)		Tensile modulus (GPa)		
	503			434		13		303		72		

roughness. The surface roughness and form error are shown in **Figures 3** and **4**.

3 MATERIAL AND METHOD

3.1 Workpiece Materials and Cutting Tools

The cutting tools used were chosen from the Helix Tools Catalog[12] to machine Aluminum 7075-T651. The chemical composition and mechanical properties of the Al 7075-T6 material are given in **Table 1**. Cutting tools of 6, 8 and 12 mm diameters, with two teeth, were employed for milling the experimental surfaces. Details of the tools are given in **Figure 5** and **Table 2**. The cutters were held in a BT-40 taper tool holder.

Table 2: The dimensional and mechanical properties of the cutting tools
Tabela 2: Dimenzije in mehanske lastnosti orodja

Tool diameter (d_1)	d_2	l_1	l_2	No. of Teeth	Helix Angle
6	6	80	13	2	30°
8	8	100	19	2	30°
12	12	100	26	2	30°

The experiments were conducted using a CNC Johnford VMC Model three-axis CNC milling machine equipped with a maximum spindle speed of 12,000 rpm and a 10-kW drive motor, as shown in **Figure 6**. This machine was designed to make 3-axis linear and circular interpolations via ISO format programs in metric and imperial units. Its control unit was a FANUC series O-M. The measurement of the cutting forces occurring during the machining was performed with a Kistler 9265B transducer. The CNC part-manufacturing programs were created by employing CATIA V5 R17 software on a personal computer containing an Intel Pentium IV chip and operating at 2.80 GHz. A cutting experiment was

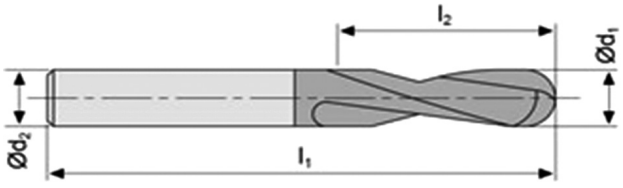

Figure 5: The ball-end milling tool
Slika 5: Orodje s kroglasto glavo

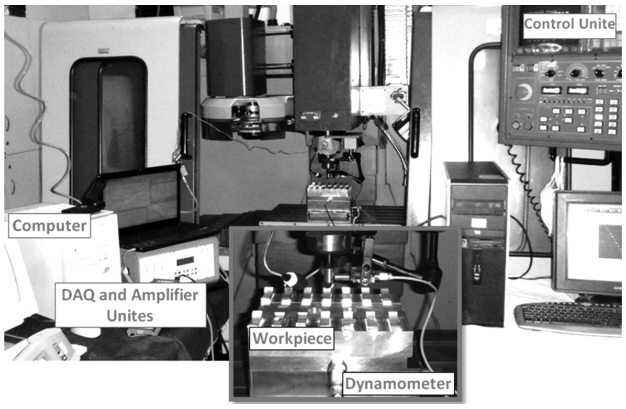

Figure 6: Experimental set-up
Slika 6: Eksperimentalna postavitev

developed to measure the tool forces using a Kistler 9257A three-axis load cell. The cutting forces were generated during free-form surface machining with a ball-end mill. The experiment involved the collection of three orthogonal channels of force data while cutting the free-form surface in a piece of Al 7075-T651 alloy using different tool path strategies and employing 6, 8 and 12 mm diameter ball-end mills.

Several program packages were used in the evaluation of the data and in the experimental design of the study. The specimen was designed in CATIA V5 R17,which is a universal software used in various industries, including aerospace, construction, machinery, and electronics.The same software was also employed, on a personal computer containing an Intel Pentium IV chip and operating at 2.80 GHz, for the creation of the CNC part-manufacturing programs used in the study. Minitab 15, Matlab and Office software programs were employed for the generation of the graphics, the analysis of the outcomes and the experimental design. Rapidform X0V2 software was used for obtaining the numerical values and the determination of the form error.

3.2 Method

G-codes were produced using a program package under machining conditions that were determined through experimental design. The remaining chip analyses after the roughing cut and the finishing operation were conducted during machining simulation in the program package. The cutting force was measured and

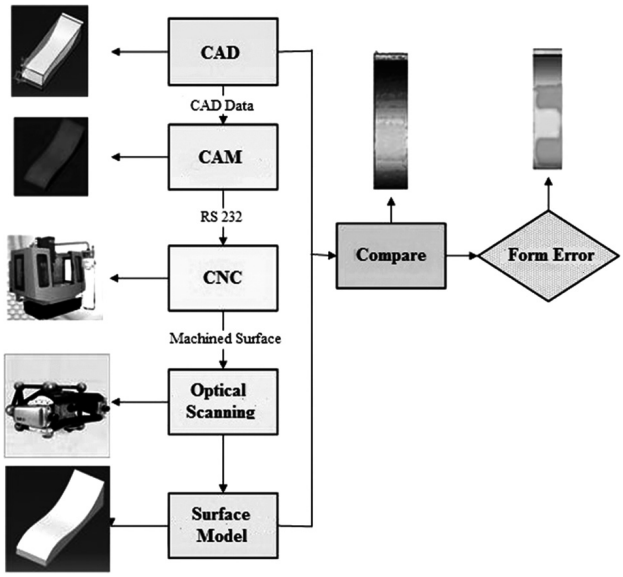

Figure 7: Stages of the form-error determination
Slika 7: Stopnje določanja napake oblike

the correlation between the remaining chips and the cutting force was determined. The comparison method used was one frequently used in previous studies for a determination of the form error in machined surfaces. In addition, surface roughness measurements were conducted. Then, the minimization of the surface roughness and the form error was achieved using a Grey Relational Analysis. The resultant form errors, the surface roughness, the correlation between form errors and cutting force and the relationship between remaining chip and the cutting force were analyzed.The stages in the determination of the form error are presented in **Figure 7**.

3.3 Grey Relational Analysis Method

While only one outcome is optimized in the Taguchi method, multiple outcomes can be optimized in a Grey Relational Analysis[8]. For this reason, the Grey Relational Analysis method, allowing optimization of multiple outcomes, was chosen in the study and the optimization process was carried out in the following three phases.

1. Normalization of experiment results (the lowest is the best)
2. Calculation of the Grey relational coefficient
3. Calculation of the Grey relational degree

The normalization operation, the first step, was conducted using the below equation according to "the-lowest-is-the-best" approach[13].

$$x_i(k) = \frac{\max y_i(k) - y_i(k)}{\max y_i(k) - \min y_i(k)} \quad (1)$$

Here, $x_i(k)$ refers to the value at the i series and k row after normalization, min $y_i(k)$ refers to the minimum value at the i series, max $y_i(k)$ refers to the maximum value at the i series and $y_i(k)$ refers to the original value at the i series and k row[9].

A calculation of the Grey Relational coefficient, which is the second step, is done using the equation[13]:

$$\xi_i(k) = \frac{\Delta\min + \xi\Delta\max}{\Delta 0_i(k) + \xi\Delta\max} \quad (2)$$

Here, ξ is a distinguishing coefficient between 0 and 1. Studies demonstrate that the value of ξ does not affect the sorting that will occur after the calculation of the Grey Relational degree. $\Delta 0_i$ is the amount of deviation between the reference series and the normalization values. Δmin refers to the minimum value of the deviation sequence from the reference series and Δmax refers to the maximum value of deviation sequence from the reference series.

The third step, the calculation of the Grey Relational degree, determines the level of correlation between the γ_i reference series and the comparison series.This degree is estimated with the following equation[14]:

$$\gamma_i = \sum_{k=1}^{n} \xi_i(k) \quad (3)$$

3.4 Experimental Design

The cutting conditions in **Table 3** were determined by taking into account the constraints of the measurement instruments, the recommendations of the cutting-tool manufacturer and the related literature. Furthermore, the hold height was detected as five times the diameter of ball-end mill; the chip depth was determined as 0.2 times the diameter of ball-end mill maximum in the roughing cut; and the chip share left for the finishing operation was detected as 0.3 mm. The cutting speed was selected as 45 m/min for the roughing cut and 55 m/min for the

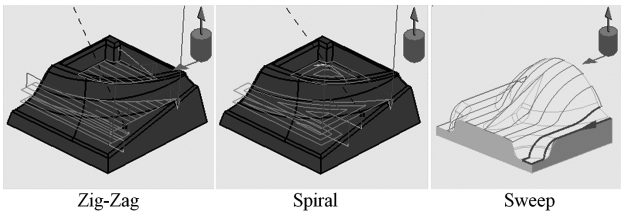

Figure 8: Machining strategies
Slika 8: Obdelovalne strategije

Table 3: Determined factors and their levels
Tabela 3: Določeni faktorji in njihovi nivoji

	Factors		
	A Cutting tool diameter (mm)	B Roughing cut	C Finishing operation
Level 1	6	zigzag_ longitudinal	sweep_upward
Level 2	8	zigzag_ latitudinal	sweep_downward
Level 3	12	spiral	sweep_latitudinal

finishing operation. Moreover, while the machining sensitivity was detected as 0.1 mm for the roughing cut, it was determined as 0.01 mm. for the finishing operation. In the experimental design method the L9 orthogonal array was selected for 3 factors and the condition, in which each factor has 3 levels (**Table 4**).

In the experiments, a zigzag and a spiral were employed as a machining strategy in the roughing cut and sweep was used in the finishing operation. The machining strategies are given in **Figure 8**.

Table 4: Experimental design according to the L9 orthogonal array
Tabela 4: Načrtovanje preskusov skladno z ortogonalno porazdelitvijo L9

Exp. No.	A	B	C
1	1	1	1
2	1	2	2
3	1	3	3
4	2	1	2
5	2	2	3
6	2	3	1
7	3	1	3
8	3	2	1
9	3	3	2

4 RESULTS AND DISCUSSION

4.1 Measurement of the Form Errors and the Surface Roughness

A comparison method was exercised, which is one of the most preferred methods for a determination of the form error in recent years. This method is based on a comparison of design surface (**Figure 9**), called the original surface, and the surface obtained by scanning using an optical method after the machining.

In order to determine the machining errors of the workpieces, a BreuckmannoptoTOP-HE coded structured light system was used. A three-dimensional optical measuring system with a strong light source drops on the fringes of the different textural properties to the body. These coded lights on the surface of the body are deformed depending on the direction of the characteristic features of the object. The coded lights are directed towards the surface of the workpiece in order to have a special angle (**Figure 10**). This angle is referred to as triangulation. By an analysis of the information about the fringe projection's deformation, up to 1 million points of 3D coordinates are obtained within few seconds. Therefore, the point cloud that contains information in the surface of the object is created. With the help of computer, it is possible to measure the reference of the object or the point-cloud surface. Then, CAD modeling, an application of reverse engineering, is possible with the help of the point cloud. Also, digitization systems are used during the process of resolving as a technological convenience. As a result of optical scanning, the point cloud and polygon mesh data were obtained. Finally, the scanned data were registered into the CAD data to calculate and display the deviations of the two data sets by using the software.[15]

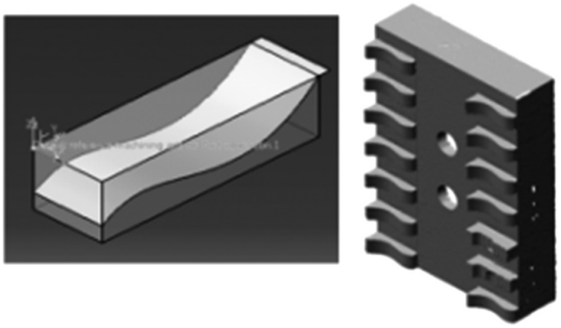

Figure 9: Test part designed in Catia V5 R17
Slika 9: Preskusni deli, načrtovani s Catia V5 R17

Figure 10: Machined real surface using different tool-path strategies
Slika 10: Realne površine, obdelane z različno strategijo poti orodja

As understood in the section Experimental Design, nine experiments were conducted and the image of the machined surfaces was obtained via optical scanning.

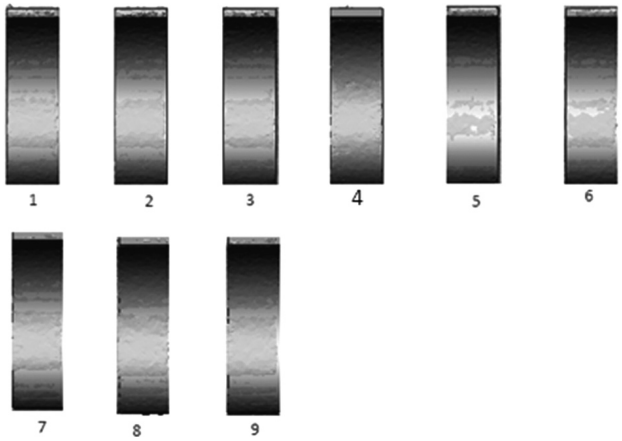

Figure 11: Superimposition of the design surface and the machined surface via scanning
Slika 11: Superpozicija načrtovane in obdelane površine s skeniranjem

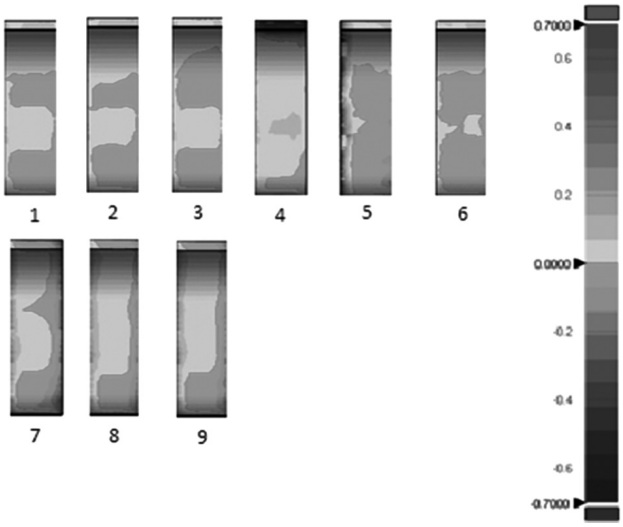

Figure 12: Machining surface errors
Slika 12: Napake obdelave površine

A comparison method will be employed to determine the form error. Therefore, the surfaces obtained from the machined surface via the scanning and design surface will be compared (**Figure 11**). Therefore, the surfaces should be overlapped in a precise manner. By screening the design surface (nominal data) and the machined surface via scanning (scanning data) and using the Rapidform package program, they are superposed precisely (best fit). Afterwards, an analysis to determine the difference among all the surfaces, in other words, the form error denominated as a deviation from the main form was conducted (**Figure 12** and **Table 5**).

Finally, control points with equal intervals of 0.5 mm were assigned across the surface in such a way that they will pass through the midpoint of the machined surface for each piece and the numerical values of the form error in each of these points were obtained (**Figure 13**).

The surface roughness values were measured using MahrPerthometer Concept roughness measuring instrument.

Table 5: Form error and roughness values obtained from the experiments
Tabela 5: Napake oblike in hrapavosti, dosežene pri preskusih

Exp. No.	A	B	C	Surface Roughness *Ra* (μm)	Form Error (mm)
1	1	1	1	1.130	0.086
2	1	2	2	1.100	0.099
3	1	3	3	2.550	0.096
4	2	1	2	1.150	0.120
5	2	2	3	2.170	0.147
6	2	3	1	1.360	0.089
7	3	1	3	1.660	0.098
8	3	2	1	0.850	0.172
9	3	3	2	1.240	0.124

4.2 Influence of the Machining Strategies on the Form Error

The machining strategies have a significant influence on the form error in free-form surface machining. Free-form surfaces usually demand extremely long tool paths, because of the surface complexity, that results in extreme values of the form error. Various cutter paths have different path lengths, though they remove an identical amount of workpiece material. Removing nearly the same amount of material in a shorter time reduces the cycle time; however, it raises the machining forces and the tool deflection.

After machining free-form surfaces by using the CNC machine that was mentioned in Section 4.1, the surface errors were measured with a 3-dimensional optical measuring system. The details of the experimental set-up were given in Section 3.1. The measured data points on the surface were compared with the CAD

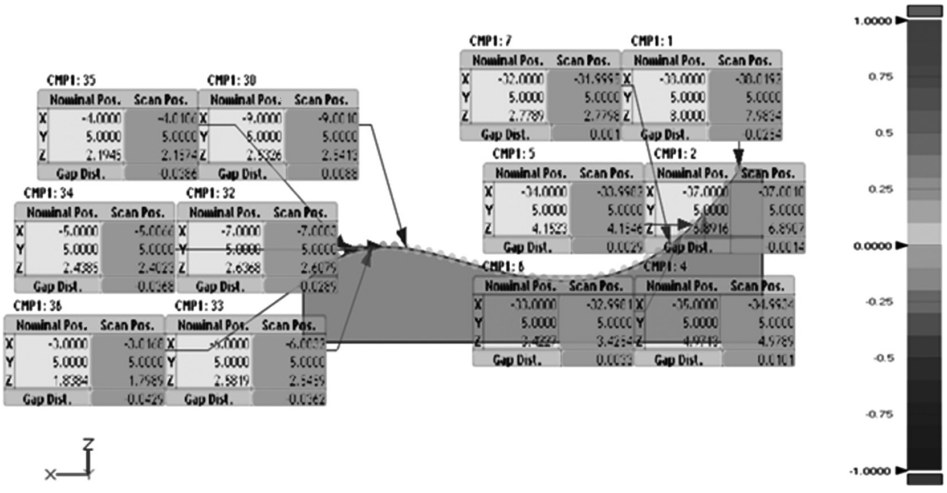

Figure 13: Assigned control points and numerical outcomes
Slika 13: Pripadajoče kontrolne točke in numerično dosežene

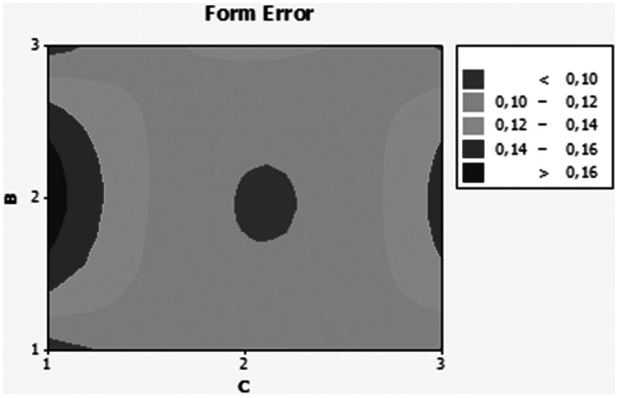

Figure 14: The effect of the roughing-cut strategy (B) and the finishing-operation strategy (C) on the form error
Slika 14: Učinek strategije grobe (B) in fine obdelave (C) na napako oblike

data, which is obtained in the first step. It should be noted that these surfaces are machined with a roughing-cut strategy, since we were expecting the surface errors to be large compared to the finishing operation strategy case. The effect of the roughing-cut strategy (B) and the finishing-operation strategy (C) on the form error results, which are the deviation from the CAD model, are presented in **Figure 14**.

4.3 Influence of the Cutting Tool Diameter on the Form Error

In rough machining strategies, when a ball-end mill with a large diameter is used, the form error increases (**Figure 15**). In particular, in the Zigzag_latitudinal machining method, with a 12-mm-diameter cutting tool, the form-error values increase. When an 8-mm-diameter cutting tool is used in the sweep_latitudinal process method, a finishing strategy, the form error had high values (**Figure 16**). These high values show that the cutter tool started machining from the workpiece and the machining is on the entries and exits where the process is finished.

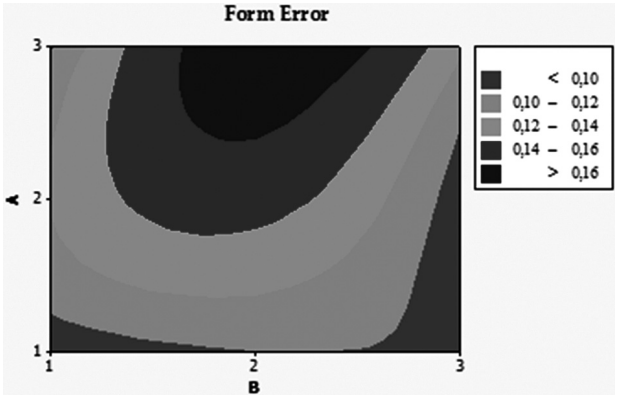

Figure 15: The effect of the cutting-tool diameter (A) and the roughing-cut strategy (B) on the form error
Slika 15: Vpliv premera orodja (A) in strategije grobe obdelave na napako oblike

4.4 Form Error and Surface Roughness Optimization

Implementations of the Grey relational analysis method, whose implementation steps were presented in the previous section, were made. First of all, normalization was performed according to the "lowest-is-the-best" approach and then, deviations from the reference series were calculated. Afterwards, the Grey relational degree of each experiment was calculated and the experiments were sorted with respect to their Grey relational degrees.

When the experimental results given in the table are normalized according to the "lowest-is-the-best" approach, the values in **Table 6** are obtained.

Table 6: Normalization outcomes
Tabela 6: Normalizirani izsledki

Exp. No.	Surface Roughness *Ra* (μm)	Form Error (mm)
1	0.835	1.000
2	0.853	0.849
3	0.000	0.884
4	0.824	0.605
5	0.224	0.291
6	0.700	0.965
7	0.524	0.860
8	1.000	0.000
9	0.771	0.558

Table 7: Values of the deviation from the reference value
Tabela 7: Deviacije od referenčne vrednosti

Exp. No.	Surface Roughness *Ra* (μm)	Form Error (mm)
1	0.165	0.000
2	0.147	0.151
3	1.000	0.116
4	0.176	0.395
5	0.776	0.709
6	0.300	0.035
7	0.476	0.140
8	0.000	1.000
9	0.229	0.442

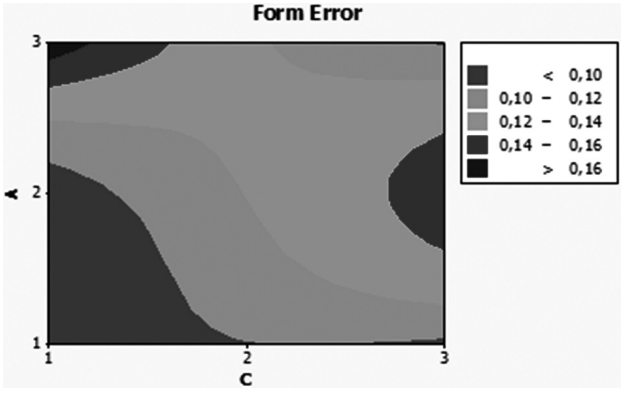

Figure 16: The effect of cutting-tool diameter (A) and the finishing-operation strategy (C) on the form error
Slik 16: Učinek premera orodja (A) in strategije kočne operacije (C) na napako oblike

The deviation values, which were obtained by removing the normalization outcomes of the surface roughness and the form error calculated from the reference value, are given in **Table 7**.

The Grey relational coefficient values of each output variable are given in **Table 8**.

Table 8: Grey relational coefficients
Tabela 8: Koeficienti Grey odvisnosti

Exp. No.	Surface Roughness *Ra* (μm)	Form Error (mm)
1	0.752	1.000
2	0.773	0.768
3	0.333	0.811
4	0.739	0.558
5	0.392	0.413
6	0.625	0.935
7	0.512	0.782
8	1.000	0.333
9	0.685	0.531

The Grey relational degrees related to each experiment are presented in **Table 9**.

Table 9: Grey relational degrees
Tabela 9: Stopnje Grey odvisnosti

Exp. No.	Grey Relational Degree	Sorting
1	0.876	1
2	0.770	3
3	0.572	8
4	0.649	5
5	0,403	9
6	0.780	2
7	0.647	6
8	0.667	4
9	0.608	7

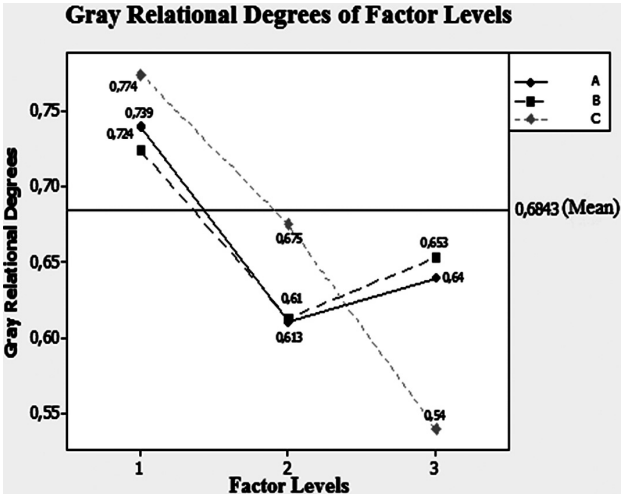

Figure 17: Grey relational degrees of factor levels
Slika 17: Stopnja odvisnosti za nivoje faktorjev

The calculated Grey relational degrees of the factor levels are presented in **Figure 17** and **Table 10**.

Table 10: Grey relational degrees of the factor levels
Tabela 10: Nivoji faktorjev Grey odvisnosti

	Factors		
	A	B	C
Level 1	0.739	0.724	0.774
Level 2	0.610	0.613	0.675
Level 3	0.640	0.653	0.540

As seen in the table, A1, B1 and C1 were detected as the most effective parameters on the outcome. The factor levels that will represent the lowest form error and surface roughness value under the conditions for the machining parameters and the limitations in the experimental design were determined in the above-mentioned way.

4.5 The Correlation between the Cutting Force and the Form Error

The cutting forces for the roughing cut and finishing operation were measured with a Kistler 9265B transducer during the cutting operation. Cutting forces occurred during the finishing operation, which has an actual impact on the form error, were the evaluated and the correlation between form error and cutting force were examined.

When the cutting force values obtained from the finishing operation were examined, it was determined that the greatest cutting force was obtained in the fifth and the eighth experiments. From the analysis of the remaining chips it was observed that the maximum number of chips remained in the fifth and eight experiments after the roughing cut and as a result of this situation. This leads to the highest cutting force having taken place in the afore-mentioned experiments.

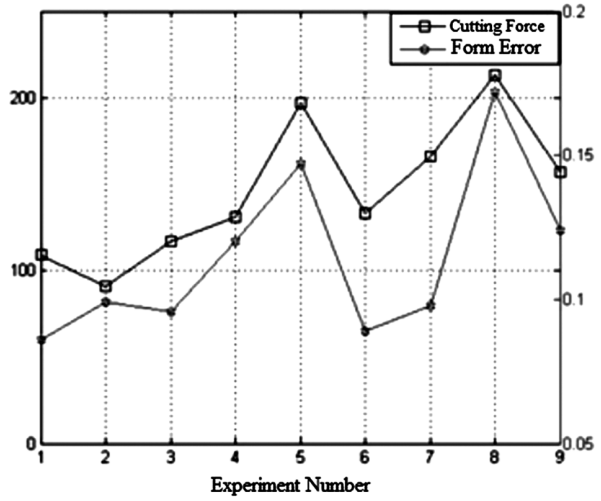

Figure 18: Graphical illustration of the relationship between the cutting force and the form error
Slika 18: Grafični prikaz odnosa med silo rezanja in napako oblike

The correlation between the cutting force and the form error is graphically exhibited in **Figure 18** and also numerically displayed in **Table 11**.

Table 11: Numerical illustration of the relationship between the cutting force and the form error
Tabela 11: Številčni prikaz odnosa med silo rezanja in napako oblike

Exp. No.	A	B	C	Cutting Force (N)	Form Error (mm)
1	1	1	1	109	0.0859
2	1	2	2	91	0.0991
3	1	3	3	117	0.0958
4	2	1	2	131	0.1203
5	2	2	3	197	0.1471
6	2	3	1	133	0.0890
7	3	1	3	166	0.0978
8	3	2	1	213	0.1721
9	3	3	2	157	0.1239

5 CONCLUSIONS

It was determined that surfaces are perfect within the limits of the machining tolerance, and that differences exist between the design and machined surface. This stems from the displacement that occurred in the cutting tool, on which the forces during cutting have an effect and a uniform chip thickness is not conserved. For the finishing operation when a SSYI operation with two schemas is performed, before a semi-roughing operation in the package programs, different amounts of chips remain, depending on the roughing-cut strategy and the cutting-tool diameter. This situation leads to an increase in the cutting forces during the finishing operation and, consequently, to a directly proportional increase in the form error. Therefore, in this case, the use of a semi-roughing operation will decrease the form error and the maximum number of chips remained in experiments numbers 5 and 8 (roughing cut strategy: Zigzag_latitudinal). As result, the maximum form error was obtained in experiments 5 and 8 and there is a proportional relationship between the cutting force and the form error. In addition, it was found that, as the cutting-tool diameter increases, the roughness decreases considerably. The optimum parameters were found to be A1, B1 and C1 through the Grey relational analysis method.

In further studies, an algorithm may be developed for a compensation of the form error that can be integrated into the CAM programs and so its validity can be checked.

6 REFERENCES

[1] E. Bagci, The optimization of machining conditions and strategies for the enhancement of form tolerance and surface roughness values in three-axis sculptured surface machining, PhD Thesis, Institute for Graduate Studies in Pure and Applied Sciences, Istanbul 2010

[2] Y. K. Choi, A. Banerjee, Tool path generation and tolerance analysis for free-form surfaces, International Journal of Machine Tools & Manufacture, 47 (**2007**), 689–696

[3] K. A. Desai, P. V. M. Rao, Effect of direction of parameterization on cutting forces and surface error in machining curved geometries, International Journal of Machine Tools & Manufacture, 48 (**2008**), 249–259

[4] B. W. Ikua, H. Tanaka, F. Obata, S. Sakamoto, T. Kishi, T. Ishii, Prediction of cutting forces and machining error in ball end milling of curved surfaces – II Experimental verification, Journal of the International Societies for Precision Engineering and Nanotechnology, 26 (**2002**), 69–82

[5] G. M. Kim, P. J. Cho, C. N. Chu, Cutting force prediction of sculptured surface ball-end milling using Z-map, Int J Mach Tools Manufacture, 40 (**2000**) 2, 277–291

[6] M. Kaymakci, I. Lazoglu, Tool Path Selection Strategies For Complex Sculptured Surface Machining, Mach. Science and Techn., An International Journal, 12 (**2008**) 1, 119–132

[7] V. G. Dhokia, S. Kumar, P. Vichare, S. T. Newman, An intelligent approach for the prediction of surface roughness in ball-end machining of polypropylene, Robotics and Computer-Integrated Manufacturing, 24 (**2008**), 835– 842

[8] A. Antoniadis, C. Savakis, N. Bilalis and A. Balouktsis, Prediction of surface topomorphy and roughness in ball-end milling, Int J Adv Manuf Technol, 21 (**2003**), 965–971

[9] M. Kurt, S. Hartomacioglu, B. Mutlu, The effect of cutting tool geometry and machining strategies on form error during free form surface machining, International Science and Technology Conference, Famagusta, 2010, 701–707

[10] B. K. Choi, B. H. Kim, R. B. Jerard, Sculptured Surface NC Machining, Handbook of Computer Aided Geometric Design, North-Holland 2002, 543–574

[11] E. M. Trent, P. K. Wright, Metal Cutting, 4th ed., Butterworth-Heinemann, USA, 2000, 16–17

[12] http://www.helix-tools.com

[13] P. N. Singh, K. Raghukandan, B. C. Pai, Optimization by Grey relational analysis of EDM parameters on machining Al–10%SiCP composites, Journal of Materials Processing Technology, 155–156 (**2004**), 1658–1661

[14] N. Tosun, Determination of optimum parameters for multi-performance characteristics in drilling by using grey relational analysis, Int J Adv Manuf Technol, 28 (**2006**), 450–455

[15] http://www.defnemuhendislik.com/en.html

UDK 621.791:669.715
Original scientific article/Izvirni znanstveni članek

ISSN 1580-2949
MTAEC9, 46(3)215(2012)

FRICTION-STIR WELDING OF HIGH-STRENGTH ALUMINIUM ALLOYS AND A NUMERICAL SIMULATION OF THE PLUNGE STAGE

VRTILNO TORNO VARJENJE VISOKOTRDNIH ALUMINIJEVIH ZLITIN IN NUMERIČNA SIMULACIJA FAZE TALJENJA

Milenko Perovic[1], Darko Veljic[2], Marko Rakin[3], Nenad Radovic[3], Aleksandar Sedmak[4], Nikola Bajic[2]

[1]Chamber of Economy of Montenegro, Podgorica, Montenegro
[2]IHIS Science & Technology Park Zemun, Belgrade, Serbia
[3]Faculty of Technology and Metallurgy, University of Belgrade, Serbia
[4]Faculty of Mechanical Engineering, University of Belgrade, Serbia
mperovic@pkcg.org

Prejem rokopisa – received: 2011-09-12; sprejem za objavo – accepted for publication: 2012-01-27

This paper defines a set of welding parameters for the Friction-Stir Welding (FSW) of two forged panels of the alloy EN AW 7049A in a T652 temper and discusses the plunge stage of FSW using numerical modeling. This multi-component aluminum alloy is characterized by high strength, reduced plasticity and poor weldability. Observations of the macrostructure and microstructure clearly showed typical zones of a FSW joint and the appropriate grain sizes. The finest grains were observed within the nugget, while the coarsest grains are found to be in the HAZ. The ultimate tensile strength is 80.3 % of the parent material. A coupled thermo-mechanical model was developed to study the temperature fields and the plunge force of the alloy EN AW 7049A under different rotating speeds, (300, 400 and 500) r/min, during the FSW process of the plunge stage. A three-dimensional FE model has been developed in ABAQUS/Explicit using the arbitrary Lagrangian–Eulerian formulation, the Johnson–Cook material law and Coulomb's Law of Friction. Numerical results indicate that the maximum temperature in the FSW process can be increased with an increase in the rotational speed, which can be used to reduce the plunge force.

Keywords: friction-stir welding, welding parameters, metallography, mechanical test, numerical simulation, plunge stage, temperature, force

V članku je opisana vrsta parametrov za vrtilno torno varjenje (FSW) dveh kovanih panelov iz zlitine EN AW 7049A, popuščene po T652, in talilna faza FSW z uporabo numeričnega modeliranja. Za to večkomponentno aluminijevo zlitino so značilne visoka trdnost, majhna plastičnost in slaba varivost. Opazovanja makro- in mikrostrukture so jasno pokazala tipične cone FSW-spoja in ustrezne velikosti zrn. Raztržna trdnost je pri 80,3 % trdnosti osnovnega materiala. Povezan termomehanski model je bil razvit za raziskovanje temperaturnih polj in silo taljenja EN AW 7049A-zlitine pri različnih hitrosti vrtenja (300, 400 in 500) r/min med vrtilnim tornim varjenjem za talilno fazo FSW-procesa. Tridimenzionalni FE-model je bil razvit v ABAQUS/Explicit z uporabo arbitrarne Lagrange-Eulerjeve formulacije, Johnson-Cookovih zakonov o materialu in Coulombovega zakona o trenju. Numerični rezultati kažejo, da se lahko najvišja temperatura pri FSW-procesu poviša s povečanjem hitrosti vrtenja, ki lahko zmanjša silo potopa.

Ključne besede: vrtilno torno varjenje, varilni parametri, metalografija, mehanski preizkusi, numerična simulacija, faza taljenja, temperatura, sila

1 INTRODUCTION

Friction-Stir Welding (FSW) is a solid-state joining technique invented and patented in the late 1991 by The Welding Institute (TWI) at Cambridge, U. K.[1]

FSW is a process, in which a specially shaped cylindrical tool is rotated and plunged into the abutting edges of the parts to be welded as shown in **Figure 1**[1–3]. As the tool is moved along the joint line, the friction from the rotating tool heats the material to the extent that it plastically deforms and flows from the front of the tool to the back, where it subsequently cools and produces a weld, i.e., a weld is created by a combined action of frictional heating and mechanical deformation due to the rotating tool. The tool has a circular section except at the end where there is a threaded probe, or a more complicated flute, and the junction between the cylindrical portion and the probe is known as the shoulder. The probe penetrates the welding plate, while the shoulder rubs against the top surface. The use of FSW provides

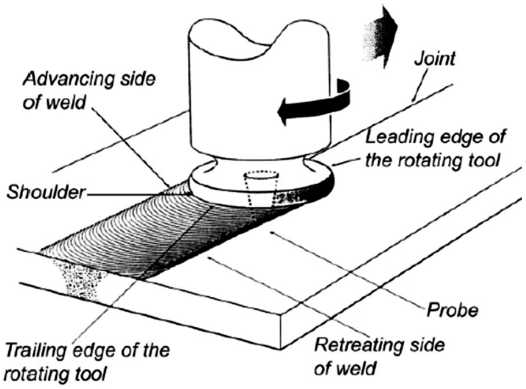

Figure 1: Schematic illustration of the FSW process[4]
Slika 1: Shematičen prikaz FSW-varjenja[4]

high-quality welds, without any void, cracking or distortion, of the materials that typically exhibit poor fusion weldability. The development of the welding technology comprises an estimation of the optimum rotation and translational speeds, with an aim to introduce the optimum heating (frictional and adiabatic). Different factors influence these parameters, like the type of the base material (a set of mechanical and physical properties), the thickness of the plates, the forging force, etc.

FSW is a very modern welding process with a great future use, primarily due to a variety of possible combinations of dissimilar materials to be welded and the possibility to be controlled efficiently. FSW can be used for joining many types of materials and material combinations: aluminum and its alloys, copper and its alloys, lead-magnesium alloys, magnesium and aluminum, zinc, titanium and its alloys, mild steel, and metal matrix composites (MMCs) based on aluminum and plastics[4].

A friction-stir weld joint in aluminum alloys consists of four major microstructural zones as shown in **Figure 2**.

The heat-affected zone (HAZ) lies close to the weld center. The material has experienced a thermal cycle, so the modifications in mechanical properties and in the microstructure are noticed. However, no plastic deformation occurs in this zone. The thermo-mechanically affected zone has been plastically deformed by the friction-stir welding tool, and the heat from the process also exerts some influence on the material. The weld nugget represents a recrystallized area in the TMAZ in aluminum alloys.

Compared with the conventional welding techniques, FSW possesses many advantages, such as the absence of melting, a low number of defects, low distortion, etc. FSW can even join thin and thick sections. The process can be applied to produce both butt and lap joints as well as T-joints. FSW is being successfully applied to the aerospace, automobile and shipbuilding industries.

The presence of defects in the form of cracks in the welded joints, caused by the melting of high-strength aluminum alloys is a very serious technological problem. It is particularly problematic in the case of the alloy series EN AW 7XXX (Al-Zn-Mg-Cu). Due to this limitation, the application of these alloys had been significantly hampered before the introduction of FSW into the mass production, at the end of the last century. The introduction of FSW has significantly improved their weldability and broadened the application of various welded components, including even some very complex elements used in the aerospace industry and in the military production. In the case of EN AW 7049A, which is a multi-component alloy of a quadruple phase composition, high strength is accomplished with the thermal precipitation based on the particles with various chemical compositions. For example, in addition to improving the hardness of the alloy, an addition of copper also results in improved plasticity, resistance to fatigue and stress corrosion[6].

The aim of this paper is to suggest the parameters for experimental welding of two forged panels made of the EN AW 7049A alloy in a T652 temper and to evaluate the plunge stage by using numerical modelling.

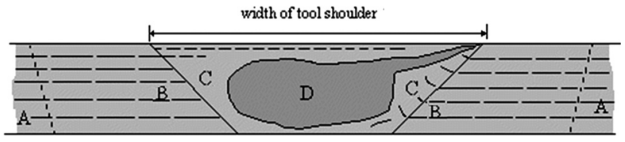

Figure 2: Microstructure of the transverse cross-section.[5] A: Base material/unaffected material, B: Heat-affected zone (HAZ), C: Thermo-mechanically affected zone (TMAZ), D: Weld nugget (Part of the thermo-mechanically affected zone)

Slika 2: Mikrostruktura na prečnem prerezu.[5] A: osnovni material, B: toplotno vplivana cona (HAZ), C: termomehansko vplivana cona (TMAZ), D: varilni koren (del termo-mehansko vplivane cone)

2 EXPERIMENT – FSW

2.1 Preparation of the welding plate

Friction-stir welding is conducted on thermally processed and machine prepared forged elements with

Figure 3: Thermally processed and machine prepared forged elements for FSW with the dimensions of 180 mm × 65 mm × 5 mm

Slika 3: Termično procesirane, obdelane pripravljene kovane plošče dimenzije 180 mm × 65 mm × 5 mm, pripravljene za FSW

Figure 4: Specimen for sample making with the dimensions of 680 mm × 580 mm × 13 mm

Slika 4: Plošča za pripravo vzorcev dimenzij 680 mm × 580 mm × 13 mm

the dimension of 180 mm × 65 mm × 5 mm (**Figure 3**), made of an alloy produced in commercial industrial conditions. A specimen for sample making was a panel with the dimensions of 680 mm × 580 mm × 13 mm (**Figure 4**), a hardness of 175 HB, and made of raw aluminium, where the alloying elements were added as clean metal alloys, or master alloys. It passed all phases of the technological procedure: thermo-mechanical processing, casting of a raw billet, two-level homogenisation, cutting and preparation for forging, free forging and forging in a tool, hardening, pressing of 1 % and 3 %, and artificial ageing.

To eliminate the potential heat influence on the initial microstructure and on the experimental results, the panels were cut with a water jet and afterwards skimmed of saw chips, and made in specified measurements with an intensive cooling of the treated surface.

2.2 Material properties

The chemical composition of EN AW 7049A-T652 aluminium, obtained by using an OE quantometer ARL with electronic samples "Pechiney", is as follows: Aluminum (Al) – Balance, Cu – 1.45, Mg – 2.15, Mn – 0.27, Fe – 0.23, Si – 0.10, Zn – 7.20, Ti – 0.015, Cr – 0.13, Zr – 0.13, V – 0.004, B – 0.003. The thermal and mechanical properties used in this model are given in **Table 1**.

Table 1: Mechanical characteristics of the parent material EN AW 7049A[7]
Tabela 1: Mehanske lastnosti osnovnega materiala EN AW 7049A[7]

Material properties	Value
Young's Modulus of Elastic (GPa)	71.7
Poisson's Ratio	0.33
0.2 % Yield Strength $R_{0.2}$/MPa	570
Tensile Strength R_m/MPa	650
Thermal Conductivity (W/(m K))	130
Coefficient of Thermal Expansion ($°C^{-1}$)	24.7×10^{-6}
Density (kg/m³)	2810
Specific Heat Capacity (J/(kg °C))	960
Temperature Melt (°C)	477
Elongantion A, %	7.5

2.3 Equipment for the procedure implementation, tools and process parameters

Experimental welding was performed with an adapted machine tool – a universal vertical milling machine, with the power of the electromotor driving the vertical milling-machine arbor being 18 kW, a gradual setting of the number of revolutions being between 80 r/min and 1450 r/min and the traverse speed ranging from 12.4 mm/min to 175 mm/min. The image of the machine is given in **Figure 5**. The backing plate with the dimensions of 300 mm × 200 mm × 25 mm (**Figure 6**), made of quenched and tempered steel 42CrMo4, thermally processed at 850 MPa and surface tempered at

Figure 5: Tool for the friction-stir welding with a backing plate on water desk
Slika 5: Orodje za vrtilno torno varjenje s podporno ploščo na vodni mizi

Figure 6: Backing plate
Slika 6: Podporna plošča

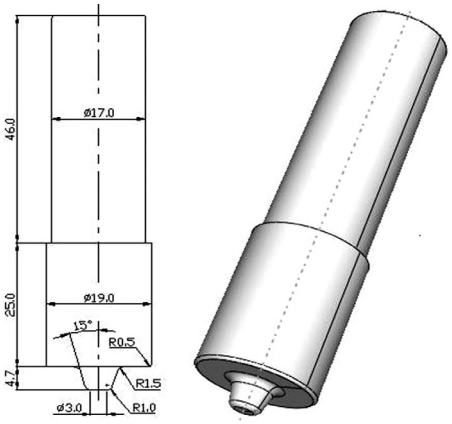

Figure 7: Welding tool used for the experiment and numerical analysis
Slika 7: Varilno orodje, uporabljeno za preizkuse in numerično analizo

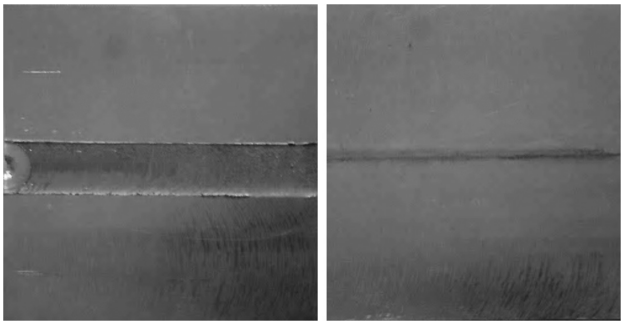

Figure 8: Photographic presentation of the face and the reverse of a welded joint
Slika 8: Posnetek prednje in hrbtne strani zvarjenega spoja

(44 ± 2) HRc, was fastened to a workbench with an improvised machine for FSW. The welding tool was inserted in the fastened head of the main milling-machine arbor and it is presented in **Figure 7**. The material of the tool is steel x155CrVMo121. The tool was thermally treated up to the surface hardness of (61 ± 1) HRc.

The pieces were fastened to the backing plate without turning down the edges and after that the vertical head of the milling machine, with the inserted tool in the tapered elastic capsule, was placed in the contact position on the central line of the joined pieces. All the process parameters were held constant during the welding. The welding parameters in the plunge phase were as follows: the plunge speed was 12 mm/min, the plunge depth of the pin was 4.9 mm, the plunge depth of the shoulder was 0.2 mm, the rotation speed was 400 r/min, the plunge time was 24.5 s. The welding parameters in the linear welding phase were as follows: the plunge depth of the shoulder was 0.2 mm, the rotation speed was 400 r/min, and the welding speed was 24 mm/min.

The welded experimental panel, whose appearance after the welding is presented in **Figure 8**, was tested on a hypersonic device with a flat probe and with the beam-transmission direction going from the bottom side towards the face of the metal weld in order to find any possible occurance of a metal discontinuity in the sample.

2.4 Mechanical testing of a welded joint of EN AW 7049A T652

The tensile test is conducted in accordance with the standard MEST EN 10002-1:2008 on the machine INSTRON 105. The test results obtained from the specimens taken normally from the welding direction are given in **Table 2**. The yield point is an apparent value measured at the elongation of 0.2 %. The tensile strength of a welded joint is about 20 % lower than that of the parent material and the apparent yield stress is almost a third bigger in the parent material than in a welded joint. The crack location of a specimen on the tension test is situated in the transition zone going from the nugget to the remaining zone of the thermomechanically affected zone.

Table 2: Mechanical characteristics of the welded joint of EN AW 7049A T652
Tabela 2: Mehanske lastnosti zvarjenega spoja EN AW 7049A T652

Trial number	Mechanical properties		
	$R_{0.2}$ /MPa	R_m/MPa	A/%
1	384	522	9.5

2.5 Microstructural evaluation

Due to the etching in the Keller's reagent, the macrostructure of the welded metal was clearly differentiated, as shown in **Figure 8**. The advancing and the retreating sides of the two regions, right and left from the centre of the welded joint, are also clearly visible. These are the

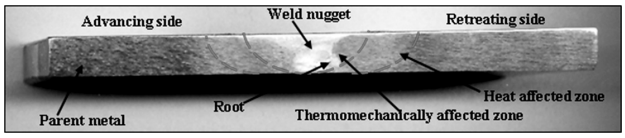

Figure 9: Macrostructure of a FSW joint
Slika 9: Makrostruktura FSW-spoja

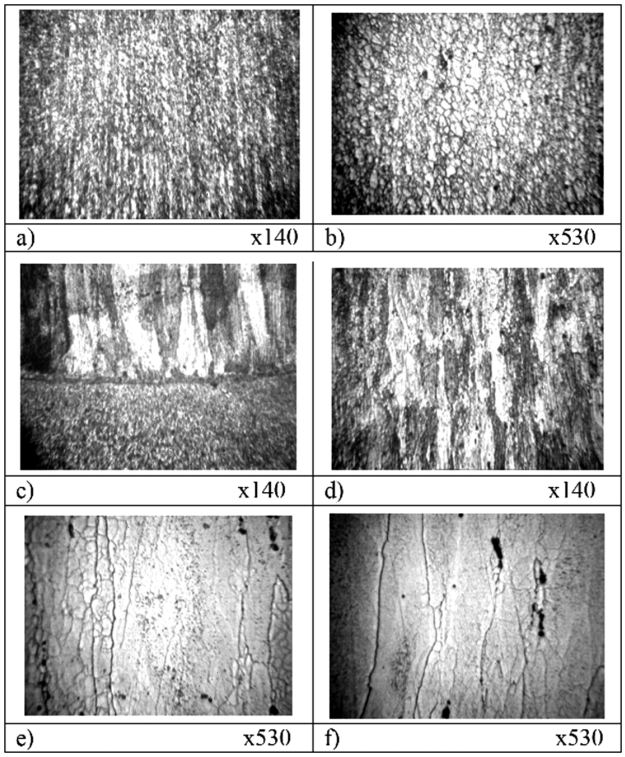

Figure 10: Microstructures obtained in a weld joint of a FS welded EN AW 7049A T652 alloy: a) weld root, b) nugget, c) transition zone between the nugget area and the thermomechanical influence, d) thermomechanicly affected zone, e) heat affected zone and f) base material zone
Slika 10: Mikrostruktura v zvarjenem FSW-spoju zlitine EN AW 7049A T652: a) koren zvara, b) jedro, c) prehod med jedrom in področjem termomehanskega vpliva, d) cona termomehanskega vpliva, e) cona toplotnega vpliva in f) osnovni material

side, where the directions of the tool-rotation vector and the welding-speed vector overlap, and the side where they have opposite directions. The macrostructure consists of the thermomechanically affected zone, the heat affected zone and the base metal zone, as shown in **Figure 9**. The thermomechanically affected zone (TMAZ) has two recognizable areas: the weld nugget and the weld root although there are authors who consider the nugget zone to be separate from the welded joint, including the root as its part.

A metallographic analysis of the sample was executed with the light microscope NEOPHOT 21 having magnifications of 100-times and 1000-times. The thermomechanically affected zone in the nugget and the root region is situated at the place of the pin-tool traverse and immediately underneath its top. This is a fine-grained recrystalized zone, slightly displaced toward the back side, as shown in **Figures 10a** and **b**. The transition region of these areas in the thermomechanically affected zone is clearly visible even with small magnifications: small equiaxed grains are in the nugget, while the larger grains are placed within the TMAZ, as shown in **Figure 10c**. The remaining part of the TMAZ zone is dominantly characterized with deformed grains and its structure consists of larger grains, shown in **Figure 10d**. The neighbouring, heat affected zone (HAZ), is characterized with the elongated grains with little recrystallized grains and with a series of intermetallic phases, shown in **Figure 10e**. Its microstructure is very simillar to the microstructure of the base material, shown in **Figure 10f**.

3 MODEL DESCRIPTION

A coupled thermo-mechanical three-dimensional FE model has been developed in ABAQUS/Explicit using the arbitrary Lagrangian–Eulerian formulation and the Johnson–Cook material law. The contact forces are modelled with Coulomb's Law of Friction, making the contact condition highly solution dependent[8–12].

3.1 Geometry, boundary conditions and the finite-element mesh

The dimension of the welding plate in the numerical model of the plunge stage is 50 mm × 50 mm × 5 mm. The three-dimensional numerical model is based on the C3D8RT element type, which is a thermo-mechanically coupled hexahedral element with 8-nodes, each having trilinear displacement and temperature degrees of freedom. This element produces a uniform strain (the first-order reduced integration) and contains hourglass control[12]. The mesh consists of 23608 nodes and 20972 elements. The tool and the backing plate are modeled as a rigid surface having no thermal degrees of freedom. The main tool geometry in the FE model is similar to the experimental tool shown in **Figure 6**. The numerical model of the welding plate, the tool and the backing plate is shown in **Figure 11**.

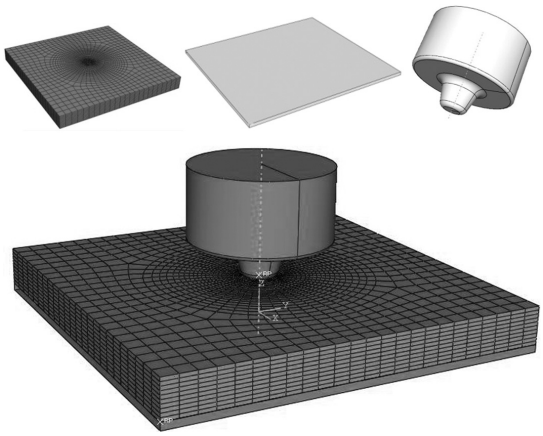

Figure 11: Numerical model of the welding plate, the tool and the backing plate

Slika 11: Numerični model varilne plošče, orodje in podporna plošča

3.2 Thermal model

In general, heat generation comes from two sources: the frictional heating at the tool welding plate interface and the plastic energy dissipation due to shear deformation in the nugget zone. The governing equation for the heat-transfer process during the plunge phase of the FSW process can be written as:

$$\rho c \frac{\partial T}{\partial t} = \frac{\partial T}{\partial x}\left[k_x \frac{\partial T}{\partial x}\right] + \frac{\partial T}{\partial y}\left[k_y \frac{\partial T}{\partial y}\right] + \frac{\partial T}{\partial z}\left[k_z \frac{\partial T}{\partial z}\right] + \dot{q}_p \quad (1)$$

where ρ is the density, c is the specific heat, k is the heat conductivity, T is the temperature, t is the time, $\dot{q}_p$ is the heat generation coming from the plastic energy dissipation due to shear deformation, and x, y, and z are spatial coordinates[12–17]. The rate of the heat generation due to the plastic energy dissipation, $\dot{q}_p$, is computed from:

$$\dot{q}_p = \eta \sigma \dot{\varepsilon}^{pl} \quad (2)$$

where η is the factor of converting mechanical to thermal energy (0.9)[12], σ is the shear stress, and $\dot{\varepsilon}^{pl}$ is the rate of the plastic strain. The heat generation caused by the frictional heating between the tool and the work pieces can be written as:

$$\dot{q}_f = \frac{4}{3}\pi^2 mPNR^3 \quad (3)$$

where $\dot{q}_f$ is the frictional heat generation, μ is the coefficient of friction, P is the traction, N is the rotational speed and R is the surface radius.

3.3 Johnson-Cook elastic–plastic model

In the thermo-mechanically affected zone (TMAZ) a very large deformation takes place during the process. The interaction of the flow stress with the temperature, the plastic strain and the strain rate is essential for

modeling the FSW process. For this reason the Johnson-Cook elastic–plastic model is selected. The formulation for this model is empirically based. The elastic–plastic Johnson–Cook material law is given by[9]:

$$\sigma_y = \left[A + B(\varepsilon_p)^n\right] \cdot \left[1 + C\left(\frac{\dot{\varepsilon}_p}{\dot{\varepsilon}_0}\right)\right] \cdot \left[1 - \left(\frac{T - T_{\text{room}}}{T_{\text{melt}} - T_{\text{room}}}\right)^m\right] \quad (4)$$

where T_{melt} = 477 °C is the melting point or the solidus temperature, T_{room} = 20 °C is the ambient temperature, T/°C is the effective temperature, A = 570 MPa is the yield stress, B = 350 MPa is the strain factor, n = 0.4 is the strain exponent, m = 1.5 is the temperature exponent, C = 0.12 the strain rate factor. A, B, C, n, T_{melt}, T_{room} and m are the material/test constants for the Johnson–Cook strain-rate dependent yield stress for 7049A T652[12].

4 RESULTS AND DISCUSSION

The analysis of the experimental welding of the forged panels of alloy EN AW 7049A in the state of the maximum-hardness values (T652) showed that the elongation of the welded joint is bigger than that of the parent material, which can be explained with the formation of a structure with small grains in the mixed zone.

A coupled thermo-mechanical model was developed to study the temperature fields and the plunge force of alloy EN AW 7049A under different rotating speeds: (300, 400 and 500) r/min during the FSW process of the plunge stage. **Figure 11** shows the coordinates of point T(9.5, 0, 0) used for measuring the temperature dependence of the time.

The heat transfer through the bottom surface of the welding plate is controlled with the heat transfer coefficient of 1000 W/(m^2 K). A constant friction coefficient of 0.3 is assumed between the tool and the welding plate and the penalty contact method is used to model the contact interaction between the two surfaces. The heat convection coefficients on the surface of the welding plate are h = 10 W/(m^2 K) with the ambient temperature of 200 °C [9]. **Figure 12** shows the temperature fields in the transverse cross-section near the tool/matrix interface after 22.8 s, when the plunge speed is 12 mm/min and the rotation speed is 400 r/min. The temperature field is symmetric.

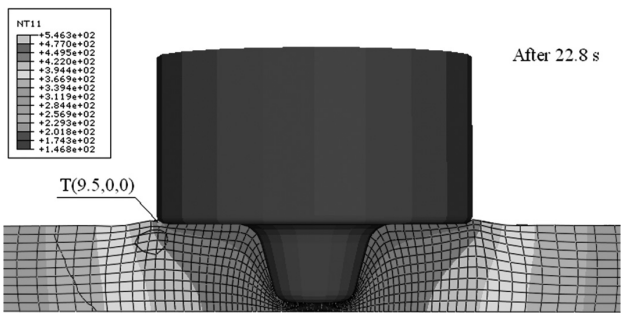

Figure 12: Temperature fields in the transverse cross-section near the tool/matrix interface after 22.8 s, when the rotation speed is 400 r/min and the plunge speed is 12 mm/min

Slika 12: Temperaturna polja na prečnem prerezu blizu mejne površine orodje – matica po 22,8 s, ko je bila hitrost vrtenja 400 r/min in hitrost trna 12 mm/min

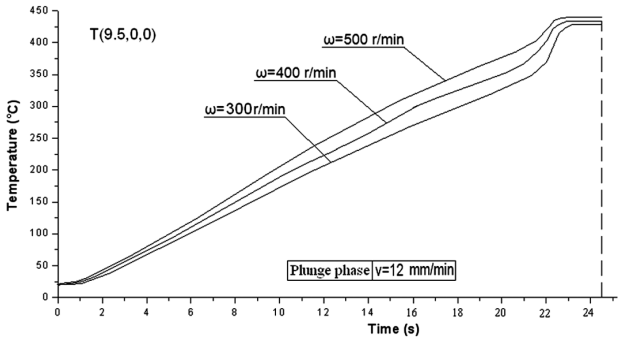

Figure 13: Temperature dependence of the time (point T) during the plunge stage

Slika 13: Razmerje med časom in temperaturo (točka T) v območju trna

Figure 13 shows the temperature dependence of the time for the plunge stage, when the rotation speeds are (300, 400 and 500) r/min in point T(9.5,0, 0).

Numerical results indicate that the temperature in the FSW process can be increased with an increase in the rotational speed and that the maximum temperature is lower than the melting point of the welding material (T_{melt} = 477 °C – **Figure 12**). The maximum temperature created by the FSW ranges from 80 % to 90 % of the melting temperature of the welding material.

Figure 14 shows the plunge-force dependence of the time during the plunge stage of the FSW process. At the start of the FSW, during the initial plunging, due to a lack of generated heat, deformation strengthening occurs, leading to an increase of force, Pos1. After establishing the contact between the rotating pin and the welding plate, the generated heat leads to an increase in the temperature. This temperature increase decreases the

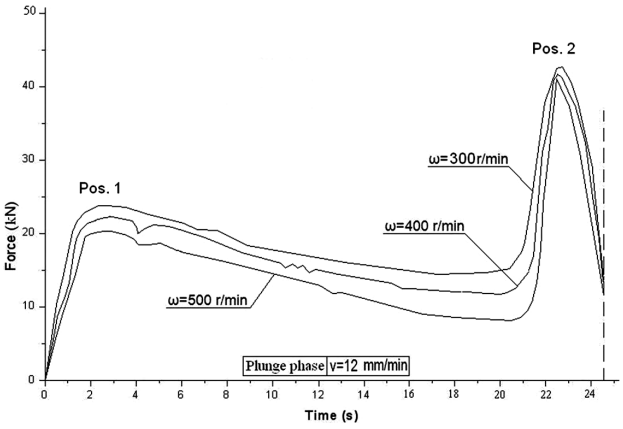

Figure 14: Force dependence of the time during the plunge stage

Slika 14: Odvisnost med silo in časom v območju trna

resistance to deformation, both though easier cross-slip and possible recovery and/or recrystallization. The resulting behavior is a decrease in force with a prolongation of time. This trend continues until the moment of contact between the tool shoulder and the welding plate when the force experiences a sharp increase, followed by an equally sharp decrease. The increase is related to the friction between the cold tool shoulder and the welding plate. Again cold deformation and work hardening occur prior to the heating introduced by the friction. The intense heat generation leads to a deformation under high temperatures, resulting in a decrease of the resistance to deformation, i.e. to a sharp fall of force.

5 CONCLUSIONS

The observations of the macrostructure and the microstructure clearly showed typical zones of a FSW joint made of the EN AW 7049A – T652 alloy. The finest grains were observed within the nugget, while the coarsest grains were found to be in the HAZ. The ultimate tensile strength was at 80.3 % of the parent material. This behaviour is related to an intense plastic-deformation influence of the heat generated due to the surface-friction plastic deformation.

The temperature in the matrix under the tool must be lower than the melting temperature. The maximum temperature created by FSW ranges from 80 % to 90 % of the melting temperature of the welding material. When the rotational speed is increased, the region of high temperature can be increased. The temperature field is symmetric. After establishing the contact between the rotating pin and the welding plate, as well as the tool shoulder and the welding plate, the force starts to increase and reaches a peak value indicated by Pos 1 and Pos 2. The force drops from Pos 1 to Pos 2 because of the material plasticity and softens due to high stress and temperature increase. When the rotational speed is increased, the plunge force can be reduced.

6 REFERENCES

[1] H. Aydin, A. Bayram, U. Esme, Y. Kazancoglu, O. Guven, Application of grez relation analysis (GRA) and taguchi method for the parametic optimization of friction stir welding (FSW) process, Mater. Tehnol., 44 (**2010**) 4, 205–211

[2] D. Veljic, Technology of Friction Stir Welding of Aluminium Alloys, M.Sc. Thesis, Faculty of Mechanical Engineering, University of Belgrade

[3] Z. W. Chen, S. Cui, Tool-workpiece interaction and shear layer flow during friction stir welding of aluminium alloys, Transaction of Nonferrous Metal Society of China, 17 (**2007**), 258–261

[4] http://www.twi.co.uk

[5] http://www.twi.co.uk/ Microstructure Classification of Friction Stir Welds

[6] M. Vratnica, Microstructural properties and mechanical properties of highly hard aluminium alloys of different grade of purity, doctoral thesis, Faculty of Technology – Metallurgy, Belgrade, Serbia, 2000

[7] The Project of production planning for the alloy PD33 – internal report – SOUR Aluminium Plant Titograd, Titograd, SFRY, 1983

[8] Z. Zhang, J. Bie, H. Zhang, Effect of Traverse/Rotational Speed on Material Deformations and Temperature Distributions in Friction Stir Welding, J. Mater. Sci. Technol., 24 (**2008**), 907–913

[9] H. Schmidt, J. Hattel, A local model for the thermo-mechanical conditions in friction stir welding, Modelling Simul. Mater. Sci. Eng., 13 (**2005**), 77–93

[10] Abaqus Inc., Analysis – User's Manual v.6.7, 2007

[11] D. Veljic, M. Perovic, B. Medjo, M. Rakin, A. Sedmak, H. Dascau, Thermo-mechanical modeling of Friction Stir Welding, The 4th International Conference, Innovative technologies for joining advanced materials, Timisoara, 2010, 171–176

[12] H. Dascau, A. Sedmak, M. Rakin, D. Veljic, M. Perovic, B. Medjo, N. Bajic, Numerical simulation of the plunge stage in friction stir welding – different tools, The 5th International Conference, Innovative technologies for joining advanced materials, Timisoara, 15, 2011, 1–4

[13] K. Park, Development and analisys of ultrasonic assisted friction stir welding process, Doctor of Philosophy (Mechanical Engineering) in The University of Michigan, 2009

[14] S. Vijay, Thermo-mechanical and Microstructural Issues in Joining Similar and Dissimilar Metals by Friction Stir Welding, A Dissertation Presented to the Graduate Faculty of Mechanical Engineering Southern Methodist University, 2006

[15] H. Zhang, Z. Zhang, J. Chen, 3D modeling of material flow in friction stir welding under different process parameters, Journal of Materials Processing Technology, 183 (**2007**), 62–70

[16] S. Guerdoux, L. Fourment, 3D numerical simulation of different phases of friction stir welding, Modelling Simul. Mater. Sci. Eng., 17 (**2009**)

[17] M. Grujicic, T. He, G. Arakere, H. V. Yalavarthy, C. F. Yen, B. A. Cheeseman, Fully coupled thermomechanical finite element analysis of material evolution during friction-stir welding of AA5083, Proceedings of the Institution of Mechanical Engineers, Part B: Journal of Engineering Manufacture, 224 (**2010**) 4, 609–625

UDK 691:620.1:691.5
Original scientific article/Izvirni znanstveni članek

ISSN 1580-2949
MTAEC9, 46(3)223(2012)

MICROSTRUCTURAL AND PHYSICAL-MECHANICAL ANALYSES OF THE PERFORMANCE OF NANOSTRUCTURED AND OTHER COMPATIBLE CONSOLIDATION PRODUCTS FOR HISTORICAL RENDERS

MIKROSTRUKTURA IN FIZIKALNO-MEHANSKE LASTNOSTI NANOSTRUKTURNIH IN DRUGIH KOMPATIBILNIH PROIZVODOV ZA UTRJEVANJE ZGODOVINSKIH OMETOV

Giovanni Borsoi, Martha Tavares, Maria do Rosário Veiga, António Santos Silva

Laboratório Nacional de Engenharia Civil, Av do Brasil 101, Lisboa, Portugal
gborsoi@lnec.pt

Prejem rokopisa – received: 2011-09-27; sprejem za objavo – accepted for publication: 2012-02-24

The surface consolidation of historical renders, directed to restore cohesion and stability, is based on the use of materials with aggregating properties. This operation is usually achieved with the use of inorganic or mineral consolidants, which are preferred to organic ones, due to the better compatibility and durability.
Based on the results of previous studies, two mineral-compatible products were selected: a commercial dispersion of calcium hydroxide nanoparticles in propanol and a calcium-silicate product, consisting of a limewater dispersion of ethyl silicate. The consolidation products were applied to mortar specimens in order to assess their efficacy by determining their microstructural and physical-mechanical properties, before and after the consolidation treatment. Microstructural (optical and SEM microscopy) and chemical analyses of the consolidation products and of the consolidated samples were performed. The physical-mechanical analyses, i.e., the superficial hardness, is reported too.

Keywords: consolidation products, compatibility, nanoproducts, SEM/EDS

Utrjevanje površine zgodovinskih ometov z vidika ohranjanja kohezije in stabilnosti temelji na uporabi materialov z vezivno sposobnostjo. To se navadno doseže z uporabo neorganskih ali mineralnih utrjevalcev, ki so v prednosti pred organskimi zaradi boljše skladnosti in zdržljivosti.
Na podlagi predhodnih študij sta bili izbrani dve vezivi: komercialna disperzija delcev kalcijevega hidroksida v propanolu in proizvod na osnovi kalcijevega silikata, ki vsebuje apnovico, dispergirano v etil silikatu. Namen uporabe vzorcev veziv na vzorcih malte je bil ugotoviti njihovo učinkovitost z določitvijo mikrostrukture in fizikalno-mehanskih lastnosti, pred obdelavo z vezivom in po njej. Izvršene so bile raziskave mikrostrukture (svetlobna in SEM-mikroskopija), kemijska analiza vzorcev veziv in vzorcev po utrjevanju, fizikalno-mehanski preizkusi, poročamo pa tudi o trdoti površine.

Ključne besede: utrjeni proizvodi, kompatibilnost, nanoproizvodi, SEM/EDS

1 INTRODUCTION

A common degradation phenomenon in historic mortars is the loss of cohesion of the binder-aggregate system, which is usually followed by the superficial material loss and a loss of mechanical strength, usually as a consequence of chemical and biological phenomena that can modify the nature of the binder[1].

The restitution of cohesion between the mortar's particles, turned friable by the loss of binder, is achieved through the application of organic or mineral consolidants. The first experimentations on silicates, fluorides, barite and limewater were done in the 19th century[2]; subsequently in the 20th century there was the introduction of polymers, such as acrylics and epoxy resins, which are easier to apply and present better adhesiveness, but do not obey the fundamental rules of physical-chemical compatibility with the substrate. Inorganic consolidants are becoming preferred due to their better compatibility and durability; the best known inorganic consolidants are calcium hydroxide (limewater), barium hydroxide, ethyl silicate, calcium oxalate and calcium tartrate.

The aim of this work is the experimental characterization of two different, compatible, consolidant products, i.e., a traditional compatible product, such as a limewater, mixed with ethyl silicate, and a commercial alcoholic dispersion of nanoparticles of calcium hydroxide, which presents an innovative consolidant product.

2 MATERIALS

2.1 Specimens – Mortar samples preparation

In order to simulate a mortar with a loss of cohesion, different mortar specimens were prepared; the binder/aggregate ratio of 1 : 4 (in volume) was chosen in order to get the desired effect of a low-cohesion mortar, without significant loss of material. The aggregate used was graduated siliceous sand obtained from a mixture of three different calibrated sands with mean particle sizes <2 mm. After the optimization of the mortar composition, different samples were prepared, such as mortar

prisms 40 mm × 40 mm × 160 mm and ceramic bricks 28 cm × 19 cm with a single mortar layer of 1.5 cm thickness.

2.2 Properties and application of the consolidant products on lime-mortar specimens

The effectiveness of the limewater, considered the most traditional consolidant product, is known and previous studies provided good results[3,4], beyond the economic advantage and full compatibility. However, limewater usually contains not more than 2 g/L of calcium hydroxide, which only guarantees a low consolidation effect[2], unless it is applied in a large number of cycles.

We have decided to explore the efficiency of limewater, matured in a closed container for some years, mixed with a commercial ethyl silicate (Estel 1000®, CTS). The application of this product causes the formation of amorphous silica gels, which act as a consolidant, ensuring an increase of the mechanical resistance[5]. A low concentration of ethyl silicate was used (5 %), in order to moderately increase the mechanical strength.

Nanolime dispersions of calcium hydroxide are white-to-opal solutions containing stable calcium hydroxide nanoparticles dispersed in an alcoholic medium, usually isopropanol. The nanoparticles have a hexagonal-shaped form and a size range between 50 nm and 600 nm[6]; the reduced dimension of $Ca(OH)_2$ particles guarantees a deeper penetration inside the smaller pores. We have used a commercial nanolime (Nanorestore®, CTS).

An analysis of the selected consolidation products was made considering the important characteristics linked to an optimal application, including the pH, setting times and dry residues (**Table 1**).

Table 1: Characteristics of the consolidation products
Tabela 1: Značilnosti veziv

Consolidation product	pH	Dry residue (g/L)	Setting time (min)
Limewater + Ethyl Silicate (5 %)	9.2	3.51	20
Nanolime	7.2	1.78	120

The applications were made in a conditioned room, at 23 °C and 50 % RH, using a manual-spraying technique (ten consecutive applications) at a distance of 20–30 cm [3,7].

3 METHODS

3.1 Characterization of the consolidant treatments

The evaluation of the efficacy of the consolidant treatments was carried out through the use of different tests, executed before and after treatments (90 d from the consolidant product application).

The improvement of the mechanical resistance was checked by the durometer hardness (Shore A, PCE Group)[8,9]. The surfaces of mortar specimens were observed with an Olympus SZH stereoscopic microscope and the images were recorded digitally.

The microstructural observations and the elemental analyses were performed on specimens previously sputtered with a gold film by SEM JEOL JSM-6400, coupled with an Oxford Instruments energy-dispersive spectrometer (EDS).

4 RESULTS AND DISCUSSION

4.1 Durometer hardness (Shore A)

The superficial hardness of the specimens was verified 90 d after the application of the product through a durometer (Shore A). As shown in **Figure 1**, an improvement in the superficial hardness of the treated specimens is evident.

The nanolime consolidant presents a moderate increase in the superficial hardness (18 %) compared to the untreated specimens, while the treatment of limewater mixed with ethyl silicate registered a greater increase (28 %); the values reflected the trend of previous studies that were made on ancient lime-based mortars[7,10].

4.2 Microscopic observations by stereozoom microscopy

Stereozoom observations were made in order to evaluate the morphological and microstructural variations due to the consolidation treatments. In comparison with the untreated specimens (**Figure 2a**), which present wide pores and micro-cracks, the specimens treated with a limewater dispersion of ethyl silicate (**Figure 2b**) show a more compact surface and an increase in the porosity. Otherwise, the product presents a discontinuous distribution, forming planar agglomerates in the surface.

On the other hand, specimens treated with nanolime (**Figure 2c**) present a more uniform distribution of the consolidation product and homogeneous infilling of the matrix voids; moreover, fewer microcracks were visible.

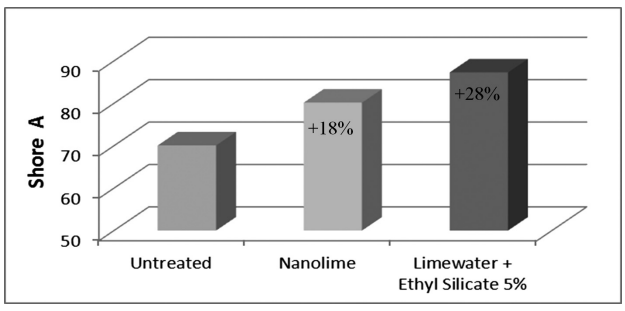

Figure 1: Superficial hardness and relative increases of the treated mortars (durometer Shore A)
Slika 1: Trdota površine in njeno relativno povečanje v obdelanih maltah (trdometer Shore A)

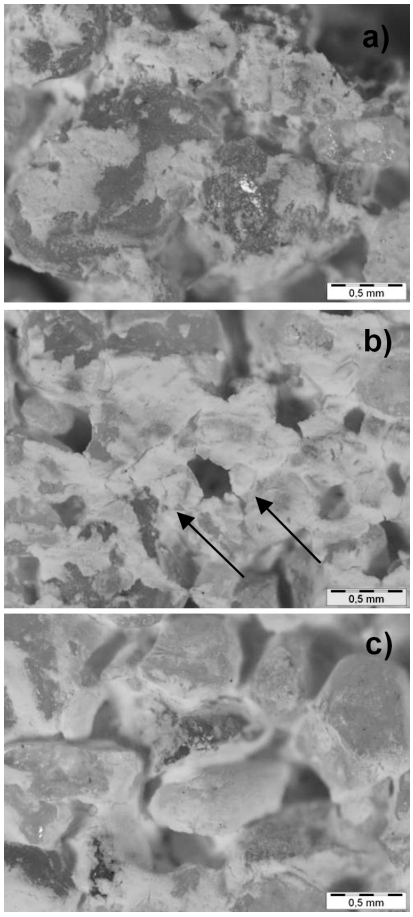

Figure 2: Stereozoom microphotographs (magnification 40-times): a) untreated specimen; b) specimen treated with limewater solution of 5% ethyl silicate and relative planar aggregates (arrows); c) specimen treated with nanolime

Slika 2: Posnetki s stereomikroskopom (povečava 40-kratna): a) neobdelan vzorec; b) vzorec, obdelan s 5-odstotno raztopino apnovice in etil silikata in relativno ploskimi površinami veziva (puščica); c) vzorec, obdelan z nanodelci apna

Macroscopically, both products show few differences in comparison to the untreated mortar, and seem to induce only a slight whitening on the surface.

4.3 Microstructural observations by SEM-EDS

The specimen treated using limewater with ethyl silicate (**Figure 3a, b**) shows the formation of platelike aggregates of calcium-silica gels. Indeed, the quick reaction in the alkaline aqueous solution of limewater rapidly forms calcium-silica gel; this gel transforms itself into a xerogel due to the evaporation of the solvent, and the presence of $CaCO_3$ seems to modify the xerogel vesicular microstructure.

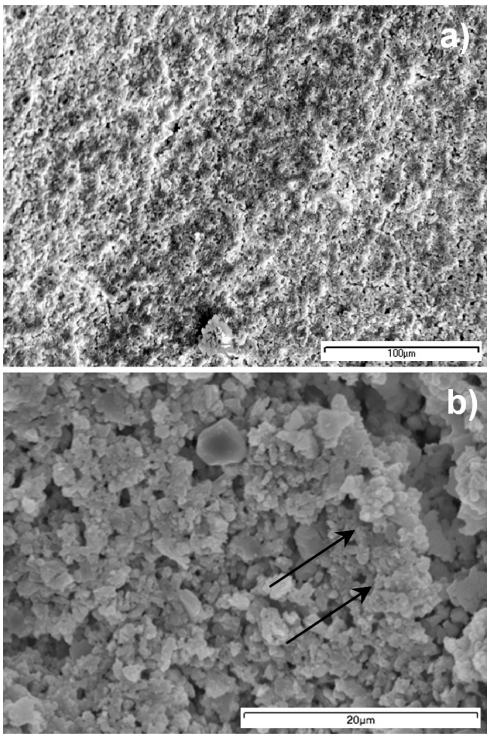

Figure 4: SEM microphotographs of the mortar, treated with nanolime: a) homogeneous distribution of the nanolime in the mortar paste; b) clusters of nanolime particles (arrows) mixed with the original binder

Slika 4: SEM-posnetek malte, obdelane z nanodelci apna: a) homogena razporeditev nanodelcev apna v malti; b) skupek nanodelcev apna (puščica), zmešan s prvotnim vezivom

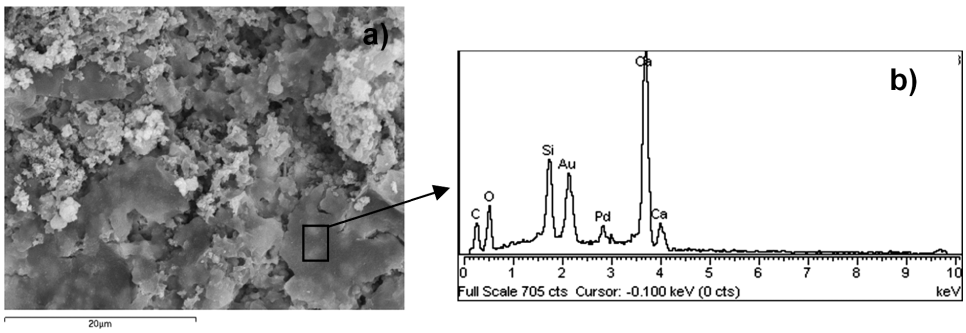

Figure 3: SEM/EDS images of the specimen, treated with limewater-ethyl silicate solution: a) presence of platelike shaped of calcium-silica gel on the mortar surface and b) corresponding EDS spectrum

Slika 3: SEM/EDS-sliki vzorca, obdelanega z raztopino etil silikata v apnovici: a) prisotnost ploščatih oblik kalcij-silicijevega gela na površini vzorca malte in b) ustrezen EDS-spekter

According to recent studies[11], calcium carbonate actually aids the development of shorter linear chains of tetrahedral silica and linear silicate structure, which can explain the rapid formation of a granular gel with a platelike shape.

The SEM/EDS observations of the mortars treated with the nanolime product show micro-sized clusters of calcitic formations; the distribution and morphology of these nanostructured particles show a homogeneous consolidation film. The consolidation film of nanolime is characterized by the presence of plate-like nanoparticles that aggregate into micro-sized clusters, which are compact and polydispersed (**Figure 4**).

According to previous studies[12], the carbonation of nanolime particles originate in oriented crystal grains, which promote the agglomeration of the particles.

Moreover, beyond the chemical, physical and mechanical compatibility, Rodriguez-Navarro et al.[13] have shown that plate-like lime nanoparticles have a great capacity to absorb water (which acts as a lubricating film), guaranteeing a good plasticity and avoiding the mechanical stress inside the treated mortar.

5 CONCLUSIONS

The analysis evidenced some differences between the two products. The obtained results of the mechanical resistance, evaluated through the durometer hardness and the flexural and compressive strength, show that the highest mechanical increase was obtained with the limewater dispersion of ethyl silicate, while the alcoholic dispersion of nanolime particles guarantees a moderate improvement in the mechanical resistance. Microscopical and microstructural observations using stereozoom microscopy and scanning electron microscopy show that the limewater dispersion of ethyl silicate has a consolidation effectiveness on the treated surface, due to the formation of plate-like aggregates of calcium silica gels; however, these planar aggregates can physically interfere in the penetration depth of the consolidant. A limewater dispersion of ethyl silicate is also a good consolidation product, ensuring the restitution of superficial cohesion to the treated mortar. In any case it is recommended only for mortars with a superficial loss of cohesion, because of the reduced depth penetration.

Otherwise, nanolime particles permit a homogeneous distribution on the treated substrate; the platelike nanoparticles present a specific crystallographic orientation that could contribute to an agglomeration process. The nanolime dispersion appears as promising consolidant product for lime mortars with a loss of cohesion, ensuring an optimum penetration and distribution in the matrix binder; however, this dispersion does not seem to guarantee a large improvement in the mechanical resistance, so the use of nanolime is recommended for mortars with reduced loss of cohesion, or to combine the use of this product with other consolidation product.

Acknowledgements

This study was developed within a project (Limencontech – Conservation and durability of historical renders: compatible techniques and materials) financed by FCT – *Fundação para a Ciência e a Tecnologia* (Portugal).

6 REFERENCES

[1] L. Toniolo, A. Paradisi, S. Goidanich, G. Pennati, Mechanical behaviour of lime based mortars after surface consolidation, Construction and Building Materials, 25 (**2010**) 4, 1553–1559

[2] E. Hansen, E. Doehne, J. Fidler, J. Larson, B. Martin, M. Matteini, C. Rodrigues-Navarro, E. Sebastian Pardo, P. Price, A. de Tagle, J. M. Teutonico, N. Weiss, A review of selected inorganic consolidants and protective treatment for porous calcareous materials, Reviews in Conservation, (**2003**) 4, 13–25

[3] M. Tavares, R. Veiga, A. Fragata, Conservation of old renderings – The consolidation of renders with loss of cohesion. Proceeding of 1st Historical Mortars Conference HMC08 – Characterization, Diagnosis, Conservation, Repair and Compatibility, Lisbon, 2008

[4] M. Drdácký, Z. Slízkova, Calcium hydroxide based consolidation of lime mortars and stone. Proceeding of 1st Historical Mortars Conference HMC08 – Characterization, Diagnosis, Conservation, Repair and Compatibility, Lisbon, 2008

[5] W. Domaslowski, J. W. Lucaszewicz, Possibilities of silica application in consolidation of stone monument. Proceeding of 6th International Congress on Deterioration and Conservation of Stone, 12–14 September 1998, Torun, Nicholas Copernicus University Press, 239

[6] L. Dei, B. Salvadori, Nanotechnology in cultural heritage conservation: nanometric slaked lime saves architectonic and artistic surface from decay, Journal of cultural Heritage, 7 (**2006**), 110–115

[7] M. Tavares, R. Veiga, A. Fragata, J. Aguiar, Consolidation of renderings simulating stone in the façade of LNEC's building. Proceeding of Stone Consolidation in Cultural Heritage, International Symposium, Lisbon, May, 2008, 121–129 (http://conservarcal.lnec.pt)

[8] ASTM, American Standard for Testing and Materials: Standard Test Method for Rubber Property – Durometer Hardness, ASTM D2240, 2004

[9] ISO, International Organization for Standardization (1997): Rubber – Determination of indentation hardness by means of pocket hardness meter. ISO 7619:1997

[10] A. Santos Silva, G. Borsoi, R. Veiga, A. Fragata, M. Tavares, F. Llera, Physico-chemical characterization of the plasters from the church of Santissimo Sacramento in Alcântara, Lisbon. Proceeding of 2nd Historic Mortars Conference HMC10 and RILEM 203-RHM Final Workshop, 22–24 September, Prague, Czech Republic, 2010, 345–357

[11] E. Zendri, G. Biscontin, I. Nardini, S. Rialto, Characterization and reactivity of silicatic consolidants, Construction and Building Materials, 21 (**2007**), 1098–1106

[12] P. López-Arce, L. S. Gomez-Villalba, L. Pinho, M. E. Fernández-Valle, M. Álvarez de Buergo, R. Fort, Influence in the porosity and relative humidity on consolidation of dolostone with calcium hydroxide nanoparticles; effectiveness assessment with non-destructive techniques, Materials Characterization, 61 (**2010**), 168–184

[13] C. Rodriguez-Navarro, E. Ruiz-Agudo, M. Ortega-Huertas, E. Hansen, Nanostructure and irreversible colloidal behaviour of $Ca(OH)_2$: implications in cultural heritage conservation, Langmuir, 21 (**2005**), 10948–10957

UDK 678.7:533.9
Original scientific article/Izvirni znanstveni članek

ISSN 1580-2949
MTAEC9, 46(3)227(2012)

ETCHING RATES OF DIFFERENT POLYMERS IN OXYGEN PLASMA

ŠTUDIJ HITROSTI JEDKANJA RAZLIČNIH POLIMEROV V KISIKOVI PLAZMI

Alenka Vesel[1], Tomaž Semenič[2]

[1]Department of Surface Engineering, Jožef Stefan Institute, Jamova cesta 39, 1000 Ljubljana, Slovenia
[2]Faculty of Physics, University of Ljubljana, Jadranska 19, 1000 Ljubljana, Slovenia
alenka.vesel@ijs.si

Prejem rokopisa – received: 2011-10-14; sprejem za objavo – accepted for publication: 2012-02-13

The etching rates of different polymers in oxygen plasma was compared. The plasma was created in an electrodeless, radiofrequency discharge at a frequency of 27.12 MHz and a power of 200 W. The oxygen pressure was fixed at 75 Pa. The degradation of the polymers by oxidation with plasma particles was monitored by measuring the weight loss of the polymer samples. The samples were weighed just before mounting into the plasma reactor, and then again just after the plasma treatment. The following polymers were used in this study: PET (amorphous and semi-crystalline), PMMA, PS, LDPE, HDPE, PVC and PTFE. The polymer-etching rate was increasing linearly with treatment time. This was explained by the heating of the samples during the plasma treatment. The only exception was the PTFE, where the etching rate was constant. For the PVC polymer extremely high etching rates were observed. However, a characteristic of the PMMA polymer was a very low etching rate at the beginning, which was followed by an exponential increase of the etching rate with treatment time.

Keywords: polymer, etching rates, gravimetric measurements, oxygen plasma

Preučevali smo hitrosti jedkanja različnih polimerov v radiofrekvenčni kisikovi plazmi. Plazmo smo ustvarili v brezelektrodni razelektritvi s frekvenco 27,12 MHz in močjo RF generatorja 200 W. Tlak kisika med obdelavo je bil 75 Pa. Degradacijo polimera zaradi oksidacije, ki jo povzročajo plazemski delci, smo ugotavljali z meritvijo izgube mase polimernih vzorcev. Vzorce smo stehtali pred izpostavo plazmi in takoj po obdelavi. V raziskavi smo uporabili naslednje polimere: amorfni in semikristalinični PET, PMMA, PS, LDPE, HDPE, PVC in PTFE. Hitrost jedkanja polimerov je linearno naraščala s časom obdelave. To smo razložili s segrevanjem vzorca med obdelavo. Edina izjema je bil polimer PTFE, kjer je bila hitrost jedkanja konstantna. Za polimer PVC smo izmerili neprimerljivo visoke hitrosti jedkanja. Značilnost polimera PMMA pa je bila zelo nizka hitrost jedkanja na začetku, nato je sledil eksponentni porast hitrosti jedkanja z naraščajočim časom obdelave.

Ključne besede: polimer, jedkanje, gravimetrične meritve, kisikova plazma

1 INTRODUCTION

Polymer materials are nowadays widely used in many different applications, especially in the food industry as a packaging material and in medicine as a suitable material for different medical devices and body implants.[1–4] The cleanliness and sterility of polymers is a very important factor in avoiding unwanted complications. While methods for the sterilization of the materials have been elaborated decades ago, and only the sterilization of very delicate components that do not withstand high-temperature treatment (i.e., polymers) represent a problem, less encouraging results have been obtained during the cleaning of components with complex shapes. This unsatisfactory cleanliness represents a problem, although a device might be sterile: the remains of dead bacteria as well as traces of body liquids or tissue often remain toxic. From this point of view it is clear that the existing cleaning techniques are far from being perfect. Even though in many cases aggressive reagents are excellent for the removal of organic residues, the application of such reagents is limited in medicine since they are usually toxic themselves. An advanced technique for the removal of organic materials that has been introduced recently is based on the application of a heavily non-equilibrium gaseous plasma.[8] This technique is called discharge cleaning. Reactive particles created in a gaseous plasma are capable of interacting with impurities even at low temperature.[9] The technology is nowadays used in many branches of industry, including the microelectronics, electrical and automotive industries. Although the plasma treatment proved useful for the sterilization[10–13] of simple medical devices, the wide application of non-equilibrium plasma technology is still not foreseen in medicine. The reason for this is a lack of reliable experimental data. While the interaction probabilities for a limited number of materials with gaseous plasma particles are known,[14] the literature on the interaction of chemically reactive plasma particles with organic materials (blood proteins, etc.) found as contaminants on the surface of medical devices is extremely scarce.[6,7] Furthermore, the interaction probabilities with substrate polymer materials are also important,[15–18] if we want to avoid the surface modification and degradation of the polymers upon discharge cleaning. Namely, it is known that plasma treatment, which is usually performed in oxygen-containing gases, causes oxidation (functionalization) of a polymer material.[14,19] This

oxidation of a polymer leads to polymer etching (material removal), which can be an unwanted effect. On the other hand, etching can be very important in some applications, like the selective etching of organic inks, where etching is used to study the distribution of pigments in an organic matrix.[20–22] The aim of this paper is to present the results of systematic measurements of the removal rates for different polymers that are used in everyday life.

2 EXPERIEMENTAL

The following polymers (from Goodfellow Ltd) were used in this study: amorphous and semi-crystalline polyethylene terephthalate (PET), polymethyl methacrylate (PMMA), polystyrene (PS), low- and high-density polyethylene (LDPE, HDPE), polyvinyl chloride (PVC) and polytetrafluroethylene (PTFE). The chemical structure of these polymers is shown in **Figure 1**. The samples were cut into square pieces with a size of 2 cm × 2 cm to ensure a high area-to-mass ratio. Only the PVC and PMMA samples were prepared as 1 cm × 1 cm square pieces due to a shortage of the material.

Plasma etching of the polymers was performed in a cylindrical discharge tube made of Pyrex glass with a length of 0.5 m and an inner diameter of 36 mm. The system was pumped with a two-stage, oil rotary pump with a pumping speed of 16 m^3 h^{-1}. The plasma was created with an inductively coupled RF generator, operating at a frequency of 27.12 MHz and a nominal power of about 200 W. Commercially available oxygen was leaked into the discharge chamber. The oxygen pressure was fixed at 75 Pa. The plasma parameters were measured with a double Langmuir probe and a catalytic probe. The plasma density was of the order of 10^{15} m^{-3}, the electron temperature about 3 eV, and the density of neutral oxygen atoms of the order of 10^{21} m^{-3}. The samples were placed on a glass holder and mounted directly to the plasma glow region.

The degradation of polymers by oxidation with plasma particles was monitored by measuring the weight loss of the polymer samples. The samples were weighed just before mounting into the plasma reactor, and then again just after the plasma treatment. A Radwag XA 110 professional microbalance was used. The accuracy of the measurements is, according to the producer, 0.01 mg. Samples were washed in ethanol and dried before weighing in order to remove any impurities or degradation products from the surface.

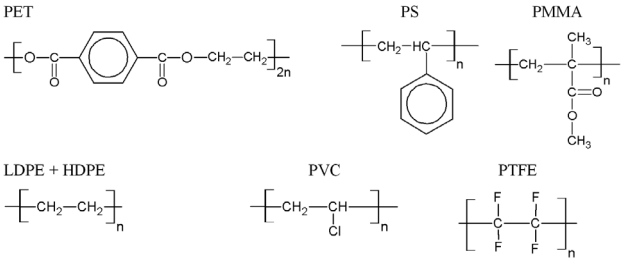

Figure 1: Chemical structure of selected polymers
Slika 1: Kemijska struktura izbranih polimerov

3 RESULTS AND DISCUSSION

The etching of different polymer materials due to an interaction with plasma radicals was measured. Polymer etching (material removal) is initiated by the abstraction of a hydrogen atom and the formation of a free radical.[18,23] Polymer radical site formation affects the bond strengths in polymers and can lead to bond breaking or chain scission and thus to the formation of low-molecular-weight volatile fragments.[23] The mass loss of a polymer material after plasma treatment was measured by gravimetry and the corresponding etching rate (ξ) was calculated with the equation:

$$\xi = \frac{d}{t} = \frac{V}{At} = \frac{\Delta m/\rho}{At} \quad (1)$$

where d is the thickness of the etched layer, t is the plasma etching time, Δm is a change in the polymer mass due to etching, ρ is the polymer density, and A is the area of the polymer surface exposed to plasma. A comparison of the physical characteristics (density, melting temperature etc.) of the polymers is shown in **Table 1**. These polymers have a different sensitivity to high temperatures. Therefore, some of the polymers started to melt very quickly after turning on the

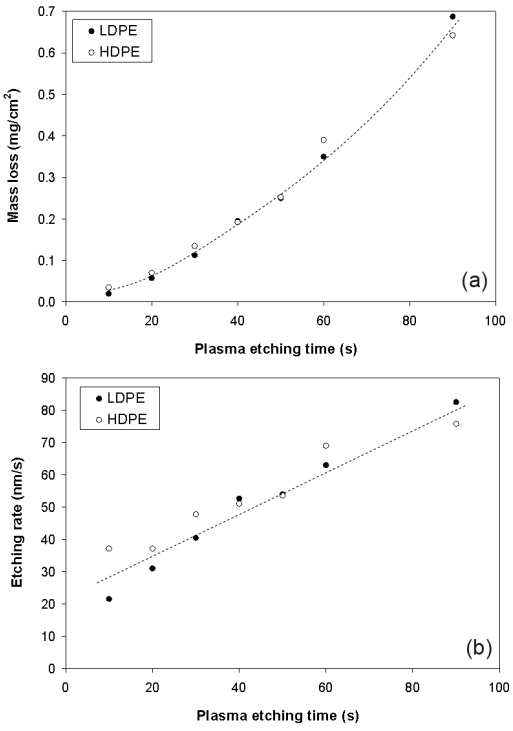

Figure 2: a) Comparison of the mass loss and b) etching rates of LDPE and HDPE polymers versus etching time
Slika 2: a) Primerjava izgube mase in b) hitrosti jedkanja polimerov LDPE in HDPE v odvisnosti od časa plazemskega jedkanja

discharge. In **Table 1** we also show the maximum working temperature as recommended by the producer and the treatment time at which the polymer melting occurred. Polymers that were treated for longer times showed a higher mass loss, which was easier to measure. Therefore, the calculated etching rates for longer treatment times are more accurate than for shorter treatment times where the differences in the polymer mass were very small.

Table 1: Comparison of the physical characteristics of different polymers and their etching rates
Tabela 1: Primerjava fizikalnih karakteristik različnih polimerov in njihovih hitrosti jedkanja

Polymer	Thickness (mm)	Density (g/cm^3)	Melting T/°C	Max. working T/°C	Time when melting starts	Etching rate at 20 s of treatment
PVC	0.50	1.40	100	50–75	~30 s	178 nm/s
LDPE	1.00	0.92	110	50–90	~100 s	31 nm/s
HDPE	1.00	0.95	130	55–120	~100 s	34 nm/s
PMMA	0.50	1.19	160	50–90	/	6 nm/s
PS	0.125	1.05	240	50–95	~40 s	13 nm/s
PET A	0.25	1.3–1.6	< 260	115–170	~40 s	27 nm/s
PET B	0.25	1.3–1.6	260	115–170	~100 s	35 nm/s
PTFE	0.20	2.20	327	180–260	/	18 nm/s

Figures 2 to **5** (upper figures) show the weight-loss measurements for different polymers versus treatment time. The corresponding etching rates, which were cal-

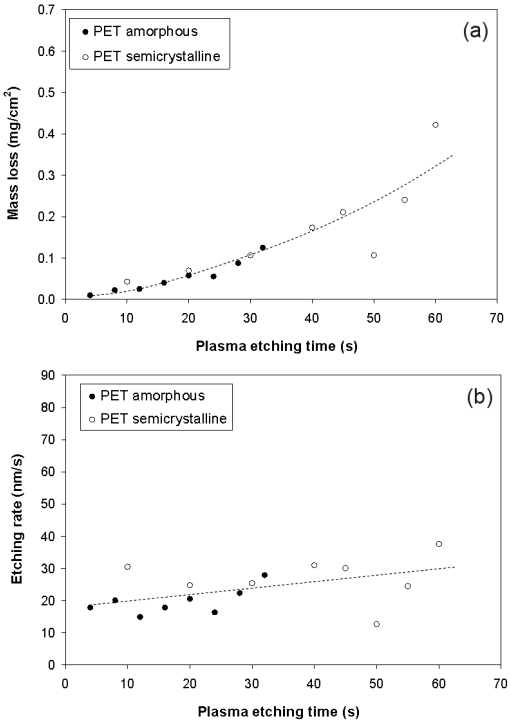

Figure 3: a) Comparison of the mass loss and b) etching rates of amorphous and semi-crystalline polymer PET versus etching time
Slika 3: a) Primerjava izgube mase in b) hitrosti jedkanja amorfnega in semikristaliničnega polimera PET v odvisnosti od časa plazemskega jedkanja

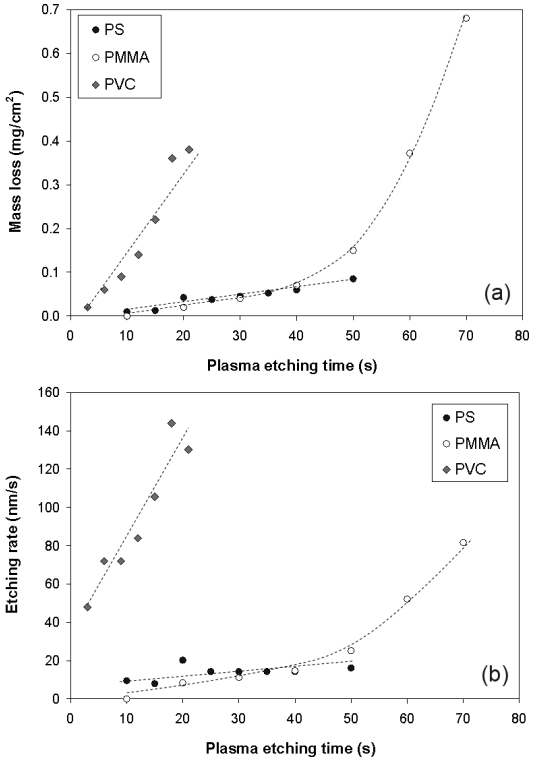

Figure 4: a) Comparison of the mass loss and b) etching rates of polymers PS, PVC and PMMA versus etching time
Slika 4: a) Primerjava izgube mase in b) hitrosti jedkanja polimerov PS, PVC in PMMA v odvisnosti od časa plazemskega jedkanja

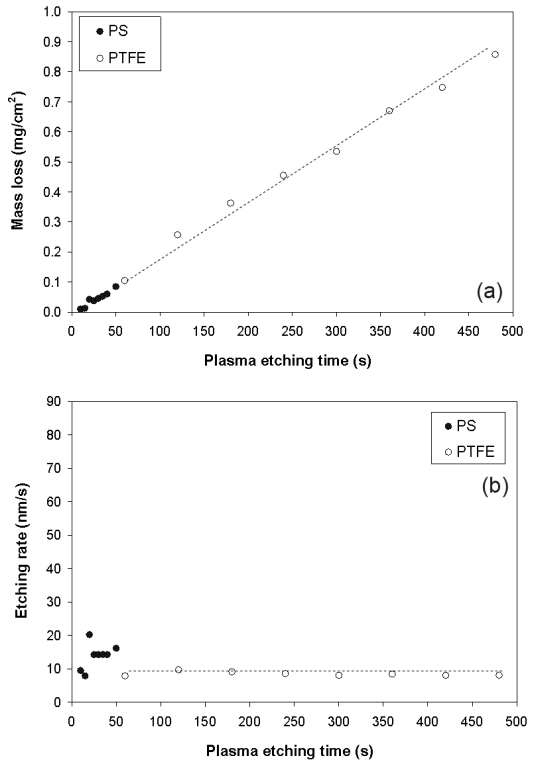

Figure 5: a) Comparison of the mass loss and b) etching rates of polymers PTFE and PS versus etching time
Slika 5: a) Primerjava izgube mase in b) hitrosti jedkanja polimerov PTFE in PS v odvisnosti od časa plazemskega jedkanja

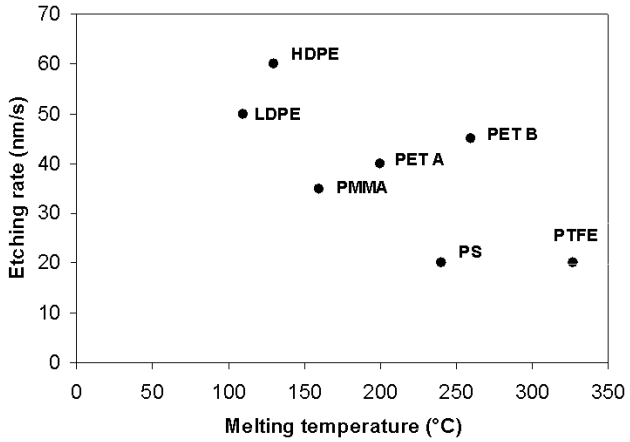

Figure 6: Dependence of the polymer-etching rate (at 60 s of treatment) on its melting temperature. Values of etching rates for some polymers were extrapolated. PET A and B refer to amorphous and semi-crystalline PET, respectively.

Slika 6: Odvisnost hitrosti jedkanja (pri 60 s obdelave) od temperature tališča polimera. Vrednosti za nekatere polimere so bile ekstrapolirane. Oznaki PET A in B se nanašata na amorfni oz. semikristalinični PET.

culated according to Eq. (1), are shown in lower **Figures 2** to **5**. In particular, **Figure 2** shows a comparison of the removal rates of the LDPE and HDPE polymers. From the upper figure we can see that there is no significant difference in the mass loss of the LDPE and HDPE polymers, although one would expect a more pronounced etching of the LDPE polymer, which has a lower crystallinity. A similar effect is observed for the amorphous and semi-crystalline polymer PET (**Figure 3**).

A comparison of the polymers PS, PMMA and PVC is shown in **Figure 4**. The etching rates of the polymer PS are similar to that of the PET and LDPE/HDPE. While for the PMMA and PVC polymers we can observe completely different behavior. Namely, for the PVC polymer we can observe an enormously high etching rate, which linearly increases with time. While for the PMMA polymer we can observe a very low etching rate at low treatment times, which after a certain time exponentially increases and becomes very high. The unusual behavior of the polymers PVC and PMMA can be explained by polymer degradation. PMMA is sensitive to oxidation and UV radiation and it may spontaneously depolymerize (i.e., after the formation of a free radical a chain-reaction mechanism starts and the polymer loses the monomer one by one). Similarly, PVC may, at elevated temperatures, release hydrogen chloride gas HCl (side-group elimination). It was also reported that chlorine-containing polymers, when treated with oxygen plasma, may modify plasma in such a way that it etches polymers at a much enhanced rate due to the presence of Cl and Cl^* species.

From **Figures 2** to **4** we can conclude that the polymer-etching rate is linearly increasing with treatment time. This is probably due to thermal effects, i.e., with increasing treatment time the temperature of the polymer also increases.[14] Furthermore, a high temperature facilitates polymer degradation. In agreement with a linear increase of the polymer-etching rates with treatment time we can observe a parabolic increase of the mass loss with treatment time. This is not the case for the PTFE polymer (**Figure 5**), where we have observed a constant polymer-etching rate (independent of the treatment time) and the linear removal of the polymer material with time. The polymer PTFE is known to be chemically very inert, and therefore its surface functionalization by plasma is not very efficient.[24–26]

When comparing the etching rates of different polymers we could not find any good correlation between the chemical structure and the polymer-etching rate. It was reported that aromatic polymers are more stable against etching in oxygen plasma[15,23] and in our case we have found a very slow etching rate for the PS polymer. Also, the average etching rate for the aromatic PET polymer is slightly lower than for aliphatic polyethylene PE.

We have also tried to find a correlation between the melting temperature and the polymer-etching rate. The result is shown in **Figure 6**. Although we can see a general trend that polymers with a lower melting temperature have higher etching rates, the differences between the etching rates of the different polymers are not very high. Here we should also note that the values for the etching rates shown in **Figure 6** are those that polymers would have at 60 s of treatment. For those polymers that were already melted at this treatment time and for the PMMA the values were linearly extrapolated. Last but not least, the calculated etching rates at 20 s of treatment for different polymers are shown in **Table 1** as well.

4 CONCLUSIONS

The etching rates of different polymers in oxygen plasma were compared. The mass removal rate was monitored by measuring the weight loss of the polymer samples. When comparing the etching rates of different polymers we could not find any good correlation between the chemical structure and the polymer-etching rate. The polymer-etching rate was increasing linearly with treatment time. This effect was explained by the heating of the samples during the plasma treatment that facilitates the polymer degradation. The only exception was the PTFE, where the etching rate was found to be constant. For the PVC polymer, extremely high etching rates were observed. However, a characteristic of the PMMA polymer was a very low etching rate at the beginning, which was followed by an exponential increase in the etching rate with treatment time. The measured etching rates were roughly in the following order: PVC > PMMA > PE > PET > PTFE > PS.

Acknowledgement

This project was supported by Slovenian Research Agency, Project 2010/II-100 (Toward ecologically benign alternative for cleaning of delicate biomedical instruments).

5 REFERENCES

[1] J. Jagur-Grodzinski, Polym. Adv. Technol., 17 (**2006**), 395–418
[2] B. Kasemo, Surface Science, 500 (**2002**), 656–677
[3] D. Klee, H. Höcker, Adv. Polym. Sci., 149 (**2000**), 1–57
[4] T. Desmet, R. Morent, N. De Geyter, C. Leys, E. Schacht, P. Dubruel, Biomacromolecules, 10 (**2009**) 9, 2351–2378
[5] O. Kylian, H. Rauscher, D. Gilliland, F. Bretagnol, F. Rossi, J. Phys. D: Appl. Phys., 41 (**2008**) 9, 095201
[6] F. Rossi, O. Kylian, H. Rauscher, D. Gilliland, L. Sirghi, Pure Appl. Chem., 80 (**2008**) 9, 1939–1951
[7] O. Kylián, H. Rauscher, L. Sirghi, F. Rossi, J. Phys.: Conf. Series, 100 (**2008**), 062017
[8] A. Drenik, A. Vesel, M. Mozetic, J. Nucl. Mater., 386–388 (**2009**), 893–895
[9] A. Doliska, A. Vesel, M. Kolar, K. Stana-Kleinschek, M. Mozetic, Surf. Interface Anal., 44 (**2012**), 56–61
[10] A. von Keudell, P. Awakowicz, J. Benedikt, V. Raballand, A. Yanguas-Gil, J. Opretzka, C. Flötgen, R. Reuter, L. Byelykh, H. Halfmann, K. Stapelmann, B. Denis, J. Wunderlich, P. Muranyi, F. Rossi, O. Kylian, N. Hasiwa, A. Ruiz, H. Rauscher, L. Sirghi, E. Comoy, C. Dehen, L. Challier, J. P. Deslys, Plasma Process. Polym., 7 (**2010**) 3–4, 327–352
[11] M. Moisan, J. Barbeau, S. Moreau, J. Pelletier, M. Tabrizian, L'H. Yahia, Int. J. Pharm., 226 (**2001**), 1–21
[12] K. Lee, K. H. Paek, W. T. Ju, Y. Lee Y, J. Microbiol., 44 (**2006**), 269–275
[13] G. Kamgang-Youbi, J. M. Herry, M. N. Bellon-Fontaine, J. L. Brisset, A. Doubla, M. Naïtali, Appl. Environ. Microbiol., 73 (**2007**), 4791–4796
[14] I. Junkar, U. Cvelbar, A. Vesel, N. Hauptman, M. Mozetic, Plasma Processes. Polym., 6 (**2009**) 10, 667–675
[15] G. N. Taylor, T. M. Wolf, Polym. Eng. Sci., 20 (**1980**) 16, 1087–1092
[16] V. Hody, T. Belmonte, T. Czerwiec, G. Henrion, J. M. Thiebaut, Thin Solid Films, 506–507 (**2006**), 212–216
[17] M. Mafra, T. Belmonte, F. Poncin-Epaillard, A. S. D. S. Sobrinho, A. Maliska, Plasma Chem. Plasma Process., 28 (**2008**) 4, 495–509
[18] T. Belmonte, C. D. Pintassilgo, T. Czerwiec, G. Henrion, V. Hody, J. M. Thiebaut, J. Loureiro, Surf. Coat. Technol., 200 (**2005**) 1–4, 26–30
[19] C. M. Chan, T. M. Ko, H. Hiraoka, Surf. Sci. Rep., 24 (**1996**) 1–2, 1–54
[20] M. Kunaver, M. Klanjsek Gunde, M. Mozetic, A. Hrovat, Dyes Pigm., 57 (**2003**) 3, 235–243
[21] M. Kunaver, M. Mozetic, M. Klanjsek Gunde, Thin Solid Films, 459 (**2004**) 1/2, 115–117
[22] F. D. Egitto, Pure Appl. Chem., 62 (**1990**) 9, 1699–1708
[23] N. Vandencasteele, H. Fairbrother, F. Reniers, Plasma Process. Polym., 2 (**2005**) 6, 493–500
[24] C. Sarra-Bournet, S. Turgeon, D. Mantovani, G. Laroche, J. Phys. D: Appl. Phys., 39 (**2006**) 16, 3461–3469
[25] M. Chen, P. O. Zamora, P. Som, L. A. Pena, S. Osaki, J. Biomater. Sci., Polym. Ed., 14 (**2003**) 9, 917–935
[26] U. König, M. Nitschke, M. Pilz, F. Simon, C. Arnhold, C. Werner, Colloid. Surf. B, 25 (**2002**), 313–324

UDK 669.715.017:620.186
Original scientific article/Izvirni znanstveni članek

ISSN 1580-2949
MTAEC9, 46(3)233(2012)

EFFECT OF A FOAMING AGENT AND ITS MORPHOLOGY ON THE FOAMING BEHAVIOUR, CELL-SIZE DISTRIBUTION AND MICROSTRUCTURAL UNIFORMITY OF CLOSED-CELL ALUMINIUM FOAMS

VPLIV VRSTE IN MORFOLOGIJE SREDSTVA ZA PENJENJE NA PROCES PENJENJA, PORAZDELITEV POR PO VELIKOSTI IN UNIFORMNOST MIKROSTRUKTURE ALUMINIJSKIH PEN Z ZAPRTIMI PORAMI

Varužan Kevorkijan[1], Srečo Davor Škapin[2], Irena Paulin[3], Uroš Kovačec[4], Monika Jenko[3]

[1]Independent Researcher, Betnavska cesta 6, 2000 Maribor, Slovenia
[2] Jožef Stefan Institute, Jamova 39, 1000 Ljubljana, Slovenia
[3]Institute of Metals and Technology, Lepi pot 11, 1000 Ljubljana, Slovenia
[4]Impol LLT, d. o. o., Partizanska 38, 2310 Slovenska Bistrica, Slovenia
varuzan.kevorkijan@impol.si

Prejem rokopisa – received: 2011-10-20; sprejem za objavo – accepted for publication: 2011-11-07

A quantitative evaluation of the microstructure of aluminium foams and, particularly, any quantitative comparison is a very demanding and complex issue. In this work, the cell-size distribution (CSD) was proposed as the most efficient approach for their assessment.
The foams were made by the powder metallurgy (P/M) route, by applying titanium hydride and dolomite powders of five different average particle sizes as the foaming agents.
The average size of the pores and the pore-size distribution were estimated by assessing optical and scanning electron micrographs of as-polished foam bars by applying the point-counting method and image-analysis software.
The uniformity of the CSD in the foamed samples with closed cells was studied as a function of the particle size distribution of the foaming agents, the average particle size of the applied AlSi12 powders, the concentration of the foaming agents, the foaming temperature and the foaming time.
Generally, the samples foamed with the dolomite foaming agent had a more uniform cell-size distribution and a lower average bubble size. The most uniform cell-size distribution was achieved in the foam samples foamed with the minimum amount of the mass fraction (w = 0.5 %) of dolomite powder grades, having the lowest average particle size and a narrow particle-size distribution. In contrast, in samples made from coarser and less-uniform grades of foaming agents, the cell-size distribution was broader, with a significantly higher fraction of large bubbles. Longer foaming times and higher foaming temperatures also led to foam samples with a less-uniform microstructure.
Based on the experimental findings and theoretical considerations regarding aluminium-foam microstructural development, the preconditions for stable bubble growth into a homogeneous and uniform foam structure were modelled and compared with the experimentally determined values.

Keywords: aluminium foams, comparison of different foaming agents and processing parameters, microstructural characterisation, modelling of microstructural development

Kvantitativna karakterizacija in primerjava mikrostruktur različnih vzorcev aluminijskih pen sta zelo zahtevni ter zapleteni nalogi. Naša raziskovalna skupina se je odločila za način, kjer kvantitativna karakterizacija mikrostrukture aluminijskih pen temelji na določanju porazdelitve por po velikosti (PPV).
Vzorce pen smo izdelovali s postopkom metalurgije prahov. Kot sredstvo za penjenje smo uporabili pet vrst titanhidridnih in dolomitnih prahov z različno porazdelitvijo delcev po velikosti.
Povprečno velikost por in porazdelitev por po velikosti v vzorcih aluminijskih pen smo ugotavljali s slikovno analizo posnetkov njihove mikrostrukture, narejenih s svetlobno in vrstično elektronsko mikroskopijo.
Enakomernost porazdelitve velikosti por v vzorcih pen smo preučevali v odvisnosti od porazdelitve velikosti sredstva za penjenje, povprečne velikosti uporabljenih prahov AlSi12, koncentracije sredstva za penjenje in temperature ter časa penjenja.
Na splošno so imeli vzorci, ki smo jih penili z dolomitom, veliko bolj enakomerno oz. ožjo porazdelitev velikosti por ter manjšo povprečno velikost. Najožjo porazdelitev por po velikosti smo opazili v vzorcih pen, izdelanih iz najfinejših dolomitnih prahov, z ozko porazdelitvijo delcev po velikosti ter najnižjo masno koncentracijo (0,5 %) sredstva za penjenje. V nasprotju s tem je bila v vzorcih aluminijskih pen, izdelanih iz bolj grobih vrst dolomitnih prahov, s širšo porazdelitvijo delcev po velikosti, tudi porazdelitev por po velikosti širša z naraščajočim deležem velikih por. Poleg tega se je izkazalo, da je stopnja uniformnosti mikrostrukture pen odvisna v veliki meri od temperature in časa penjenja, pri čemer je s podaljšanjem časa in višanjem temperature penjenja porazdelitev velikosti por postajala vse širša.
Eksperimentalne rezultate in teoretične ugotovitve o razvoju mikrostrukture aluminijskih pen z zaprto poroznostjo smo strnili v model, ki predpisuje pogoje nastanka homogene in uniformne strukture pen.

Ključne besede: aluminijeve pene, primerjava različnih sredstev za penjenje in procesnih parametrov, karakterizacija mikrostrukture, model razvoja mikrostrukture

1 INTRODUCTION

Closed-cell aluminium foams are a promising class of lightweight structural materials with a unique combination of properties resulting in their cellular structure. However, at the same time, the cellular structure of the aluminium foams also introduces several difficulties, particularly in achieving foams with a constant and uniform quality, which is an important prerequisite for their broad commercialisation in more demanding applications.

The assurance of a constant, uniform and repeatable quality and the properties of aluminium foams are based on the development of a homogeneous microstructure, especially in the cell-size distribution, cell morphology and wall thickness. The development of such a repeatable and homogeneous foam microstructure is influenced by several parameters, which should be carefully and completely controlled.

The following parameters are the most important:

- Selection of the foaming agent (hydrides, carbides, etc.),
- The average size and particle morphology of the foaming agent,
- The chemical composition of the foaming agent's surface (e.g., the level of oxidation, etc.),
- The concentration and homogeneity of the distribution of the foaming agent in the aluminium matrix,
- The homogeneity of the aluminium matrix,
- The temperature and time of foaming,
- The cell coalescence and coarsening.

A quantitative evaluation of the microstructure of aluminium foams and, particularly, their quantitative comparison is a very demanding and complex issue[1]. As a rule, and quite independently of the applied foaming procedure, the microstructure of aluminium foams is rather heterogeneous, with a significant amount of irregularities and non-homogeneities affected by the movement of the foam in the liquid and/or semi-solid state.

The cell-size distribution (CSD) is one of the most important determinants of the level of aluminium foam microstructural uniformity. Although limited to just a representative area of the microstructure of the entire foam sample, the CSD is one of the most suitable quantitative parameters of the aluminium foam microstructural investigation. A mutual correlation between the CSD and the aluminium-foam processing parameters has not yet been established.

Hence, the purpose of this work was to investigate the interdependence of the most frequently applied processing parameters (time, temperature, particle size distribution of foaming agent, concentration of foaming agent in foamable mixture, etc.) on the cell-size distribution and the density of aluminium foams made by the powder metallurgy (P/M) route. Recently, the identical methodology was reported for evaluating the foaming behaviour, cell-size distribution and microstructural uniformity of Al panels made from hot-rolled precursors[2].

2 EXPERIMENTAL PROCEDURE

2.1 Foaming agents

Titanium hydride (supplier: AG Materials Inc., USA) and dolomite powders (supplier: Granit, d. o. o., Slovenska Bistrica, Slovenia) of five different average particle sizes were applied as foaming agents. The average particle size of the powders used in the experiments is listed in **Table 1**. The particle size distribution of the powdered foaming agents was measured using a laser particle analyser (Malvern Mastersizer 2000). The relative error of the measurement was within ±1%.

Table 1: The average particle size and cumulative particle size distribution of the TiH_2 and dolomite powders applied as foaming agents

Tabela 1: Povprečna velikost delcev in porazdelitev delcev po velikosti TiH_2 in dolomitnega prahu, uporabljenih kot sredstvo za penjenje

TiH_2 powders	TIH-003B	TIH-0420	TIH-3242	TIH-2032	TIH-1020
Average particle size (μm)	3.1	20.4	40.8	60.3	110.4
Cumulative particle size distribution (μm)					
D_{10}	1.2	13.1	23.4	45.8	80.4
D_{25}	2.8	17.4	32.5	53.8	97.3
D_{50}	3.1	20.4	40.8	60.3	110.4
D_{75}	3.3	23.7	50.4	69.2	129.8
D_{90}	5.7	41.4	65.9	82.3	151.1
Uniformity of particle size distribution (μm)					
$D_{90} - D_{10}$	4.5	28.3	42.5	36.5	70.7
Dolomite powders	D-1	D-2	D-3	D-4	D-5
Average particle size (μm)	3.4	5.2	10.1	20.8	35.7
Particle size distribution (μm)					
D_{10}	1.6	3.9	5.6	11.2	28.6
D_{25}	2.3	4.7	8.6	15.9	33.0
D_{50}	3.4	5.2	10.1	20.8	35.7
D_{75}	3.5	5.6	11.8	23.1	36.9
D_{90}	4.2	6.0	13.7	27.2	39.2
Uniformity of particle size distribution (μm)					
$D_{90} - D_{10}$	3.0	2.1	8.1	16.0	10.6

In the case of dolomite powder, part of the as-received powder (D-5) with an average particle size of 35 μm was additionally milled in a planetary mill (in acetone with Al_2O_3 balls) for various times (10, 30, 60 and 120) min and laboratory sieved to provide fractions (D-1, D-2, D-3 and D-4) with a lower average particle size.

The applied TiH_2 and dolomite powders had relatively narrow particle size distributions and different average particle sizes. In the case of commercial grades of TiH_2 powders, the average particle size (D_{50}) was within the range of 3 μm to 110 μm, while in the case of

laboratory sieved fractions of the milled dolomite the powders were from 3 μm to 36 μm.

The uniformity of the particle size distribution in the TiH_2 and the dolomite powders applied was different in various grades of powders. The TiH_2 powder grade TIH-003B had a very narrow particle size distribution and excellent uniformity, whereas the other TiH_2 powders were less uniform, especially the grade TIH-1200.

Generally, the uniformity of the particle size distribution in the selected dolomite powders was significantly higher than the TiH_2. However, also in that case, some grades of the applied dolomite powders (e.g., D-4) had a less uniform particle size distribution.

2.2 Aluminium powders

For most experiments, AlSi12 powder with an average particle size of 80 μm was applied. Some trials were also made with a coarser AlSi12 powder having an average particle size of 350 μm.

2.3 Concentration of foaming agent

The concentration of foaming agents (TiH_2 and dolomite) in the foaming precursors in the mass fraction was w = 0.5 %. However, in two separate sets of experiments, the concentration of foaming agents was changed systematically – in the case of TiH_2 from 0.5 % to 1.5 % and in the case of dolomite, from 0.5 % to 3.0 %. In order to reduce the number of experiments, only one grade of each foaming agent was applied – TIH-0420 in precursors with TiH_2 and D-4 in precursors with dolomite. As is evident from **Table 1**, both applied grades had the same average particle size of approx. 20 μm.

2.4 Homogenisation of foaming mixtures

Homogenisation of foaming mixtures was performed in a laboratory turbula device, by applying different homogenisation times. Thus, mixtures of AlSi12 powder and 0.5 % of TiH_2 (grade TIH-0420) or dolomite (D-4), were homogenized using two different regimes: for 10 min or 240 min.

2.5 Preparation of foaming precursors

The foams made in this work were prepared by the indirect foaming method starting from solid, foamable precursors of the AlSi12 matrix containing uniformly dispersed foaming agent particles. The foamable precursors were made using the powder metallurgy route. The homogenized mixtures of selected AlSi12 and TiH_2 or dolomite powders were uniaxially cold pressed under a pressure of 100 MPa and then additionally isostatically pressed under 950 MPa.

2.6 Foaming procedure

The precursors were foamed in a conventional batch electrical furnace with air atmosphere circulation under various experimental conditions (time, temperature) and applying the same cooling method. Before foaming, the individual precursors were inserted into a cylindrical (40 mm in diameter and 70 mm long) stainless steel mould coated with a boron nitride suspension. The mould dimensions and the precursor size (20 mm in diameter and 30 mm long) were selected to allow the complete expansion of the precursor to foam. The arrangement was placed inside a pre-heated batch furnace at a selected temperature and held for the selected holding time. After that, the mould was removed from the furnace and the foaming process was stopped by rapid cooling with pressurised air to room temperature. The thermal history of the foam sample was recorded using a thermocouple located directly in the precursor material. Precursors with the TiH_2 foaming agent were foamed in the temperature interval of 580 °C to 700 °C and a foaming time of 10 s to 180 s, while precursors with the dolomite foaming agent were foamed at a higher temperature (700 °C to 900 °C) for slightly shorter foaming times of 10 s to 120 s.

2.7 Foam density and porosity

The foam density was measured using the Archimedes method. The porosity of laboratory prepared foams was then calculated using equation: 1-(foam density/aluminium alloy density).

2.8 Microstructural investigation of foamed samples

The macro- and microstructural examinations were performed on sections obtained by precision wire cutting across the samples and on samples mounted in epoxy resin, using light and scanning electron microscopy as well as energy-dispersive x-ray spectrometry (SEM/EDS).

The average size of the pores and the pore size distribution were estimated by analysing the optical and scanning electron micrographs of as-polished foam bars applying the point-counting method and image analysis software.

2.9 A model of foam microstructure development (bubble growth)

The bubble growth can be expressed by applying a simple, stoichiometric model, in which the complete thermal decomposition of an individual TiH_2 or dolomite particle provides the gas phase for bubble nucleation and growth. Based on that simple assumption, the maximum bubble diameter depends on the maximum bubble pressure (p_{max}) determined by the Laplace equation:

$$P_{max} = (2\sigma_{lg}/r) + \rho g h + p_0 \quad (1)$$

The maximum bubble pressure, p_{max}, is the sum of the capillary ($2\sigma_{lg}/r$), hydrostatic ($\rho g h$) and atmospheric (p_0) pressures. The capillary pressure depends on the surface tension, σ_{lg}, at the gas-liquid interface and the bubble radius (r); the hydrostatic pressure is determined by the immersion depth (h) and the density of the molten aluminium alloy (ρ).

The maximum radius (r_{max}) of an isolated bubble immersed in a molten (or semi-solid) aluminium alloy can be calculated by applying the ideal gas equation:

$$P_{max}V = nRT \quad (2)$$

where n corresponds to the number of moles of gas phase inside the bubble, R is the universal gas constant, V is the bubble volume and T is the temperature.

For a spherical bubble by combining Eqs. (1) and (2), we can calculate:

$$[(2\sigma_{lg}/r) + \rho gh + p_0]\ (4/3)r_{max}{}^3\pi = nRT \quad (3)$$

In the early stage of bubble growth, only the capillary pressure ($2\sigma_{lg}/r$) needs to be considered, while in the final stage of bubble growth the only important pressure is the atmospheric (p_0). Note that for laboratory conditions, the hydrostatic pressure (ρgh) is always negligible.

In **Tables 2a** and **2b**, the maximum bubble radius, r_{max}, is calculated for various initial particle sizes (D_{50}) of individual TiH_2 and dolomite particles, assuming in all cases a complete chemical conversion without the loss of the gaseous phase.

Under these conditions, the average particle size of the foaming agent is correlated with the number of moles of gas phase using the following expression:

$$n = (d_{50}{}^3\pi)/(6M) \quad (4)$$

where M is the molar mass of the foaming agent applied. The maximum bubble radius, r_{max}, is finally determined by the formula:

$$r_{max} = d_{50}\ [RT/(8\ M\ p_0)] \quad (5)$$

Table 2a: Maximum bubble radius for TiH_2 particles with a different initial particle size (D_{50})

Tabela 2a: Maksimalni premer pore iz TiH_2 delcev različne začetne velikosti (D_{50})

The average particle size of TiH_2 (μm)	3	20	40	75	140
Maximum bubble radius, r_{max}/μm	27	180	404	676	1263

Table 2b: Maximum bubble radius for bubbles created by dolomite particles of different initial particle size (D_{50})

Tabela 2b: Maksimalni premer pore iz delcev dolomita različne začetne velikosti (D_{50})

The average particle size of dolomite (μm)	3	5	10	20	35
Maximum bubble radius, r_{max} /μm	20	34	66	134	234

3 RESULTS AND DISCUSSION

The influence of the type, average particle size and particle size distribution of the foaming agent on the density, average cell size and cell-size distribution in aluminium foam samples is reported in **Tables 3a** and **3b**.

The uniformity of the cell-size distribution in foamed samples was studied as a function of the particle size distribution of the foaming agents (**Tables 3a** and **3b**), the average particle size of the applied AlSi12 powders (**Table 4**), the concentration of foaming agents (**Tables 5a** and **5b**), foaming temperature (**Table 6**) and foaming time (**Table 7**).

A typical microstructure of the obtained aluminium foam samples is presented in **Figure 1**.

Generally, the samples foamed with dolomite foaming agent had a more uniform cell-size distribution

Table 3a: Experimentally determined density and cell-size distribution of aluminium foam samples as a function of TiH_2 foaming-agent morphology. Foaming conditions: 700 °C, 120 s.

Tabela 3a: Eksperimentalno izmerjene vrednosti gostote in porazdelitve velikosti por v vzorcih aluminijskih pen, izdelanih pri različnih koncentracijah delcev TiH_2, uporabljenega kot penila. Pogoji penjenja: 700 °C, 120 s.

Type of foaming agent	TiH_2				
Powder grade	TIH-003B	TIH-0420	TIH-3242	TIH-2032	TIH-1020
Density of aluminium foam (% of T. D.)	24.2 ± 1.2	25.6 ± 1.3	21.8 ± 1.1	18.9 ± 0.9	17.1 ± 0.9
Cell-size distribution (mm)					
D_{10}	2.6 ± 0.3	2.5 ± 0.3	4.3 ± 0.4	6.2 ± 0.6	8.4 ± 0.8
D_{25}	2.9 ± 0.3	2.6 ± 0.3	4.8 ± 0.4	6.6 ± 0.7	8.7 ± 0.8
D_{50}	3.1 ± 0.3	2.7 ± 0.3	4.9 ± 0.5	6.8 ± 0.7	8.9 ± 0.9
D_{75}	4.0 ± 0.4	3.2 ± 0.3	5.5 ± 0.6	8.0 ± 0.8	10.2 ± 1.0
D_{90}	6.4 ± 0.6	4.9 ± 0.5	7.0 ± 0.7	10.7 ± 1.1	12.5 ± 1.3
Uniformity of cell-size distribution (μm)					
$D_{90} - D_{10}$	3.8 ± 0.4	2.4 ± 0.2	2.7 ± 0.3	4.5 ± 0.5	4.1 ± 0.5

Table 3b: Experimentally determined density and cell-size distribution of aluminium foam samples as a function of the dolomite foaming agent morphology. Foaming conditions: 700 °C, 120 s.

Tabela 3b: Eksperimentalno izmerjene vrednosti gostote in porazdelitve velikosti por v vzorcih aluminijskih pen, izdelanih pri različnih koncentracijah delcev dolomita, uporabljenega kot penila. Pogoji penjenja: 700 °C, 120 s.

Type of foaming agent	Dolomite				
Powder grade	D-1	D-2	D-3	D-4	D-5
Density of aluminium foam (% of T. D.)	13.7 ± 0.7	14.9 ± 0.7	16.3 ± 0.8	15.4 ± 0.8	13.1 ± 0.7
Cell-size distribution (mm)					
D_{10}	2.6 ± 0.3	2.2 ± 0.3	2.2 ± 0.2	2.2 ± 0.2	2.9 ± 0.3
D_{25}	2.7 ± 0.3	2.3 ± 0.3	2.2 ± 0.2	2.3 ± 0.2	3.0 ± 0.3
D_{50}	2.8 ± 0.3	2.5 ± 0.3	2.2 ± 0.2	2.3 ± 0.2	3.1 ± 0.3
D_{75}	3.2 ± 0.3	2.8 ± 0.3	2.4 ± 0.2	2.6 ± 0.3	3.4 ± 0.3
D_{90}	3.9 ± 0.4	4.2 ± 0.4	4.4 ± 0.4	4.5 ± 0.5	4.6 ± 0.5
Uniformity of cell-size distribution (μm)					
$D_{90} - D_{10}$	1.3 ± 0.1	2.0 ± 0.2	2.2 ± 0.2	2.3 ± 0.2	1.7 ± 0.2

Table 4: Experimentally determined correlation between the average size of AlSi12 particles in the foaming precursor and the density and the cell-size distribution in samples of aluminium foam. Foaming conditions: 700 °C, 120 s.

Tabela 4: Eksperimentalno ugotovljena odvisnost gostote vzorcev aluminijskih pen v odvisnosti od povprečne velikosti delcev AlSi12 prahu v prekurzorju za penjenje. Pogoji penjenja: 700 °C, 120 s.

The average particle size of AlSi12 (μm)	80 ± 10		350 ± 10	
Type and grade of foaming agent	TIH-0420	D-4	TIH-0420	D-4
Density of Al foam (% T. D.)	24.6 ± 1.2	15.1 ± 0.8	23.3 ± 1.2	12.9 ± 0.6
Cell-size distribution (mm)				
D_{10}	2.6 ± 0.3	2.1 ± 0.2	3.5 ± 0.4	2.8 ± 0.3
D_{25}	2.8 ± 0.3	2.3 ± 0.2	3.8 ± 0.4	3.1 ± 0.3
D_{50}	2.9 ± 0.3	2.4 ± 0.2	3.9 ± 0.4	3.3 ± 0.3
D_{75}	3.2 ± 0.3	2.7 ± 0.3	4.3 ± 0.4	3.6 ± 0.4
D_{90}	5.0 ± 0.5	4.6 ± 0.5	7.1 ± 0.7	6.7 ± 0.7
Uniformity of cell-size distribution (μm)				
$D_{90} - D_{10}$	2.4 ± 0.2	2.3 ± 0.2	3.6 ± 0.4	3.9 ± 0.4

Table 5a: Experimentally determined density and cell-size distribution of aluminium foam samples as a function of the concentration of TiH_2 foaming agent (TIH-0420). Foaming conditions: 700 °C, 120 s.

Tabela 5a: Eksperimentalno ugotovljene vrednosti gostote in porazdelitve velikosti por v vzorcih aluminijske pene, v odvisnosti od koncentracije TiH_2 kot sredstva za penjenje (TIH-0420). Pogoji penjenja: 700 °C, 120 s.

Concentration of TiH_2 (*w*/%)	0.5	1.0	1.5
Density of Al foam (% T. D.)	25.9 ± 1.3	23.8 ± 1.2	21.2 ± 1.1
Cell-size distribution (mm)			
D_{10}	2.6 ± 0.3	3.2 ± 0.3	3.3 ± 0.3
D_{25}	2.7 ± 0.3	3.5 ± 0.3	3.8 ± 0.3
D_{50}	2.8 ± 0.3	3.7 ± 0.4	5.1 ± 0.5
D_{75}	3.0 ± 0.3	4.2 ± 0.3	5.5 ± 0.6
D_{90}	4.6 ± 0.5	8.4 ± 0.3	10.4 ± 1.0
Uniformity of cell-size distribution (μm)			
$D_{90} - D_{10}$	2.0 ± 0.2	5.2 ± 0.6	7.1 ± 0.7

Table 5b: Experimentally determined density and cell-size distribution of aluminium foam samples as a function of the concentration of dolomite foaming agent (D-4). Foaming conditions: 700 °C, 120 s.

Tabela 5b: Eksperimentalno ugotovljene vrednosti gostote in porazdelitve velikosti por v vzorcih aluminijske pene, v odvisnosti od koncentracije dolomita kot sredstva za penjenje (D-4). Pogoji penjenja: 700 °C, 120 s.

Concentration of dolomite (*w*/%)	0.5	1.0	1.5
Density of Al foam (% T. D.)	15.4 ± 0.8	12.8 ± 0.6	11.1 ± 0.6
Cell-size distribution (mm)			
D_{10}	2.0 ± 0.2	2.4 ± 0.2	2.9 ± 0.3
D_{25}	2.3 ± 0.2	2.9 ± 0.3	3.3 ± 0.3
D_{50}	2.5 ± 0.3	3.2 ± 0.3	4.7 ± 0.5
D_{75}	2.7 ± 0.3	4.8 ± 0.6	5.1 ± 0.5
D_{90}	5.8 ± 0.6	7.6 ±0.8	9.7 ± 1.0
Uniformity of cell-size distribution (μm)			
$D_{90} - D_{10}$	3.8 ± 0.4	5.2 ± 0.5	6.8 ± 0.7

and a lower average bubble size. The most uniform cell-size distribution was achieved in foam samples foamed with the minimum amount (w = 0.5 %) of dolomite powder grades (D-1, D-2) having the lowest average particle size and narrow particle size distribution. In contrast, in samples made from coarser and less-uniform grades of foaming agents, the cell size distribution was wide-ranging, with a significantly higher fraction of large bubbles. In addition, a longer foaming time and higher foaming temperatures also led to foam samples with a less-uniform microstructure.

The experimentally determined values of the average bubble radius reported in **Tables 2a** and **2b** are at least one order of magnitude higher that those predicted by the model. The reason for this difference is due to the effects limiting the stability of individual bubbles, which are not considered by the model. These effects are bubble flow, drainage, rupture or coalescence, and coarsening.

From the difference between the theoretically predicted and experimentally determined values of the bubble radius, it is possible to estimate the stability of the real foam systems considered in this work. The experimental findings clearly confirm that coarser bubbles are more stable that finer ones. In addition, it is also evident that the stability of bubbles is much higher in foams created by dolomite particles than in the counterparts foamed by TiH_2. However, in both cases the average bubble sizes are proportional to the average initial size of the foaming particles – finer foaming particles create finer bubbles, while coarser particles create larger bubbles, as was predicted by the model.

On the other hand, the density of aluminium foam samples was inversely proportional to the bubble radius: foam samples with finer bubbles (**Tables 3a** and **3b**) had a higher density and, vice versa, foam samples with larger bubbles were specifically lighter. At the same time

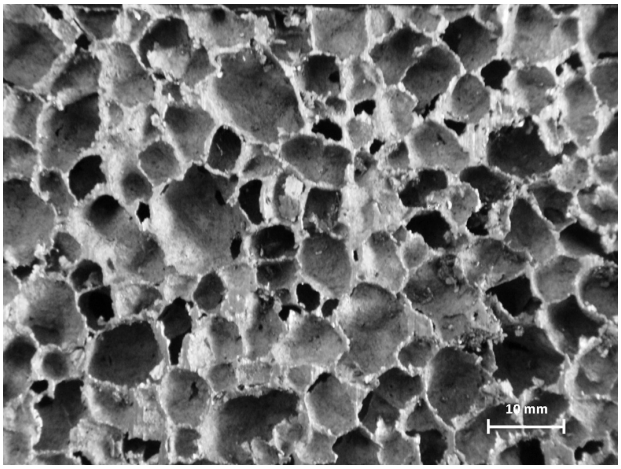

Figure 1: SEI of microstructure of aluminium foam sample foamed by applying TIH-3242 TiH_2 foaming agent. Foaming conditions: 700 °C, 120 s.

Slika 1: SEM-posnetek vzorca aluminijske pene, izdelane s pomočjo TIH-3242 TiH_2 sredstva za penjenje. Pogoji penjenja: 700 °C, 120 s.

Table 6: Experimentally measured density and cell-size distribution of foam samples at various foaming temperatures. Foaming time: 120 s.

Tabela 6: Eksperimentalno izmerjene vrednosti gostote in porazdelitve velikosti por v vzorcih aluminijske pene, izdelanih pri različnih temperaturah penjenja. Pogoji penjenja: 120 s.

Type and grade of foaming agent	TiH_2 (TIH-0420)			Dolomite (D-4)		
Foaming temperature (°C)	600	650	700	700	800	900
Foam density (% T. D.)	25.9 ±1.3	24.3 ±1.2	23.7 ±1.2	17.2 ±0.9	16.1 ±0.8	15.8 ±0.8
Cell-size distribution (mm)						
D_0	2.0 ±0.2	2.4 ±0.2	2.7 ±0.3	1.7 ±0.2	1.9 ±0.2	2.0 ±0.2
D_{25}	2.1 ±0.2	2.5 ±0.3	2.9 ±0.3	1.8 ±0.2	2.0 ±0.2	2.2 ±0.2
D_{50}	2.6 ±0.3	2.8 ±0.3	3.3 ±0.3	2.0 ±0.2	2.2 ±0.2	2.3 ±0.2
D_{75}	3.0 ±0.3	3.2 ±0.3	3.7 ±0.4	2.9 ±0.2	3.1 ±0.3	3.4 ±0.3
D_{100}	4.3 ±0.4	4.8 ±0.5	5.4 ±0.5	4.1 ±0.4	4.5 ±0.5	4.9 ±0.5
Uniformity of cell-size distribution (μm)						
$D_{90} - D_{10}$	2.3 ±0.2	2.4 ±0.2	2.7 ±0.3	2.4 ±0.2	2.6 ±0.3	2.9 ±0.3

Table 7: Experimentally measured density and cell-size distribution of aluminium foam samples at various foaming times. Foaming temperature: 700 °C.

Tabela 7: Eksperimentalno izmerjene vrednosti gostote in porazdelitve velikosti por v vzorcih aluminijskih pen, izdelanih pri različnih časih penjenja. Pogoji penjenja: 700 °C.

Type and grade of foaming agent	TiH_2 (TIH-0420)			Dolomite (D-4)		
Foaming time (s)	10	90	180	10	60	120
Foam density (% T. D.)	31.4 ±1.6	28.7 ±1.4	25.2 ±1.3	23.7 ±1.2	18.1 ±0.9	15.5 ±0.8
Cell-size distribution (mm)						
D_{10}	1.7 ±0.2	2.2 ±0.2	2.5 ±0.3	1.5 ±0.2	1.9 ±0.2	2.1 ±0.2
D_{25}	1.8 ±0.2	2.3 ±0.2	2.6 ±0.3	1.6 ±0.2	2.1 ±0.2	2.2 ±0.2
D_{50}	1.9 ±0.2	2.4 ±0.2	2.8 ±0.3	1.6 ±0.2	2.0 ±0.2	2.3 ±0.2
D_{75}	2.7 ±0.3	2.9 ±0.3	3.3 ±0.3	2.5 ±0.3	2.8 ±0.3	3.5 ±0.4
D_{90}	3.7 ±0.4	4.4 ±0.4	4.9 ±0.5	3.5 ±0.4	4.1 ±0.4	5.0 ±0.5
Uniformity of cell-size distribution (μm)						
$D_{90} - D_{10}$	2.0 ±0.2	2.2 ±0.2	2.4 ±0.2	2.0 ±0.2	2.2 ±0.2	2.9 ±0.3

and under the same foaming conditions (temperature, time), foams made using dolomite had a significantly lower density than samples with a similar cell size foamed by TiH_2.

The foaming of precursors made from two grades of AlSi12 powder (**Table 4**) resulted in foam samples with a bubble radius proportional to the average size of the AlSi12 powders. Independently of the kind of foaming agent (TiH_2 or dolomite), coarser AlSi12 powder resulted in foams with larger bubble radius.

As evident from the cell-size distribution data listed in **Tables 5a** and **5b**, an increase in the foaming-agent concentration (either TiH_2 or dolomite) led to the formation of foams with larger bubbles and a lower density. However, also in that case, samples foamed with dolomite had smaller bubbles and lower densities.

Finally, an increase in the foaming temperature and time (**Tables 6** and **7**) also favoured the formation of coarser bubbles. Again, the coarsening tendency was found to be higher in samples foamed by TiH_2.

The experimentally developed foam microstructures were mainly influenced by a slowing down of the level of foam movement (i.e., the foam stability) attained in particular trials. The slowing down of the movement of the foam includes the prevention of flow (the movement of bubbles with respect to each other caused either by external forces or changes in the internal gas pressure during foaming), drainage (flow of liquid metal through the foam), coalescence (sudden instability in a bubble wall leading to its disappearance) and coarsening (slow diffusion of gas from smaller bubbles to bigger bubbles).

4 CONCLUSION

The effects of a foaming agent and its morphology on the foaming behaviour, cell-size distribution and microstructural uniformity of closed-cell aluminium foams were investigated. Furthermore, a model of the microstructural development (bubble growth and stabilisation) was developed and compared with the experimental findings.

According to the experimental findings, samples foamed with the dolomite foaming agent had a more uniform cell-size distribution and a lower average bubble size. The most uniform cell-size distribution was achieved in foam samples foamed with the minimum amount (w = 0.5 %) of dolomite powder grades having the lowest average particle size and a narrow particle size distribution. In contrast, in samples made from coarser and less-uniform grades of foaming agents, the cell-size distribution was broader, with a significantly higher fraction of large bubbles. In addition, longer foaming times and higher foaming temperatures also led to foam samples with a less-uniform microstructure.

Acknowledgement

This work was supported by funding from the Public Agency for Research and Development of the Republic of Slovenia (ARRS – Grant L2-2410), as well as the Impol Aluminium Company and Bistral, d. o. o., from Slovenska Bistrica, under contract No. 2410-0206-09.

5 REFERENCES

[1] V. Kevorkijan, S. D. Škapin, I. Paulin, B. Šuštaršič, M. Jenko, Mater. Tehnol., 44 (**2010**) 6, 363–371

[2] V. Kevorkijan, U. Kovačec, I. Paulin, S. D. Škapin, M. Jenko, Mater. Tehnol., 45 (**2011**) 6, 537–544

UDK 536.65:536.42
Original scientific article/Izvirni znanstveni članek

ISSN 1580-2949
MTAEC9, 46(3)239(2012)

SIMULATION OF LATENT-HEAT THERMAL STORAGE INTEGRATED WITH ROOM STRUCTURES

SIMULACIJA HRANJENJA LATENTNE TOPLOTE, INTEGRIRANE V SOBNIH STRUKTURAH

Pavel Charvat[1], Tomas Mauder[1], Milan Ostry[2]

[1]Brno University of Technology, Faculty of Mechanical Engineering, Technicka 2896/2, 616 69 Brno, Czech Republic
[2]Brno University of Technology, Faculty of Civil Engineering, Veveri 331/95, 602 00 Brno, Czech Republic
charvat@fme.vutbr.cz

Prejem rokopisa – received: 2011-10-20; sprejem za objavo – accepted for publication: 2012-02-13

The phase change of a material is accompanied by a release or absorption of a considerable amount of heat. That makes a phase change a phenomenon effectively usable in various thermal storage applications. There are many materials with a melting temperature lying within the thermal comfort range for indoor environments. These materials can be utilized in building-integrated thermal storage. The performance of such latent-heat thermal storage integrated with the room structures was investigated through numerical simulations and experiments. The studied case involved two adjacent rooms of the same dimensions. The hydrated-salt-based phase-change material (PCM) was used as a thermal storage medium. A comparative approach was adopted in which the internal structures of one of the rooms contained the PCM, while the structures in the other room did not. The simulation model of the rooms was created in the numerical simulation tool TRNSYS 17, and this model was coupled with a PCM model created in MATLAB. The enthalpy method was used for the simulation of the phase change. This approach allowed for different time steps in the room model and the PCM model (the time step in the PCM model needed to be much shorter). The data from the real-scale experiments (ventilation rates, temperature of supply air, outdoor temperature, solar radiation intensity, etc.) as well as the physical properties of the PCM acquired in the laboratory testing were used as inputs to the simulation models. The analysis of the results was carried out, in which the simulation results were compared with the experimentally obtained data.

Keywords: latent-heat storage, phase-change materials, building simulations

Fazno spremembo materiala spremlja sproščanje ali absorpcija velike količine toplote. Zato je fazna sprememba pojav, ki se lahko na različne načine učinkovito uporablja s hranjenjem toplote. Obstaja več vrst materialov, ki imajo tališče v toplotnem razponu, ki velja za notranje prostore. Ti materiali se lahko uporabljajo v hranilnikih toplote, ki se integrirajo v konstrukcije. Številne numerične simulacije in eksperimenti so že bili izvedeni za ocenjevanje učinkovitosti takšnih hranilnikov latentne toplote, ki so integrirani v sobne strukture. Obravnavani primer je vključeval dva sosednja prostora enakih dimenzij. Fazno spremenljiv material (PCM), ki temelji na hidratirani soli, je bil uporabljen kot sredstvo shranjevanja toplote. Uporabljen je bil primerjalni način, pri katerem so notranje strukture v enem prostoru vsebovale PCM, medtem ko ga strukture v drugem prostoru niso. Simulacijski model prostorov je bil izveden z orodjem za simulacije TRNSYS 17, ta model pa je bil združen z modelom PCM, ki je bil ustvarjen v laboratoriju MATLAB. Za simulacijo fazne spremembe je bila uporabljena metoda entalpije. S tem načinom je bilo mogoče ustvariti stopnje v prostorskem modelu in modelu PCM z različnimi časovnimi dimenzijami (časovna stopnja v modelu PCM je morala biti znatno krajša). Podatki, ki so bili pridobljeni iz eksperimentov v realnem stanju (razmerja prezračevanja, temperatura dovodnega zraka, zunanja temperatura, intenzivnost sončnega sevanja itd.), ter fizične lastnosti materialov PCM, ki so bili pridobljeni pri laboratorijskih preizkusih, so bili uporabljeni kot vhodni podatki za simulacijske modele. Izvedena je bila analiza podatkov, kjer so se rezultati simulacije primerjali s podatki, pridobljenimi med eksperimenti.

Ključne besede: hranjenje latentne toplote, fazno spremenljivi materiali, simulacija gradnje

1 INTRODUCTION

The increasing demand for energy conservation and thermal comfort in built environments has led to the study of new approaches and materials in building construction. Thermal storage integrated with building structures can contribute to energy conservation in buildings through the reduction of peak cooling or heating loads. The phase change of a material is accompanied by the release or absorption of a considerable amount of heat and that makes such a phase change a phenomenon that is effectively usable in various thermal storage applications. Many materials or their mixtures have a melting temperature in the thermal comfort range of built environments. Advances in materials science and chemistry have allowed for fine-tuning of the material properties for the specific applications. The use of phase-change materials (PCMs) in building structures has been the subject of considerable interest in the past decade. This interest is documented by numerous papers that address this issue.[1–3]

2 EXPERIMENTAL SET-UP

The studied case involves two adjacent rooms of the same dimensions and geometry. A comparative approach was adopted in which the internal structures of one of the rooms contained the PCM, while the structures in the other room did not. A schematic view of the rooms can be seen in **Figure 1**.

The aluminum containers with DELTA®-COOL24 PCM were installed in one of the rooms. The dimensions of the containers are 455 mm × 305 mm × 10 mm. The naked aluminum containers filled with a PCM represent

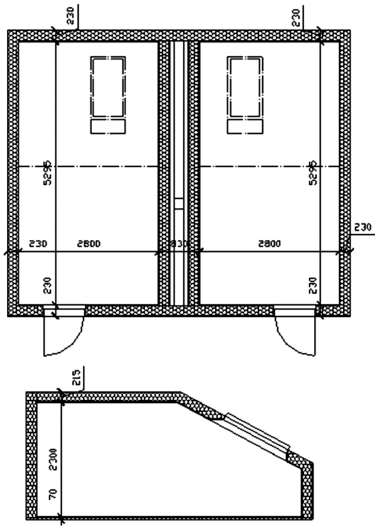

Figure 1: Experimental rooms
Slika 1: Eksperimentalni prostori

one of the best thermal storage options in terms of heat transfer and heat-storage density per unit of surface area. Each container accommodated about 1.1 kg of the PCM with a thermal capacity of 150 kJ/kg in the melting range between 22 °C and 28 °C. This represented a thermal storage capacity of over 1 MJ/m^2 in the indicated temperature range.

The compositions of the multi-layer walls of the test rooms are shown in **Figure 2**. The thermo-physical properties of the wall materials needed for the simulation (such as thermal conductivity, density, specific heat capacity) were obtained from the Czech national standard ČSN 73 0540-3 and they are summarized in **Table 1**.

Table 1: Thermo-physical properties of the wall materials
Tabela 1: Toplotno-fizikalne lastnosti stenskih materialov

Material	ρ/(kg/m^3)	c/(J/(kg K))	k/(W/m K)
Plaster-board	750	1060	0.22
Mineral wool	300	880	0.079

Table 2: Thermo-physical properties of the PCM
Tabela 2: Toplotno-fizikalne lastnosti fazno spremenljivih materialov

PCM	ρ/(kg/m^3)	c/(J/(kg K)	k/(W/mK)
Solid	1600	2700	1.12
Liquid	1500	2200	0.56
Melting range	22–28 °C		
Melting energy	158 kJ/kg		

The thermo-physical properties of the DELTA®-COOL24 PCM, as stated by the manufacturer, are in **Table 2**.

The thermo-physical properties of the PCM were also investigated by means of differential scanning calorimetry with the use of the Q200 calorimeter. The obtained melting range was approximately 20–30 °C with an evaluated thermal capacity of 166 kJ/kg in that range.

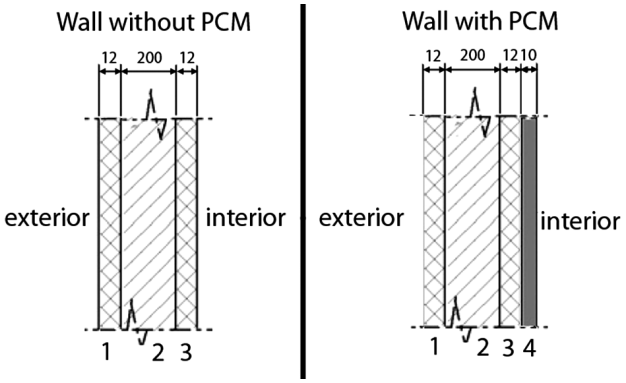

Figure 2: Composition of the walls: (1, 3) plasterboard, (2) mineral wool, (4) PCM
Slika 2: Sestava sten: (1, 3) mavčne plošče, (2) mineralna volna, (4) PCM

The samples used for DSC testing are rather small, which is a problem because the PCM is a mixture of several substances and such a small sample may not have the same composition as a much larger volume of the PCM in the container. Moreover, the thermo-physical properties of the hydrated-salt PCMs are very sensitive to moisture content, which can change during the acquisition and testing of the sample. The heat flux vs. temperature plot obtained by differential scanning calorimetry is shown in **Figure 3**.

The experimental and numerical results presented in this paper correspond to a time period of 2 weeks in the summer of 2009 (between August 11 and August 24). The experiments took place at the Faculty of Civil Engineering in the city of Brno in the Czech Republic. The data obtained from the test-room experiments were used as the inputs for the numerical simulations (ventilation rates, temperature of supply air, outdoor temperature, solar radiation intensity).

3 MATHEMATICAL MODEL AND SIMULATION

The above-described case of latent-heat storage in building structures was numerically simulated with the

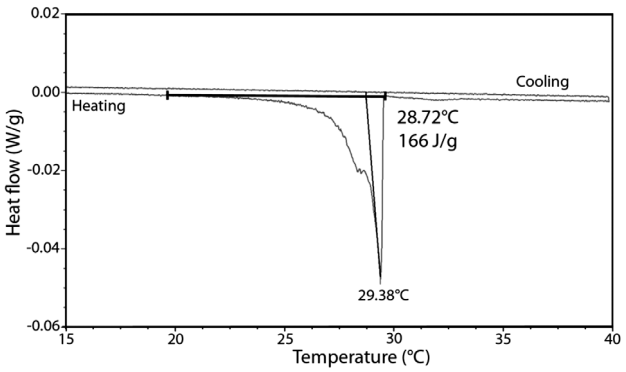

Figure 3: Heat flux vs. temperature plot obtained by DSC
Slika 3: Toplotni tok v primerjavi s temperaturnim razponom, pridobljenim z DSC

use of coupling between the TRNSYS (Transient System Simulation tool) and MATLAB. The simulated problem can be classified as transient heat transfer involving a phase change. Over the years, a number of related computational works have employed various techniques in the analysis of phase-change problems.[4,5] Most analytical solutions dealing with 1-D geometries for very particular sets of boundary conditions cannot be generalized to more complex problems. With the introduction of high-speed digital computers for mathematical modeling, the numerical simulations have become quite an economical and fast approach to solving many engineering problems. The phase-change problem can be solved by a numerical analysis that involves either the finite-difference or the finite-element methods. The finite-difference method was used in the simulations described in this paper. The phase change was modeled with the use of the latent-heat-accumulation approach that is sometimes referred to as the enthalpy method. In the basic enthalpy scheme, the enthalpy is used as the primary variable and the temperature is calculated from a defined enthalpy-temperature relation[6]:

$$H = \int_0^T \left(\rho(\xi) c(\xi) - \rho(\xi) \Delta H \frac{\partial f_s}{\partial T} \right) \mathrm{d}\xi \qquad (1)$$

where H/(J/m^3) is the volume enthalpy, ΔH/(J/kg) is the latent-heat coefficient, ρ/(kg/m^3) is the density, c/(J/kg K) is the specific heat capacity and f_s/(–) is the solid fraction.

A 1-D model of the multi-layer wall with an interior layer containing the PCM (**Figure 2**) was created in MATLAB. The 1-D simplification seemed to be justified by the assumption of uniform boundary conditions over the entire surface of the wall on each side. The temperature distribution in the wall can be obtained from the Fourier equation, which for the 1-D case reads as[3–5]:

$$\frac{\partial H}{\partial \tau} = k(T) \frac{\partial^2 T}{\partial x^2} \qquad (2)$$

where k/(W/m K) is the thermal conductivity, T/K is the temperature, τ/s is the real time and x/m is the space coordinate.

The finite-difference method was used to solve the Fourier equation. The continuous information contained in the exact solution of the differential equation is replaced by the discrete temperature values T_i^n in the numerical solution. The subscript i concerns the space coordinate and the superscript n is the time coordinate. The explicit finite-difference scheme according to the enthalpy method with the non-equidistant space steps is:

$$H_i^{n+1} = H_i^n + \Delta\tau k(T) \left(\frac{\dfrac{T_{i+1}^n - T_i^n}{\Delta x_i} - \dfrac{T_i^n - T_{i-1}^n}{\Delta x_{i-1}}}{\dfrac{\Delta x_i - \Delta x_{i-1}}{2}} \right) \qquad (3)$$

The initial and boundary conditions for the equations (2) and (3) must be provided. The initial condition describes the initial temperature distribution in the multi-layer wall and it was obtained from the measurement in the studied case.

The model of the test rooms was created in the TRNSYS tool and this model was coupled with the described model of the multi-layer wall created in MATLAB. The air temperature in the room obtained from TRNSYS was used as a boundary condition for the heat transfer at the wall, which was handled by the MATLAB model, and the wall surface temperature from MATLAB was returned to the TRNSYS as a boundary condition for the next time step. A time step of 60 seconds was used in the TRNSYS model, while the MATLAB model used a much shorter time step of 1 s (to address the phase change properly). The communication between MATLAB and TRNSYS was provided through the TRNSYS type 155.

The stability condition for the explicit formula was used according to the unconditionally stable fully

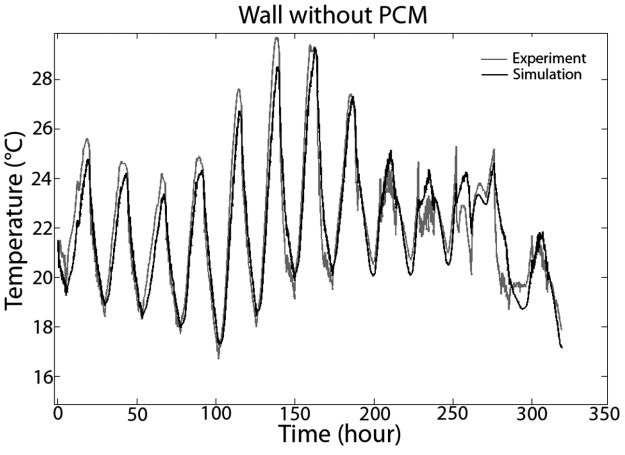

Figure 4: Measured and simulated temperatures in room 1
Slika 4: Izmerjene in simulirane temperature v prostoru 1

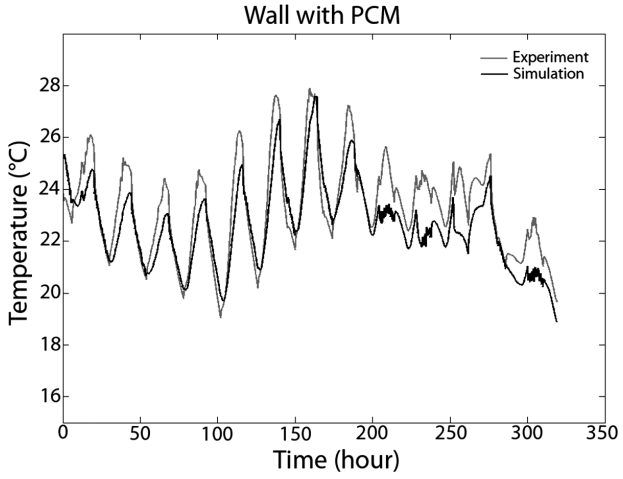

Figure 5: Measured and simulated temperatures for room 2
Slika 5: Izmerjene in simulirane temperature v prostoru 2

explicit finite-difference solution of the solidification problems.[5]

4 RESULTS AND DISCUSSION

The experimental data was available in 15-minute intervals, while the simulations were performed with a time step of 1 min. The experimental data was re-sampled to the simulation time step using the quadratic interpolation in order that the data could be used as boundary conditions for the simulations.

The results of the simulation for the experimental room without the PCM compared with the experimentally obtained data can be seen in **Figure 4**. The chart shows a relatively good agreement of the simulated and measured room temperatures. The maximum difference between the measured and simulated temperature was 1 °C.

The results for the experimental room with the walls containing the PCM are shown in **Figure 5**. The maximum difference between the measured and simulated temperature is 2.5 °C. There can be several explanations for this discrepancy. The uniform boundary condition (air temperature, heat-transfer coefficient) was applied to the entire surface of the walls containing the PCM in the numerical model. The distribution of the heat-transfer coefficient over the wall surface was not thoroughly investigated in the experiment. Also, the heat-transfer case was assumed to be 1-D with the heat flux in the direction of the normal to the surface of the wall. The observations made in the experimental room indicated that the melting and solidification of the PCM in the containers was not uniform with pockets of solid PCM at the bottom of the containers (separation due to gravity).

If we compare the temperatures in the experimental room (**Figures 4** and **5**) we can see that the presence of the PCM reduces the air-temperature fluctuations in the room. This reduction can improve the thermal comfort of the occupants, which corresponds with the findings of other authors[3].

5 CONCLUSION

A numerical model of a multi-layer wall containing a phase-change material was developed. This model was coupled with the TRNSYS simulation tool and employed for the simulation of experiments that were carried out in the experimental rooms. A good agreement was achieved between the simulation results and the experimental data in terms of the general trends. However, the simulation model was not always able to predict the indoor temperature with an accuracy necessary for practical applications. Further development of the model is in progress. Both the experimental investigations and the numerical simulations showed that the phase-change material integrated with the wall structure attenuated the air-temperature fluctuations in the room.

Acknowledgement

The authors gratefully acknowledge the financial support from the project OC10051 of the Czech Ministry of Education and the project ED0002/01/01 – NETME Centre, and the Junior Research Project on BTU BD13102003.

6 REFERENCES

[1] R. Baetens, P. B. Jelle, A. Gustavsen, Phase change materials for building applications: A state-of-the-art review, Energy and Buildings, 42 (**2010**) 9, 1361–1368

[2] V. Butala, U. Stritih, Experimental investigation of PCM cold storage, Energy and Buildings, 41 (**2009**) 3, 354–359

[3] F. Kuznik, J. Virgone, J. Roux, Energetic efficiency of room wall containing PCM wallboard: A full-scale experimental investigation, Energy and Buildings, 40 (**2008**) 2, 148–156

[4] M. Muhieddine, É. Canot, R. March, Various approaches for solving problems in heat conduction with phase change, International Journal on Finite Volumes, 6 (**2009**) 1, 20

[5] R. Tavakoli, P. Davami, Unconditionally stable fully explicit finite difference solution of solidification problems, Metallurgical and Materials Transactions B, 38 (**2007**) 1, 121–142

[6] F. Kavička, J. Stetina, B. Sekanina, K. Stransky, J. Dobrovska, J. Heger, The optimization of a concasting technology by two numerical models, Journal of Materials Processing Technology, 185 (**2007**) 1–3, 152–159

UDK 678.84
Original scientific article/Izvirni znanstveni članek

ISSN 1580-2949
MTAEC9, 46(3)243(2012)

SHAPE-MEMORY POLYMERS FILLED WITH SiO_2 NANOPARTICLES

POLIMERI Z OBLIKOVNIM SPOMINOM, POLNJENI S SiO_2 NANODELCI

Iulia Andreea Bocsan[1], Marjetka Conradi[2], Milena Zorko[3], Ivan Jerman[3], Liana Hancu[1], Marian Borzan[1], Maarten Fabre[4], Jan Ivens[5]

[1]Technical University of Cluj Napoca, Romania
[2]Institute of Metals and Technology, Slovenia
[3]National Institute of Chemistry, Slovenia
[4]Lessius University College, Campus De Naye, Belgium
[5]Katolieke Universiteit Leuven, Department of Metallurgy and Materials Engineering, Belgium
iulia.bocsan@tcm.utcluj.ro

Prejem rokopisa – received: 2011-10-20; sprejem za objavo – accepted for publication: 2012-02-20

In this paper we discuss the mechanical and thermal properties of shape-memory polymer composites (SMPCs) filled with SiO_2 nanoparticles. A series of SMPC samples was prepared using a commercially provided shape-memory polymer (SMP) filled with different mass fractions of 600-nm and 130-nm SiO_2 particles. The mechanical properties of the SMPCs were determined by performing three-point bending (3PB) and Izod impact tests. The thermomechanical and thermal behaviors were investigated using differential scanning calorimetry (DSC) and dynamic mechanical analysis (DMA).

Keywords: shape-memory polymer, SiO_2 nanoparticles, impact test, three-point bending, DMA, DSC

V članku obravnavamo mehanske in termične lastnosti polimernih kompozitov z oblikovnim spominom (SMPC), polnjenih s SiO_2-nanodelci. Serija SMPC-vzorcev je bila pripravljena z uporabo komercialnega polimera z oblikovnim spominom (SMPC), v katerega je bila dodana različna količina 600 nm in 130 nm SiO_2-delcev. Mehanske lastnosti SMPC so bile določene s tritočkovnim upogibnim preskusom in z žilavostnim preskusom Izod. Termomehansko in toplotno vedenje materiala je bilo preiskovano z uporabo diferenčne vrstične kalorimetrije (DSC) in z dinamično mehansko analizo (DMA).

Ključne besede: polimer z oblikovnim spominom, SiO_2-nanodelci, žilavostni preskus, tritočkovni upogibni preskus, DMA, DSC

1 INTRODUCTION

Shape-memory polymers (SMP) are stimuli-responsive materials, which have generated significant research interest in the past few years.

If an SMP is subject to deformation, large internal stress can be stored in the cross-linking structure by cooling the polymer below its switch transition temperature. By heating the polymer above the switch transition temperature, the SMP recovers its permanent shape as a result of releasing internal stress stored in the cross-linking structure[1]. For the thermoset SMPs the switching temperature is the glass transition temperature T_g.

Their capability to retain an imposed, temporary shape and to recover the initial, permanent shape upon exposure to an external stimulus depends on the "functional determinants" that, in simplistic terms, can be divided into structural/morphological and processing/environmental factors[2].

The major drawback of shape-memory polymers is the low recovery stress, limiting the size of commercial components to a few centimeters; the recovery stress of larger components is insufficient with regard to the initial shape because of the higher weight. The solution is the reinforcing of the SMP with particles or with fibers.

The properties of the final composite products are significantly affected by many factors such as processing techniques, filler distribution, interface, filler size, aspect ratio and matrix nature[1].

2 EXPERIMENTS

This research is based on the experimental work that involved the preparation of the SMPC and the mechanical and thermomechanical testing. A series of SMPC samples were prepared using a commercially provided SMP, filled with different mass fractions of 600-nm and 130-nm fumed silica. 130-nm silica nanoparticles were provided by Riedel-de Haën (Silica Cab-osil), while 600-nm silica particles were synthesized following the Stöber–Fink–Bohn method[3]. To prevent agglomeration, silica particles were initially treated with silane, IO7 T7(OH)3 (trisilanol isooctyl polyhedral oligomeric silsesquioxane, POSS) following the procedure as suggested by Wheeler et al.[4]

Four types of plates were prepared mixing the commercially available epoxy-based thermoset SMP Veriflex from Cornerstore Industries with a transformation temperature (T_g) of 45 °C and the SiO_2 nanoparticles.

The quantity of the SMP used is the same for all the plates. Veriflex is made of two components, A and B, as

marked by the manufacturer. For the mixing A and B are used in the ratio of 100/32,34. First, the nanoparticles were mixed with the component B and subjected to ultrasound in the ultrasonic device for 20 minutes to obtain homogeneous dispersion of the particles. Component A was then added and manually mixed with the component B-nanoparticle dispersion and finally poured into a closed vertical mould made of aluminum (Al) with the inner cavity thickness of 3 mm. The polymerization was realized in an oven following the manufacturer's instructions. Using this method the following four types of SiO_2-filled SMPCs were created:

1. a SMP with a 0.32 % volume fraction (vf) of 130-nm SiO_2 (recipe R1)
2. a SMP with a 0.32 % (vf) of 600-nm SiO_2 (recipe R2)
3. a SMP + SiO_2 with a 0.5% (vf) of 600-nm SiO_2 (recipe R3)
4. a SMP + SiO_2 with a 1% (vf) of 600-nm SiO_2 (recipe R4)

The mechanical behavior of the SMP + SiO_2 was investigated through the following series of tests: the Izod impact and three-point bending tests.

The thermomechanical behavior of the SMP + SiO_2 was determined by using the dynamic mechanical analysis (DMA) and the differential scanning calorimetry (DSC) methods and equipment. The scanning electron microscopy (SEM) images were used to provide information about the fractured surface structure of the SMP + SiO_2 designed samples.

Because of the high-volume fraction of the particles, the R3 and R4 plates were too soft and difficult to be extracted from the mould and it was not possible to obtain proper samples just for the DCS analysis.

For each group of the tests, specimen shapes and sizes have been chosen according to the relevant standards and also in such a way that they were compatible with the capabilities and requirements of the available testing devices.

The thermal properties are included in the key characteristics of the SMPs, especially T_g. To characterize the viscoelastic nature of the SMPCs, TA Instruments Q800 equipment was used for applying the DMA method. The SMP and SMP + SiO_2 samples were cut to 9 mm in width and 30 mm in length in order to fit the single cantilever beam. At a frequency of 1 Hz, after the chamber was cooled down to 0 °C, the temperature was ramped at 2 °C/min until it reached 80 °C. As a result, the storage modulus E', the loss modulus E'', and the loss factor tan $\delta = E''/E'$ were obtained.

To have a better understanding of different values for T_g, the DSC analysis on the TA Instruments Q 2000 equipment was applied because it provides rapid and precise determinations by using minimum amounts of samples.

To measure the resistance to failure of the V-notched samples according to the ASTM standard D256, the Izod impact strength tests were performed on the Zwick 053650 testing machine using a 1 J impactor. Samples were cut from the top of the plate and from the bottom part in order to see the difference in the strength of the material if an eventual non-homogenous dispersion of the SiO_2 nanoparticles were to occur. Because of the long polymerization time (12 h) of the SMPCs, the particles tend to move in the bottom part of the plate.

To determine and compare the modulus of elasticity of the pure SMP and the SMP + SiO_2 samples, the three-point bending tests were performed on the Instron 5985 testing machine according to ASTM D790-03. The test was performed at a load rate of 2 mm/min.

For the SEM imaging, the samples were frozen with liquid nitrogen and fractured. The fractured surface was then analyzed.

3 RESULTS AND DISCUSSION

3.1 The thermomechanical behavior

As shown in **Figure 1** and **Table 1**, different T_g values are essentially dependent on the vf of the SiO_2 filler. This result was achieved by other researchers too. The glass transition temperature decreases significantly with an increase in the weight percentage of aluminum-nitride filled shape-memory polymer composites. A similar phenomenon was reported about the SMP filled with other particles[5].

In **Table 1** different values for T_g determined from the DMA tests using the peak of the tan δ and E' curves and also from the DSC analysis are presented. Surprisingly, the DSC analysis shows an increase of around 4 °C for the composites, while the T_g values obtained with the DMA method show a drop of 4 °C for the 130-nm filled SMP + SIO_2 and 3 °C for the 600-nm filled SMP + SiO_2.

The T_g values are above the ambient temperature (25 °C) for all the SMPCs except for SMP + SiO_2 1 % 600 nm, which is 21.34 °C according to the DSC.

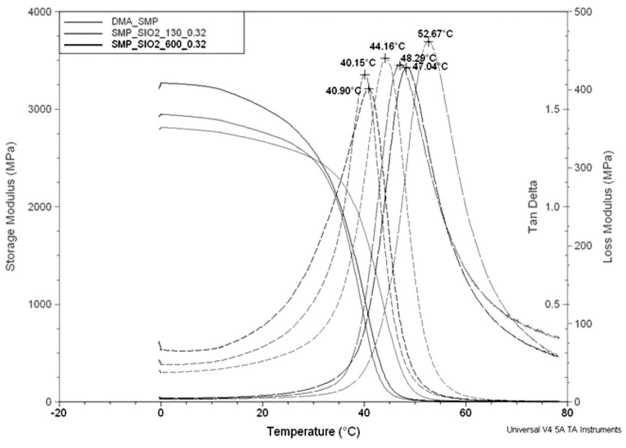

Figure 1: DMA curves overlay
Slika 1: Prekrivanje krivulj DMA

Table 1: T_g values
Tabela 1: Vrednosti T_g

Sample	SMP	R1	R2	R3	R4
DSC (°C)	33.56	38.41	39.53	30.43	21.34
Loss Modulus (°C)	44.16	40.15 ±0.30	41.40 ±0.30		
Tan δ (°C)	52.67	47.04 ±0.30	48.82 ±0.30		

Figure 1 presents the development of the storage modulus (solid lines), the loss modulus (long dashes) and tan δ (short dashes) as a function of temperature.

Figure 2 plots the DSC results of the pure resign and the composite samples during heating. The T_g temperature was taken at the median point in the glass transition temperature range.

The strain storage and the recovery behavior of a shape-memory polymer system must be well understood in order to design a device or a process that may use the polymer properties.[6]

The storage modulus (**Table 2**) is approximately the same at the temperatures lower than T_g and transforming above T_g significant differences can be observed because of the different T_g values of the SMPCs.

The storage modulus has a maximum value for the SMP + SiO_2 0.32 % 600 nm, indicating that the stiffness of this SMPC is the highest among all the tested samples.

Table 2: Storage-modulus values at different temperatures
Tabela 2: Modul shranjevanja pri različnih temperaturah

Sample name	SMP	R1	R2
E'(0 °C)	2875 ± 210	2575 ± 220	3241 ± 100
E'(25 °C)	2484 ± 390	2330 ± 300	2969 ± 50
E'(45 °C)	611,6 ± 90	87.78 ± 10	287.3 ± 30
E'(55 °C)	18 ± 2	6.29 ± 2	11.32 ± 1
E'(65 °C)	4,8 ± 1	2.82 ± 1	4.641± 0.2
E'(75 °C)	2,3 ± 0,4	1.89 ± 1	3.265 ± 0.1

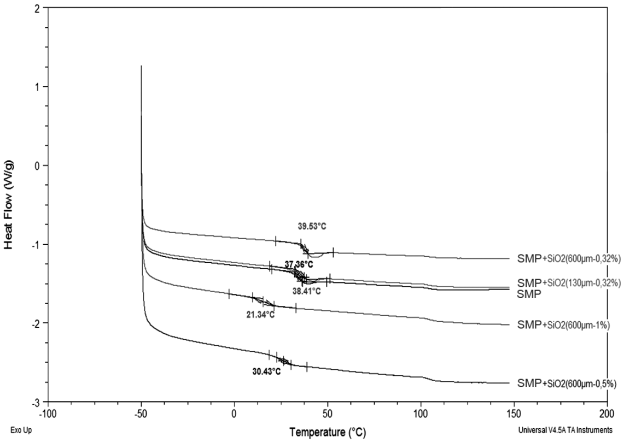

Figure 2: DSC analysis results
Slika 2: Rezultati DSC-analize

3.2 The mechanical behavior

Izod impact strength testing results are shown in **Table 3**. It is demonstrated that the SiO_2 filler contributes to the increase in the impact resistance of a SMP. The values for the pure SMP had also been determined and presented before by the authors. It is also important to note the difference between the results obtained from the top and the bottom of the part samples. As the particles agglomerate at the bottom, during the polymerization process, both 130-nm and 600-nm SiO_2-filled SMPC samples from the bottom show a higher impact resistance than the samples cut from the top part of the plates.

Table 3: Izod impact test results
Tabela 3: Rezultati udarnega preskusa Izod

Sample	Impact energy (J)	Impact energy/ Notch length (J/m)	Impact resistance (kJ/m^2)
SMP	0.09	7.39	2.54
R1 top	0.11	8.95	3.08
R1 botom	0.11	9.07	3.12
R2 top	0.11	9.27	3.36
R2 botom	0.15	12.07	4.37

Table 4: Three-point bending test results
Tabela 4: Rezultati tritočkovnega upogibnega preskusa

Sample	SMP	R1	R2
Modulus Load-Elongation (GPa)	2.44	1.94	2.14
Extension at Maximum Load (mm)	6.86	6.78	6.97
Maximum Load (N)	96.56	98.63	89.95

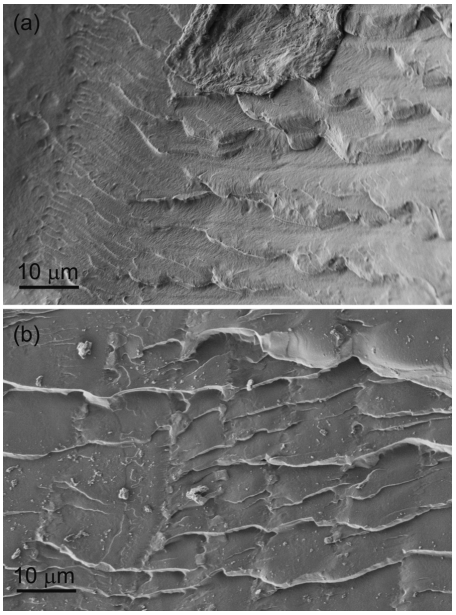

Figure 3: SEM images of the SMP fractured surfaces: a) SMP + 600 nm SiO_2, b) SMP + 130 nm SiO_2
Slika 3: SEM-posnetek površine preloma SMP: a) SMP + 600 nm SiO_2, b) SMP + 130 nm SiO_2

The three-point bending test results (**Table 4**) do not show any important change in the modulus of elasticity of the SiO_2-filled SMPCs.

3.3 SEM imaging

In **Figure 3** we can see the SEM images of the fractured samples, the SMPCs filled with 600-nm and 130-nm SiO_2 particles. Due to a small concentration of the SiO_2 particles, their arrangement in the SMPCs was not observed. There is, however, a clear difference in the formation of the steps on the fractured surfaces as the silica fillers serve as stress concentrators controlling the crack formation upon the fracture. In the 600-nm SiO_2 sample, the steps are higher, more pronounced and less sharp, whereas in the 130-nm SiO_2 sample the steps are sharper and lower.

4 CONCLUSION

This work describes the development of the new intelligent composite materials with better mechanical and thermomechanical properties than the pure SMP resign.

A controlled variation of the T_g, E'' and E' is fundamental in the use of the SMPs in industrial applications. The DMA analysis showed the improvement of the thermomechanical properties of the SMPCs and also the change in the T_g values by adding the SiO_2 nanofiller. This indicates a possibility of designing the SMPCs with different T_g even by adding a small amount such as a 0.32 % volume fraction of the filler.

However, the long polymerization time is an issue concerning the homogeneous dispersion of the particles, which tend to agglomerate at the bottom of the plate.

Although valuable information has been so far obtained during the mechanical testing, many tests are still needed in order to fully understand the material.

Acknowledgment

This paper was supported by the project "Doctoral studies in engineering sciences for developing the knowledge-based society – SIDOC", contract no. POSDRU/88/1.5/S/60078; the project was co-funded by the European Social Fund through the Sectorial Operational Program Human Resources 2007–2013 and the contract IDEI 205, nr.655/2009.

5 REFERENCES

[1] Q. Meng, J. Hu, A review of shape memory polymer composites and blends, Composites: Part A, 40 (**2009**), 1661–1672

[2] T. Pretsch, Review on the Functional Determinants and Durability of Shape Memory Polymers, Polymers, 2 (**2010**), 120–158

[3] W. Stöber, A. Fink, E. Bohn, Controlled growth of monodisperse silica spheres in the micron size range, Journal of Colloid and Interface Science, 26 (**1968**) 1, 62–69

[4] M. Zorko, S. Novak, M. Gaberscek, Fast fabrication of mesoporous SiC with high and highly ordered porosity from ordered silica templates, Journal of Ceramic Processing research, 12 (**2011**) 6, 654–659

[5] M. Y. Razzaq, L. Frormann, Thermomechanical Studies of Aluminum Nitride Filled Shape Memory Polymer Composites, Polym. Compos., 28 (**2007**) 3, 287–293

[6] K. Gall, P. Kreiner, D. Turner, M. Hulse, Shape-memory polymers for microelectromechanical systems, Journal of Microelectromechanical Systems, 13 (**2004**) 3, 472–483

UDK 544.6:669.721.5
Original scientific article/Izvirni znanstveni članek

ISSN 1580-2949
MTAEC9, 46(3)247(2012)

MAGNESIUM ALLOYS FOR HYDROGEN STORAGE

MAGNEZIJ ZA SKLADIŠČENJE VODIKA

Dalibor Vojtěch, Vítězslav Knotek

Department of Metals and Corrosion Engineering, Institute of Chemical Technology, Prague, Technická 5, 166 28 Prague 6, Czech Republic
dalibor.vojtech@vscht.cz

Prejem rokopisa – received: 2011-10-20; sprejem za objavo – accepted for publication: 2012-02-14

Several as-cast, binary Mg-Ni and ternary Mg-Ni-Mm (Mm = mischmetal) alloys were studied with respect to hydrogen storage. The alloys were hydrided using a new, electrochemical process to find the most promising alloy. The electrochemical hydriding process consisted of the electrolysis of a 6-M KOH solution in which the hydrided alloy was the cathode. The structures of both the as-cast and hydrided alloys were investigated by light microscopy, electron microscopy and x-ray diffraction. The hydrogen concentration was measured using glow-discharge spectrometry. It was observed that the structures of all the studied alloys contained a significant volume fraction of disperse eutectic mixtures that represented good paths for the inward hydrogen diffusion. The maximum hydrogen mass concentration of 1.6 % was thus achieved in the Mg-26Ni alloy with an almost purely eutectic structure. In the hypoeutectic and hypereutectic alloys the hydrogen concentrations were lower. The mechanism of the hydriding process is discussed in relation to the observed structural features of the alloys.

Keywords: hydrogen storage, magnesium, electrochemistry

Raziskano je bilo več litih binarnih Mg-Ni in ternarnih Mg-Ni-Mn (Mn = kovina) zlitin s stališča vezave vodika. Zlitine so bile hidrirane z novimi elektrokemijskimi procesi, da bi se našla najbolj primerna. Elektrokemijsko hidriranje se je izvršilo z elektrolizo v raztopini 6-M KOH s hidrirano zlitino kot katodo. Mikrostruktura je bila preiskana z optičnim in elektronskim mikroskopom in rentgensko difrakcijo. Koncentracija vodika je bila merjena s spektrometrijo tlivne razelektritve. Ugotovljeno je bilo, da vse raziskane zlitine vsebujejo pomembnen volumenski delež dispergiranih evtektičnih zmesi, ki so imele dobro pot za difuzijo vodika navznoter. Največja masna koncentracija vodika 1,6 % je bila dosežena pri zlitini Mg-26Ni s skoraj čisto evtektično mikrostrukturo. V hipo- in hiperevtektičnih zlitinah je bila manjša koncentracija vodika. Mehanizem procesa hidriranja je obravnavan v odvisnosti od opaženih značilnosti mikrostruktur.

Ključne besede: skladiščenje vodika, magnezij, elektrokemija

1 INTRODUCTION

Magnesium alloys show a relatively high strength-to-weight ratio, making them of interest in many structural applications in automotive and aerospace industries. In addition, there are some potential non-structural applications of magnesium. Among them, hydrogen storage in magnesium alloys has been extensively studied.

Hydrogen is considered as one of the potential fuels for cars of the future. Great efforts have been exerted to find a simple, inexpensive and safe method for its storage. Today, three basic methods of hydrogen storage are considered[1]: 1. liquid hydrogen in heat-insulated tanks, 2. compressed hydrogen in pressure tanks, and 3. storage in the solid state, i.e., either adsorption in porous materials having a high specific surface or absorption in appropriate metals and alloys to form metallic hydrides. At present, the first method is commonly employed in the prototypes of "hydrogen cars". Hydrogen can be directly mixed with air and supplied to the engine, or it can be introduced into a fuel cell to produce electric power[1]. However, the main drawback of liquid-hydrogen storage is the high energy consumption associated with cooling to about –250 °C and liquefying. It was reported that this energy may represent up to 30 % of the total energy obtainable from the stored gas[1]. Moreover, another disadvantage is the continuous loss of hydrogen through evaporation (about 1 % per day[1]). However, evaporation losses can be significantly reduced by storing liquid hydrogen in insulated pressure vessels (cryo-compressed hydrogen storage)[2]. The second approach does not need much energy but it achieves a relatively low gravimetric density of hydrogen – about 1 %[1]. In addition, there are safety risks arising from high pressure or liquid hydrogen storage.

For all these reasons, the storage of hydrogen in a solid phase has attracted a great deal of attention in the past three decades. In particular, systems based on magnesium hydrides have been extensively studied because magnesium is a light and relatively inexpensive metal and because MgH_2 achieves an excellent hydrogen gravimetric density of 7.6 %. During absorption, a magnesium alloy reacts with the gaseous hydrogen to form hydrides that are stable at room temperature. At elevated temperatures, the hydride is decomposed to evolve gaseous hydrogen, which can then be introduced either directly into a combustion engine or into a fuel cell. Pure MgH_2, however, suffers from a high thermodynamic stability, resulting in slow kinetics of the hydrogenation/dehydrogenation. Therefore, various attempts have been made to reduce its thermodynamic stability, mainly including alloying with transition or rare-earth metals (Ni, Fe, Nd, Ce)[3]. Although a lot of effort has been exerted in past years to develop inexpensive

hydrogen-storage materials based on magnesium, there is no commercially applied system at present.

There are several methods to synthesize Mg-based hydrides, but their common feature is that they involve the reaction of a metallic phase and gaseous hydrogen, usually at elevated temperatures and high pressures. Intensive milling of metallic powders in a hydrogen atmosphere has become a widely employed process[4]. However, from the technological and energy-consumption points of view, the synthesis of hydrides from metallic powder and hydrogen is inefficient, expensive and dangerous. For these reasons, it cannot compete with other hydrogen storage methods and fossil fuels.

In our work we present a new process of hydride production – electrochemical hydriding. Electrochemical hydriding overcomes the major drawbacks of traditional synthesis (summarized above), since it does not need gaseous hydrogen, high pressures and temperatures. Instead, hydrogen evolves from the water, which is a very cheap and easily available compound. In addition, this process occurs at mild temperatures. Atomic hydrogen, produced by the electrolysis of a water solution, directly enters a cathode made of an appropriate alloy, which can then serve as a source of hydrogen.

2 EXPERIMENT

In our work, several Mg-Ni-Mm (Mm=mischmetal containing 45 % Ce, 38 % La, 12 % Nd and 4 % Pr), see **Table 1**, were hydrided by an electrochemical process (hereafter, all concentrations are in mass fraction, *w*/%). Mg-Ni alloys have been studied as prospective hydrogen-storage materials, because nickel is known to significantly support hydrogen absorption and desorption. Other alloys also contain mischmetal, i.e., an alloy containing rare-earth metals, which is also assumed to support hydriding behavior. The alloys were prepared by melting of pure metals in an induction furnace under argon. The ingots of 200 mm in length and 20 mm in diameter were gravity cast into a metal mould. Afterwards, the ingots were cut into 0.5-mm-thick coupons for electrochemical hydriding. Prior to the hydriding the surface of the coupons was mechanically polished.

Table 1: Chemical compositions (in *w*/%) of hydrided magnesium alloys (Mm-mishmetal)
Tabela 1: Kemična sestava hidriranih zlitin magnezija (Mm – kovina) v masnih deležih, *w*/%

alloy	element (*w*/%)		alloy	element (*w*/%)	
	Ni	Mm		Ni	Mm
Mg	–	–	Mg-35Ni	34.8	–
Mg-11Ni	10.9	–	Mg-10Ni-5Mm	10.3	5.4
Mg-26Ni	26.4	–	Mg-24Ni-5Mm	24.0	5.5

Electrochemical hydriding was performed in a 6-mol/l KOH solution at 80 °C and 100 A/m^2 current density. The hydriding time was 8 h. The alloys were immersed in the electrolyte, connected to a DC source and polarized as the cathode, while a graphite rod of 10 mm in diameter and 100 mm in length was used as the anode. The current density was adjusted to prevent the excessive evolution of gaseous hydrogen.

The structure and phase composition of the as-cast and hydrided alloys were observed by using light (LM) and scanning electron microscopy (SEM, Tescan Vega 3), energy-dispersion spectrometry (EDS, Oxford Instruments Inca 350) and x-ray diffraction (XRD, X Pert Pro). To measure the concentrations of hydrogen, glow-discharge spectrometry (GDS, Profiler 2) was employed. The GDS analyzer was calibrated with respect to MgH_2.

3 RESULTS AND DISCUSSION

3.1 Structures

Light micrographs of the investigated alloys are illustrated in **Figure 1**. The Mg-11Ni alloy (**Figure 1a**) has a hypoeutectic composition and its microstructure is thus dominated by the α-Mg dendrites (light) and the α-Mg+Mg_2Ni eutectic (dark). The Mg-26Ni alloy (**Figure 1b**) approaches the eutectic point in the Mg-Ni phase diagram[5]; therefore, its structure is dominated by an α-Mg+Mg_2Ni eutectic mixture. In contrast, the structure of the hypereutectic Mg-35Ni alloy (**Figure 1c**) contains the α-Mg+Mg_2Ni eutectic mixture (dark) and also the primary Mg_2Ni phase (light). The MgNi10Mm5 alloy (**Figure 1d**) consists of the primary α-Mg dendrites (light) and a ternary α-Mg+Mg_2Ni+ $Mg_{12}Mm$ eutectic mixture. The $Mg_{12}Mm$ phase means a solid solution of

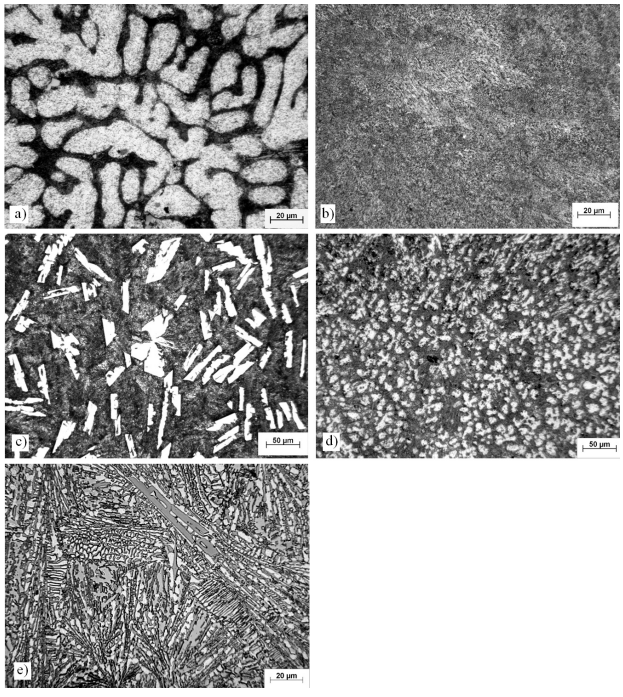

Figure 1: Microstructures of the investigated alloys: a) Mg-11Ni, b) Mg-26Ni, c) Mg-35Ni, d) Mg-10Ni-5Mm, e) Mg-24Ni-5Mm (LM)
Slika 1: Mikrostruktura raziskanih zlitin: a) Mg-11Ni, b) Mg-26Ni, c) Mg-35Ni, d) Mg-10Ni-5Mm, e) Mg-24Ni-5Mm (LM)

isostructural $Mg_{12}La$ and $Mg_{12}Ce$ (space group Immm) phases. The Mg-24Ni-5Mm alloy (**Figure 1e**) is dominated by the α-Mg+ Mg_2Ni+ $Mg_{12}Mm$ eutectic mixture. It is observed that in all the investigated binary and ternary alloys, there are relatively significant volume fractions of eutectic structures. These structures are very fine, despite the relatively slow cooling during gravity casting. Therefore, there is a high area of phase boundaries that represent efficient paths for hydrogen diffusion in materials.

3.2 Hydrogen concentrations

Hydrogen concentrations measured after 8-hour hydriding of the alloys are shown in **Figure 2**. It can be seen that the pure Mg cannot be hydrided by the electrochemical method, because the H concentration is below the GDS detection limit. The best hydriding efficiency is observed for the binary Mg-26Ni alloy, which achieved a hydrogen mass concentration of 1.6 %. This concentration approaches those in common hydrides based on transition metals prepared by the pressure and high-temperature synthesis from elements (usually less than 2 %).

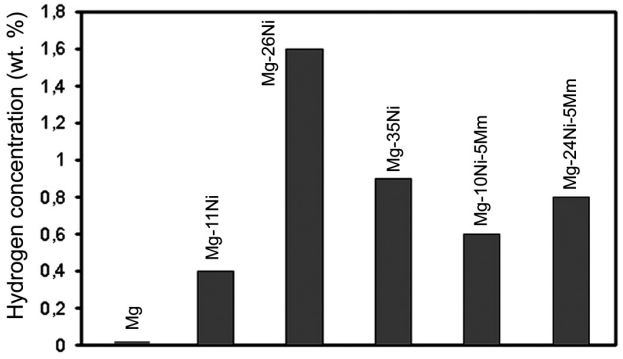

Figure 2: Hydrogen concentrations in the hydrided alloys (GDS)
Slika 2: Koncentracija vodika v hidriranih zlitinah (GDS)

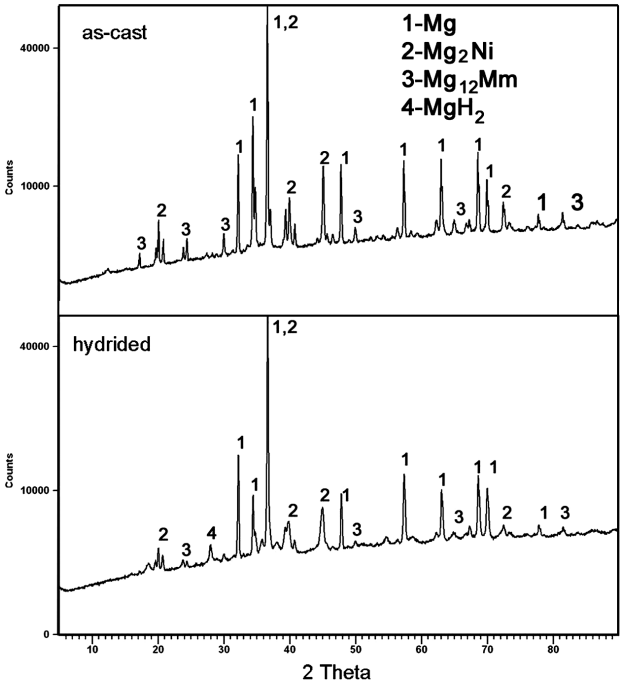

Figure 3: XRD patterns of the as-cast and hydrided Mg-24Ni-5Mm alloy
Slika 3: XRD-spekter lite in hidrirane zlitine Mg-24Ni-5Mm

To reveal the electrochemical hydriding mechanism, an XRD pattern of the alloys was measured both before and after hydriding. The results are similar for all the alloys and are thus illustrated only for the Mg-24Ni-5Mm alloy in **Figure 3**. One can see that the XRD pattern of the as-cast alloy contains peaks of Mg, Mg_2Ni and $Mg_{12}Mm$ phases, which is in accordance with the structure in **Figure 1e**. In contrast, the hydrided alloy contains a new peak, which can be assigned to the MgH_2 phase. Other hydrides like, for example, Mg_2NiH_4, MmH_3, Mg_2MmNiH_7, often observed in Mg-Ni-Mm alloys hydrided in gaseous hydrogen[6,7], are not found after electrochemical hydriding, suggesting that all the hydrogen is chemically bonded only with magnesium. The reason is probably that the electrochemical hydriding temperature was not sufficient for the formation of complex or Mm-based hydrides.

A three-step mechanism of electrochemical hydriding of the Mg-Ni-Mm alloys can be suggested on the basis of the presented chemical and structural investigations:

First step: Electrochemical reaction on the cathode surface produces atomic hydrogen:

$$H_2O + e^- \rightarrow H + OH^- \quad (1)$$

Second step: Atomic hydrogen enters the cathode. When it penetrates into the Mg phase, a layer of MgH_2 forms rapidly, due to the negligible solid solubility of the hydrogen in the magnesium. Such a layer would prevent hydrogen from further diffusion into the cathode material. For this reason the hydrogen concentration in the pure magnesium is negligible (**Figure 2**). In the binary and ternary alloys it is likely that hydrogen diffuses along boundaries between the Mg, Mg_2Ni and $Mg_{12}Mm$ phases and also inside the Mg_2Ni phase, where it forms an interstitial solid solution:

$$Mg_2Ni + X\ H \rightarrow Mg_2NiH_X \quad (2)$$

The X value depends on the hydrogen content and it generally ranges between 0 and 0.3. Both Mg_2Ni and Mg_2NiH_X have a hexagonal crystal lattice (space group $P6_222$). For this reason, these phases are not distinguishable in the XRD patterns in **Figure 3**.

Third step: Atomic hydrogen diffusing inside the alloy reacts with the surrounding Mg phase to form MgH_2:

$$Mg + 2\ H \rightarrow MgH_2 \quad (3)$$

With this mechanism the hydrogen is able to penetrate deeply into the material, which is necessary to achieve high hydrogen concentrations. The mechanism suggested explains why the highest hydrogen concentration is observed in the eutectic Mg-26Ni alloy (**Figure 2**).

This alloy contains a very fine eutectic mixture (**Figure 1b**) with a high volume fraction of phase boundaries, which represent good paths for hydrogen diffusion. The hypo- and hypereutectic Mg-Ni alloys contain primary crystals that slow down the inward penetration of the hydrogen. By comparing the eutectic Mg-26Ni and Mg-24Ni-5Mm alloys, one can see that the former achieved a higher H-concentration (**Figure 2**). One explanation may be in the more disperse eutectic structure of the binary alloy compared to the ternary one (**Figures 1b and 1e**).

4 CONCLUSIONS

The presented work demonstrates a new method of hydrogen storage in a solid phase – electrochemical hydriding. Using this method the electric current is directly transformed to metallic hydrides, like with electric batteries. In contrast to batteries, direct electrochemical hydriding of the alloys with appropriate compositions may produce materials having a much higher density of stored energy. Such materials can serve as portable hydrogen sources, for example, for fuel cells in hydrogen-fuelled cars. Our work implies that appropriate alloys having fine eutectic structures can achieve H-concentrations approaching those in commercial hydrides. As a result they are promising materials for hydrogen storage.

Acknowledgements

The research on hydrogen-storage materials is supported by the Czech Science Foundation (project no. 104/09/0263). The authors also would like to thank the Ministry of Education, Youth and Sports of the Czech Republic for its financial support (project no. MSM6046137302 and MSMT no. 21/2011).

5 REFERENCES

[1] D. K. Ross, Vacuum, 80 (**2006**), 1084
[2] R. K. Ahluwalia, J. L. Peng, Int. J. Hydrogen Energy, 33 (**2008**), 4622
[3] H. Wang, L. Z. Ouyang, M. Zeng, J. Alloy. Compd., 375 (**2004**), 313
[4] L. Li, T. Akiyama, J. I. Yagi, Int. J. Hydrogen Energy, 26 (**2001**), 1035
[5] W. F. Gale, T. C. Totemeier, Smithells Metals Reference Book, 8th ed., Elsevier, Amsterdam 2004, 11–383
[6] Y. Wu, J. Alloy. Compd., 466 (**2007**), 176
[7] L. Z. Ouyang, J. Alloy. Compd., 466 (**2007**), 124

UDK 616-089.843:66.017-022.532:669.295
Original scientific article/Izvirni znanstveni članek

ISSN 1580-2949
MTAEC9, 46(3)251(2012)

ASPECTS OF TITANIUM-IMPLANT SURFACE MODIFICATION AT THE MICRO AND NANO LEVELS

OBLIKE MODIFIKACIJE TITANOVIH IMPLANTATOV NA MIKROMETRSKEM IN NANOMETRSKEM NIVOJU

Iva Milinković[1], Rebeka Rudolf[2], Karlo T. Raić[3], Zoran Aleksić[1], Vojkan Lazić[1], Aleksandar Todorović[1], Dragoslav Stamenković[1]

[1]University of Belgrade, School of Dental Medicine, Dr Subotica 8, Belgrade, Serbia
[2]University of Maribor, Faculty of Mechanical Engineering, Smetanova 17, 2000 Maribor, Slovenia
[3]University of Belgrade, Faculty of Technology and Metallurgy, Karnegijeva 4, Belgrade, Serbia
karlo@tmf.bg.ac.rs

Prejem rokopisa – received: 2011-10-21; sprejem za objavo – accepted for publication: 2011-12-18

The shape and chemical composition, as well as the macro- and microtopography, of an implant surface have been studied widely as the major factors that positively influence implant osseointegration. Titanium and titanium alloys have been used extensively over the past 20 years as biomedical materials in orthopedic and dental surgery because of their good mechanical properties, corrosion resistance, no cell toxicity, and very poor inflammatory response in peri-implant tissue, which confirms their high biocompatibility. Their favorable biological performance is attributed to a thin native oxide film that forms spontaneously on the titanium surface. It is well established that surface roughness plays an important role in implant fixation. Accordingly, some authors have indicated the existence of an optimal range of surface roughness.
The titanium surface can be either chemically or physically modified, or both, in order to improve biomaterial–tissue integration. Different treatments are used to modify the titanium surface. Hydroxyapatite coatings, preceded or not by acid etching, are used to create a rough, potentially bioactive surface. Oxide blasting treatments, either with or without chemical etching, are used to develop rough surfaces. Thick oxide films obtained by anodic or thermal oxidation have been used to accelerate the osseointegration process. The ideal microtopography of the surface is still unknown, however, because it is very difficult to associate surface properties with clinical results.
As more accurate knowledge is required, several Ti surfaces have been analyzed and the endosseous implant surface modified on the micro level has been thoroughly studied. Additionally, the production of gold (Au) nanoparticles to be added to the micron-scale modified surface has been performed. In this respect, an appropriate overview of our results is given.

Keywords: Ti implant, surface modification, microlevel, Au nanoparticles

Oblika, kemična sestava in makro- ter mikrotopografija površine implantata so bile raziskovane kot najpomembnejši dejavnik, ki pozitivno vpliva na kostni prirast. Titan in njegove zlitine se uporabljajo več kot 20 let kot biomedicinski material v ortopedski in zobni kirurgiji zaradi dobrih mehanskih lastnosti, odpornosti proti koroziji, zaradi celične netoksičnosti in majhne vnetne reakcije s periplantatnim tkivom, kar vse potrjuje njihovo biokompatibilnost. Ugodno biološko vedenje se pripisuje tanki naravni oksidni plasti, ki spontano nastane na površini titana. Znano je, da ima hrapavost površine pomebno vlogo pri pritrditvi implantata. Temu ustrezno so nekateri avtorji omenili obstoj nekega optimalnega območja hrapavosti površine.
Oblika površine titana se lahko spremeni kemijsko ali fizikalno ali na oba načina, kar poveča prirast biomateriala. Za spremembo oblike površine se uporablja več načinov. Hidroksiapatitna prekritja s predhodnim jedkanjem ali brez jedkanja s kislino se uporabljajo za tvorbo grobe, potencialno bioaktivne površine. Peskanje z oksidnim prahom s kemijskim jedkanjem ali brez njega se tudi uporablja za ustvarjanje grobe površine. Debele plasti oksida, nastale z anodno ali termično oksidacijo, se uporabljajo za pospešitev procesa kostnega prirastka. Idealna mikrotopografija površine je še vedno neznana, zato ker je težko uskladiti lastnosti površine s kliničnimi rezultati. Ker je potrebno boljše poznavanje, je bilo analiziranih več površin titana in modificirana površina implantata je bila na mikronivoju natačno preiskana. Dodatno so bili uporabljeni nanodelci zlata (Au) za dodatek na mikronivoju spremenjene površine. Ustrezen pregled doseženih rezultatov je predstavljen v tem prispevku.

Ključne besede: Ti-implantat, sprememba oblike površine, mikronivo, nanodelci Au

1 INTRODUCTION

According to the European Association of Biomaterials, materials that are developed to be implanted into human tissues are called biomaterials and need to have a high biocompatibility. Biocompatibility of the material assumes that the material is not associated with any local or systemic damage to the organism, whereas the biological environment, in which the material is implanted, does not cause any changes to the material itself. Biomaterials must not show any toxic, allergogenic, cancerogenic or radioactive activity. Additionally, within the tissue-implant interaction, any kind of material damage, due to corrosion, dissolving or biodegradation, is not allowed.

Dental implants (**Figure 1**) are widely used in modern dental practice as a substitute for lost dentition.

Shape, chemical composition, as well as the macro- and microtopography of the implant surface, have been widely studied as major factors that positively influence implant osseointegration. Ossseointegration is a biological phenomenon associated with a direct structural and functional contact between a vital bone and non-vital implant, without connective tissue insertion.[1] Titanium and titanium alloys have been commonly used over the past 20 years as biomedical materials in orthopedic and

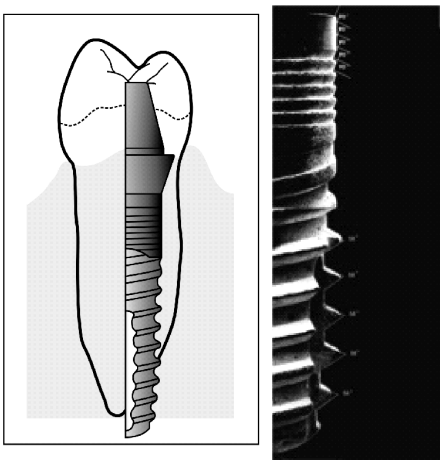

Figure 1: Dental implant
Slika 1: Zobni implantat

dental surgery because of their good mechanical properties, corrosion resistance, cell toxicity absence, as well as very poor inflammatory response in peri-implant tissues, which confirms a high biocompatibility[1].Their favorable biological performance is attributed to a thin native oxide film that is spontaneously formed on the titanium surface. The titanium surface can either be chemically or physically modified, or both, in order to improve the biomaterial–tissue integration.

2 IMPLANT-SURFACE MODIFICATION

The shape of a dental implant has been thoroughly studied, providing scientists and clinicians with implants of adequate macrodesign with different dimensions that enable proper osseointegration. The most widely used implants are screw-shaped endosseous implants, either with parallel walls or with a tapered (root-like) design. The further development of biomaterials in modern implantology is associated with implant micro-design improvement, leading to the creation of different concepts of implant-surface modification.

It is well established that surface roughness plays an important role in implant fixation. Compared to initially used implants with machined polished surfaces, implants with rough surfaces have shown superior results, while enhancing bone apposition and regeneration on the bone-to-implant contact. The distribution of the surface roughness of successfully implanted and clinically biofunctional materials is shown in **Figure 2**. The surface roughness that is manipulated to have a range from 1 μm to 50 μm is associated with an excellent implant survival rate.[2] Accordingly, some authors indicated the existence of an optimal range of surface roughness.[3,4] It is considered that a moderate surface roughness, i.e. 1.5–5μm, has a positive influence in the healing process and implant primary stability.

For implant-surface modification, mechanical, chemical and physical methods are applied, as well as their combination. Mechanical methods, including machining, grinding, polishing, and blasting, involve physical treatment, shaping, or the removal of the material's surface. The objectives of mechanical surface modification are to obtain specific surface topographies and roughness, to remove surface contamination, and/or to improve the adhesion in subsequent bonding steps. Chemical methods involve chemical treatment, electrochemical treatment (anodic oxidation), sol–gel, chemical vapor deposition (CVD), and biochemical modification. During the above-mentioned treatments, electrochemical or biochemical reactions occur at the interface between titanium and a solution. Physical methods, during which chemical reactions do not occur, are thermal spraying and physical vapor deposition. The formation of a surface-modified layer, films or coatings on titanium and its alloys are mainly attributed to thermal, kinetic, and electrical energy.

In practice, different treatments are used to modify the titanium surface. Hydroxyapatite coatings, preceded or not by acid etching, are used to create a rough,

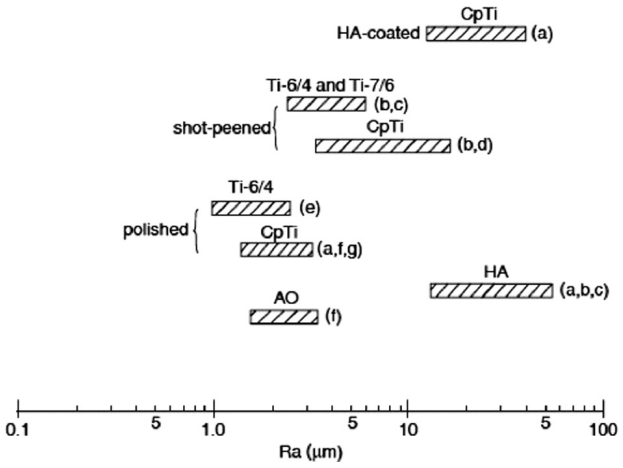

Figure 2: Distribution of implant surface roughness[4]
Slika 2: Pregled hrapavosti površine implantata[4]

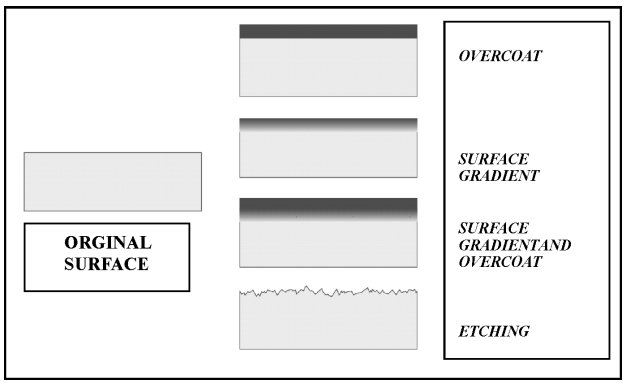

Figure 3: Schematic representations of different plasma methods to modify the surfaces of biomaterials[6]
Slika 3: Shematičen prikaz različnih plazemskih metod za modifikacijo biomaterialov[6]

potentially bioactive surface. Oxide blasting treatments, either with or without chemical etching, are used to develop rough surfaces, and thick oxide films obtained by anodic or thermal oxidation have been used to accelerate the osseointegration process. However, other characteristics, such as oxide thickness, oxide crystallinity and ions present in the external layer, may also influence the bone bonding.

Therefore, the ideal microtopography of the surface is still unknown, because it is very difficult to associate surface properties with clinical results. Although more accurate knowledge is required, different surfaces have been submitted to controlled clinical trials and are commercially available.

3 MICROSTRUCTURED SURFACES

As stated above, implant-surface modification aims to increase the surface roughness and the surface for bone-to-implant contact. Implant surface design affects the amount of osseointegration. A surface topography on the micrometer scale can increase the bone-to-implant contact because of its enhanced biomechanical properties, providing an environment for easier contact osteogenesis, as well as signals for the cell interactions.

It has been shown[5] that an implant surface modified on the micron-level is associated with a faster and increased osseointegration and bone-to-implant contact, when compared to polished Ti surfaces.

In implant surface topography engineering, artificial surface roughening is achieved with a combination of two different processes:

– Coating of the implant surface with an additional layer
– Implant surface erosion with blasting or etching protocols

Plasma-surface modification (PSM) is an efficient and economical surface-treatment technique with the unique advantage that the surface properties and biocompatibility can be enhanced selectively, while the bulk attributes of the materials remain unchanged (**Figure 3**).[6]

Laser-surface modification or laser-surface texturing presents a relatively novel and popular technique of surface modification. Its advantages are associated with precise, targeted and guided surface roughening, controlling the roughening dimension. with a controlled surface, roughening an adequate micron-scale topography can be obtained, in respect to the bone cells' shape, structure and orientation.[7]

4 NANOSTRUCTURED SURFACES

In recent years there has been a growing interest in the possible influence of nanostructured implant surfaces on bone healing and apposition. The nanoscale modification of a Ti implant surface can modify both the topography and the chemistry of the surface itself.

Types of surface modifications (**Figure 4**) on the nanolevel are:[8]

A) Self-assembled monolayers, which can induce chemical and topographical surface modification, resulting in novel physical and/or biochemical surface properties
B) Deposition and chemical modification techniques on the nanoscale ($x \leq 100$ nm), which can realize a distribution on the micron-scale ($y \geq 100$ nm)
C) Compaction techniques applied on the nanoscale ($x \leq 100$ nm), which can realize a distribution on the nanoscale
D) Isotropic surfaces on the nanoscale ($x \leq 100$ nm), obtained by subtractive and additive methods. The distribution can occur either on the nano- or on the micron-scale.

Possible methods developed in surface modification on the atomic (nano) level are:

– Self-assembling of monolayers
– Physical approach (particle compaction, ion-beam deposition)
– Chemical approach (acid etching, peroxidation, NaOH oxidation or anodisation)
– Nanoparticle deposition (sol-gel, crystalline deposition)
– Lithography

Regarding cell behavior in the contact with nano-modified surfaces, different cell reactions, such as protein adsorption, cell adhesion, cell proliferation or cell differentiation and spreading can be expected.

In comparison to conventional micrometer-structured surface modification, three types of nano-stuctured surface modifications have been developed so far:

Surface coating with a nano-structured diamond layer (diamond-like carbon, DLC). Increased mechanical properties in terms of hardness, wear resistance, corrosion resistance and longevity, as well as better biocompatibility have been achieved. The layers are applied to the implant surface by CVD.

Surface coating with nanoparticles of hydroxyapatite (HA) or crystalline calcium phosphate (CaP), which enhances both the contact to the bone and to the metal. When compared to microparticle coatings of the same

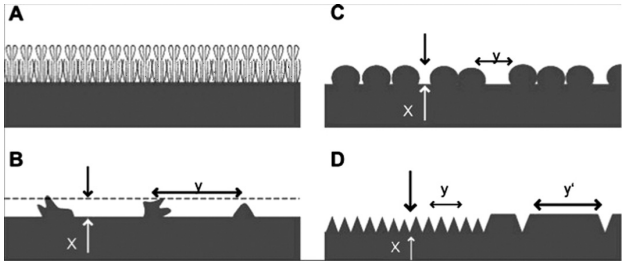

Figure 4: Nanoscale surface modification[8]
Slika 4: Modifikacije površine na nanonivoju[8]

materials, the abrasion and loosening of the particles is decreased, thus diminishing the negative properties of these materials. It has been proved that nanoparticles of HA improve the osteoblast adhesion, proliferation and mineralisation

A surface coating of ceramic fused to metal materials, increases the chemical bonding, which results in a better hardness and wear resistance

Regarding all the above stated, surface modification on the nanolevel can be achieved by using different techniques and materials. One of the possibilities is the use of a dental alloy with a high gold content because of the exceptional biological compatibility of gold and its high electrochemical resistance, functionality and longevity.[9,10] Gold is compatible with gingival tissues and is not susceptible to oxidation and the accumulation of dental plaque.

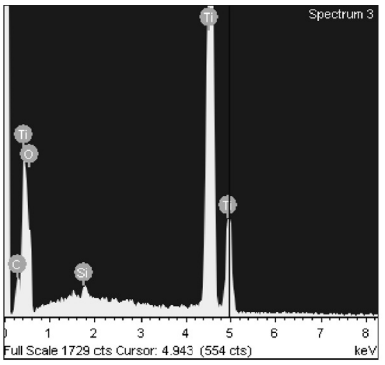

Spectrum	C	O	Na	Al	Si	Ca	Ti	V
Spectrum 3	2.17	18.55			0.44		78.84	
Max.	2.17	18.55	0.00	0.00	0.44	0.00	100.00	2.91

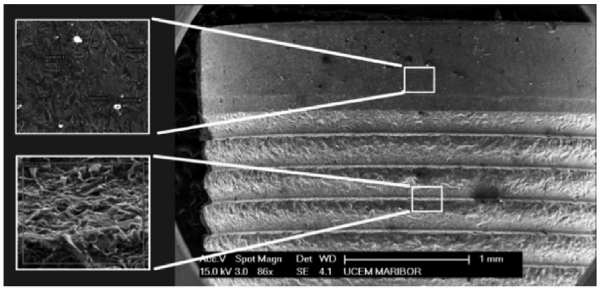

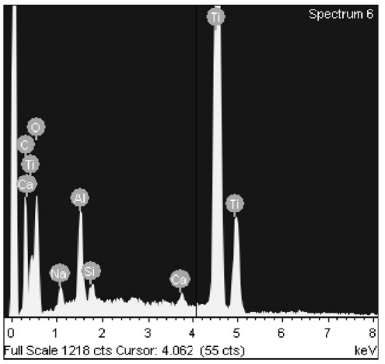

Spectrum	C	O	Na	Al	Si	Ca	Ti	Total
Spectrum 6	8.96	22.10	0.72	2.45	0.45	0.57	64.74	100.00
Max.	8.96	22.10	0.72	2.45	0.45	0.57	64.74	

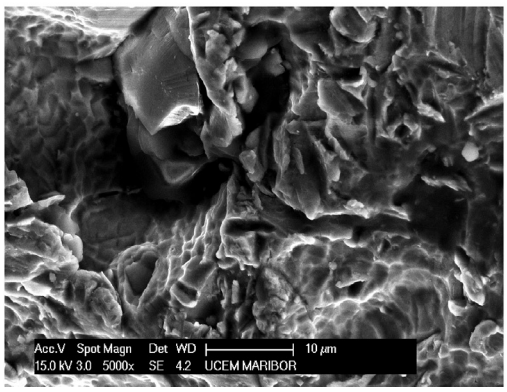

Figure 5: Micron-scale implant surface on SEM

Slika 5: SEM-posnetek površine implantata na mikrometrskem nivoju

5 RESULTS

Several samples of endosseus implants commonly used in modern dental practice were submitted for SEM analysis. The implant macrodesign shows two parts of an implant, a collar and implant body with threads. Both parts were analyzed using SEM microscopy and the analysis of their chemical composition.

The microstructure of the implant surface is shown in **Figure 5**. Since the chemical analysis showed a higher content of Na, Al, C, O and Ca at the implant body, compared to the implant neck, it can be concluded that the surface was modified by blasting techniques with Al_2O_3 and SiC.

a)

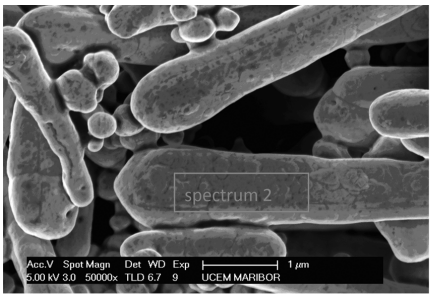

b)

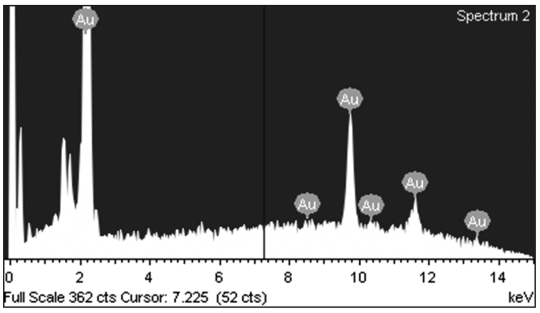

Element	*weight%*	*atom%*
Au M	*100,00*	*100,00*
Total	*100,00*	

Figure 6: Structural analysis: a) SEM micrograph of Au fibers, b) spectrum of EDS analysis marked as "spectrum 2" in **Figure 6a**. (Quantification spectrum for the rectangular area in **Figure 6a**.)

Slika 6: Strukturna analiza: a) SEM-posnetek Au niti, b) spekter EDS-analize, označen kot "spekter 2" na **sliki 6a** (kvantifikacija spektra za pravokotno površino na **sliki 6a**)

At the bottom of **Figure 5** the magnified part of the implant body is presented. It is clearly seen that the surface morphology is ranging within the micrometer scale. At the microlevel up to 10 μm, an interesting surface morphology, presenting diluted spaces, as well as surface shells, represents an adequate platform for the osteoblast cell adhesion and spreading. The main author's idea was whether the addition of nanoparticles onto the presented micrometer-scale surface morphology would result in benefits, such as faster cell attachment, spreading and differentiation. On the nanolevel, we have managed to obtain ideal gold (Au) nanoparticles and nanofibers, as shown in **Figure 6**. Gold (Au) nanoparticles and nanofibers were formed by ultrasonic spray pyrolysis.[11,12]

The nanoparticles could be added to the implant surface by: (i) spray deposition techniques or (ii) plasma deposition techniques. Good nanoconfiguration of the particles could improve the cell activity on the implant surface, whereas nanofibers can serve as an additional matrix for bone cells, thus improving osseointegration and the bone-to-implant contact.

6 DISCUSSION AND CONCLUSIONS

The classical protocol of osseointegration was based on the success of the uncoated cpTi, treaded root-form implant. Long-term clinical data support the use of this material as an ideal dental implant. Ti is osseoinductive and it may create physical-chemical bonds with the bone. However, current data substantiate the use of a variety of implant surface biomodifications, coatings, as well as geometries to attain osseointegration.

Therefore, the next step in the upgrading of the quality of the implant surfaces was the addition of coatings onto the implant in the following ways: a) metal-to-metal; b) ceramic-to-metal; and c) biologically active molecules on metal, on ceramics or diverse functional carriers. Ti has been used to date as a biological substrate for many osteoconductive and osteoinductive, inorganic or organic coatings: ceramics of different kinds, glass, adhesion proteins, extracellular bone matrix proteins, growth factors and cytokines. The primary goal of the coated implants was to combine the benefit of a bioactive surface layer with the properties of the substrate, i.e., the strength of the underlining metal.

As described above, the particle size of the coating layer, or surface topography, plays one of the key roles in terms of material properties and its behavior in contact with living tissues.

Implant surface properties, such as micro-roughness and nano-roughness, are essential components to be discussed in terms of implant osseointegration, as well as bone-to-implant contact. An interesting fact is that different structures of the implant surface are to be found on the micrometer and nanometer scale. It has been noticed that a smooth surface on the microlevel is not necessarily smooth on the nanolevel. Nevertheless, an arranged surface structure shown on the microscale does not have to be arranged when observed within the nanoscale.[10]

Since a stronger and faster bone response is found in the nano-modified implant surfaces, which has to be taken into consideration is the possible coating detachment and its behavior within the tissue, in the period of time. It also has to be studied whether the nanoscale modification can alter the surface reactivity.

The biological properties of gold (Au) and gold alloys have already been confirmed and found an important place in dental prosthodontics.[9] Nevertheless, there is limited data on their use as a substrate layer in implantology. A substrate production in forms of nanoparticles and nanofibers of Au,[11,12] and its addition to an implant surface, is a complex method that could result in an ideal surface topography. The effect of an Au nanolayer could be extraordinarily positive due to its biocompatible properties and, additionally, associated with the positive effects of nanosurfaces.

Acknowledgement

This paper is part of the Eureka project E! 5831 Cell – Ti. The authors gratefully acknowledge the Ministry of Higher Education, Science and Technology of the Republic of Slovenia and the Ministry of Science and Technological Development of the Republic of Serbia.

7 REFERENCES

[1] P. I. Brånemark, Osseointegration and its experimental background, J Prosthet Dent., 50 (**1983**) 3, 399–410

[2] X. Liu, P. K. Chub, C. Dinga, Surface modification of titanium, titanium alloys, and related materials for biomedical applications, Materials Science and Engineering R, 47 (**2004**), 49–121

[3] A. Wennerberg, C. Hallgren, C. Johansson, S. Danelli, A histomorphometric evaluation of screw-shaped implants each prepared with two surface roughnesses, Clin Oral Implants Res., 9 (**1998**) 1, 11–9

[4] P. Gehrke, J. Neugebauer, Implant surface design: Using biotechnology to enhance osseointegration, Dental Implantology Update, 14 (**2003**), 57–64

[5] D. Buser, R. K. Schenk, S. Steinemann, J. P. Fiorellini, C. H. Fox, H. Stich, Influence of surface characteristics on bone integration of titanium implants. A histomorphometric study in miniature pigs, J Biomed Mater Res., 25 (**1991**) 7, 889–902

[6] P. Chu, J. Y. Chen, L. P. Wang, N. Huang, Plasma-surface modification of biomaterials, Materials Science and Engineering R, 36 (**2002**), 143–206

[7] A.Y. Fasasi, S. Mwenifumbo, N. Rahbar, J. Chen, M. Li, A. C. Beye, C. B. Arnold, W. O. Soboyejo, Nano-second UV laser processed micro-grooves on Ti6Al4V for biomedical applications, Materials Science and Engineering C, 29 (**2009**), 5–13

[8] G. Mendonça, D. B. Mendonça, F. J. Aragão, L. F. Cooper, Advancing dental implant surface technology-from micron- to nanotopograph, Biomaterials, 28 (**2008**), 3822–35

[9] K. Raić, R. Rudolf, B. Kosec, I. Anžel, V. Lazić, Nanofoils for soldering and brazing in dental joining practice and jewellery manufacturing, Mater. Tehnol., 43 (**2009**) 1, 3–10

[10] A. Wennerberg, T. Albrektsson, On implant surfaces: a review of current knowledge and opinions, Int J Oral Maxillofac Implants., 25 (**2010**) 1, 6

[11] S. Stopić, B. Friedrich, T. Volkov-Husovic, K. Raić, Mechanism and kinetics of nanosilver formation by ultrasonic spray pyrolysis – Progress report after successful up-scaling (Part 1), Metall, 64 (**2010**) 10, 474–7

[12] S. Stopic, B. Friedrich, T. Volkov-Husovic, K. Raić, Mechanism and kinetics of nanosilver formation by ultrasonic spray pyrolysis – Progress report after successful up-scaling (Part 2), Metall, 65 (**2011**) 4, 147–50

UDK 536.2:519.61/.64
Original scientific article/Izvirni znanstveni članek

ISSN 1580-2949
MTAEC9, 46(3)257(2012)

NUMERICAL STUDY OF HEAT-TRANSFER ENHANCEMENT OF HOMOGENEOUS WATER-Au NANOFLUID UNDER NATURAL CONVECTION

NUMERIČNA ANALIZA POVEČANJA PRENOSA TOPLOTE HOMOGENE NANOTEKOČINE VODA-Au POD POGOJI NARAVNE KONVEKCIJE

Primož Ternik[1], Rebeka Rudolf[2,3], Zoran Žunič[4]

[1]Private Researcher, Bresterniška ulica 163, 2354 Bresternica, Slovenia
[2]University of Maribor, Faculty of Mechanical Engineering, Smetanova 17, 2000 Maribor, Slovenia
[3]Zlatarna Celje, d. d., Kersnikova ul. 19, 3000 Celje, Slovenia
[4]AVL-AST, Trg Leona Štuklja 5, 2000 Maribor, Slovenia
pternik.researcher@gmail.com

Prejem rokopisa – received: 2011-10-21; sprejem za objavo – accepted for publication: 2012-02-01

A numerical analysis is performed to examine the heat transfer of colloidal dispersions of Au nanoparticles in water (Au nanofluids). The analysis used a two-dimensional enclosure under natural convection heat-transfer conditions and has been carried out for the Rayleigh number in the range of $10^3 \leq Ra \leq 10^5$, and for the Au nanoparticles' volume-fraction range of $0 \leq \varphi \leq 0.10$.
We report highly accurate numerical results indicating clearly that the mean Nusselt number is an increasing function of both Rayleigh number and volume fraction of Au nanoparticles. The results also indicate that a heat-transfer enhancement is possible using nanofluids in comparison to conventional fluids. However, low Rayleigh numbers show more enhancement compared to high Rayleigh numbers.

Keywords: natural convection, water-Au nanofluid, heat transfer, numerical modelling

V prispevku smo numerično analizirali prenos toplote v koloidnih disperzijah nanodelcev zlata v vodi (Au-nanotekočine). Pri tem smo obravnavali dvodimenzionalno kotanjo pod pogoji naravne konvekcije za vrednosti Rayleighevega števila $10^3 \leq Ra \leq 10^5$ in volumenske koncentracije Au-nanodelcev $0 \leq \varphi \leq 0{,}10$.
Rezultati analize kažejo, da je srednje Nusseltovo število naraščajoča funkcija obeh, tako Rayleighevega števila kot volumenskega deleža Au-nanodelcev. Prikazani rezultati nakazujejo, da lahko prenos toplote izboljšamo z uporabo Au-nanotekočin namesto navadnih tekočin. Pri tem pa je pozitivni učinek na prenos toplote izrazitejši pri nižjih vrednostih Rayleighevega števila.

Ključne besede: naravna konvekcija, nanotekočina voda-Au, prenos toplote, numerično modeliranje

1 INTRODUCTION

Today more than ever, ultra-high-performance heat transfer plays an important role in the development of energy-efficient heat-transfer fluids required in many industries and commercial applications. However, conventional heat-transfer fluids (e.g. water, oil or ethylene glycol) are inherently poor heat transfer fluids. Nanofluid, a term coined by Choi[1] in 1995, is a new class of heat-transfer fluids developed by suspending nanoparticles, such as small amounts of metal, non-metal or nanotubes in the fluids. The goal of nanofluids is to achieve the highest possible thermal properties at the smallest possible volume concentrations with a uniform dispersion and a stable suspension of nanoparticles in host fluids.

Buoyancy-induced flow and heat transfer is an important phenomenon used in various engineering systems. Some applications are solar thermal receivers, vapour absorption refrigerator units[2] and electronic cooling, selective laser melting processes[3], etc. Several researchers have been focused on numerical modelling of such flows. Oztop and Abu-Nada[4] studied the two-dimensional natural convection of various nanofluids in partially heated rectangular cavities and reported that the type of nanofluid is the key factor for a heat-transfer enhancement. They obtained the best results with Cu nanoparticles. Hwang et al.[5] studied natural convection of a water-based Al_2O_3 nanofluid in a rectangular cavity heated from below. They investigated the convective instability of the flow and heat transfer and reported that the natural convection of the nanofluid becomes more stable when the volume fraction of nanoparticles increases. Ho et al.[6] studied the effects on the nanofluid heat transfer caused by viscosity and thermal conductivity in a buoyant enclosure. They demonstrated that the usage of different models for viscosity and thermal conductivity has a major impact on the heat transfer and flow characteristics.

The effect of the inclination angle on the heat-transfer enhancement under natural convection has been studied by Oztop et al.[7] (for water-based Al_2O_3 and TiO_2 nanofluids) and by Abu-Nada and Oztop[8] (for water-based Cu nanofluids). They reported that the effect of the

inclination angle on the percentage of a heat-transfer enhancement becomes insignificant at a low Rayleigh number, but it decreases the enhancement of heat transfer with a nanofluid. Last but not least, the inclination angle is reported to be a good control parameter for both pure and nanofluid-filled enclosures.

Although quite some work has been done in this area, it is still safe to conclude that there is a lack of numerical studies of the heat characteristics of the nanofluids containing Au nanoparticles. The present work is therefore directed to study the natural convection heat-transfer characteristics of the water-based Au nanofluids for the Rayleigh number in the range of $10^3 \leq Ra \leq 10^5$ and for the volume fraction of $0 \leq \varphi \leq 0.10$.

2 NUMERICAL MODELLING

The standard finite volume method is used to solve the coupled conservation equations of mass, momentum and energy. This method has been used successfully in a number of recent studies to simulate generalized Newtonian fluid flows[9,10]. In this framework a second-order central differencing scheme is used for the diffusive terms and a third-order QUICK scheme for the convective terms. The coupling of the pressure and velocity is achieved using the well-known SIMPLE algorithm. The convergence criteria were set to 10^{-8} for all residuals.

2.1 Governing equations

For the present study, a steady-state flow of an incompressible water-based Au nanofluid is considered. It is assumed that both the fluid phase and the nanoparticles are in thermal equilibrium. Except for the density, the properties of the nanoparticles and the fluid are taken to be constant. **Table 1** presents the thermophysical properties of water and gold at the reference temperature. It is further assumed that the Boussinesq approximation is valid for the buoyancy force.

The governing equations (mass, momentum and energy conservation) for a steady, two-dimensional laminar and incompressible flow are:

$$\frac{\partial v_i}{\partial x_i} = 0 \tag{1}$$

$$\rho_{\mathrm{nf}} v_j \frac{\partial v_i}{\partial x_j} - \frac{\partial}{\partial x_j}\left(\eta_{\mathrm{nf}} \frac{\partial v_i}{\partial x_j}\right) = = -\frac{\partial p}{\partial x_i} + (\rho\beta)_{\mathrm{nf}}\, g(T - T_{\mathrm{C}}) + \frac{\partial}{\partial x_j}\left(\eta_{\mathrm{nf}} \frac{\partial v_j}{\partial x_i}\right) \tag{2}$$

$$(\rho c_{\mathrm{p}})_{\mathrm{nf}} v_j \frac{\partial T}{\partial x_j} = \frac{\partial}{\partial x_j}\left(c_{\mathrm{nf}} \frac{\partial T}{\partial x_j}\right) \tag{3}$$

where the cold wall temperature T_C is taken to be the reference temperature for evaluating the buoyancy term $(\rho\beta)_{\mathrm{nf}} g(T - T_C)$ in the momentum conservation equation.

The relationships between the properties of the nanofluid (*nf*) and those of the pure fluid (*f*) and the pure solid (*s*) are given with the following empirical models[7]:

- Density:

$$\rho_{\mathrm{nf}} = (1-\varphi)\rho_{\mathrm{f}} + \varphi\rho_{\mathrm{s}}$$

- Dynamic viscosity:

$$\eta_{\mathrm{nf}} = \frac{\eta_{\mathrm{f}}}{(1-\varphi)^{2.5}}$$

- Thermal expansion:

$$(\rho\beta)_{\mathrm{nf}} = (1-\varphi)(\rho\beta)_{\mathrm{f}} + \varphi(\rho\beta)_{\mathrm{s}}$$

- Heat capacitance:

$$(\rho c_{\mathrm{p}})_{\mathrm{nf}} = (1-\varphi)(\rho c_{\mathrm{p}})_{\mathrm{f}} + \varphi(\rho c_{\mathrm{p}})_{\mathrm{s}}$$

- Thermal conductivity:

$$k_{\mathrm{nf}} = k_{\mathrm{f}} \frac{k_{\mathrm{s}} + 2k_{\mathrm{f}} - 2\varphi(k_{\mathrm{f}} - k_{\mathrm{s}})}{k_{\mathrm{s}} + 2k_{\mathrm{f}} + \varphi(k_{\mathrm{f}} - k_{\mathrm{s}})}$$

Table 1: Thermo-physical properties of the Au nanofluid
Tabela 1: Termo-fizikalne lastnosti Au-nanotekočine

	ρ (kg/m^3)	c_{p} (J/kg K)	k (W/m K)	β (1/K)
Pure water	997.1	4179	0.613	2.1×10^{-4}
Au	19320	128.8	314.4	1.416×10^{-7}

2.2 Geometry and boundary conditions

The simulation domain and the expected temperature distribution are shown schematically in **Figure 1**. The two vertical walls of the square enclosure are kept at different constant temperatures ($T_H - T_C$), whereas the other boundaries are considered to be adiabatic in nature. Both velocity components (i.e., v_x and v_y) are identically zero on each boundary because of the no-slip condition and impenetrability of the rigid boundaries. The temperatures for cold and hot vertical walls are specified (i.e. $T(x = 0) = T_H$ and $T(x = L) = T_C$). The adiabatic temperature boundary conditions for the horizontal insulated boundaries are given by $\partial T/\partial y = 0$ at $y = 0$ and $y = L$.

In the present study, the heat-transfer rates (along the hot vertical wall) in a square enclosure (of the dimension

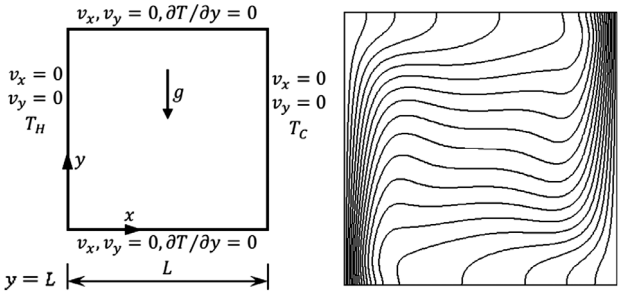

Figure 1: Schematic diagrams of the simulation domain (left) and the expected temperature field (right)
Slika 1: Shematični prikaz območja simulacije (levo) in pričakovano temperaturno polje (desno)

L), with differentially heated side walls, filled with Au nanofluid are expressed in terms of the local and mean Nusselt number as follows:

$$Nu(y) = \frac{k_{\mathrm{nf}}}{k_{\mathrm{f}}} \frac{\partial T(y)}{\partial x}\Big|_{x=0} \frac{L}{T_{x=0} - T_{\mathrm{C}}} \tag{4}$$

$$\overline{Nu} = \int_0^L \frac{Nu(y)\mathrm{d}y}{L} \tag{5}$$

and compared with the heat-transfer rate obtained in the case of pure water ($\varphi = 0$) with the same nominal Rayleigh number. Here the Rayleigh number *Ra* represents the ratio of the strengths of the thermal transports due to buoyancy to the thermal diffusion and is defined in the following manner:

$$Ra = \frac{\rho_{\mathrm{nf}} (\rho c_{\mathrm{p}})_{\mathrm{nf}}\, g\beta_{\mathrm{nf}} (T_{\mathrm{H}} - T_{\mathrm{C}}) L^3}{\eta_{\mathrm{nf}}\, k_{\mathrm{nf}}} \tag{6}$$

2.3 Grid-dependency study

The grid independence of the results has been established on the basis of a detailed analysis of three different uniform meshes: *M*1(50 × 50), *M*2(100 × 100) and *M*3(200 × 200). For the general primitive variable ϕ the grid-converged (i.e. extrapolated to the zero element size) value, according to Richardson extrapolation, is given as[9,10]:

$$\phi_{\mathrm{ext}} = \phi_{M3} - \frac{(\phi_{M2} - \phi_{M3})}{(r^{\mathrm{p}} - 1)}$$

where ϕ_{M3} is obtained on the basis of the finest grid, ϕ_{M2} is the solution based on the next level of coarse grid, $r = 2$ is the ratio between the coarse and fine grid spacing and $p = 2.88$ is the actual order of accuracy.

Table 2: Effect of mesh refinement upon the mean Nusselt number ($\varphi = 0$, $Ra = 10^5$)
Tabela 2: Vpliv zgoščevanja mreže na srednjo vrednost Nusseltovega števila ($\varphi = 0$, $Ra = 10^5$)

Mesh *M*1	Mesh *M*2	Mesh *M*3	$\overline{Nu}_{\mathrm{ext}}$	*e*
4.704	4.721	4.723	4.724	0.008 %

The numerical error $e = \left|(\phi_{M3} - \phi_{\mathrm{ext}})/\phi_{\mathrm{ext}}\right|$ for the mean Nusselt number $\overline{Nu}$ is presented in **Table 2**. It can be seen that the differences with grid refinement are exceedingly small and the agreement between mesh *M*3 and extrapolated value is extremely good; the discretisation error for $\overline{Nu}$ is well below 0.01 %. Based on this the simulations in the remainder of the paper were conducted on mesh *M*3 which provided a reasonable compromise between high accuracy and computational efficiency.

2.4 Benchmark comparison

In addition to the aforementioned grid-dependency study, the simulation results have also been compared with the well-known benchmark data of de Vahl Davis[11] relating to natural convection of air ($Pr = 0.71$) in a square cavity for the values of the Rayleigh number $10^3 \leq Ra \leq 10^5$. The comparisons between the present simulation results with the corresponding benchmark values are extremely good and entirely consistent with our grid-dependency studies. The comparison is summarised in **Table 3**.

Table 3: Comparison of the present results with the benchmark results
Tabela 3: Primerjava dobljenih rezultatov z referenčnimi

	$Ra = 10^3$		$Ra = 10^4$		$Ra = 10^5$	
	$Nu_{\max}$	$\overline{Nu}$	$Nu_{\max}$	$\overline{Nu}$	$Nu_{\max}$	$\overline{Nu}$
Present study	1.506	1.118	3.531	2.245	7.722	4.521
de Vahl Davis	1.505	1.118	3.528	2.243	7.717	4.519

3 RESULTS AND DISCUSSION

Figure 2 presents a variation of the local Nusselt number (Equation 4) along the hot wall for different values of *Ra*. In the conduction dominated heat-transfer mechanism, **Figure 2a**, the variation of the local *Nu* is similar for all solid volume fractions. Up to $y/L \approx 0.10$ it is characterized with a constant value and with a further increase in the *y*/*L* local Nusselt number decreases. In addition, it can be observed that the values of *Nu* along the whole hot wall are greater in the case of a higher volume fraction of the Au nanoparticles.

As the *Ra* increases, **Figure 2b**, the maximum of the local Nusselt number ($Nu_{\max}$) is shifted away from the

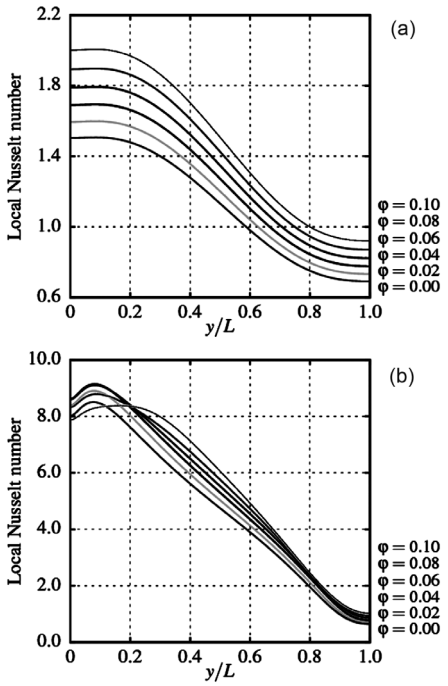

Figure 2: Variation of the local Nusselt number along the hot wall for: a) $Ra = 10^3$ and b) $Ra = 10^5$
Slika 2: Spreminjanje lokalnega Nusseltovega števila vzdolž tople stene za: a) $Ra = 10^3$ in b) $Ra = 10^5$

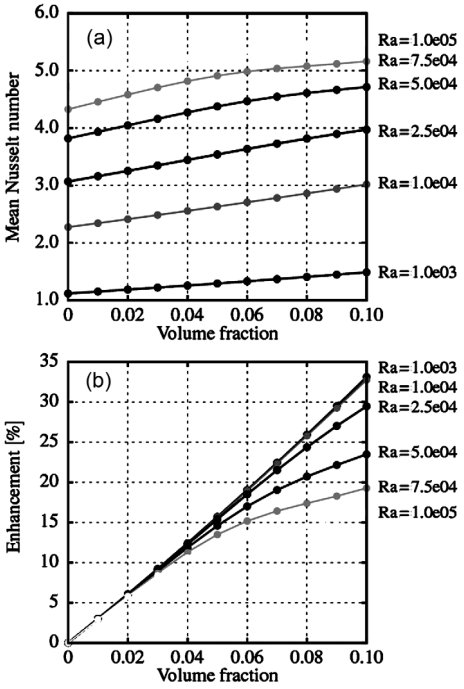

Figure 3: a) Variation of the mean Nusselt number along the hot wall and b) the heat-transfer enhancement due to an addition of Au nanoparticles

Slika 3: a) Spreminjanje srednjega Nusseltovega števila vzdolž tople stene in b) povečanje prenosa toplote zaradi dodanih Au-nanodelcev

bottom adiabatic wall and is an increasing function of the solid volume fraction up to $\varphi = 0.04$. With the higher values of the solid volume fraction, Nu_{max} starts to decrease and its location is shifted further away from the bottom adiabatic wall.

Regardless of the *Ra* value, the decrease in *Nu* is more pronounced in the $0.2 < y/L < 0.8$ region and it attains the minimum value at the upper wall ($y/L = 1.0$).

The variation of the mean Nusselt number (Equation 5) along the hot wall with a solid volume fraction is shown in **Figure 3a** indicating that $\overline{Nu}$ increases with an increasing φ. For $Ra \leq 10^4$, where the heat transfer is conduction dominated, the distribution of $\overline{Nu}$ is completely linear. The distribution of the mean Nusselt number becomes increasingly non-linear with the strengthening of the convective transport in the cases of higher values of *Ra* for all volume fractions of Au nanoparticles.

The previous discussions indicate that, generally, heat transfer is enhanced with an addition of nanoparticles. To estimate the enhancement of the heat transfer in the case of Au nanofluid and in the case of pure fluid ($\varphi = 0$), the enhancement is defined[6]:

$$E = \frac{\overline{Nu}(\varphi) - \overline{Nu}(\varphi = 0)}{\overline{Nu}(\varphi = 0)} \times 100\% \qquad (6)$$

The enhancement of heat transfer is plotted with respect to the Au nanoparticles volume fraction at different Rayleigh numbers as shown in **Figure 3b**. Considering the whole range of Rayleigh numbers, the figure illustrates that heat transfer increases in the case of an increasing solid volume fraction φ. It is interesting to observe that the heat-transfer enhancement is an increasing linear function of the volume fraction in the cases of the lower values of the Rayleigh number ($Ra \leq 10^4$), while the higher values of the Rayleigh number ($Ra > 10^4$) are characterized with a non-linear increase in the heat-transfer enhancement.

Finally, the enhancement of the heat transfer for $\varphi \leq 0.03$ is similar for all the values of *Ra* and as the volume fraction further increases, the heat transfer is greater with the low Rayleigh numbers than with the high Rayleigh numbers. This is related to the difference between the conduction dominated mechanism for the heat transfer at a low *Ra* and the convection mechanism at a high *Ra*.

4 CONCLUSIONS

In the present study, the heat-transfer characteristics of the steady laminar natural-convection water-based Au nanofluids in a square enclosure with differentially heated side walls have been numerically studied. The effects of the Rayleigh number ($10^3 \leq Ra \leq 10^5$) and the solid-volume fraction ($0 \leq \varphi \leq 0{,}10$) have been systematically investigated.

The influence of computational grid refinement on the present numerical predictions was studied throughout the examination of the grid convergence for the natural convection at $Ra = 10^5$. By utilizing extremely fine meshes, the resulting discretisation error for $\overline{Nu}$ is well below 0.01 %.

The numerical method was validated for the case of the convection of air ($Pr = 0.71$) in a square cavity, and its results are available in the open literature. A remarkable agreement of our results with the benchmark results of de Vahl Davis[11] yields sufficient confidence in the present numerical procedure and its results.

The highly accurate numerical results confirmed some important points, such as:

- Both the increasing value of the Rayleigh number and the solid-volume fraction of the nanoparticles augment the heat-transfer rate (the mean Nusselt number).
- The mean Nusselt number $\overline{Nu}$ is an increasing function of both, the Rayleigh number *Ra* and the volume fraction φ of the Au nanoparticles.
- The effect of the highly conductive nanoparticles on the heat-transfer enhancement is more significant at the low values of the Rayleigh number (the conduction-dominated heat transfer).

Acknowledgements

The research leading to these results was carried out within the framework of a research project "Production

technology of Au nano-particles" (L2-4212) that was funded by the Slovenian Research Agency (ARRS).

5 REFERENCES

[1] S. U. S. Choi, Enhancing thermal conductivity of fluids with nanoparticles, Developments Applications of Non-Newtonian Flows, 66 (**1995**), 99–105

[2] D. Micallef, C. Micallef, Mathematical model of a vapour absorption refrigeration unit, International Journal of Simulation Modelling, 9 (**2010**), 86–97

[3] N. Contuzzi, S. L. Campanelli, A. D. Ludovico, 3D finite element analysis in the selective laser melting process, International Journal of Simulation Modelling, 10 (**2011**), 113–121

[4] H. F. Oztop, E. Abu-Nada, Numerical study of natural convection in partially heated rectangular enclosures filled with nanofluids, International Journal of Heat and Fluid Flow, 29 (**2008**), 1326–1336

[5] K. S. Hwang, J. H. Lee, S. P. Jang, Buoyancy-driven heat transfer of water-based Al_2O_3 nanofluids in a rectangular cavity, International Journal of Heat and Mass Transfer, 50 (**2007**), 4003–4010

[6] C. J. Ho, M. W. Chen, Z. W. Li, Numerical simulation of natural convection of nanofluid in a square enclosure: effects due to uncertainties of viscosity and thermal conductivity, International Journal of Heat and Mass Transfer, 51 (**2008**), 4506–4516

[7] H. F. Oztop, E. Abu-Nada, Y. Varol, K. Al-Salem, Computational analysis of non-isothermal temperature distribution on natural convection in nanofluid filled enclosures, Superlattices and Microstructures, 49 (**2011**), 453–467

[8] E. Abu-Nada, H. F. Oztop, Effects of inclination angle on natural convection in enclosures filled with Cu–water nanofluid, International Journal of Heat and Fluid Flow, 30 (**2009**), 669–678

[9] I. Biluš, P. Ternik, Z. Žunič, Further contributions on the flow past a stationary and confined cylinder: Creeping and slowly moving flow of Power law fluids, Journal of Fluids and Structures, 27 (**2011**), 1278–1295

[10] P. Ternik, New contributions on laminar flow of inelastic non-Newtonian fluid in the two-dimensional symmetric expansion: Creeping and slowly moving conditions, Journal of Non-Newtonian Fluid Mechanics, 165 (**2010**), 1400–1411

[11] G. de Vahl Davis, Natural convection of air in a square cavity: a bench mark numerical solution, International Journal for Numerical Methods in Fluids, 3 (**1983**), 249–264

UDK 669.245:620.17
Original scientific article/Izvirni znanstveni članek

ISSN 1580-2949
MTAEC9, 46(3)263(2012)

OPTIMIZATION OF THE MECHANICAL PROPERTIES OF THE SUPERALLOY NIMONIC 80A

OPTIMIRANJE MEHANSKIH LASTNOSTI SUPERZLITINE NIMONIC 80A

Raza Sunulahpašić[1], Mirsada Oruč[2], Mustafa Hadžalić[2], Milenko Rimac[2]

[1]University of Zenica, Faculty of Metallurgy and Materials Science, 72000 Zenica, Bosna and Herzegovina
[2]University of Zenica, Institute "Kemal Kapetanović", 72000 Zenica, Bosna and Herzegovina
raza.sunulahpasic@famm.unze.ba

Prejem rokopisa – received: 2011-10-23; sprejem za objavo – accepted for publication: 2012-01-06

The superalloy Nimonic 80A has found its major application in the production of the parts for the vehicle and airplane industries. It is a relatively expensive material and it is very important to reduce its production costs to acceptable levels. The aim of this research was to produce the superalloys with varying supplements of alloying elements.
The investigations carried out included chemical testing and the testing of the mechanical properties of the superalloy Nimonic 80A, followed by a regression analysis of the obtained data to show the influence of certain alloying elements that can significantly affect the improvement of the mechanical properties of Nimonic 80A.
The results of the regression analysis are the equations with which, on the basis of the known chemical composition, i.e., the content of the main alloying elements – Al, Ti and Co – the mechanical properties of the materials at increased temperatures can be predicted. On the basis of the obtained squared regression equations, an optimization of the chemical composition for the selected values of the mechanical properties was carried out.

Keywords: Nimonic 80A, mechanical properties, regression analysis, optimization

Glavni področji za uporabo in izdelavo delov iz superzlitine Nimonic 80A sta avtomobilska in letalska industrija. Zlitina je relativno drag material, zato je zelo pomembno, da se zmanjšajo stroški njene proizvodnje na sprejemljiv nivo. Namen te raziskave je bila izdelava superzlitine z različnim dodatkom legirnih elementov.
Opravljene preiskave so vključevale kemijsko analizo in preskušanje mehanskih lastnosti superzlitine Nimonic 80A, sledila pa je regresijska analiza dobljenih podatkov, da bi pokazali vpliv legirnih elementov na izboljšanje mehanskih lastnosti Nimonic 80A.
Rezultati regresijske analize so enačbe, ki omogočajo napovedovanje mehanskih lastnosti zlitine pri povišanih temperaturah na podlagi kemijske analize, to je vsebnosti legirnih elementov Al, Ti in Co. Na podlagi dobljenih regresijskih enačb je bilo izvršeno optimiranje kemijske sestave za izbrane vrednosti mehanskih lastnosti.

Ključne besede: Nimonic 80A, mehanske lastnosti, regresijska analiza, optimizacija

1 INTRODUCTION

The superalloy Nimonic 80A is a wrought nickel-based alloy (min. 65 % Ni) containing chromium (20 %), with minor additions of carbon, cobalt and iron, as well as major alloying elements of aluminum (1 % to 1.8 %), titanium (1.8 % to 2.7 %) (according to DIN 17742 its alloy mark is NiCr20TiAl, W.Nr. 2.4952, 2.4631).

This alloy has good mechanical properties and good corrosion resistance at both ambient and elevated temperature. It is designed for the operation at temperatures of up to 815 °C)[1,2], for the parts exposed to high stresses in the temperature range from 600–750 °C[3].

The Ni-based superalloy Nimonic 80A is a multi component alloy that gains its appropriate microstructure and precipitation strength at higher temperatures through the precipitation hardening. The precipitation hardening is obtained by forming γ' phases Ni_3 (Al, Ti). A further strengthening and increase of resistance at elevated temperatures is gained by adding Co[4,5]. The alloying elements that largely affected the mechanical properties of the superalloy Nimonic 80A were Al, Ti and Co.

The surveys carried out included chemical testing and tensile testing of the superalloys Nimonic 80A at a temperature of 750 °C, on the basis of which a regression analysis of the impact of the chemical composition on the mechanical properties was conducted.

This paper presents the results of the tensile tests at a temperature of 750 °C of the superalloys Nimonic 80A, as well as the functional dependence of the influences of the major alloying elements on the mechanical properties.

It also presents an analysis of the influence of the mass fractions (w/%) of Al, Ti and Co on the tensile properties at elevated temperatures (750 °C). The objective function sets the parameters for finding the content of the elements Al, Ti and Co, as well as their interactions, which will give the optimum (selected) mechanical properties of the superalloys Nimonic 80A used at an operating temperature.

2 DESIGN OF EXPERIMENT

For the specific analysis of the influence of the alloying elements on the tensile properties, the multi-

factorial experiment was proposed. The MATLAB software (version 7.0) and its module Model-Based Calibration Toolbox was used for designing the experiments[6]. The essence of this method is in the planning, the implementation and the analysis of the appropriate number of experimental measurements of the tensile properties of the alloy Nimonic 80A through simultaneous variation of the main factors (x_1 = w(Al); x_2 = w(Ti); x_3 = w(Co). The influential factors were the contents of Al (x_1), Ti (x_2) and Co (x_3). The second-order mathematical model, i.e., the square regression model was assumed. The equation of the second-order regression model can be successfully used as a base for exploring the field of optimum. This approach enables an analysis of not only the individual effects of the factors, but also of their mutual, i.e., coupled effects, as well as determining the optimum values of the factors[5].

According to the 2nd plan of the experiments, the number of melts was determined. The factors were varied at two levels, with repeated experiments for each point of the plan. Tests were conducted using 16 different melts[7].

The making of the melts and the tensile testing were performed at the University of Zenica, "Kemal Kapetanović" Institute. The results of the chemical analysis are shown in **Table 1**. The results of the chemical analysis of the used melts are in accordance with the standard chemical composition for the Nimonic 80A superalloy (DIN 17742, alloy designation NiCr20TiAl). After being forged and rolled into φ = 15 mm bars, the tested materials were heat treated using the standard parameters for this type of superalloys. The standard heat treatment consists of a solution annealing at 1080 °C/8 h and cooling in the air to the room temperature, followed by the precipitation annealing at 720 °C/16 h and cooling in the air[4]. The testing of the tensile properties was carried out in the Laboratories for Mechanical Testing of the "Kemal Kapetanović" Institute, Zenica (**Table 1**). The specimens for testing and tensile testing were prepared in line with Standard BAS EN 10002-5 (for the testing at an elevated temperature)[8].

3 ANALYSIS OF EXPERIMENTAL RESULTS

On the basis of the testing and the statistical-data analysis, the optimum regression equation, as a system response, was chosen for $R_{p0,2}$ (equation 1) and R_m (equation 2) at a temperature of 750 °C:

$$R_{p0,2} = -112.58x_1 + 662.85x_2 - 509.02x_3 + 70.86x_1x_2 - 15.72x_1x_3 - 49.76x_2x_3 + 20.58x_1^2 - 124.83x_2^2 + 245.11x_3^2 \quad (1)$$

$$R_m = -127.11x_1 + 1039.83x_2 - 798.58x_3 + 122.98x_1x_2 + 15.77x_1x_3 - 14.94x_2x_3 - 44.48x_1^2 - 244.91x_2^2 + 300.78x_3^2 \quad (2)$$

In general, an appropriate regression equation provides important information about the influence of the factors on the regression coefficients. The values of the tensile properties calculated with regression equations, (1) and (2), have a very good match with the points obtained with the experiments and are given in **Table 1**.

Table 1 also lists deviations of values $R_{p0,2}$ and R_m obtained by using the model (regression equation K_M), related to the experimentally obtained values for $R_{p0,2}$ and R_m (K_E) and calculated with the following general expression:

$$\text{Deviation} = \frac{(K_M - K_E)}{K_E} \cdot 100\ (\%)$$

Table 1: Chemical composition of Nimonic 80A and a review of the experimental and the model values of the tensile properties of the specimens at a temperature of 750 °C

Tabela 1: Kemijska sestava Nimonic 80A in pregled eksperimentalnih in modelnih vrednosti nateznih trdnosti vzorcev pri temperaturi 750 °C

Melt	Content elements, w/%			$R_{p0,2}$/MPa		Deviation /%	R_m/MPa		Deviation /%
	Al	Ti	Co	Experim.	Model		Experim.	Model	
V1647	1.14	2.13	1.67	558	542.7	–2.7	679	681.8	0.4
V1653	1.66	1.82	0.90	533	512.3	–3.9	658	643.3	-2.2
V1651	1.08	2.9	0.83	604	609.4	0.9	673	674.5	0.2
V1669	1.68	2.92	1.88	686	674.4	–1.7	764	741.9	-2.8
V1648	1.20	1.90	0.89	503	505.1	0.4	662	674.5	1.9
V1656	2.14	1.87	1.89	617	614.0	–0.5	680	680.6	0.1
V1652	1.07	2.79	1.83	560	596.9	6.6	677	675.5	-0.2
V1672	1.81	2.8	1.09	634	653.7	3.1	708	711.4	0.5
V1664	0.93	1.69	1.90	532	518.4	–2.6	648	642.9	-0.8
V1654	1.53	1.86	0.87	518	519.9	0.4	660	667.9	1.2
V1671	1.15	2.78	1.10	592	567.0	–4.2	664	646.0	-2.7
V1670	1.40	2.73	1.69	609	605.9	–0.5	685	696.3	1.6
V1665	0.98	1.71	1.04	400	427.9	7.0	606	585.1	-3.5
V1657	1.59	1.80	1.82	521	541.6	3.9	647	655.2	1.3
V1666	1.13	2.66	1.57	583	561.4	–3.7	633	655.6	3.5
V1668	1.64	2.67	1.16	615	616.4	0.2	693	703.0	1.4

Table 2: Statistical characteristics of the used model
Tabela 2: Statistične značilnosti uporabljenega modela

Tensile properties	R^2	Coefficient correlation R	Standard error	SS regression	SS residual	Ficher test		Significant
						Tabular	Model	
$R_{p0,2}$	0.9990	0.9995	26.95303	5197281.74	5085.261	3.69	794.91	YES
R_m	0.9998	0.9996	19.04061	7220737	2537.815	3.69	2212.98	YES

Statistical characteristics of the used model are given in **Table 2**.

Taking into account that regression surfaces cannot be presented in a three-dimensional space, the independent variables are successfully replaced by their average values. Presentation of the 3D model for different values of changeable variables in a specific interval is given in **Figure 1**.

An equation (1 and 2) can be used to calculate the default characteristics at 750 °C by entering the specific values of certain factors. This provides the values for $R_{p0,2}$ and R_m that are close to the experimentally obtained amounts.

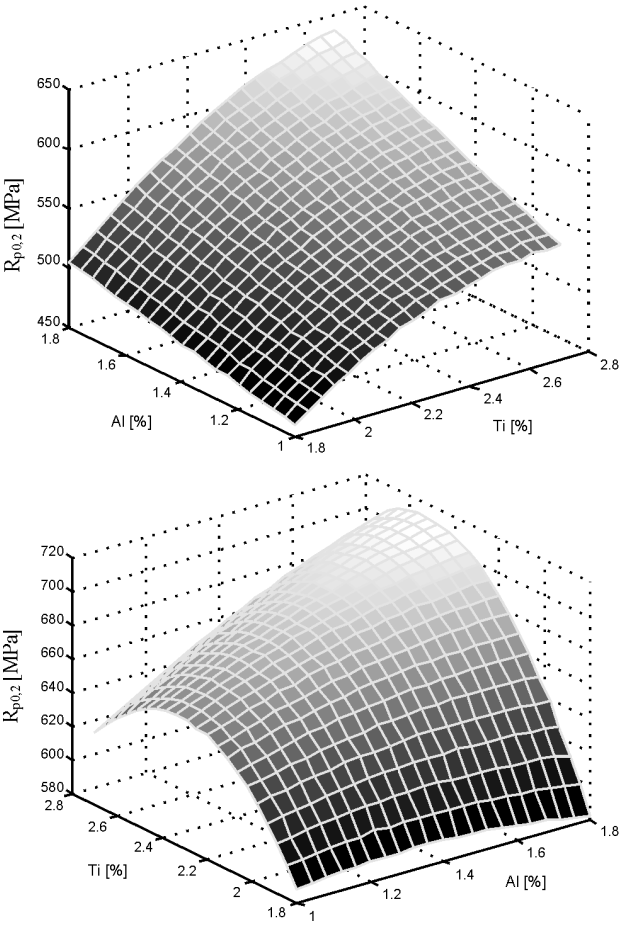

Figure 1: Functional dependence of $R_{p0,2}$, R_m and the influencing factors w(Al), w(Ti) and w(Co)
Slika 1: Funkcijska odvisnost $R_{p0,2}$, R_m in vplivnih faktorjev (masni deleži w(Al), w(Ti) in w(Co))

Those surfaces that represent a three-dimensional space can be easily reproduced and interpreted by designers as well as by technology engineers.

4 DISCUSSION

4.1 Determining the optimum values of the influential parameters x_i for the yield strength y_i ($R_{p0,2}$)

In this example a three-factor model was applied. The varied values of the influential factors of x_i, w(Al), w(Ti) and w(Co), relating to the corresponding plan matrix, are known, and so is the parameter of the investigated processes y_i after conducting the experimental tests, i.e., the value of $Y^{(E)}_{(\max)i} = R^{(E)}_{p0,2(\max)i}$ (equation 1).

The coordinates of possible optimum point in the investigated area, i.e., the global optimum is determined by solving the system of algebra equations derived from the conditions $\partial y / \partial x_i = 0$.

This requirement of the regression equation (1) in the considered case is reduced to a system of three linear algebra equations:

$$\begin{aligned} \partial y/\partial x_1 &= 41.16x_1 + 70.86x_2 - 15.72x_3 = 112.58 \\ \partial y/\partial x_2 &= 70.86x_1 - 249.65x_2 - 49.76x_3 = -662.85 \\ \partial y/\partial x_3 &= -15.72x_1 - 49.76x_2 + 490.22x_3 = 509.02 \end{aligned} \quad (3)$$

whose solutions are: $x_1 = 1.8$; $x_2 = 2.7$ and $x_3 = 2$, where $x_1 = w$(Al), $x_2 = w$(Ti) and $x_3 = w$(Co).

Since these values belong to the investigated area, the regression equation (1) has a global optimum, i.e., the next maximum value for $(R_{p0,2})_{max} = 725.28$ MPa.

The question is whether the maximum value is also the optimum value for a given alloy. Taking into account that the alloy with the maximum value of yield strength is difficult to use in plastic processing and has lower ductile characteristics, the optimum value for the mean yield strength ($R_{p0,2}$) is used in line with the reference source[8]. At the operating temperature of 750 °C the superalloy Nimonic 80A has a yield strength of $R_{p0,2}$ = (420–620) MPa, and this value was also used as *the optimum value*.

In this case the solutions of the linear algebraic equations (3) are: $x_1 = 1.4$ % Al, $x_2 = 2.09$ % Ti and $x_3 = 1.365$ % Co.

Curves were presented in the form of a graph (**Figure 2**) resulting from the intersection of the surface correlation with the parallel planes (the planes at the same level). In each plane there is a part of the plane of the intersection (the value of the yield strength). With their help it is easy to determine the variation domain of the

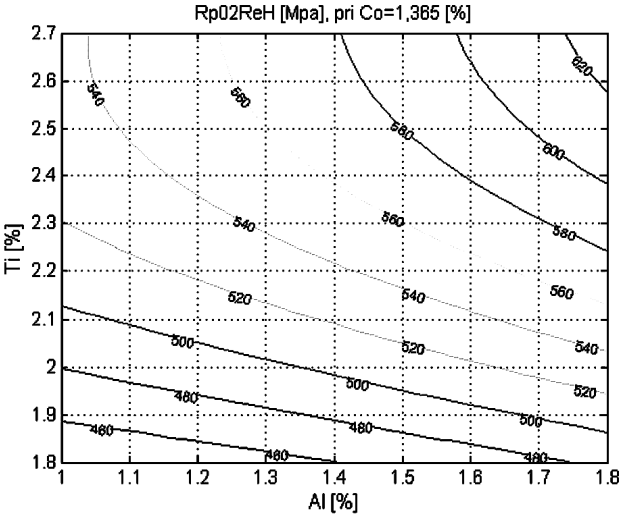

Figure 2: Graphical presentation of the yield-strength curves for Nimonic 80A according to the equation (1)
Slika 2: Grafični prikaz krivulj meje tečenja za Nimonic 80A, skladno z enačbo (1)

analyzed parameters that are suitable for optimizing the yield strength (1).

From the given graph it can be observed that *the selected* optimum field of the yield strength (500–540 MPa) can be obtained with a series of combinations of the content of w(Ti) = (2.1–2.7) % and the content of w(Al) = (1–1.8) % with the stated content of Co.

4.2 Determining the optimum values of the influential parameters x_i of the tensile strength y_i (R_m)

The equation of the regression models of the second order (equation 2) is used as the basis for the research in the area of the optimum tensile strength R_m at 750 °C. Determination of the (optimum) values of the influential parameters x_i for y_i – the tensile strength (R_m) – can be done:

1. by establishing optimum values of the parameters for $R_{p0,2}$,
2. by establishing the adopted optimum value of R_m.

4.2.1 Determination of R_m with the set optimum values of the parameters for $R_{p0,2}$

Determined optimum values of the influential parameters $R_{p0,2}$ were used as the base for exploring the field of strength (R_m). These values belong to the studied area and Figure 1 shows the regression equation (2) (hypersurface) in the multidimensional space (hyperspace).

The Superalloy Nimonic 80A used at the operating temperature of 750 °C, with the set optimum values of the influential parameters being $x_1 = 1.4$, $x_2 = 2.09$ and $x_3 = 1.365$, has the following value of the tensile strength: $R_m = 656.05$ MPa. This value is at the lower limit of the tensile strength R_m = (620–820) MPa that is given in the literature[9,10].

When the criteria of the optimum values of the tensile strength are set it is necessary to determine the values of the influential parameters.

4.2.2 Determining the optimum values of the influential parameters adopted for the optimum R_m

The regression equation (2) was used to explore the optimum area. The coordinates of the possible optimum points in the studied area were determined by solving a system of algebraic equations obtained from the condition $\partial y / \partial x_i = 0$. Using this condition the regression equation (2) was reduced to a system of three linear algebraic equations:

$$\begin{aligned}
\partial y / \partial x_1 &= -88.96x_1 + 122.98x_2 + 15.77x_3 = 127.11 \\
\partial y / \partial x_2 &= 122.98x_1 - 489.82x_2 - 14.98x_3 = -1039.83 \qquad (4) \\
\partial y / \partial x_3 &= 15.77x_1 - 14.946x_2 + 601.56x_3 = 798.58
\end{aligned}$$

whose solutions regarding the maximum values are: $x_1 = 1.8$, $x_2 = 2.52$ and $x_3 = 2$.

Since these values belong to the studied area the regression equation (2) has a global optimum with the maximum value of $R_{m\ max}$ = 837,49 MPa.

In a case of choosing the optimum value for the tensile strength with the maximum values for the contents of w(Al), w(Ti) and w(Co), the criteria for choosing the optimum value is the same as for choosing the optimum value of the yield strength.

Based on[9], the superalloy Nimonic 80A, used for the operating temperature of 750 °C, has a R_m = (620–820) MPa and the medium tensile strength R_m = 720 MPa can be adopted as the optimum value. The solutions of the linear algebra equations (4) in this case are: $x_1 = 1.4$ % Al, $x_2 = 2.52$ % Ti and $x_3 = 1.705$ % Co.

For the purpose of optimizing (2) shown in a graphic form (**Figure 3**) the regression equation is suitable for the tensile strength.

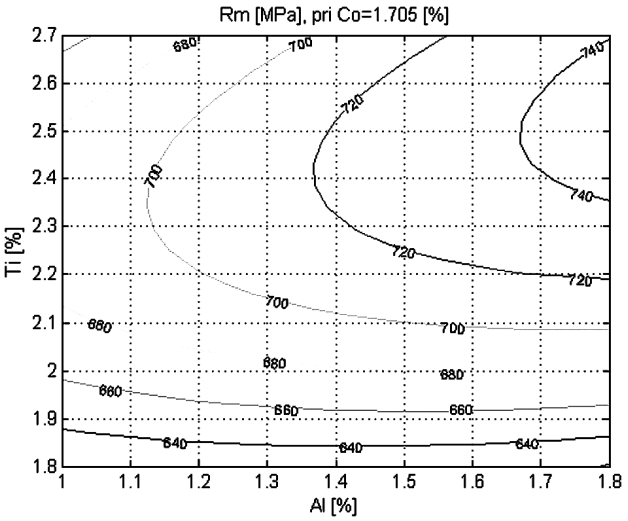

Figure 3: Graphical presentation of the tensile-strength curves for Nimonic 80A according to equation (2)
Slika 3: Grafični prikaz krivulj natezne trdnosti Nimonic 80A, skladno z enačbo (2)

Aa analysis of the gained results indicates that the samples made of superalloys Nimonic 80A have relatively good values of the influential parameters *w*(Al, Ti, and Co). The obtained results allow the selection of the best ratio of *w*(Al) and *w*(Ti) relative to *w*(Co) in order to obtain the desired values of the mechanical properties. In this case the reduction in the tensile strength Rm, i.e., its maximum value was achieved by adjusting *w*(Al) and *w*(Ti). An increase in the value of *w*(Co) in the range of 1–1.7% does not significantly affect ± 2.64 % a decrease or an increase in R_m.

The result of the research and an insight into the qualitative and quantitative strength contributions of the superalloy Nimonic 80A to all the acting strengthening mechanisms was a design of an acceptable theoretical model for the formation of optimum strength. On the basis of the known chemical composition, i.e., the content of the main alloying elements – Al, Ti and Co – the regression equations are gained and the mechanical properties of the materials shown at elevated temperatures can be predicted. On the basis of the square regression equations an optimization of the chemical composition of materials for the selected values of mechanical properties was carried out.[4,11]

5 CONCLUSIONS

After analyzing an experimental investigation of the influence of the contents of aluminium, titan and cobalt on the tensile properties of the superalloy Nimonic 80A at 750 °C the following can be concluded:

- A mathematical model that establishes a corellation between the main alloying elements (Al, Ti and Co) and the mechanical properties shown at 750 °C is both adequate and accurate;
- All the selected parameters relating to the chemical composition, being varied with regard to two levels, affect the mechanical properties, i.e., all of them are significant;
- In the real working conditions each influential parameter has a different influence and a different effect on the tensile properties. Ti and Al have a high impact on them. Increasing the contents of these elements leads to an improvement in the tensile properties. The influence of Co on the tensile properties is lower than the influence of the other two elements;
- Equations (1) and (2) can be used for the calculation of the tensile properties at 750 °C for the specific values of individual factors. The values for $R_{p0,2}$, and R_m were in accordance with the experimental results.
- The conducted research and analysis provide a methodology for determining the parameters of the process and decision making in terms of a proper design of the structure of the superalloy Nimonic 80A.
- The numerical analysis, carried out under the proposed methodology, can provide reliable parameters influencing the behavior of the materials at the temperature of 750 °C under a static load. Further analysis may be excluded which reduces costly and time-consuming experimental tests.
- The obtained results allow the selection of the best (optimum) ratio of the aluminum and titanium contents relative to the content of cobalt;
- The performed research and analysis provide a contribution towards a methodology for determining influential parameters of the process and decision making in terms of a proper design of the structure of the superalloys Nimonic 80A;

It is obvious that the proposed methodology can successfully solve various complex tasks of modeling, numerical simulation and optimization of an alloy composition.

6 REFERENCES

[1] W. Betteridge, J. Heslop, The Nimonic Alloys and Other Nickel – Base High-Temperature Alloys, Sec.Ed., Edward Arnold (Publishers) Limited, London 1974

[2] W. Betteridge, Nickel and Alloys, Industrial Metals Series, London, 1977

[3] E. O. Ezugwu, J. Bonney, Y. Yamane, An Overview of the Machinability of Aeroengine Alloys, Journal of Materials Processing Technology, 134 (**2003**), 233–253

[4] R. Sunulahpašić, Optimizacija mehaničkih i strukturnih osobina superlegure Nimonic 80A namijenjene za rad na povišenim temperaturama u autoindustriji, doktorska disertacija, Univerzitet u Zenici, Fakultet za metalurgiju i materijale, Zenica, 2011

[5] D. Montgomery, Design and analysis of experiments, John Wiley & Sons, Inc., New York, 2001

[6] R. H. Brian, L. L. Ronald, M. R. Jonathan, A Guide to Matlab, Cambridge University Press, 2006

[7] S. Ekinović, Metode statističke analize u Mikrosoft Excel-u, Univerzitet u Zenici, Mašinski fakultet, Zenica, 2008

[8] BAS EN 10002-5 Metalni materijali – Ispitivanje zatezanjem – Dio 5 – Metoda ispitivanja na povišenoj temperaturi (EN 10002-5:1991)

[9] http://www.specialmetals.com/documents/Nimonic% 20alloy% 2080A.pdf

[10] M. Oruč, R. Sunulahpašić, Savremeni metalni materijali, Univerzitet u Zenici, Fakultet za metalurgiju i materijale, Zenica, 2005

[11] N. S. Stoloff, Wrought and P/M Superalloys, METALS HANDBOOK, Properties and Selection: Irons, Steels, and High-perfomance Alloys, 10th ed. vol. 1, ASM 1990

UDK 669.18:658.5
Original scientific article/Izvirni znanstveni članek

ISSN 1580-2949
MTAEC9, 46(3)269(2012)

BATCH-FILLING SCHEDULING AND PARTICLE SWARMS

IZDELAVA DELOVNIH NALOGOV ZA JEKLARNO IN ROJI DELCEV

Miha Kovačič[1], Božidar Šarler[2]

[1]ŠTORE STEEL, d. o. o., Železarska cesta 3, SI-3220 Štore, Slovenia
[2]Laboratory for Multiphase Processes, University of Nova Gorica, Vipavska 13, SI-5000, Nova Gorica, Slovenia
miha.kovacic@store-steel.si

Prejem rokopisa – received: 2011-10-24; sprejem za objavo – accepted for publication: 2012-01-31

Štore Steel Ltd faces a problem of producing a large number (approximately 1400) of different steel compositions in relatively small quantities (approximately 15 t). This production is performed in batches of predetermined quantities (50–53 t). The purpose of this paper is to present a methodology for optimizing the production of predetermined steel grades in predetermined quantities before the customers' deadline and in such a way as to reduce the non-planned and ordered quantities with the date before the deadline and minimize the number of batches. The particle-swarm method was used for the optimization. The results of the research have been used in practice since 2006. Since then the production of non-planned and ordered quantities were reduced from 17.17 % to 10.12 %.

Keywords: steelmaking, continuous casting, steel grade, work orders, scheduling, optimization, particle-swarm optimization

Štore Steel, d. o. o., se spopada s problemom majhnih naročil (v povprečju 15 t) ter izdelavo ogromne količine različnih kvalitet jekla (več kot 1400). Jeklo se izdeluje v šaržah (50–53 t). V članku je predstavljena metodologija za optimiranje izdelave planiranih kvalitet in količin jekla v predvidenem roku z namenom, da se zmanjša odlita planirana količina jekla, kjer je dobavni rok daljši kot določeni, ter neplanirana količina jekla. Optimizacija je bila izvedena z roji delcev. Rezultati raziskave so uporabljeni v praksi od leta 2006, ko sta se v letu 2007 odlita planirana količina jekla, kjer je dobavni rok daljši kot določeni, ter neplanirana količina jekla, zmanjšali iz 17,17 % na 10,12 %.

Ključne besede: jeklarstvo, kontinuirano odlivanje, kvaliteta jekla, delovni nalogi, planiranje, optimizacija, optimizacija z roji delcev

1 INTRODUCTION

Štore Steel Ltd owns a small (200 000 t per year) flexible steel plant and is one of the best-known producers of flat spring steel in Europe. The company produces more than 80 steel grades with more than 1400 different customer-specific chemical compositions.

In the steel plant, scrap iron is melted in a 60 t-capacity electric arc furnace. The liquid steel is then poured into the ladle (ca. 53 t), which a crane transports to a subsequent ladle furnace, where manganese, chromium, molybdenum, nickel, vanadium and other alloying elements are added to the steel in order to meet the chemical-quality requirements. The molten steel is cast into square billets with the dimensions of 140 mm or 180 mm in a continuous caster. The billets are reheated afterwards and the steel bars of various shapes and dimensions are manufactured by means of hot rolling and finally in line with the customers' expectations, heat treated, peeled, drawn or grinded.

The steelmaking and casting represent the basic steel-production operations and play a primary role in the downstream steel production. The optimization of casting the planned batches in line with the different requirements relating to a chemical composition, ordering dates, casting quantities, etc., is an extremely challenging task. The complexity of batch planning increases with the number of different steel grades and different customers' orders.

There is a lack of descriptions of batch-filling scheduling in the open literature. The most plausible reasons for this are the reluctance of the manufacturers to expose their well-understood heuristics for forming the production schedules, and different technology or hardware specifics[1–3]. On the other hand, there are plenty of publications on casting technology and physical modelling available[4–9] at present.

One of the principal problems in the steel-production scheduling[2] is determining the scheduling of operations to be performed on molten steel during the production stage involving steelmaking and continuous casting. A theoretical basis for the time-dependent batch scheduling is, to the best of the authors' knowledge, presented only in[10,11]. Similarly,[12] explores the scheduling problem involving the production and the transportation in a steelmaking shop in order to minimize the completion time. Paper[13] deals with the schedules for casting different moulds from a number of heats, and[14] deals with the scrap-charge-optimization problem, on the basis of its chemical composition, in the secondary steel production. The last reference is most probably the most relevant with respect to the batch-filling scheduling, discussed in the present paper.

To a great extent, at Štore Steel Ltd work-order scheduling and the related tasks have been traditionally carried out by a highly skilled, expert, human scheduler. In the present paper, the particle-swarm method was considered for the generation of batch-filling schedules. During the optimization the particles 'fly' intelligently in the solution space and search for the optimal batch-filling schedules in line with the strategies of the particle-swarm algorithm. Many different work-order schedules were obtained during the optimization.

2 STRUCTURE OF WORK ORDERS

The production of steel at Štore Steel Ltd is usually deliberately carried out for a pool of 384 customers. The mean cast quantity is 14.32 t (a standard deviation of 23.77 t). Due to the constraints posed by the production, some extra cast steel is produced on top of the ordered cast quantity. This is denoted as a non-planned cast quantity.

The work orders for batch processing are generated on the basis of the customers' orders. A typical structure of work orders is presented in **Table 1**.

A work-order number is a sequential number. The cover-quality prescription and the work-order chemical limitations define the chemical composition of the related batch.

Each quality prescription includes also its own steelmaking technology (i.e., the times, temperatures, sampling, purging, oxygen activities). There are, in general, two groups of steelmaking technologies: the first is used for the extra-machinability steels[15], where the batch weight is 50 t, and the second is appropriate for the other steel qualities, where the batch weight is 53 t. In the extra-machinability steelmaking technology the molten steel in the ladle is more reactive, so the molten steel quantity (batch weight) should be smaller.

Table 1: Work-order example
Tabela 1: Zgled oblike delovnega naloga

Work order number: 0001019			
Cover quality prescription code	Chemical limitations		
732.59.2	wt% C 0.52-0.54! wt% P MAX 0.015! wt% Sn MAX 0.02! wt% As MAX 0.04!		
Quality prescription code	Customer order code	Ordered quantity (tons)	Delivery date
732.54.2	0000855022	25	30.1.2009
732.01.0	0000937001	3.5	8.11.2009
732.59.2	0000855007	1.5	30.1.2009
732.59.2	Non-planned cast quantity	23	

Tables 2, 3 and **4** show three sample-quality prescriptions (732.00.1, 732.59.2, 732.54.2) and their calculated chemical limits. The chemical limitations are calculated on the basis of the quality-prescription limits and the simple instructions presented in **Figures 1** and **2**. If the chemical target value for a chemical element is prescribed in a quality prescription, it means that the ladle-furnace operator has to obtain the exact chemical weight percentage of the element. The internal minimum and maximum are prescribed in line with the technology procedure. The batch satisfies a customer's chemical requirements if the chemical weight percentage is within the customer's limits (minimum and maximum). Due to the technology limitations and instructions, the customers' chemical limitations are converted to internal composition limits so as to assure the customers' specifications. The briefly described instructions dictate that the in-plant chemical limitations are more restrictive than the customers' chemical limitations.

Table 2: Quality prescription 732.01.0 and its calculated chemical limits (minimum and maximum)
Tabela 2: Kakovostni predpis 732.01.0 in izračunane kemične omejitve (minimum in maksimum)

Quality prescription 732.01.0						Calculated chemical limits	
Element	Customer minimum (wt%)	Internal minimum (wt%)	Aim (wt%)	Internal maximum (wt%)	Customer maximum (wt%)	Quality prescription limits – minimum (wt%)	Quality prescription limits – maximum (wt%)
C	0.47	0.50		0.53	0.55	0.47	0.55
Si	0.15	0.20		0.35	0.40	0.15	0.40
Mn	0.70	0.80		1.00	1.10	0.70	1.10
P				0.015	0.025	0	0.025
S				0.020	0.025	0	0.025
Cr	0.90	1.00		1.10	1.20	0.90	1.20
Mo				0.05	0.08	0	0.08
Ni				0.25	0.30	0	0.30
Al		0.010	0.011	0.015	0.100	0.010	0.015
Cu				0.25	0.40	0	0.40
V	0.10	0.14		0.17	0.20	0.10	0.20
Sn				0.030		0	0.030
As						0	100
N						0	100

Table 3: Quality prescription 732.54.2 and its calculated chemical limits (minimum and maximum)
Tabela 3: Kakovostni predpis 732.54.2 in izračunane kemične omejitve (minimum in maksimum)

Quality prescription 732.54.2						Calculated chemical limits	
Element	Customer minimum (wt%)	Internal minimum (wt%)	Aim (wt%)	Internal maximum (wt%)	Customer maximum (wt%)	Quality prescription limits – minimum (wt%)	Quality prescription limits – maximum (wt%)
C	0.49	0.50		0.52	0.54	0.49	0.54
Si	0.20	0.20	0.34	0.35	0.40	0.20	0.40
Mn	0.90	0.91		1.00	1.10	0.90	1.10
P				0.015	0.015	0	0.015
S				0.015	0.015	0	0.015
Cr	0.90	0.91		1.00	1.20	0.90	1.20
Mo				0.04	0.08	0	0.08
Ni				0.10	0.20	0	0.20
Al	0.010	0.010	0.011	0.015	0.025	0.010	0.025
Cu				0.25	0.25	0	0.25
V	0.10	0.11		0.14	0.20	0.10	0.20
Sn				0.015		0	0.015
As				0.035	0.040	0	0.040
N						0	100

Table 4: Quality prescription 732.59.2 and its calculated chemical limits (minimum and maximum)
Tabela 4: Kakovostni predpis 732.59.2 in izračunane kemične omejitve (minimum in maksimum)

Quality prescription 732.59.2						Calculated chemical limits	
Element	Customer minimum (wt%)	Internal minimum (wt%)	Aim (wt%)	Internal maximum (wt%)	Customer maximum (wt%)	Quality prescription limits – minimum (wt%)	Quality prescription limits – maximum (wt%)
C	0.51	0.52	0.52	0.55	0.55	0.52	0.55
Si	0.25	0.25	0.34	0.35	0.40	0.25	0.35
Mn	0.95	1.00	1.00	1.10	1.10	1.00	1.10
P				0.015	0.020	0	0.020
S				0.008	0.008	0	0.008
Cr	1.05	1.10	1.10	1.20	1.20	1.10	1.20
Mo				0.05	0.06	0	0.05
Ni				0.20	0.20	0	0.20
Al		0.010	0.011	0.015	0.040	0.010	0.015
Cu				0.25	0.25	0	0.25
V	0.10	0.15	0.16	0.18	0.25	0.15	0.18
Sn				0.025		0	0.025
As						0	100
N				0.016		0	0.016

In fact, all three of the quality prescriptions presented, match the chemical composition of the 50CrV4 (W. NR. 1.8159) spring steel. For example, at the moment there are 53 quality prescriptions for the 50CrV4 steel existing in the company, and it is not possible to chemically combine all of them.

On the basis of the selected customers' orders and their quality prescriptions (732.00.1, 732.59.2, 732.54.2), it

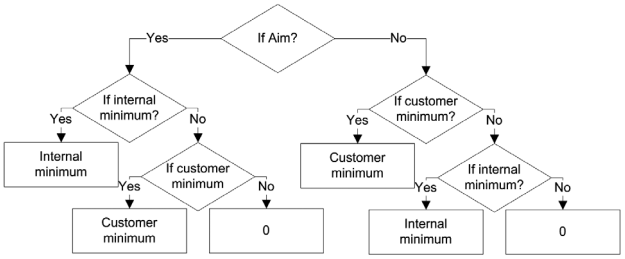

Figure 1: Instructions for defining the quality-prescription minimum limit
Slika 1: Pravila za določanje minimuma kakovostnega predpisa

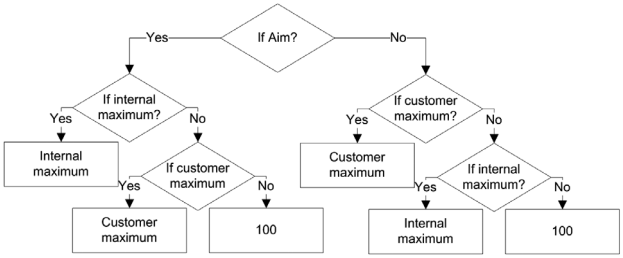

Figure 2: Instructions for defining the quality-prescription maximum limit
Slika 2: Pravila za določanje maksimuma kakovostnega predpisa

Table 5: Batch chemical limitations
Tabela 5: Kemijske omejitve šarže

	Quality prescription 732.01.0 limits (wt%)		Quality prescription 732.54.2 limits (wt%)		Quality prescription 732.59.2 limits (wt%)		Batch chemical limitations (wt%)	
Element	Minimum	Maximum	Minimum	Maximum	Minimum	Maximum	Minimum	Maximum
C	0.47	0.55	0.49	0.54	0.52	0.55	0.52	0.54
Si	0.15	0.40	0.20	0.40	0.25	0.35	0.25	0.35
Mn	0.70	1.10	0.90	1.10	1.00	1.10	1.00	1.10
P	0	0.025	0	0.015	0	0.020	0	0.015
S	0	0.025	0	0.015	0	0.008	0	0.008
Cr	0.90	1.20	0.90	1.20	1.10	1.20	1.10	1,2
Mo	0	0.08	0	0.08	0	0.05	0	0.05
Ni	0	0.30	0	0.20	0	0.20	0	0.20
Al	0.010	0.015	0.010	0.025	0.010	0.015	0.010	0.015
Cu	0	0.40	0	0.25	0	0.25	0	0.25
V	0.10	0.20	0.10	0.20	0.15	0.18	0.15	0.18
Sn	0	0.030	0	0.015	0	0.025	0	0.015
As	0	100	0	0.040	0	100	0	0.040
N	0	100	0	100	0	0.016	0	0.016

is possible to easily calculate the batch chemical limitations (**Table 5**) in line with the instructions in **Figures 1** and **2**.

The logic for defining the cover-quality prescription is as follows: The quality prescription with the highest number of chemical-element limitations among the selected work-order quality prescriptions is defined as the cover quality prescription. In such a case, the ladle operator uses the technology prescribed in line with the cover-quality prescription and adjusts the steelmaking technology according to the required chemical composition. In the case of a customer's order for the extra-machinability steels included in the work-order quality prescriptions, its quality prescription automatically becomes a cover quality prescription.

3 PARTICLE-SWARM BATCH SCHEDULING

At the beginning of a batch scheduling, a grouping based on the ordered quantities is performed. The ordered quantities are divided into groups with a similar chemical composition. An ordered quantity fits into a group if the group already includes one or more ordered quantities with a similar chemical composition (a similar quality prescription).

After the grouping of the ordered quantities the particle-swarm method is used for the batch-filling scheduling[14].

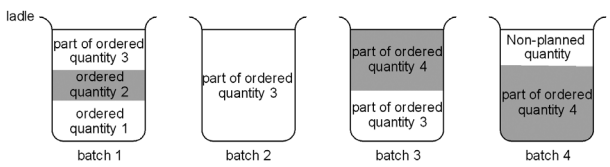

Figure 3: Work order schedule – the organism
Slika 3: Nabor delovnih nalogov – organizem

The "particle" structure is conditioned with the nature of the problem – the consecutive events – that the batch is cast consecutively. The biggest problem is in dealing with the batch-filling schedule – an organism evaluation.

4 BATCH-FILLING SCHEDULES AS PARTICLES

The batch-filling schedules are in fact the work-order sequences and can be presented as a sequence of batches with the ordered quantities (**Figure 3**). **Figure 3** shows the customer's ordered quantities cast within 4 batches. The ordered quantity 3 is cast within 3 batches, the ordered quantity 4 within 2 batches, and all the other ordered quantities within one batch. The non-planned cast quantity can be found in the last batch – batch 4.

Hence, the organism in **Figure 3** can be written down as a sequence: Ordered quantity 1 – Ordered quantity 2 – Ordered quantity 3 – Ordered quantity 4.

The principal task is to form a batch-filling sequence based on a customer's ordered cast quantities, quality prescriptions, delivery dates, and any other instructions.

5 FORMATION AND EVALUATION OF WORK ORDERS

The deadline must be defined in terms of the delivery date for the ordered quantities. This means that all quantities should be cast in terms of that delivery date. The batch weight is defined in line with the steelmaking technology – for extra-machinability steels, the batch weight is 50 t and for the other steel qualities the batch weight is 53 t.

Individually ordered quantities from the ordered-quantities pool are added to the work order until the batch weight is reached. If the last added quantity exceeds the batch weight, which is usually the case, a

partial quantity is added to one or more consecutive work orders. As a rule, partial quantities are added to the consecutive work order only when they exceed 5 %. Small orders of up to 5 t should not be split between different batches, i.e., they should be cast within one batch.

For each ordered quantity, the chemical composition is checked against the quality prescriptions for the added quantity as well. In the event that a chemical composition does not fit the chemical prescriptions for the added quantities, the actual work order is filled with a non-planned quantity and the quantity is added to the consecutive work order (orders), which is (are) filled according to the previously mentioned guidelines.

The work orders for quantities with a delivery date beyond the defined deadline are automatically abandoned.

The evaluation of a work-order schedule consists of the following three parts:

O_1 The number of additional ordered quantities, where the ordered quantities are not cast within one batch (for instance, as seen in Figure 3, we have to cast the ordered quantity 3 in 2 additional batches, and the ordered quantity 4 in one additional batch, so that the total number of additional ordered quantity parts, where the ordered quantities are not cast within one batch is, in this case, 3);

O_2 Non-planned cast quantities in tons;

Table 6: Quality-prescription quantities in October 2009 and their calculated chemical limits
Tabela 6: Količine za kakovostne predpise v oktobru 2009 in njihove izračunane kemijske omejitve

Quality Pre-scription code	Steel quality	Ordered Quantity (tons)	C (wt%)	Si (wt%)	Mn (wt%)	P (wt%)	S (wt%)	C (wt%)r	M (wt%)o	Ni (wt%)	Al (wt%)	Cu (wt%)	V (wt%)	Sn (wt%)	As (wt%)	N (wt%)
108.15.0	44MnSiVS6	30.192	0.42-0.47	0.5-0.7	1.3-1.6	MAX 0.035	0.02-0.035	MAX 0.25	MAX 0.07	MAX 0.25	0.016-0.03	MAX 0.25	0.1-0.13	MAX 0.03		
108.33.0	38MnVS5	121.5	0.35-0.4	0.5-0.7	1.2-1.5	MAX 0.035	0.045-0.06	0.15-0.25	MAX 0.08	MAX 0.3	0.02-0.038	MAX 0.25	0.08-0.13	MAX 0.03		0.015-0.018
108.70.1	38MnVS6 (extra machinability)	18.944	0.41-0.44	0.3-0.5	1.1-1.4	MAX 0.035	0.03-0.035	0.15-0.25	MAX 0.08	0.15-0.25	0.01-0.03	MAX 0.3	0.13-0.15	MAX 0.03		0.011-0.02
127.11.5	61SiCr7	83.841	0.57-0.65	1.6-1.8	0.7-1	MAX 0.02	MAX 0.015	0.25-0.4	MAX 0.08	MAX 0.3	0.015-0.025	MAX 0.25	MAX 0.1	MAX 0.02		
140.11.1	CSN 15230.3	18.038	0.24-0.34	0.17-0.37	0.4-0.8	MAX 0.035	MAX 0.035	2.2-2.5	MAX 0.05	MAX 0.2	0.02-0.035	MAX 0.25	0.1-0.2	MAX 0.03		
193.31.0	27MnCrB5	18.352	0.25-0.3	0.15-0.35	1-1.4	MAX 0.035	MAX 0.035	0.3-0.6	MAX 0.05	MAX 0.2	0.02-0.035	MAX 0.25	MAX 0.05	MAX 0.03		
193.52.0	30MnB5	26.374	0.27-0.3	0.1-0.3	1.05-1.2	MAX 0.035	MAX 0.035	MAX 0.3	MAX 0.08	MAX 0.3	0.02-0.035	MAX 0.4	MAX 0.1	MAX 0.02		
193.54.0	28MnCrB7-2	53.872	0.26-0.28	0.15-0.25	1.68-1.78	MAX 0.03	0.02-0.04	0.48-0.53	MAX 0.1	MAX 0.3	0.02-0.05	MAX 0.25	MAX 0.1	MAX 0.02		MAX 0.012
503.14.0	St 37-2	4.019	0.14-0.17	0.15-0.5	0.4-1.4	MAX 0.035	MAX 0.035	MAX 0.3	MAX 0.08	MAX 0.3	0.02-0.035	MAX 0.4	MAX 0.1	MAX 0.03		MAX 0.009
503.31.1	RSt 37-2	97.65	0-0.08	0-0.08	0.28-0.45	MAX 0.02	MAX 0.02				0.015-0.025				MAX 0.012	
516.17.1	Cm45	13.616	0.43-0.48	0.15-0.35	0.6-0.7	MAX 0.035	0.02-0.035	0.17-0.23	MAX 0.07	MAX 0.25	0.01-0.05	MAX 0.25	MAX 0.05	MAX 0.03		
523.00.0	C75	46.176	0.7-0.8	0.15-0.35	0.6-0.8	MAX 0.045	MAX 0.045	MAX 0.3	MAX 0.08	MAX 0.3	0.02-0.1	MAX 0.4	MAX 0.1	MAX 0.03		
524.11.0	C70	0.918	0.65-0.75	0.25-0.35	0.8-0.9	MAX 0.02	MAX 0.02	0.2-0.3	MAX 0.05	MAX 0.2	0.015-0.05	0.05-0.25	MAX 0.1	MAX 0.03		
615.12.0	C22E	30.251	0.16-0.19	MAX 0.1	0.3-0.4	MAX 0.015	MAX 0.015	MAX 0.2	MAX 0.1	MAX 0.2	0.02-0.035	MAX 0.2	MAX 0.05	MAX 0.03		
623.32.0	70MnVS4	218.093	0.69-0.72	0.15-0.25	0.8-0.9	MAX 0.015	0.06-0.07	0.1-0.2	MAX 0.06	MAX 0.2	MAX 0.03	MAX 0.25	0.14-0.15	MAX 0.03		0.013-0.016
625.13.1	C50	105.08	0.5-0.53	0.2-0.35	0.8-0.9	MAX 0.03	0.015-0.02	0.23-0.3	MAX 0.08	0.15-0.24	0.02-0.035	MAX 0.25	MAX 0.1	MAX 0.03		0.008-0.013
635.36.5	C35R	23.088	0.36-0.39	0.2-0.4	0.65-0.8	MAX 0.03	0.02-0.035	0.2-0.3	MAX 0.08	MAX 0.3	0.02-0.03	MAX 0.25	MAX 0.1	MAX 0.03		
636.11.1	C45	515.41	0.47-0.5	0.2-0.35	0.7-0.8	MAX 0.035	0.02-0.025	0.24-0.29	MAX 0.08	0.15-0.2	0.02-0.035	MAX 0.25	MAX 0.1	MAX 0.03		0.008-0.013
705.13.3	SAE 1141	54.6	0.39-0.43	0.2-0.3	1.4-1.55	MAX 0.03	0.08-0.092	MAX 0.3	MAX 0.08	MAX 0.3	0.015-0.02	MAX 0.3				
711.00.1	41Cr4	26.869	0.38-0.45	0.2-0.4	0.6-0.9	MAX 0.035	MAX 0.035	0.9-1.2	MAX 0.08	MAX 0.3	0.02-0.1	MAX 0.4	MAX 0.1	MAX 0.03		
711.14.0	41Cr4	15.333	0.38-0.45	0.2-0.4	0.6-0.9	MAX 0.035	MAX 0.035	0.9-1.2	MAX 0.08	MAX 0.3	0.02-0.1	MAX 0.4	MAX 0.1	MAX 0.03		
718.70.2	16MnCr5 (extra machinability)	55.388	0.14-0.19	0.2-0.4	1-1.3	MAX 0.035	0.02-0.035	0.8-1.1	MAX 0.08	MAX 0.3	0.02-0.1	MAX 0.4	MAX 0.1	MAX 0.03		MAX 0.015
724.24.0	42CrMo4	38.438	0.38-0.45	0.15-0.4	0.6-0.9	MAX 0.035	0.02-0.035	0.9-1.2	0.15-0.3	MAX 0.25	0.02-0.045	MAX 0.25	MAX 0.1	MAX 0.03		
732.01.0	50CrV4	150.341	0.47-0.55	0.15-0.4	0.7-1.1	MAX 0.025	MAX 0.025	0.9-1.2	MAX 0.08	MAX 0.3	0.01-0.015	MAX 0.4	0.1-0.2	MAX 0.03		
732.03.0	51CrV4	9.709	0.47-0.55	0.15-0.4	0.7-1.1	MAX 0.025	MAX 0.025	0.9-1.2	MAX 0.08	MAX 0.3	0.01-0.015	MAX 0.4	0.1-0.2	MAX 0.03		
732.12.5	51CrV4	67.113	0.51-0.54	0.2-0.35	1-1.1	MAX 0.015	MAX 0.015	1.1-1.2	MAX 0.08	MAX 0.2	0.01-0.015	MAX 0.25	0.1-0.2	MAX 0.02	MAX 0.04	
732.13.5	51CrV4	141.563	0.51-0.56	0.2-0.35	1-1.2	MAX 0.015	MAX 0.015	1.1-1.25	MAX 0.08	MAX 0.2	0.01-0.015	MAX 0.25	0.1-0.2	MAX 0.02	MAX 0.04	
732.18.1	51CrV4	5.661	0.47-0.51	0.15-0.4	0.7-0.85	MAX 0.025	MAX 0.025	0.9-1	MAX 0.08	MAX 0.25	0.01-0.04	MAX 0.25	0.1-0.25	MAX 0.025		
732.19.1	51CrV4	11.485	0.51-0.55	0.15-0.4	0.85-0.95	MAX 0.025	MAX 0.025	0.95-1.1	MAX 0.08	MAX 0.25	0.01-0.04	MAX 0.25	0.1-0.25	MAX 0.025		
732.20.2	51CrV4	58.785	0.51-0.55	0.15-0.4	0.9-1.1	MAX 0.025	MAX 0.025	1.05-1.2	MAX 0.08	MAX 0.25	0.01-0.04	MAX 0.25	0.1-0.25	MAX 0.025		
732.21.2	51CrV4	27.675	0.52-0.54	0.2-0.35	0.95-1.1	MAX 0.025	MAX 0.025	1.1-1.2	MAX 0.07	MAX 0.2	0.01-0.015	MAX 0.25	0.12-0.2	MAX 0.025		
732.24.4	50CrV4	69.967	0.47-0.55	0.2-0.4	0.7-1.1	MAX 0.035	MAX 0.035	0.9-1.2	MAX 0.05	MAX 0.2	0.01-0.015	MAX 0.25	0.1-0.2	MAX 0.03		MAX 0.012
732.26.2	51CrV4	17.263	0.51-0.54	0.2-0.35	0.9-1.05	MAX 0.02	MAX 0.015	1-1.1	MAX 0.04	MAX 0.2	0.01-0.015	MAX 0.25	0.11-0.15	MAX 0.025		
732.27.3	51CrV4	31.69	0.51-0.55	0.15-0.4	0.95-1.1	MAX 0.025	MAX 0.025	1.1-1.2	MAX 0.08	MAX 0.25	0.01-0.04	MAX 0.25	0.1-0.25	MAX 0.025		
732.54.2	51CrV4	636.408	0.49-0.54	0.2-0.35	0.9-1.1	MAX 0.015	MAX 0.015	0.9-1.2	MAX 0.08	MAX 0.2	0.01-0.015	MAX 0.25	0.1-0.2	MAX 0.02	MAX 0.04	
732.59.2	50CrV4	427.379	0.52-0.55	0.25-0.35	1-1.1	MAX 0.02	MAX 0.008	1.1-1.2	MAX 0.06	MAX 0.2	0.01-0.015	MAX 0.25	0.15-0.18	MAX 0.025	MAX 0.016	
732.62.0	50CrV4	6.83	0.47-0.55	0.2-0.4	0.7-1.1	MAX 0.02	MAX 0.01	0.9-1.2	MAX 0.08	MAX 0.2	0.01-0.015	MAX 0.25	0.1-0.2	MAX 0.03		MAX 0.012
732.66.0	51CrV4	37.37	0.47-0.5	0.2-0.4	0.7-1.1	MAX 0.035	MAX 0.035	0.9-1.2	MAX 0.08	MAX 0.3	0.01-0.015	MAX 0.25	0.1-0.25	MAX 0.03		MAX 0.012
741.33.3	15CrNiS6	4.144	0.12-0.17	0.15-0.4	0.4-0.6	MAX 0.035	0.02-0.035	1.4-1.7	MAX 0.08	1.4-1.7	0.02-0.1	MAX 0.25	MAX 0.1	MAX 0.03		MAX 0.013
775.13.0	23MnNiMoCr5-4	25.693	0.21-0.24	0.15-0.25	1.25-1.4	MAX 0.02	MAX 0.012	0.5-0.6	0.5-0.6	1-1.1	0.02-0.05	MAX 0.25	MAX 0.1	MAX 0.02		MAX 0.012
779.27.1	16MnCrS5	414.9	0.14-0.17	0.2-0.35	1-1.1	MAX 0.035	0.02-0.03	0.8-0.9	MAX 0.05	MAX 0.15	0.02-0.03	MAX 0.25	MAX 0.1	MAX 0.03		MAX 0.013
779.71.4	16MnCrS5 (extra machinability)	40.848	0.17-0.19	0.15-0.3	1-1.1	MAX 0.025	0.03-0.035	0.9-1	MAX 0.07	MAX 0.15	0.02-0.03	MAX 0.28	MAX 0.1	MAX 0.02		0.01-0.012
780.10.0	20MnCrS5	52.8	0.2-0.23	0.15-0.25	1.3-1.4	MAX 0.025	0.02-0.03	1.2-1.3	0.07-0.1	0.15-0.25	0.02-0.03	MAX 0.25	MAX 0.1	MAX 0.03		0.008-0.012
780.13.2	20MnCr5	138.45	0.17-0.22	0.2-0.35	1.1-1.4	MAX 0.03	0.015-0.035	1-1.3	MAX 0.1	MAX 0.35	0.02-0.05	MAX 0.25	MAX 0.1	MAX 0.02		
781.00.1	18CrNiMo7-6	17.997	0.15-0.21	0.2-0.4	0.5-0.6	MAX 0.035	MAX 0.035	1.5-1.8	0.25-0.35	1.4-1.7	0.02-0.1	MAX 0.4	MAX 0.1	MAX 0.03		
781.18.1	19CrNiMo7-6	228.75	0.15-0.17	0.2-0.35	0.52-0.62	MAX 0.03	0.018-0.025	1.55-1.65	0.25-0.35	1.42-1.52	0.02-0.03	MAX 0.25	MAX 0.1	MAX 0.03		

O_3 All the customers' quantities in tons with the delivery date ahead of the deadline.

For a proper evaluation of the optimum solution, weights were also used: $w_1 = 4$, $w_2 = 1$ and $w_3 = 1$ for each evaluation part (O_1 – number of additional ordered quantity parts, O_2 – non-planned cast quantities, and O_3 – all the customers' quantities in tons with the delivery date ahead of the deadline). The weights were selected according to the expert scheduler's advice and the preliminary test runs. The respective evaluation function can be simply written as:

$$f_e = w_1 \cdot O_2 + w_2 \cdot O_2 + w_3 \cdot O_3 \quad (1)$$

6 PARTICLE-SWARM OPTIMIZATION

A problem is set in a discrete space, so that the most important task in applying the particle-swarm optimization successfully is to develop effective "problem-mapping" and "solution-generation" mechanisms. If these two mechanisms are devised successfully, it is possible to find good solutions for a given optimization problem in due time.

The particle-swarm optimization used can be described in the three following steps[14].

Let the initialization iterative generation be $k = 0$, initialization population size p_{size}, and the termination iterative generation *Maxgen*. Give birth to p_{size} initializing particles. Calculate each particle's fitness value of the initialization population, and let the first generation p_i be initialization particles, and choose the particle with the best fitness value of all the particles to be p_g (g_{Best}).

Every $p_{i,k}$ and $p_{g,k}$ crossover can get two child particles, compare them and let the smaller fitness-value particle be the final child of the predecessors. Use equation (2) to obtain the "flying" velocity v_i particles, then utilize equation (3) randomly permuting the N particles of them. Using equations (4) and (5) with the same method gives birth to the next-generation particles x_i. If the fitness value is better than the best fitness value p_i (p_{Best}) in history, let the current value be the new p_i (p_{Best}). Choose the particle with the best fitness value of all the particles to be p_g (g_{Best}). If $k = Maxgen$, go to Step 3, or else let $k = k + 1$; go to Step 2.

Put out p_g.

The changing of the particles' velocities is presented with the following equations:

$$v_{i,k+1} = p_{i,k} \otimes p_{g,k} \quad (2)$$

$$(v_{r1}, v_{r2}, \ldots, v_{rN})_{k+1} = P(v_{r1}, v_{r2}, \ldots, v_{rN}) \quad (3)$$

$$x_{i,k+1} = x_{i,k} \otimes v_{i,k+1} \quad (4)$$

$$(x_{r1}, x_{r2}, \ldots, x_{rN})_{k+1} = P(x_{r1}, x_{r2}, \ldots, x_{rN}) \quad (5)$$

where k represents the iterative generation number, and r ($1 = r = p_{size}$) is the random integer, which denotes the permuting particle, and # is a crossover denotation denoting the two particles making a crossover operator. $P(v_r)$, $P(x_r)$ refer to the permuting particles v_r and x_r. The termination criterion for the iterations is determined according to the max generation (10 000).

For each final work-order schedule 100 independent runs were performed.

In the presented algorithm, each particle of the swarm shares mutual information globally and benefits from the discoveries and previous experiences of all the other colleagues during the search process. The algorithm requires only primitive and simple mathematical operators, and is computationally inexpensive in terms of both memory requirements and time.

7 RESULTS OF THE SCHEDULING

In order to demonstrate the methodology, real data from the production in October 2009 were used. There were 196 ordered quantities with an average quantity of 21.66 t (standard deviation 37.45 t). **Table 6** lists the quality-prescription quantities (46 different quality prescriptions) and their calculated chemical limits for 196 orders. The deadline chosen was 31 October 2009.

Table 7: Ordered quantities groups
Tabela 7: Skupine naročenih količin

Ordered quantities groups #	Quality prescriptions within the group	Number of customer orders	Ordered quantities (tons)
1	108.15.0	2	30.192
2	108.33.0	2	121.5
3	108.70.1	1	18.944
4	127.11.5	14	83.841
5	140.11.1	3	18.038
6	193.31.0	2	18.352
7	193.52.0	4	26.374
8	193.54.0	1	53.872
9	503.14.0	8	4.019
10	503.31.1	7	97.65
11	516.17.1	1	13.616
12	523.00.0	1	46.176
13	524.11.0	1	0.918
14	615.12.0	1	30.251
15	623.32.0	2	218.093
16	625.13.1	2	105.08
17	635.36.5	1	23.088
18	636.11.1	3	515.41
19	705.13.3	2	54.6
20	711.00.1, 711.14.0	3	42.202
21	718.70.2	3	55.388
22	724.24.0	2	38.438
23	732.01.0, 732.03.0, 732.12.5, 732.13.5, 732.18.1, 732.19.1, 732.20.2, 732.21.2, 732.24.4, 732.26.2, 732.27.3, 732.54.2, 732.59.2, 732.62.0, 732.66.0	113	1699.239
24	741.33.3	1	4.144
25	775.13.0	2	25.693
26	779.27.1	1	414.9
27	779.71.4	4	40.848
28	780.10.0, 780.13.2	3	191.25
29	781.00.1, 781.18.1	6	246.747

Table 8: Evaluation parameters of the best organisms in the generations
Tabela 8: Parametri ovrednotenja za najboljši organizem generacij

Generation #	Number of additional ordered quantities parts	Non-planned cast quantities (tons)	Customer quantities with the delivery date ahead of the deadline (tons)	Number of work orders
0	14	36.369	62.881	20
1	13	4.779	95.752	20
2	14	36.369	66.530	20
3	14	0.622	46.909	19
4	14	1.604	45.100	19
5	14	1.604	44.992	19
6	13	1.604	44.913	19
7	13	1.604	44.913	19
8	13	1.604	44.913	19
9	11	1.604	47.144	19
10	11	1.604	47.144	19
11	10	1.604	47.597	19
12	10	1.604	47.597	19
13	10	1.604	47.597	19
14	10	1.604	47.538	19
15	10	1.604	47.197	19
16	10	1.604	47.197	19
17	10	1.604	47.138	19
18	9	10.517	38.294	19
19	9	10.517	38.694	19
20	9	10.517	37.406	19
21	9	10.517	37.406	19
22	9	10.517	37.406	19
23	9	10.517	37.406	19
24	9	10.517	37.258	19
25	9	10.517	37.258	19
26	9	10.517	37.258	19
27	9	10.517	37.230	19
28	9	10.517	37.230	19
29	9	10.517	37.230	19
30	9	10.517	37.230	19

From the quality-prescription list (**Table 6**), 29 ordered quantities groups can be formed (**Table 7**) on the basis of the instructions defined in section Formation and evaluation of work orders.

In order to make the presentation more clear, let us take a closer look at the batch-filling scheduling of the largest group – group 23. Group 23 presents, in general, the 50CrV4 (W. NR. 1.8159) spring steel. But we must state again that it is not possible to chemically combine all of the quality prescriptions. For instance, we cannot cast, within one batch, the order with the quality prescription 732.66.0 together with 732.12.5 or 732.13.5, or the quality prescription 732.18.1 with 732.59.2 or 732.54.2 (**Table 6**). In group 23 there are 113 customer orders with the total amount of 1699.239 t, an average ordered quantity of 15.0375 t, and with 52 orders within the deadline.

The particle-swarm algorithm scheduled group 23 with the following results:

- number of additional ordered quantity parts: 9
- non-planned cast quantities: 10.517 t
- customer quantities with the delivery date ahead of the deadline: 37.230 t
- number of work orders: 19.

Table 8 shows all the evaluation parameters of the best organisms (the best work-order schedule) in the generations.

The best batch-filling schedule was obtained in the 27th generation (generation 0 is a randomly generated generation). For a clearer understanding only the first five successive work orders of the best work-order schedule are presented in the following tables (**Tables 9** to **13**).

Table 9: First work order (out of 19) from the best batch-filling schedule
Tabela 9: Prvi delovni nalog (izmed 19) iz najboljšega zaporedja delovnih nalogov

Work order number: 0001020			
Cover quality prescription code	Chemical limitations		
732.54.2	/		
Quality prescription code	Customer order code	Ordered quantity (tons)	Delivery date
732.54.2	901000085507	53	30.10.2009

Table 10: Second work order (out of 19) from the best batch-filling schedule
Tabela 10: Drugi delovni nalog (izmed 19) iz najboljšega zaporedja delovnih nalogov

Work order number: 0001021			
Cover quality prescription code	Chemical limitations		
732.54.2	wt% C 0.51-0.54! wt% Cr 1.05-1.2! wt% Al 0.015-0.025!		
Quality prescription code	Customer order code	Ordered quantity (tons)	Delivery date
732.20.2	901000086002	3.148	9.11.2009
732.01.0	901000087902	5.765	8.11.2009
732.54.2	901000085507	44.087	30.10.2009

Table 11: Third work order (out of 19) from the best batch-filling schedule
Tabela 11: Tretji delovni nalog (izmed 19) iz najboljšega zaporedja delovnih nalogov

Work order number: 0001022			
Cover quality prescription code	Chemical limitations		
732.59.2	wt% Al 0.015-0.04! wt% N MAX 0.012!		
Quality prescription code	Customer order code	Ordered quantity (tons)	Delivery date
732.01.0	901000093717	16.639 t	31.10.2009
732.20.2	901000087401	5.535 t	31.10.2009
732.01.0	901000093711	5.698 t	31.10.2009
732.01.0	901000093712	11.1 t	31.10.2009
732.20.2	901000086001	5.594 t	31.10.2009
732.62.0	901000094102	6.83 t	31.10.2009
732.59.2	901000084801	1.604 t	2.11.2009

It is possible to notice that the customer order 901000085507 is included in work orders 0001020 (**Table 9**) and 0001020 (**Table 10**) – so the order is processed within two batches and thus has an additional part. The best solution is obtained, as mentioned before, when the ordered quantity is cast within one batch.

Note: we can see that the optimal batch weight (53 t) of work order 0001023 is not achieved – the non-planned cast quantity is 0.105 t, which is practically insignificant. Such a quantity is usually added to one or more ordered quantities (within 5 % of the ordered quantity).

Tabela 12: Četrti delovni nalog (izmed 19) iz najboljšega zaporedja delovnih nalogov

Table 12: Fourth work order (out of 19) from the best work-order schedule

Work order number: 0001023			
Cover quality prescription code	Chemical limitations		
732.59.2	wt% C 0.51-0.54! wt% P MAX 0.015! wt% Al 0.01-0.025! wt% Sn MAX 0.02! wt% As MAX 0.04!		
Quality prescription code	Customer order code	Ordered quantity (tons)	Delivery date
732.01.0	901000093718	5.683 t	31.10.2009
732.54.2	901000090501	31.909 t	30.10.2009
732.03.0	901000090401	9.709 t	31.10.2009
732.59.2	901000093101	5.594 t	31.10.2009
732.59.2	Non-planned cast quantity	0.105 t	

Table 13: Fifth work order (out of 19) from the best work-order schedule

Tabela 13: Peti delovni nalog (izmed 19) iz najboljšega zaporedja delovnih nalogov

Work order number: 0001024			
Cover quality prescription code	Chemical limitations		
732.54.2	wt% C 0.52-0.54! wt% P MAX 0.015! wt% Sn MAX 0.02! wt% As MAX 0.04!		
Quality prescription code	Customer order code	Ordered quantity (tons)	Delivery date
732.54.2	9010000873/1	45.028 t	30.10.2009
732.54.2	9010000855/21	3.337 t	30.10.2009
732.24.4	9010000883/10	4.635 t	30.10.2009

8 CONCLUSIONS

The present paper deals with improving the batch-filling scheduling by using the particle-swarm method. The scheduling problem was divided into the following subsequent steps:

- grouping of the ordered quantities according to their chemical composition,
- work-order representation and evaluation, and finally,
- particle-swarm algorithm-based search for the optimal batch-filling schedule.

The ordered quantities were divided into groups with a similar chemical composition, so that an ordered quantity fits into a group that already includes one or more ordered quantities with a similar chemical composition (similar quality prescriptions). This does not necessary mean that all the orders within a group can be chemically combined.

The batches are cast sequentially. The batch-filling schedules were presented as successive ordered quantities. For the evaluation of the work-order schedules, the number of additional ordered quantity parts, non-planned cast quantities in tons and all the customers' quantities with the delivery date ahead of the border-line delivery date were used.

For changing the schedules the permutation and the simple one-point crossover operators were used in the particle-swarm algorithm.

The batch-filling scheduling strategy has been implemented in Štore Steel Ltd as follows:

The period up to 2006: Only the expert knowledge of the batch scheduler was used. The non-planned and ordered quantities with the date ahead of the deadline presented 17.17 % of the total production in 2005.

The period after 2006: The particle-swarm algorithm-based search has been used to globally optimize the proper combination of the batches in order to reduce the non-planned and ordered cast quantities with the date ahead of the deadline, and to minimize the number of batches. The non-planned and the ordered quantities with the date ahead of the deadline presented 10.12 % of the total production in 2006 and in 2007. This was enhanced to 16.22 % in 2008, and 32.70 % in 2009. The reasons for the increase lie in the off-standard ordered quantities due to the global economic crisis, and not in the deficiency of the represented algorithm. These quantities would be, of course, much higher in the case of using the expert knowledge only.

Acknowledgment

The authors would like to thank Mr Jože Vrbovšek for sharing the intellectual territory. The project was funded by Štore Steel Ltd and the Slovenian Research Agency under the grant Programme Group P2-0379 Modelling of Materials and Processes.

9 REFERENCES

[1] J. S. Broughton, M. Mahfouf, D. A. Linkens, A Paradigm for the Scheduling of a Continuous Walking Beam Reheat Furnace Using a Modified Genetic Algorithm, Materials and Manufacturing Processes, 22 (**2007**), 607–614

[2] D. Pacciarelli, M. Pranzo, Production scheduling in a steelmaking-continuous casting plant, Computers and Chemical Engineering, 28 (**2004**), 2823–2835

[3] M. Kovačič, B. Šarler, Application of the genetic programming for increasing the soft annealing productivity in steel industry, Materials and Manufacturing Processes, 24 (**2009**) 3, 369–374

[4] B. Verlinden, J. Driver, I. Samajdar, R. D. Doherty, Thermo-mechanical Processing of Metallic Materials, 2007, Elsevier, Amsterdam

[5] C. Gheorghies, I. Crudu, C. Teletin, C. Spanu, Theoretical Model of Steel Continuous Casting Technology, Journal of Iron and Steel Research, International, 16 (**2009**) 1, 12–16

[6] M. Janik, H. Dyja, Modelling of three-dimensional temperature field inside the mould during continuous casting of steel, Journal of Materials Processing Technology, 157–158 (**2004**), 177–182

[7] B. G. Thomas, F. M. Najjar, Finite element modelling of turbulent fluid flow and heat transfer in continuous casting, Applied Mathematical Modelling, 15 (**1991**) 5, 226–243

[8] L. Wen-hong, X. Zhi, J. Zhen-ping, W. Biao, L. Zhao-yi, J. Guanglin, Dynamic Water Modeling and Application of Billet Continuous Casting, Journal of Iron and Steel Research, International, 15 (**2008**) 2, 14–17

[9] T. Kolenko, A. Jaklič, J. Lamut, Development of a mathematical model for continuous casting of steel slabs and billets, Mathematical and Computer Modelling of Dynamical Systems: Methods, Tools and Applications in Engineering and Related Sciences, 13 (**2007**) 1, 1744–5051

[10] C. A. Mendez, J. Cerda, I. E. Grossmann, I. Harjunkoski, M. Fahl, State-of-the-art review of optimization methods for short-term scheduling of batch processes, Computers and Chemical Engineering, 30 (**2006**), 913–946

[11] M. Azizoglu, S. Webster, Scheduling a batch processing machine with incompatible job families, Computers & Industrial Engineering, 39 (**2001**) 3, 325–335

[12] L. Tanga, J. Guanb, G. Huc, Steelmaking and refining coordinated scheduling problem with waiting time and transportation consideration, Computers & Industrial Engineering, 58 (**2010**) 2, 239–248

[13] K. Deb, A. R. Reddy, G. Singh, Optimal Scheduling of Casting Sequence Using Genetic Algorithms, Materials and Manufacturing Processes, 18 (**2009**) 3, 409–432

[14] A. Ronga, R. Lahdelmab, Fuzzy chance constrained linear programming model for optimizing the scrap charge in steel production, European Journal of Operational Research, 186 (**2008**) 3, 953–964

[15] L. Zhigang, G. Xingsheng, J. Bin, A novel particle swarm optimization algorithm for permutation flow-shop scheduling to minimize makespan, Chaos, Solitons and Fractals, 35 (**2008**) 5, 851–861

UDK 620.178.1:621.941
Original scientific article/Izvirni znanstveni članek

ISSN 1580-2949
MTAEC9, 46(3)279(2012)

THE INFLUENCE OF TOOL WEAR ON THE CHIP-FORMING MECHANISM AND TOOL VIBRATIONS

VPLIV OBRABE ORODJA NA MEHANIZEM NASTANKA ODREZKA IN VIBRACIJE ORODJA

Aco Antić[1], Petar B. Petrović[2], Milan Zeljković[1], Borut Kosec[3], Janko Hodolič[1]

[1]University of Novi Sad, Faculty of Technical Sciences, Trg D. Obradovića 6, 21000 Novi Sad, Serbia
[2]University of Belgrade, Faculty Engineering, Kraljice Marije 16, 11000 Belgrade, Serbia
[3]University of Ljubljana, Faculty of Natural Sciences and Engineering, Aškerčeva c. 12, 1000 Ljubljana, Slovenia
antica@uns.ac.rs

Prejem rokopisa – received: 2011-11-03; sprejem za objavo – accepted for publication: 2011-12-07

In this paper we review an experimental investigation of the influence of tool wear on the chip-forming mechanism and the type of segmentation while turning. A direct microscopic analysis of the chip was used to determine the correlation between the tool-wear degree and the morphology of the chip cross-section. During the machining process the vibrations on the tool carrier were measured in the vicinity of the cutting zone. An analysis of the generated chip and vibration signals during the machining confirmed the hypothesis that changes in the tool-wear degree directly impacts on the chip form and the type of segmentation. This investigation contributes to a better understanding of the chip-forming mechanism and the type of segmentation, allowing us to collect high-quality input information that could be used for the subsequent development of a system for tool-wear identification.

Keywords: tool wear, chip-forming mechanism, turning, tool vibrations

Prispevek prikazuje način eksperimentalnega določanja stopnje obrabe orodja na mehanizem nastanka in tip segmentacije odrezka pri struženju. Na podlagi neposredne mikroskopske analize odrezka je določena korelacija med stopnjo obrabljenosti orodja in morfologijo prečnega prereza odrezka. Med procesom obdelave so bile merjene vibracije nosilca orodja v neposredni bližini cone rezanja. Analizi eksperimentalnih rezultatov pri nastanku odrezka in signalov vibracij, izmerjenih v procesu obdelave, potrjujeta hipotezo, da sprememba stopnje obrabe orodja neposredno vpliva na obliko in tip segmentacije odrezka. Raziskava, opisana v tem delu, je prispevek k boljšemu razumevanju mehanizma in tipa segmentacije odrezka za kvalitetnejše definiranje vhodnih informacij za razvoj sistema za klasifikacijo stopnje obrabljenosti orodja.

Ključne besede: obraba orodja, mehanizem nastanka odrezka, struženje, vibracije orodja

1 INTRODUCTION

The timely detection and replacement of worn tools is one of the key research areas in the domain of optimizing cost-effectiveness and productivity in modern, automated manufacturing. It is estimated that an accurate and reliable system for tool-wear monitoring and identification can contribute to an increase of the cutting speed by 1–50 %. The reduction of manufacturing downtime by timely tool replacement contributes to a reduction of the total manufacturing costs by 10 % to 40 %[1]. Investigations related to an increase of the reliability and performance of systems for tool-wear monitoring are directed towards an experimental determination of the chip-forming mechanism and its influence on the machine-tool–tool–workpiece system, as well as a FEM simulation of the cutting process.[2–4] The chip-forming mechanism and the chip morphology are characteristics that provide key information about the machining process and the quality of the machined surface. The chip-forming mechanism and the type of chip segmentation exert a primary influence on both the tool life and the quality of the machined surface.[5,6] A proper identification and understanding of the chip-forming mechanism can help us to detect tool wear in the machining of harder materials and special steels.[7,8] The chip-forming mechanism, as well as its form and flow over the tool rake surface, significantly impact the tool wear and machined-surface quality. Recent investigations emphasize the importance of a parametric analysis of the mutual influence between the tool-wear degree and the chip-forming mechanism.[9,10]

The analysis of tool-wear parameters established that the most important are as follows: the crater wear on the rake face, the flank wear, and the cutting-edge wear. The chip formed in conditions of intensified cutting speeds causes increased pressure and friction on the tool rake surface, while within the tool/chip interface it directly promotes tool wear, i.e., crater wear. Dutta[11] investigated the influence of the cutting parameters on the various types of composites used in tool materials, and how they affect the quality of the machined surface and the tool-wear mechanism during machining. Among other parameters, he analyzed the macroscopic and microscopic chip structure formed under the influence of various machining regimes. The results were presented in a diagram of cutting-force components and cutting-speed dependence, tool-wear degree, and their influence on the quality of the machined surface and the tool life. Ozcatalbas[12] analyzed the macroscopic and microscopic

chip form depending on the cutting regime, also taking into consideration the tool-wear degree, as a secondary parameter. He analyzed the influence of cutting speed on the chip-cutting ratio, as well as the change of the tool-wedge geometry due to the cutting-edge build-up.

Based on "type and form" criteria, the chip is most often classified as continuous, segmented, or lamellar. **Figure 1** shows a typical image of a continuous chip, which exhibits no changes in the cross-sectional structure, with a flat upper side and no distinctive segments.

The generation of a segmented chip during machining causes impulse forces, which, in turn, generate tool vibrations. Investigations related to the registration of dynamic parameters of lamellae forming during machining encompass the acquisition and processing of various sensor signals. Antić[13] used power spectral density (PSD) sensors and a dynamometer to monitor the various dynamic parameters during machining. The obtained results were used as prerequisites for the development of an artificial neural network (ANN) for tool-wear monitoring. The development of the system for real-time signal acquisition and processing allowed the application of direct methods and techniques based on high-res, high-speed cameras in order to determine the chip parameters during machining.[14]

The simultaneous effect of high temperatures and shear stresses on the tool-rake surface cause thermal softening within the cutting zone and the generation of a segmented chip. During machining, the chip lamellae slip along a narrow zone of thermal softening, generating pronounced chip segments. The generated chip features excessive roughness on the free surface, which indicates the presence of adiabatic shear during chip generation. Pronounced chip segments most often appear during the high-speed machining of hard materials. **Figure 2** shows a segmented chip with pronounced lamellae tips on the free surface.

Beri and Gerald[15] considered the chip-forming mechanisms in the machining of tempering steels, concluding that a saw-tooth chip is generated due to thermal softening and adiabatic shear in the narrow zone.

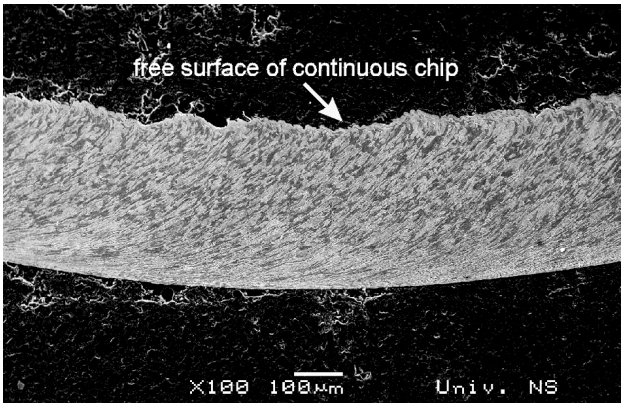

Figure 1: Continuous chip
Slika 1: Kontinuirani ostružek

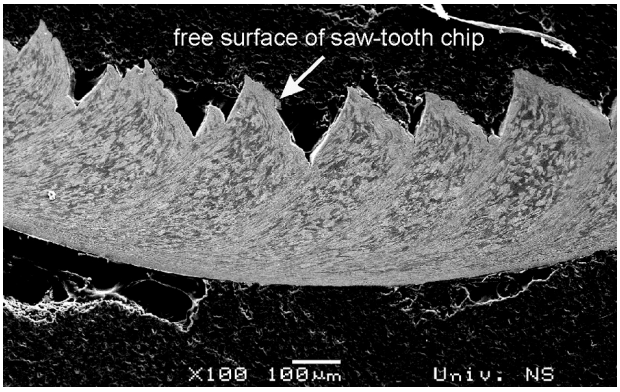

Figure 2: Segmented chip
Slika 2: Segmentiran ostružek

The goal of this investigation was to determine the dependence between the type of generated chip and the tool-wear degree during turning. Direct microscopic measurements were performed to analyze the chip cross-section. In addition, during the experiment, characteristic chip parameters were analyzed to establish a correlation with the tool wear, i.e., tool-wedge degradation.

Reviewed in the introductory section of this paper are the investigations focused on the relationship between the tool-wear degree and the chip-forming mechanism. The experiment was setup based on an analysis of previous investigations. The remaining sections review the experimental results obtained for the correlation between the tool-wear degree and the chip-forming mechanism. The final part presents some conclusions and recommendations for future investigations aimed at a better understanding of the chip-formation mechanism and the creation of requisites for the development of an intelligent system for tool-wear monitoring.

2 EXPERIMENTAL SETUP

Machining experiments were performed on a CNC GU 600 lathe manufactured by INDEX and installed in the laboratory of the Faculty of Technical Sciences in Novi Sad. The investigation of the tool-wear process encompassed the monitoring of the dominant wear mechanism through the following parameters: wear band, crater wear and tool life. In the course of the turning process, the vibration signal and the cutting force were registered at the tool shank. For each tool pass the generated chip segments were sampled. The setup of the tool sensors, as well as the dimension of workpiece used in this experiment, is shown in **Figure 3**. During the experiment two cutting speeds were employed, 180 m/min to 250 m/min, in conjunction with 0.15 mm and 0.3 mm feed rates. The cross-section of the tool shank used in the experiment was 20 mm × 20 mm. The machining was performed with P25 tool inserts designated TNMM 110408. The vibration and force signals were sampled at 625 kHz, with A/D converter

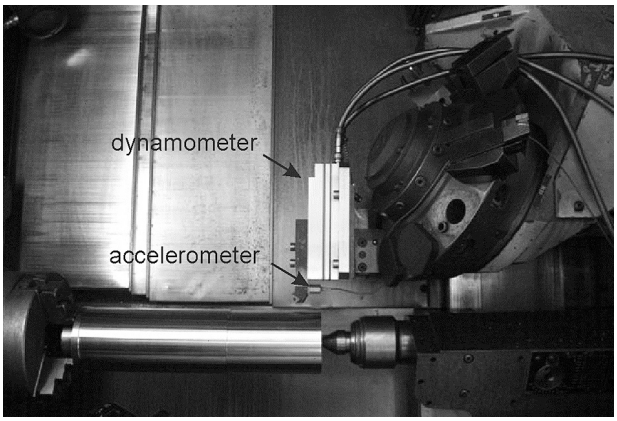

Figure 3: Experimental setup
Slika 3: Postavitev eksperimentalnega mesta

NI625 USB "National Instruments". The workpiece material, 42CrMo4, was of guaranteed mechanical and chemical properties, with a 290 HB hardness.

3 EXPERIMENTAL RESULTS

The experimental results were obtained through a combination of direct measurements of the chip characteristic dimensions on an electronic microscope, and indirect sensor measurements of the forces and vibrations. Variations in the tool-wear degree were monitored through a measurement of the wear band width (VB), which defines the tool flank wear. This measurement was performed periodically on a tool microscope. The results of the VB measurements are shown in **Figure 4** for different cutting speeds during the experiment.

The progression of the tool wear directly impacted the chip-forming mechanism and its form. The results of a direct microscopic analysis provided an insight into the relationship between the lamellae form and the geometric characteristics of the generated chip and

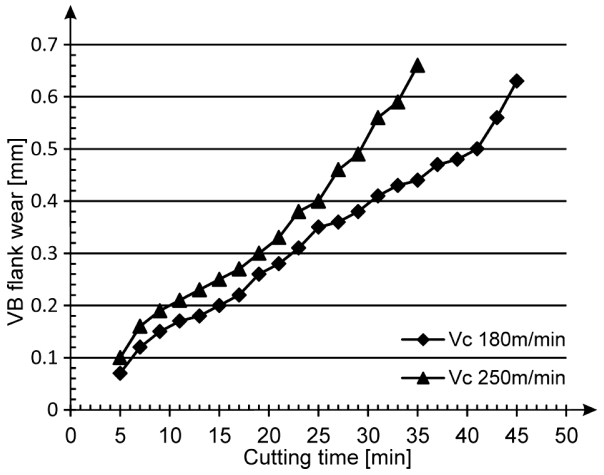

Figure 4: Change of flank wear in time
Slika 4: Potek obrabe proste ploskve

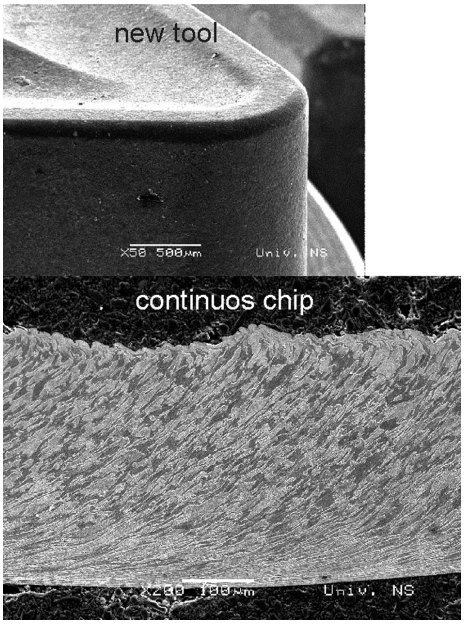

Figure 5: Continuous chip generated by a new tool insert
Slika 5: Kontinuirani ostružek, oblikovan z novim orodjem

tool-wear degree. In most of the cases a saw-tooth chip is a consequence of the adiabatic shear of the lamellae, which is visible from the cross-section of the generated chip.

3.1 Forming of a continuous chip

A continuous chip form is generated through material shear in the primary cutting zone without clearly observable segment borders in the cross-section, and without distinctive segment tips on the free chip surface. The height of the segments on the free-chip surface is very small and corresponds to the width of a single segment. The upper chip zone, closer to the free surface, is mildly wrinkled with only a slight indication of incipient lamellae, as shown in **Figure 5** (right).

Investigations have shown that that the chip form is largely influenced by changes in the tool-wedge geometry, which progresses during the machining process. **Figure 5** shows a cross-section of a continuous chip generated by a fresh tool insert. Obviously, continuous segmentation is taking place, without distinctive separation between the chip segments.

3.2 Forming of a discontinuous chip

As the wear band and the wear crater on the tool rake surface progressively grow, i.e., the cutting geometry degrades, **Figure 6**, the chip form also changes. It is evident that the formed segments were generated through a cyclical process (from the first to the last segment). After a certain machining time, due to the change in tool-wear degree, i.e., cutting geometry, the chip form begins its transformation. From the macroscopic view-

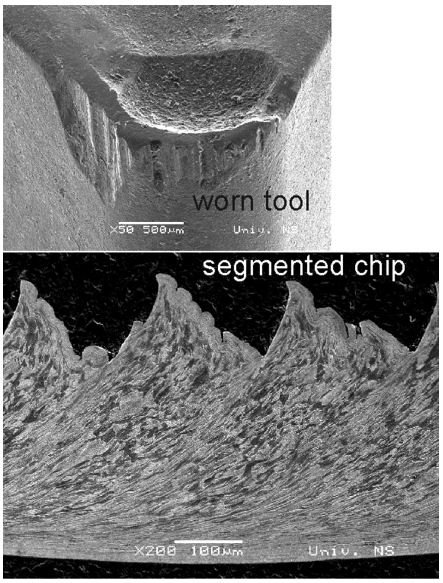

Figure 6: Saw-tooth chip generated by a worn tool
Slika 6: Nazobčana oblika ostružka, nastala pri močno obrabljenem orodju

point, the chip becomes more flat, with distinctive material slip along the basic plane. The tool side of the chip becomes wrinkled and uneven when compared to that generated by a fresh tool insert.

Grain lengthening in the material structure occurs rectilinearly within a narrow band, i.e., the primary cutting zone. It is visible on the cross-section of the generated chip, **Figure 7**. Rather than creating an initial crack and spreading the break towards the tool side of the chip through the primary cutting zone, chip segmentation occurs due to material deformation in the narrow band through thermal softening and adiabatic shear mechanisms. The absence of an initial crack and a distinctive separation of the material between segments in the upper part of the primary zone, indicates the existence of deformations and shear due to thermal softening of the basic material within a narrow zone.

With all the considered chip segments it is possible to clearly identify the change of chip-forming mechanism within the primary shear zone as well as the forming of tips on individual chip segments on the free end. The change of the chip form reflects on the vibration signal, the machined surface quality, and, consequently, the total cost of the machining energy.

4 FREQUENCY OF CHIP SEGMENTATION AND TOOL VIBRATION

Cutting-tool vibrations during machining occur due to friction on the rake and flank tool surfaces, chip segmentation, roughness of the machined surface, etc. The hypothesis of this investigation is that in the high-frequency spectrum there are warping and masking of the information content that is of interest to us. However, there are methods which allow us to extract the information content that can be used to unambiguously detect the current wear degree of the tool cutting edge.

The frequencies at which the forming of the chip lamellae occur can be calculated based on: lamellae pitch, p_c, depth of cut (thickness of undeformed chip segment), h, height of deformed chip segment, h_{ch} and cutting speed, v_c, by applying the following expression:

$$f_{lam} = \frac{v_{ch} \cdot h_{ch}}{h \cdot p_c} = \frac{v_{ch}}{\lambda \cdot p_c} \quad (1)$$

The analysis of the geometric features of the chip cross-section encompassed the following parameters: height of formed segment (tooth), distance between segments (teeth), i.e., segmentation pitch, length of undeformed tooth area, $L_{undeformed}$, length of machined tooth area, $L_{machined}$, and share angle, Φ_{seg}. A typical image of the segmented chip form with characteristic features is shown in **Figure 8**.

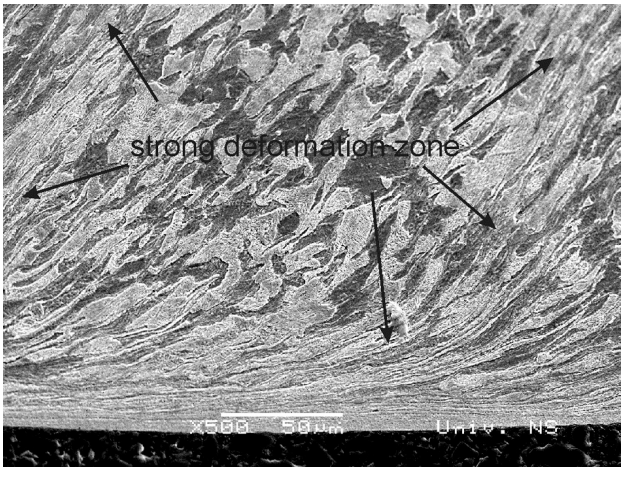

Figure 7: Coalescence of zones with intensive shear on the tool side of the chip
Slika 7: Spajanje con intenzivne deformacije (striga) na hrbtni strani ostružka

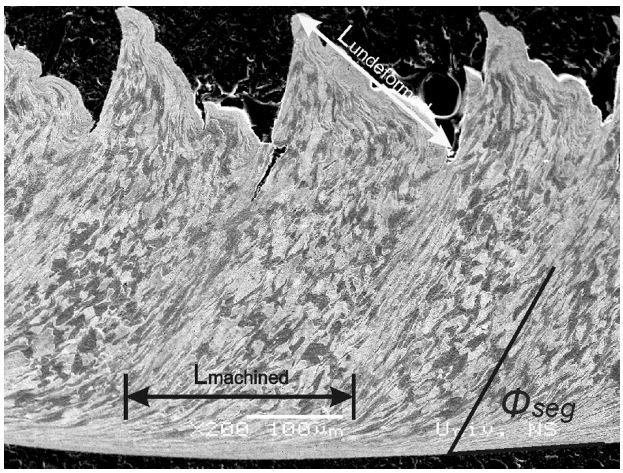

Figure 8: Geometric parameters of the chip segmentation
Slika 8: Geometrijski parametri segmentiranja ostružka

Geometric relationship between the length of the undeformed area and the length of the machined area of a single tooth is given by[16]:

$$r = \frac{L_{\text{undeformed}}}{L_{\text{machined}}} \quad (2)$$

In the case of an ideally continuous chip, this geometric relationship is $r = 1$ due to the lengths of the undeformed and machined areas being equal. In the case when $r < 1$, the newly formed segment is pushed forward along the slip plane, which causes the formation of wrinkling on the chip-free surface, while the machined segment area is elongated on the tool rake surface due to the friction coefficient. If $r > 1$, the newly formed segment is pushed forward along the slip plane towards the free surface and relieved of stresses resulting from the tool tip pressure, which results in a shorter tool-side chip area due to the lower pressure and the friction of the segment along the tool rake surface. The increase of cutting speed leads to a gradual decrease of the continuous shear and the chip becomes segmented in a periodical manner, showing very pronounced shear zones due to higher temperatures. In the shear zone, the material deformation is pronounced, while being much lower in the very segment, which can be seen in **Figure 9**. The degree of chip deformation during the cutting process can be calculated from $\varepsilon = (h_1 - h_2)/h_2$[17].

This degree of chip deformation was calculated for the five contiguous chip segments and the mean value was used as a relevant parameter. Shown in **Figure 9** are the parameters that were measured and used to calculate the degree of chip deformation.

Based on the measured parameters shown in **Figure 9**, and the calculated degrees of chip segmentation, a diagram was made that shows the correlation between tool-wear degree and chip-segmentation degree, shown in **Figure 10**.

The measurements showed that during the initial phase (fresh tool insert), for all cutting regimes, a continuous chip is generated. Once a particular tool-wear

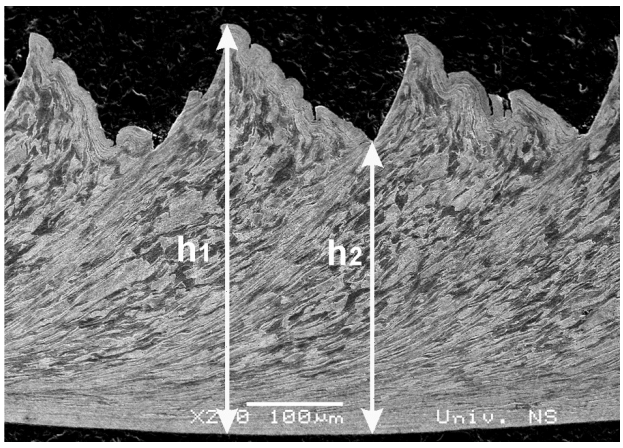

Figure 9: Parameters for calculation of the chip-deformation degree
Slika 9: Parametri za določanje stopnje deformacije ostružka

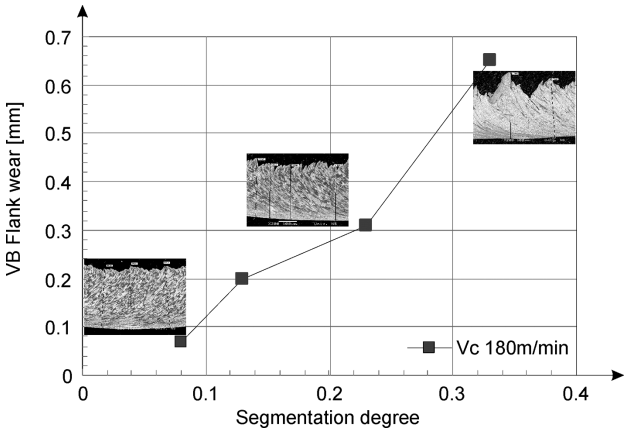

Figure 10: Correlation between chip-segmentation degree and tool wear
Slika 10: Korelacija med stopnjo segmentiranja ostružka in obrabo orodja

degree is reached, the chip changes its forming mechanism, which results in a saw-tooth chip form. This change in cross-section geometry and form is gradual and without abrupt transitions from one form to another. Certain variations in the chip-deformation degree, observed during the experiment, can be attributed to build-ups on the cutting edge, i.e., the change of cutting geometry during the cutting process.

One of the key parameters that define the character of vibrations during machining is the frequency of lamellae generation. **Figure 11** illustrates the change of frequency of chip-lamellae generation due to the variable depth of the flank wear. The frequency of chip-lamellae generation linearly decreases with the increase of flank wear depth, and increases with the progression of the depth of cut. A larger depth of cut reduces the frequency of lamellae-chip generation. Such a wide range of frequencies is the cause of large variations in the cutting force on the tool cutting edge.

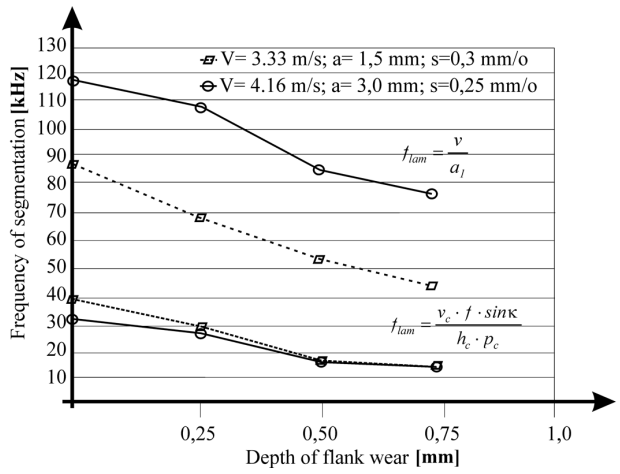

Figure 11: Dependence of the frequency of chip-lamellae generation on the tool-wear degree
Slika 11: Odvisnost frekvence nastanka lamel ostružka od stopnje obrabljenosti orodja

5 CHARACTER OF VIBRATIONS DURING THE CHIP-FORMING PROCESS

The forming of single-chip segments during the generation of a discontinuous chip results in an increased energy release and higher vibration amplitudes in comparison with a continuous chip. In addition, the consequence of discontinuous chip forming is a higher deformation energy, adiabatic shear, a varied vibration response, and the occurrence of self-excited vibrations. Tool self-excited vibrations are within the 1–50 kHz range, thus some resonance can be attributed to chip segmentation. The forming of a segmented chip can be viewed as a process of the discrete excitation of the machining system by a series of impulses whose frequency can be determined within an acceptable error margin. The vibrations occurring during machining can be detected through the response of a machining system, especially on the tool shank. An analysis of the experimental results revealed that the frequency response of the machining system varies according to the type of generated chip. The monitoring of signal, i.e., the frequency of the chip-segment forming, revealed changes in the high-frequency part of the spectrum. This was visible as an amplification of the generated signal, as shown in **Figure 12**. The frequency of lamellae generation is destabilized by the primary shear zone and the chip-forming mechanism. As already mentioned, the frequency of lamellae generation is usually higher than 10 kHz, which is beyond the measuring range of conventional accelerometers. A more pronounced peak occurrence in the analyzed vibrations spectrum was spotted at higher frequencies, closer to those characteristic of lamellae formation. The difference in signal intensities is related to a release of higher energy during the forming of a discontinued chip, as well as higher friction at the chip/tool interface. **Figure 12** illustrates the described occurrences, speaking in favour of the assumption that the vibration range above 1 kHz contains a signal that can be used for tool-wear identification. The spectrum of vibrations measured on the tool shank close to the cutting zone is a good indicator of the change in chip-forming mechanism and chip type, caused by tool-wear progression, i.e., cutting-edge degradation.

Figure 13 illustrates the spectra of signal (in [dB]) for various tool-wear degrees, with the following parameters: window = 2048; overlap = 512; pwelch (data_N (:,1), window, overlap,[], Fs). The frequency spectrum was limited to 50 kHz. The equipment used in this experiment allows measurements in a wider frequency spectrum (up to 100 kHz), but the limiting factor was the accelerator.

Besides cutting regimes, and the state and characteristics of the workpiece material, it is the tool-wear degree that also exerts a great influence on the type of chip generated during machining. The progression of the tool wear leads to a change of the chip type and form, regardless of constant machining parameters: speed, feed rate, depth of cut, and material characteristics. Changes in the chip type are caused by a variable cutting geometry, which is a function of the tool-wear degree. Changes in the cutting geometry and chip type directly influence the considered parameters within the analysed high-frequency part of the vibration spectrum.

6 CONCLUSIONS

A chip generated during the initial stage of machining (fresh tool insert) is flat-shaped with s smooth tool side, which is in full contact with tool rake surface, while the chip-free surface exhibits no segment teeth. Through widening of wear band and tool crater wear, the chip changes form and becomes rougher, wrinkled and

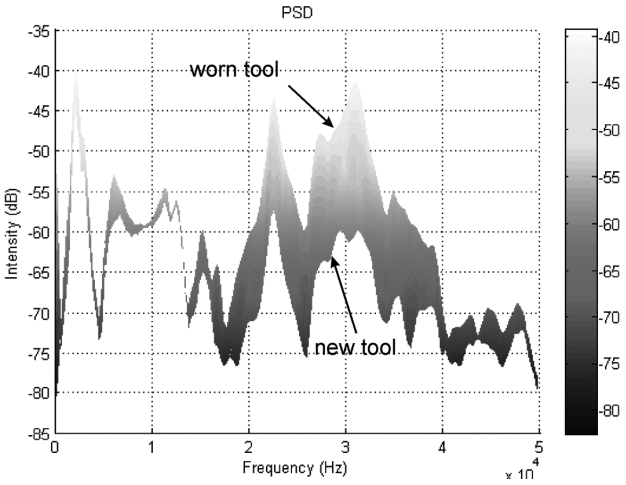

Figure 12: Energy distributions along the frequency axis for new and worn tools

Slika 12: Porazdelitev energije signala po frekvenčni osi za novo in obrabljeno orodje

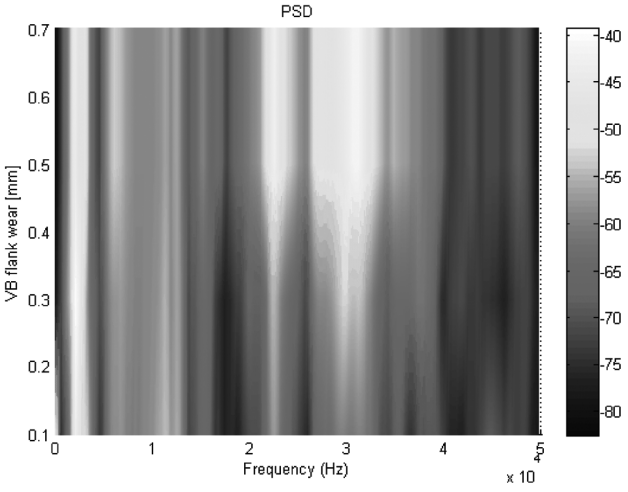

Figure 13: Variations in the vibration signal spectrum along the frequency axis, depending on tool-wear degree

Slika 13: Sprememba spektra signala vibracij po frekvenčni osi v odvisnosti od stopnje obrabljenosti orodja

chipped at the ends, while the type of chip segmentation changes into discontinuous with highly pronounced teeth on the free-chip surface. A further increase of the flank wear leads to an intensification of the chip segmentation, while the frequency of lamellae generation decreases. Plastic deformation of the material in the primary cutting zone becomes more pronounced with a distinctive border between the formed segments. The cross-section of the generated chip exhibits very pronounced wrinkles on the free side in the various zones of material deformation during machining. This indicates the combined action of stress strengthening and thermal softening, i.e., the existence of a dual action in the chip formation. The zone of thermo-plastic instability has a dominant role up until the emergence of the shear zone and the forming of chip segments, when the cutting process conforms to adiabatic shear theory. The vibration response is variable, with pronounced peaks at frequencies that correspond to the frequency of lamellae generation. The change in the chip type causes the emergence of new frequency components (harmonics), which are close to the frequency of lamellae generation, with the periodic occurrence of self-excited vibrations in the interval near the tool's end-of-life.

Acknowledgements

This paper presents a segment of the research on the project "Contemporary approaches in the development of special solutions bearing in mechanical engineering and medical prosthetics", project number TR 35025, financed by the Ministry of Education and Science of the Republic of Serbia, and research over our of mobility and scholarships in the scope of the network CEEPUS III RO 0202. University of Novi Sad, Faculty of Technical Sciences.

7 REFERENCES

[1] A. G. Rehorn, J. Jiang, P. E. Orban, International Journal of Advance Manufacturing Technology, 26 (**2005**), 693–710
[2] R. Čep, A. Janásek, B. Martinický, M. Sadílek, Technical Gazette, 18 (**2011**) 2, 203–209
[3] D. Kovačević, M. Soković, I. Budak, A. Antić, B. Kosec, Metallurgy, 51 (**2012**) 1, 113–116
[4] B. Tadić, D. Vukelić, J. Hodolič, S. Mitrović, M. Erić, Journal of Mechanical Engineering, 57 (**2011**) 5, 425–439
[5] G. Šimunović, T. Šarić, R. Lujić, Technical Gazette, 16 (**2009**) 2, 43–47
[6] J. Tepić, V. Todić, D. Lukić, M. Milošević, S. Borojević, Metallurgy, 50 (**2011**) 4, 273–277
[7] F. Cajner, D. Landek, V. Leskovšek, Mater. Tehnol., 44 (**2010**) 1, 85–91
[8] B. Mateša, D. Kozak, A. Stojić, I. Samardžić, Metallurgy, 50 (**2011**) 4, 227–230
[9] M. D. Morehead, Y. Huang, J. Luo, Machining Science and Technology, 11 (**2007**), 335–354
[10] A. Antić, D. Kovačević, M. Zeljković, B. Kosec, J. Novak-Marcinčin, RMZ – Materials and Geoenvironment, 58 (**2011**) 1, 15–28
[11] A. K. Dutta, A. B. Chattopadhyaya, K. K. Rayc, Wear, 261 (**2006**), 885–895
[12] Y. Ozcatalbas, Materials and Design, 24 (**2003**), 215–221
[13] A. Antić, J. Hodolič, M. Soković, Journal of Mechanical Engineering, 52 (**2006**) 11, 763–77
[14] M. Cotterell, G. Byrne, CIRP Annals – Manufacturing Technology, 57 (**2008**), 93–96
[15] J. Barry, B. Gerald, Transactions of the ASME, Journal of Manufacturing Science and Engineering, 124 (**2002**) 3, 528–535
[16] S. Sun, M. Brandt, M. S. Dargusch, Metallurgical and Materials Transactions A, 41 (**2010**) 6, 1573–1581
[17] G. Su, Z. Liu, International Journal of Advanced Manufacturing Technology, 51 (**2010**), 87–92

UDK 669.186
Professional article/Strokovni članek

ISSN 1580-2949
MTAEC9, 46(3)287(2012)

EVOLUTION OF THE NUMBER AND SIZE OF THE INCLUSIONS DURING STEEL TREATMENT IN A LADLE FURNACE AND IN A VACUUM CAISSON

ŠTEVILO IN VELIKOST VKLJUČKOV, NASTALIH PRI OBDELAVI JEKLA V PONOVČNI PEČI IN VAKUUMSKI KOMORI

Zdeněk Adolf[1], Jakub Jurča[2]

[1]VŠB-Technical University of Ostrava, Department of Metallurgy, 17. listopadu 15/2172, 708 33 Ostrava-Poruba, Czech Republic
[2]Evraz Vítkovice Steel, a. s., Štramberská č. p. 2871/47, 70900 Ostrava-Hulváky, Czech Republic
zdenek.adolf@vsb.cz

Prejem rokopisa – received: 2011-06-06; sprejem za objavo – accepted for publication: 2012-02-14

The production of higher steel grades, such as steel for pipelines, requires monitoring the content of inclusions in the steel. Hence, the steelmakers have to choose suitable technological procedures that ensure the highest purity of the steel. Purpose of this work was to observe the evolution of the inclusions in the steel during its refining in a ladle furnace and in a vacuum caisson. For this purpose the samples of steel were taken at various stages of the processing. In one half of the melts the steel was deoxidised by CaSi-cored wire in a ladle furnace so that it would be possible to observe the influence of the CaSi on the occurrence of inclusions after degassing in the caisson. All the heats were processed in the following technological flow: OBM converter – ladle furnace – vacuum caisson (ISSM) – continuous casting.

Keywords: steel, inclusions, calcium modification

Proizvodnja kakovostnejših jekel, kot so jekla za cevovode, zahteva tudi kontrolo vsebnosti vključkov. Zato se pri izdelavi jekla izberejo ustrezni tehnološki postopki, ki zagotavljajo visoko čistost jekla. Namen tega dela je bil ovrednotenje nastanka vključkov v jeklu med rafinacijo v ponovčni peči in vakuumski komori. V ta namen so bili vzeti vzorci v različnih fazah procesa. Polovica taline je bila dezoksidirana z oplaščeno žico CaSi v ponovčni peči z namenom raziskave vpliva CaSi na nastanek vključkov po razplinjenju v komori. Vse taline so bile izdelane po naslednjih tehnoloških postopkih: OBM konverter-ponovčna peč-vakuumska komora (ISSM)-kontinuirno litje.

Ključne besede: jeklo, vključki, modifikacija s Ca

1 INTRODUCTION

Inclusions normally deteriorate the mechanical properties of steel. For example, the results reported in[1] proved that spherical inclusions are more suitable than sharp-edged inclusions. The liquefaction of inclusions during steelmaking causes their easier rise from the liquid steel. In steels deoxidised by aluminium, Al_2O_3 inclusions are formed predominantly. These inclusions are, within the interval of the steelmaking temperatures, solid and sharp-edged. Their liquefaction is obtained by the injection of CaSi into the steel. This causes an increase in the CaO content with a subsequent drop of the liquidus temperature of the original inclusions, which may more easily rise to the melt surface and be absorbed in the slag.

2 EXPERIMENTAL

Three steel grades were chosen for the assessment of the inclusions' development, i.e., the steel marked as A

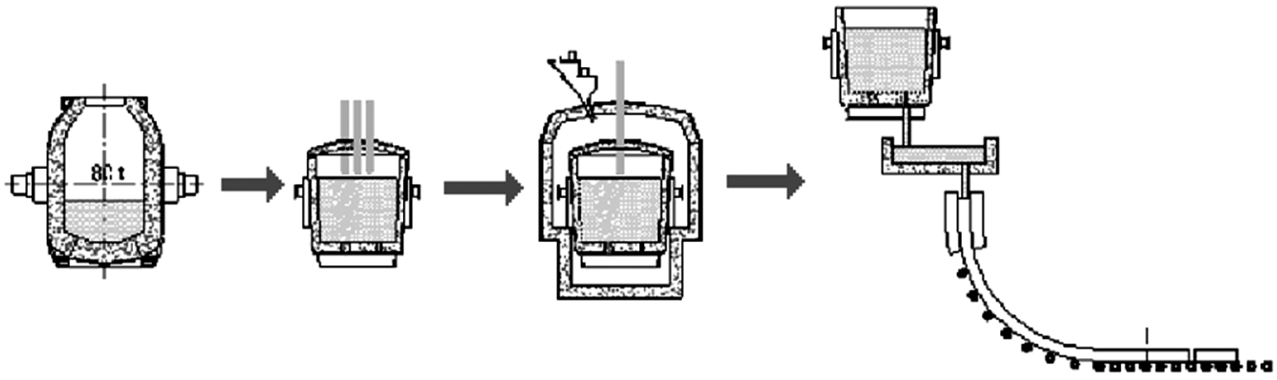

Figure 1: Steelmaking technological flow
Slika 1: Shema tehnološkega postopka izdelave jekla

Table 1: Chemical composition of the investigated steels in mass fractions, wt%
Tabela 1: Kemijska sestava preiskovanega jekla v masnih deležih, wt%

A – structural steel											
	C	Mn	Si	P	S	Cr	Al	Ti	Nb	V	N
Min.	0.10	0.3	0.20	–	–	–	0.020	–	–	–	–
Optimum	0.12	0.4	0.25	–	–	–	0.035	–	–	–	–
Max.	0.13	0.5	0.30	0.02	0.01	0.3	0.050	0.01	0.01	0.01	0.01
B – steel for ship plates											
Min.	0.150	1.40	0.3	–	–	–	0.020	–	–	–	–
Optimum	0.165	1.45	0.4	–	–	–	0.035	–	–	–	–
Max.	0.180	1.50	0.5	0.02	0.01	0.03	0.050	0.01	0.01	0.01	0.01
C – steel for pipelines											
Min.	0.08	1.35	0.20	–	–	–	0.020	0.018	0.020	0.030	–
Optimum	0.12	1.40	0.30	0.010	0.002	–	0.030	0.025	0.030	0.050	–
Max.	0.10	1.50	0.35	0.015	0.005	0.02	0.050	0.030	0.050	0.080	0.008

(structural steel), B (steel for the fabrication of ship plates), C (steel for pipelines working in an acidic environment). **Table 1** gives the chemical composition of these steels. The steel was processed in the following technological flow: basic oxygen converter OBM – ladle furnace – vacuum caisson (ISSM) – continuous casting (**Figure 1**).

For each steel the samples were taken from two heats. In the first heat Al_2O_3 inclusions were modified in the ladle furnace by CaSi and the inclusions in the second heat were not modified.

The sequence of taking the samples from heats, in which the inclusions were modified by CaSi in the ladle furnace (LF), is as follows:

1. After deoxidation of the steel by aluminium in the LF (marked after Al)
2. After injection of the cored wire with CaSi in the LF (marked after CaSi)
3. After achieving a good vacuum in the ISSM (marked in vacuum)
4. After degassing in M (marked after degassing)
5. After modification of the steel by calcium (cored wire) at the end of the heat in the ISSM (marked after Ca)

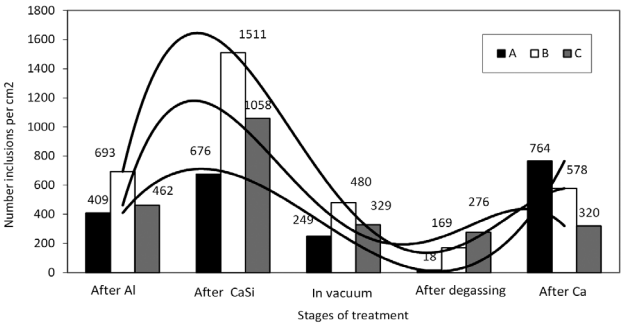

Figure 2: Number of all the inclusions in the course of the steel treatment by secondary metallurgy methods
Slika 2: Število vseh vključkov pri postopku sekundarne metalurgije izdelave jekla

Only samples 1, 3, 4 and 5 were taken from the heats, where no modification of the inclusions by CaSi was made in the ladle furnace LF. The samples were sucked into a submersible sampler and rapidly cooled in water to preserve the inclusions present in the liquid steel and to prevent the creation of inclusions during the cooling and solidification of the steel.

The objective was to assess the development of the number and size of the inclusions at individual stages of the steel treatment in the heats in which a modification by CaSi was made in comparison with the heats without this modification.

3 RESULTS AND DISCUSSION

3.1 Evaluation of the inclusions on the basis of their number and size

At first the evolution of the number of inclusions at individual stages of the steel treatment is assessed for the heats in which the inclusions were modified by CaSi in a ladle furnace. It is evident from **Figure 2** that the number of inclusions after modification by the cored wire containing CaSi increased and afterwards their number decreased considerably during degassing – regardless of the steel grade. The increase in the number of inclusions after the injection of the CaSi can be explained by the reduction of the activity of Al_2O_3 in inclusions due to their modification, which is followed by the reaction of metallic aluminium with oxygen. The vacuum treatment improves the kinetic conditions for the rise of the inclusions and the modified inclusions are quickly absorbed by the slag. The share of removed inclusions is proportional to their original number. At the end of the treatment after the degassing of the steel, altogether 95 % (grade A), 76 % (grade B) and 40 % (grade C) of the inclusions were removed, as compared to the initial number after the de-oxidation by aluminium.

After final dosing of the calcium into the degassed steel the number of inclusions increased. Due to the low oxygen content (below $5 \cdot 10^{-4}$ wt%) after degassing, the

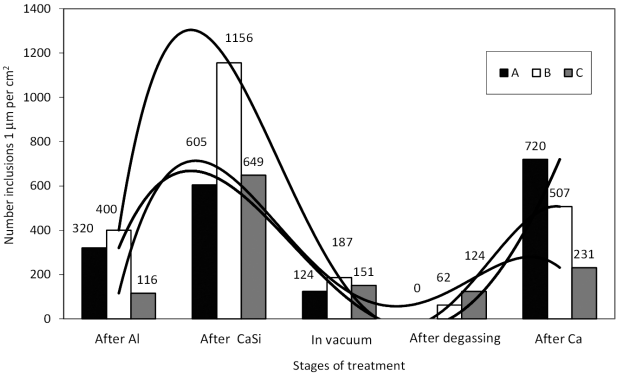

Figure 3: Number of inclusions up to the size of 1 µm for the course of the steel treatment by secondary metallurgy methods (A, B, C)

Slika 3: Število vključkov do velikosti 1 µm pri postopku sekundarne metalurgije izdelave jekla (A, B, C)

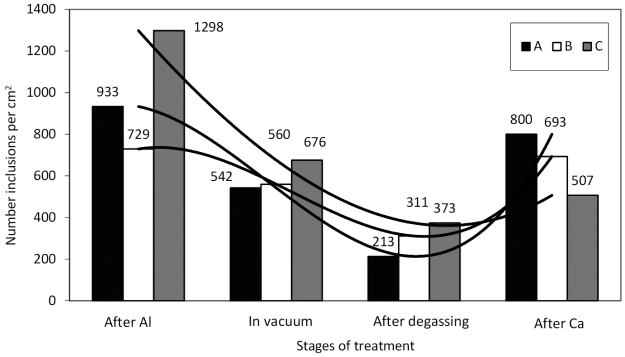

Figure 5: Number of all the inclusions in the course of steel treatment by secondary metallurgy methods without modification in the ladle furnace

Slika 5: Število vseh vključkov pri postopku sekundarne metalurgije izdelave jekla brez modifikacije v ponovčni peči

creation of new Al_2O_3 inclusions was already very limited.

A similar change in the number of inclusions during individual stages of the steel treatment was found for the smallest inclusions with a size of 1 µm (**Figure 3**).

The number of inclusions with a size from 2 µm to 5 µm did not change much after the addition of CaSi, and thus the creation of new inclusions is compensated for by their assimilation by the slag (**Figure 4**). The drop in the number of larger inclusions during degassing (in vacuum) in comparison to the smallest samples was less distinct. This indicates that larger inclusions, apart from rising from the steel, are being newly formed by the coalescence and coagulation of the smallest inclusions. A further reduction in their number occurs only after full degassing. After the dosing of the calcium cored wire the number of large inclusions does not increase, which suggests the creation of only the smallest inclusions.

A similar evolution in the number of inclusions as in **Figure 2** was also observed for the application of technological flow without modification of inclusions by CaSi in the LF (**Figure 5**). Only the total number of inclusions after degassing is higher in the case of non-modified steel. In the course of degassing the number of non-modified inclusions drops as well. After degassing, altogether 77 % (grade A), 57 % (grade B) and 71 % (grade C) of inclusions were removed, in comparison with the initial number after deoxidation by aluminium. After the final modification by calcium their number increases again, also due to the higher contents of oxygen ($7 \cdot 10^{-4}$ to $10 \cdot 10^{-4}$ wt%) in the steel, which was not modified by CaSi during the second stage.

The comparison of two technological flows from the viewpoint of the number of inclusions shows that the removal of inclusions in the course of degassing is better after modification of the steel by CaSi in the LF. Apparently, this is related to the liquefaction of the inclusions. Liquefied inclusions attain a drop shape, which reduces the melt resistance by moving the inclusions towards the surface.

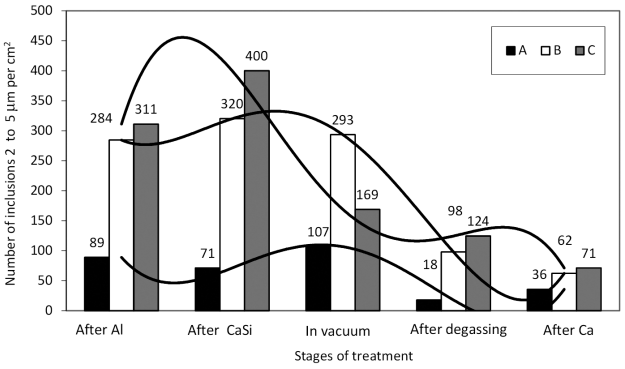

Figure 4: Number of inclusions with sizes from 2 µm to 5 µm in the course of the steel treatment by secondary metallurgy methods

Slika 4: Število vključkov velikosti od 2 µm do 5 µm pri postopku sekundarne metalurgije izdelave jekla

4 CONCLUSIONS

The following can be concluded from the results of the assessment of the evolution of the number and size of the inclusions during steel refining in a ladle furnace and in a vacuum caisson (ISSM):

- CaSi modification of the steel de-oxidised by aluminium caused, at first, an increase in the number of inclusions, which was strongly reduced during the vacuum treatment. This evolution of the occurrence of inclusions was observed particularly for the small inclusions with a size up to 1 µm.
- For larger inclusions (2 µm to 5 µm) the decrease of their number during the vacuum treatment was apparently slower due to the joining of small inclusions into larger ones.
- A similar evolution of the number of inclusions was also observed in the technological flow without any modification of the steel by CaSi. Only the overall number of inclusions was higher after the degassing.
- The final dosing of calcium into the degassed steel caused, in all the cases, an increase in the number of

inclusions, but mostly in the group of the smallest inclusions with sizes up to 1 μm.

Acknowledgements

This work was carried out within the frame of the projects of the programs TIP FR-TI1/186, FR-TI1/477 and FR-TI2/280 under the financial support of the Ministry of Industry and Trade of the Czech Republic.

5. REFERENCES

[1] V. Prešern, B. Koroušič, J. W. Hastie, Thermodynamic conditions for inclusions modification in calcium treated steel, Steel research, 62 (**1991**) 7, 289–295

UDK 691.5
Professional article/Strokovni članek

ISSN 1580-2949
MTAEC9, 46(3)291(2012)

SIMULATION OF THE SELF-HEALING OF DOLOMITIC LIME MORTAR

SIMULACIJA SAMOPOPRAVE DOLOMITNE APNENE MALTE

Barbara Lubelli[1,2], Timo G. Nijland[2], Rob P. J. van Hees[1,2]

[1]Delft University of Technology, Faculty of Architecture, Julianalaan 134, 2628 BL, Delft, The Netherlands
[2]TNO Technical Sciences, van Mourik Borekmanweg, 6, 2628XE, Delft, The Netherlands
b.lubelli@tudelft.nl

Prejem rokopisa – received: 2011-07-18; sprejem za objavo – accepted for publication: 2012-03-02

A test procedure was set up to reproduce laboratory self-healing on lime-based (both pure calcium and magnesium-calcium) mortar specimens. After a few months of testing, during which time the specimens were submitted to wet-dry cycles, thin sections of the specimens were prepared and observed using a polarization and fluorescence microscope (PFM) and a scanning electron microscope (SEM) equipped with an energy-dispersive X-ray spectrometer (EDX). The specimens prepared with dolomitic lime showed the occurrence of self-healing: a magnesium compound was observed to be filling the cracks and voids. These results suggest new possibilities for the development of dolomitic lime mortars with an increased self-healing capacity.

Keywords: self-healing, dolomitic mortar, PFM, SEM-EDX

Pripravljen je bil postopek laboratorijskega reproduciranja samopoprave vzorcev (na osnovi čistega kalcija in magnezij-kalcija) apnene malte. Po nekaj mesecih preizkušanja, med katerim so bili vzorci ciklično močeni in sušeni, so bile pripravljene tanke rezine za opazovanje s polarizacijskim in fluorescenčnim mikroskopom (PFM) ter z vrstičnim elektronskim mikroskopom (SEM), opremljenim z energijsko disperzijsko spektroskopijo (EDX). Vzorci, pripravljeni iz dolomitnega apna, so pokazali pojave samopoprave: magnezijeva sestavina je napolnila razpoke in praznine. Ti rezultati nakazujejo nove možnosti za razvoj dolomitnih apnenih malt s povečano sposobnostjo samopoprave.

Ključne besede: samopoprava, dolomitna malta, PFM, SEM-EDX

1 INTRODUCTION

Autogeneous self-healing, i.e., the repair of (micro)cracks by the material itself without intentional human intervention, is known to occur spontaneously in historic lime and lime-pozzolana mortars. The self-healing process in lime mortar can be summarized as follows: water dissolves the calcium bearing compounds and transports them from a zone rich in binder to voids and cracks present in the mortar. In this way small cracks can be filled with re-crystallized compounds in an autogeneous self-healing process. The occurrence of this phenomenon has, for example, been shown in a microscopic survey of over 1000 samples of concrete and masonry mortars in structures from different periods in the Netherlands[1,2].

The property of engineered self-healing would greatly enhance the durability of modern materials, including those for repair and restoration; a range of potential routes are open for this for different materials (e.g.,[3]). In the case of mortars, mimicking the natural behaviour of historic mortars may be a potential way. This would imply stimulation of the re-crystallization of calcium hydroxide, $Ca(OH)_2$ or carbonate, $CaCO_3$ (either calcite, aragonite or vaterite) in response to cracking. This has also been advocated for concretes (e.g.,[4,5]). However, in order to reach a durable self-healing effect, sealing of the crack by less soluble phases should be preferred.

In-situ (e.g.,[6]) and laboratory (e.g.,[7]) studies of concrete show that the exposition of concrete in seawater may result in the deposition of a surface layer of brucite, $Mg(OH)_2$, which, after deposition, protects the concrete from future degradation. Brucite is relatively insoluble; the sealing of cracks in mortar by brucite would therefore be a more definitive self-healing than by Ca phases. Engineered self-healing following the brucite path would, of course, require the presence of (soluble) magnesium in the mortar composition. A way to fulfil this bulk chemical requirement would be the use of mortars based on dolomitic lime. Such mortars have been used in different European regions from the Roman period up to the early 20th century[8,9] and are mentioned to have a better self-healing potential than pure calcium mortars[10]. This paper reports the first results of a study to prospect the self-healing potential of dolomitic lime mortars.

The main difficulty in the study of self-healing is the difficulty of reproducing and following this process in the laboratory on a realistic timescale. In the present research, an accelerated procedure has been developed that allowed us to obtain self-healing in some of the studied mortar types in a few months.

2 MATERIALS AND METHODS

Mortar specimens were prepared using different binder types and sand/aggregate ratios, in order to

evaluate the effect of these variables on the self-healing capacity of the mortar. Both calcium and dolomitic lime binders were used. Calcium lime is a traditional binder, nowadays used mainly in restoration because of its high compatibility with ancient materials. Dolomitic lime mortar was common in some European regions from the Roman period up to the early 20th century and appreciated for its long-term strength, higher than that of high calcium lime[9]. Nowadays, dolomitic lime is scarcely used because of the delayed hydration of over-burned MgO causing the pitting of popping in the mortar and the risk of formation, in a wet environment, of harmful magnesium sulphate salts in the presence of sulphates from air pollution or gypsum-containing building materials. Dolomitic lime was included in this study in order to stimulate the formation of brucite, which, being relatively insoluble, would lead to a more durable self-healing than calcium compounds. Besides, Anderegg[10] suggests dolomitic lime mortars might have a better self-healing capacity than pure calcium lime.

The following binder products were used to prepare the mortar:

- Pure calcium hydrated lime powder (Supercalco 90 by Carmeuse, NL)
- Dolomitic hydrated lime powder (by Piasco, I) having 60 % CaO, 34 % MgO and impurities of SiO_2, Al_2O_3, Fe_2O_3, CO_2 and sulphates.

Two binder/sand ratios were selected in order to investigate the influence of the amount of available lime components on the occurrence of self-healing: 1 : 3 and 1 : 1 by volume. A 1 : 3 ratio by volume is common nowadays, while higher binder/sand ratios were more usual in historic mortars[11]. Siliceous sand (CEN Standard Sand certified in accordance with EN 196-1 - ISO Standard Sand conforming to ISO 679), sieved to select the grain fraction 0.08–1 mm.

Four different types of mortar were prepared. Two specimens were made for each mortar type: one was embedded in epoxy resin just after curing to seal the specimen; the other one was used in the ageing test. The mortar specimens were prepared in moulds (4 cm × 4 cm × 16 cm) and unmoulded as soon as they achieved sufficient strength. The specimens were then cured at 20 °C/65 % RH for 2 weeks and subsequently artificially carbonated at 20 °C, 70 % RH and 1 % CO_2. Complete carbonation was checked by spraying a freshly broken surface with phenolphthalein.

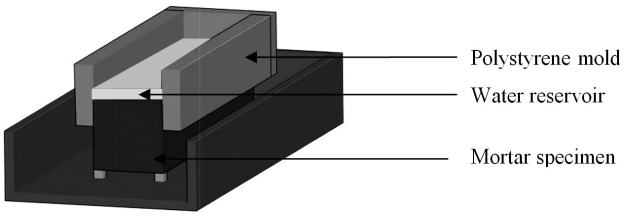

Figure 1: Test set up
Slika 1: Shematski prikaz preizkusa

At this point, the test attempting to reproduce self-healing in the laboratory could start. Specimens were immersed in boxes (one for each specimen) containing water at pH 5 obtained by the addition of CO_2. The boxes were stored at 5 °C. The low temperature and the slightly acid pH were chosen to favour the dissolution of the lime components[12]. After a period of three months, the water in the containers was removed (but preserved), and the specimens were dried at room temperature. A mould was built on the top of each specimen (**Figure 1**). The previously removed water, enriched in Ca- and Mg-compounds dissolved from the mortar in the first phase of the test, was poured on the top of the specimen, while the bottom surface was left free to dry. In this way, a percolation process was replicated. The water reservoir was refilled every two weeks in order to simulate wet-dry cycles. A total of 10 cycles were performed over a period of about 5 months. This procedure was chosen because previous research on mortar samples collected from existing structures has shown that self-healing is most frequent in those situations (like bridges, defence walls, etc.) where an intermittent (abundant) supply of water is present[2].

After a few months of cycling, the specimens were dried at 40 °C and thin sections were prepared. The thin sections, vacuum impregnated with an epoxy resin containing a fluorescent dye, were observed using polarization and fluorescence microscopy (PFM) to identify the eventual occurrence of self-healing and assess the extent of its eventual occurrence. Some of the thin sections were not covered with glass and studied using high-resolution scanning electron microscopy (SEM) (FEI NovaNanoSEM650) equipped with energy-dispersive X-ray spectroscopy for the identification of the compounds precipitated in the cracks and voids. Thin sections were prepared perpendicular to the length of the prisms.

3 RESULTS AND DISCUSSION

3.1 Polarization and Fluorescence Microscopy (PFM) observations

The PFM observations were carried out on thin sections obtained from the mortar specimens before and after the ageing test.

In the calcium lime mortar specimens, both the 1 : 1 and 1 : 3 binder/sand ratios, no significant re-precipitation of calcium compounds in the cracks and voids was observed after the test. The specimen with the binder/sand ratio 1 : 1 shows severe cracking due to shrinkage (**Figure 2**). The mortar with a lower binder/sand ratio is very lean, with a large amount of coarse pores (diameter up to 0.5 mm) (**Figure 3**). The leaching of the binder in the first phase of the test might have contributed to an increase in the already high porosity.

The specimen prepared with the dolomitic lime and the binder/sand ratio 1 : 1 also showed the presence of

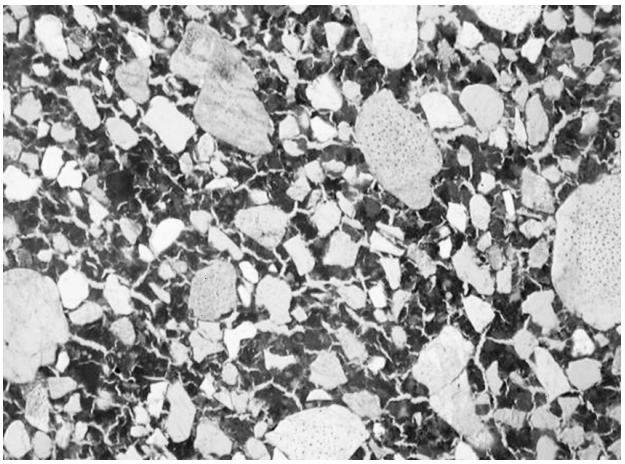

Figure 2: Micrograph showing the presence of shrinkage cracks in a calcium lime specimen with a 1 : 1 binder/sand ratio after testing (view 5.4 mm × 3.5 mm, plane polarized light)

Slika 2: Mikroposnetek, ki kaže prisotnost krčilnih razpok v kalcijevem apnenem vzorcu z razmerjem vezivo/pesek 1 : 1 po preizkusu (pogled na ploščino 5,4 mm × 3,5 mm, ravninsko polarizirana svetloba)

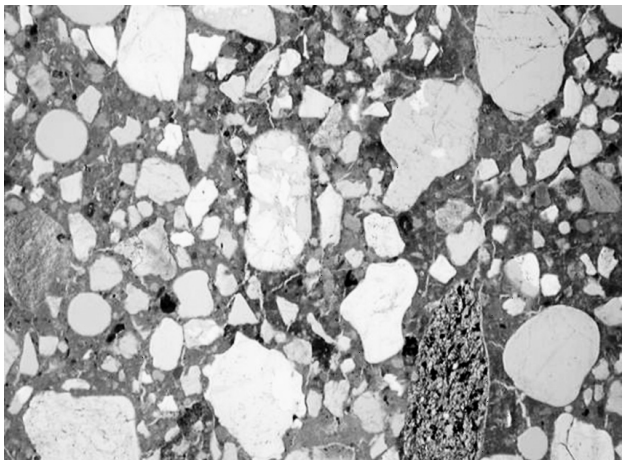

Figure 4: Micrograph showing the presence of shrinkage cracks in a magnesium lime specimen with a 1 : 1 binder/sand ratio after testing (view 5.4 mm × 3.5 mm, plane polarized light)

Slika 4: Mikroposnetek, ki kaže prisotnost krčilnih razpok v magnezijevem apnenem vzorcu z razmerjem vezivo/pesek 1 : 1 po preizkusu (pogled na ploščino 5,4 mm × 3,5 mm, ravninsko polarizirana svetloba)

shrinkage cracks, but their quantity is much less than observed in the calcium lime mortar. No self-healing is observed.

The mortar prepared with the dolomitic lime/sand ratio 1 : 3 shows the presence of large voids and cracks (**Figures 4** and **5**), similar to those observed in the calcium lime mortar. However, in this case both shrinkage cracks and irregular voids in part of the cross-section are filled with a newly precipitated compound (**Figures 6** and **7**). The absence of self-healing in the reference thin section of the specimen made before the laboratory test demonstrates that this phenomenon is due to the dissolution of the binder compounds during the immersion in water and the subsequent re-precipitation during the wet/dry cycles. The morphology of the precipitated compound differs from that of the brucite formed on the concrete during natural or laboratory exposure to sea water, which tends to form thin, pallisade-like layers on the surface[6,7], or in cracks in historic mortars, in which it may occur as tiny, radially arranged aggregates or rosettes[13]. Individual crystals are significantly larger and the oriented arrangement of tiny individual crystals is lacking. Such textures, of course, strongly depend on the reaction kinetics, the degree of saturation and the compositional gradients, etc. Optically, brucite, $Mg(OH)_2$, and hydromagnesite, $Mg_5[OH(CO)_3)_2] \cdot 4H_2O$, another possible candidate, are

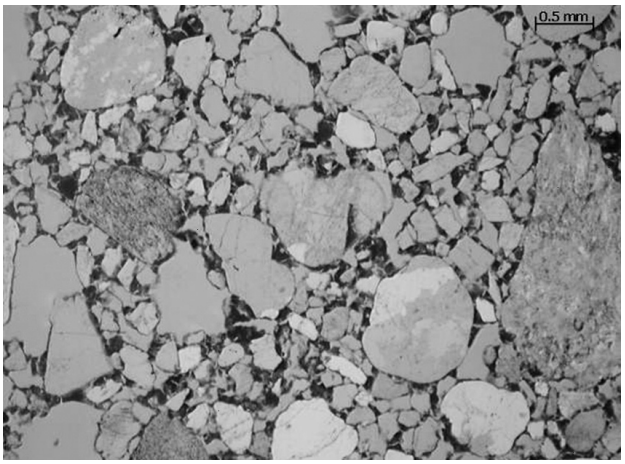

Figure 3: Micrograph showing the presence of a large quantity of coarse pores in a calcium lime specimen with a 1 : 3 binder/sand ratio after testing (view 5.4 mm × 3.5 mm, plane polarized light)

Slika 3: Mikroposnetek, ki kaže prisotnost velikega deleža grobih por v kalcijevem apnenem vzorcu z razmerjem vezivo/pesek 1 : 1 po preizkusu (pogled na ploščino 5,4 mm × 3,5 mm, ravninsko polarizirana svetloba)

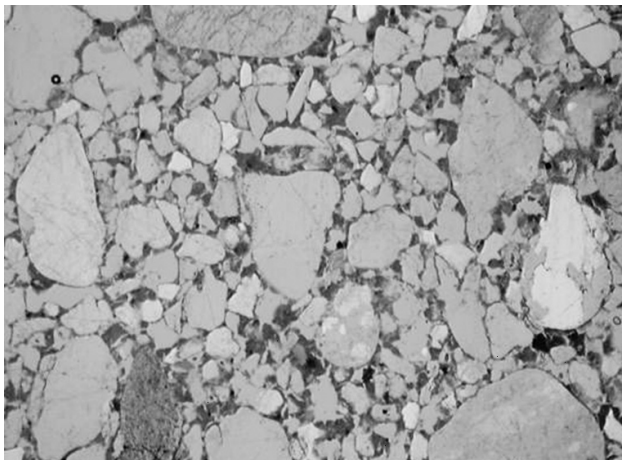

Figure 5: Micrograph showing the presence of a large quantity of coarse pores in a dolomitic lime specimen with a 1 : 3 binder/sand ratio after testing (view 5.4 mm × 3.5 mm, plane polarized light)

Slika 5: Mikroposnetek, ki kaže velik delež grobih por v dolomitnem apnenem vzorcu z razmerjem vezivo/pesek 1 : 3 po preizkusu (pogled na ploščino 5,4 mm × 3,5 mm, ravninsko polarizirana svetloba)

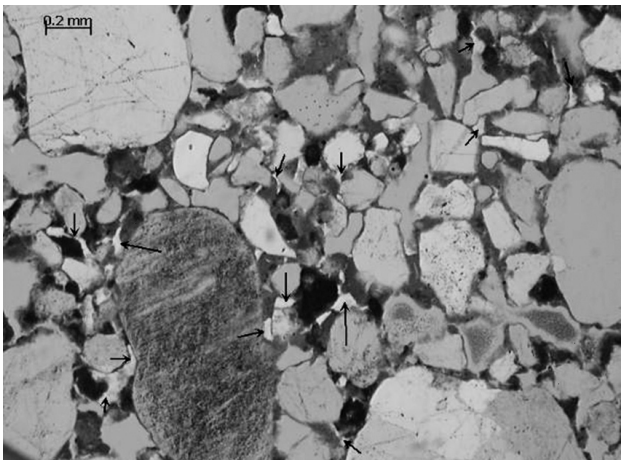

Figure 6: Micrograph showing self-healing of cracks and irregular voids in a dolomitic lime specimen with a 1 : 3 binder/sand ratio (view 1.4 mm × 0.9 mm, plane polarized light)

Slika 6: Mikroposnetek, ki kaže samopopravljene razpoke in nepravilne praznine v dolomitnem apnenem vzorcu z razmerjem vezivo/pesek 1 : 3 (pogled na ploščino 1,4 mm × 0,9 mm, ravninsko polarazirana svetloba)

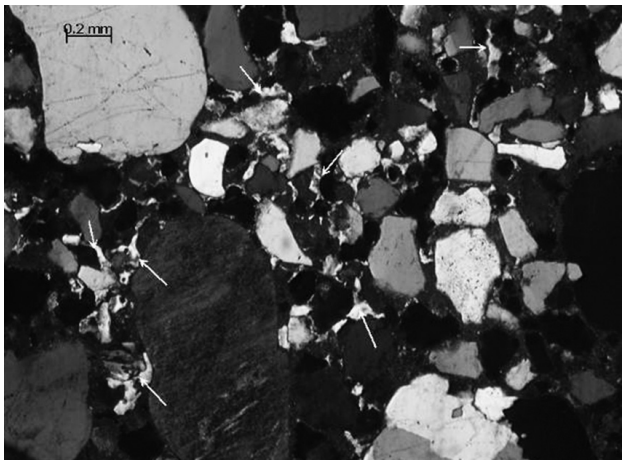

Figure 8: Micrograph of the same area of **Figure 6** showing the self-healing of cracks and irregular voids in a dolomitic lime specimen with a 1 : 3 binder/sand ratio (view 1.4 mm × 0.9 mm, cross polarized light)

Slika 8: Mikroposnetek istega področja s **slike 6**, ki kaže samopopravljene razpoke in nepravilne praznine v dolomitnem apnenem vzorcu z razmerjem vezivo/pesek 1 : 3 (pogled na ploščino 1,4 mm × 0,9 mm, navzkrižno polarizirana svetloba)

difficult to distinguish. However, the relatively large birefringence (**Figure 9**) seems to indicate hydromagnesite rather than brucite (birefringence of 0.022–0.029 and 0.015–0.021, respectively).

It appears that cracks and voids up to 100 μm can be completely healed. The amount of the cross-section through the mortar in which the self-healing occurs, is variable, 5.8 % and 0.6 % of the surface area in two different thin sections. In the domains in which self-healing occurs, by far the majority of the cracks and voids are sealed (**Figures 8** and **9**). Curiously, self-healing occurs in the mortar with a lower amount of binder. The reason for this behaviour is not clear; it might be related to the different moisture-transport properties of the two mortars.

3.2 Scanning Electron Microscopy observations

For both mortar pieces a thin section of the dolomitic lime mortar with 1 : 3 binder/sand ratio was studied by means of SEM-EDX using both BSE and SE modes. The newly precipitated compound is composed solely of Mg, except for O and C (no carbon coating was used); in the binder, Ca is present and the amount of magnesium is much lower. These results confirm that the cracks are healing with a magnesium compound, given the carbo-

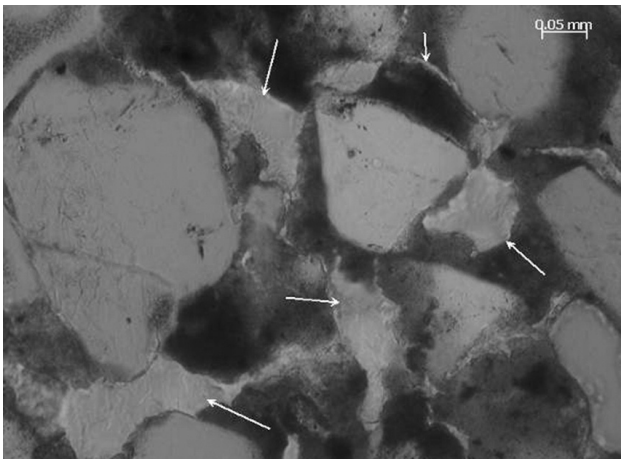

Figure 7: Micrograph showing the self-healing of cracks and irregular voids in a dolomitic lime specimen with a 1 : 3 binder/sand ratio (view 0.7 mm × 0.45 mm, plane polarized light)

Slika 7: Mikroposnetek, ki kaže samopopravljene razpoke in nepravilne praznine v dolomitnem apnenem vzorcu z razmerjem vezivo/pesek 1 : 3 (pogled na ploščino 0,7 mm × 0,45 mm, ravninsko polarizirana svetloba)

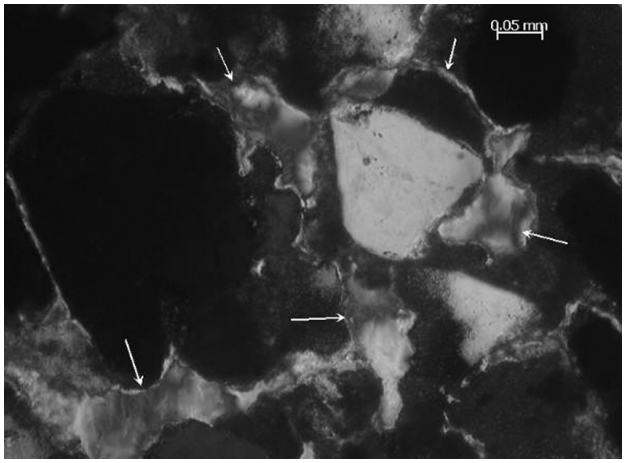

Figure 9: Micrograph of the same area of **Figure 7** showing the self-healing of cracks and irregular voids in a dolomitic lime specimen with a 1 : 3 binder/sand ratio (view 0.7 mm × 0.45 mm, cross polarized light)

Slika 9: Mikroposnetek istega področja s **slike 7**, ki kaže samopopravljene razpoke in nepravilne praznine v dolomitnem apnenem vzorcu z razmerjem vezivo/pesek 1 : 3 (pogled na ploščino 0,7 mm × 0,45 mm, navzkrižno polarizirana svetloba)

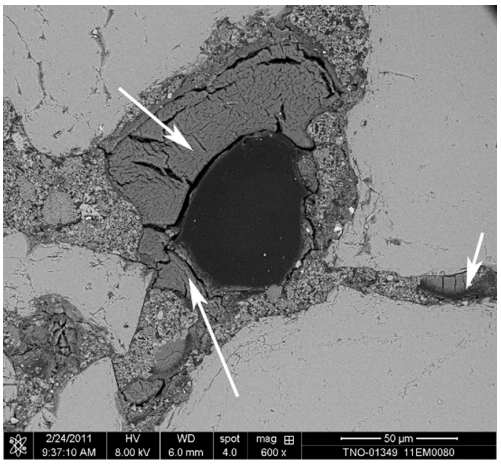

Figure 10: Micrograph showing the partial filling of a void (indicated by the arrows) in a dolomitic lime specimen with a 1:3 binder/sand ratio (BSE mode, 600-times magnification)

Slika 10: Mikroposnetek, ki kaže delno zapolnjeno praznino (označeno s puščico) v dolomitnem apnenem vzorcu z razmerjem vezivo/pesek 1 : 3 (način BSE, povečava 600-kratna)

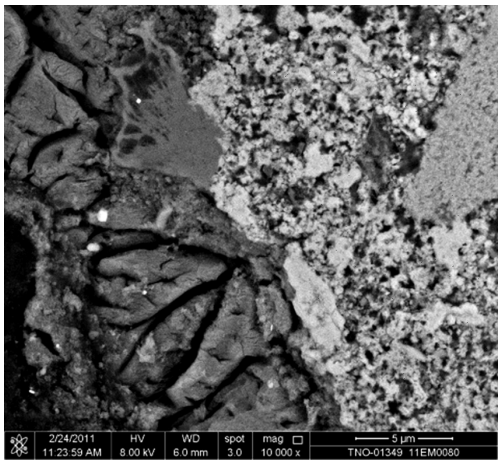

Figure 12: Micrograph showing re-precipitated crystals; thin section of the dolomitic lime specimen with a 1 : 3 binder/sand ratio (BSE mode, 10000-times magnification)

Slika 12: Mikroposnetek, ki kaže ponovno izločene kristale; tanek rez dolomitnega apnenega vzorca z razmerjem vezivo/pesek 1 : 3 (način BSE, povečava 10000-kratna)

nate presence probably hydromagnesite. **Figures 10** and **11** show examples of the newly precipitated compound (partially) filling the cracks and voids. In BSE mode, even at high magnification, individual crystals can only be distinguished with difficulty, but the precipitates seem to show shrinkage cracks (**Figures 10** to **12**). This may be due to the loss of crystal water, or, alternatively, the development of the crystals from a gel (as with brucite, cf.[14]). In SE mode the precipitates seem to be made up of a stacked platy phase (**Figure 13**).

4 CONCLUSIONS

Mortars based on dolomitic lime have a clear potential to develop self-healing by the precipitation of Mg phases. This opens up an interesting perspective for the development of future mortars with an enhanced self-healing capacity , both for new constructions as well as repair and restoration. However, several questions, including the definitive identification of the re-precipitated Mg compound and the apparently opposite dependence of self-healing on binder content, require further explanation. Another question that may be raised is whether hydromagnesite represents the final stage of the self-healing process, or whether brucite may develop from hydromagnesite over the long term. The possibility of Mg-based self-healing in dolomitic lime mortars also poses the interesting question as to whether magnesia-based cements (e.g.,[15]) would have a higher self-healing potential than traditional Portland-based cements,

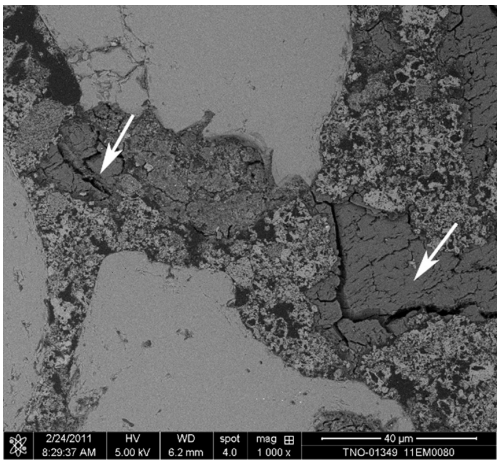

Figure 11: Micrograph showing the self-healing of a crack (indicated by the arrows) in a dolomitic lime specimen with a 1 :3 binder/sand ratio (BSE mode, 1000-times magnification)

Slika 11: Mikroposnetek, ki kaže samopopravo razpoke (označeno s puščico) v dolomitnem apnenem vzorcu z razmerjem vezivo/pesek 1 : 3 (način BSE, povečava 1000-kratna)

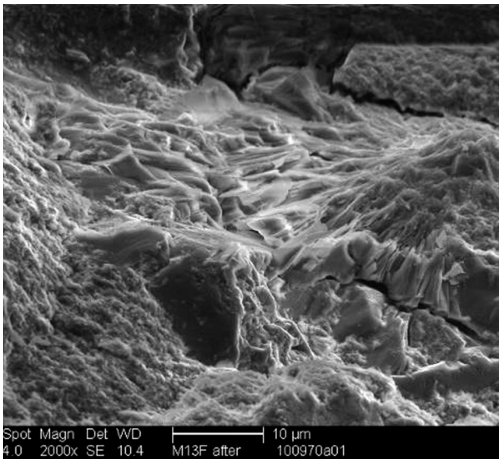

Figure 13: Micrograph showing lamellar crystals in a broken section of the dolomitic lime specimen with a 1 : 3 binder/sand ratio (SE mode, 2000-times magnification)

Slika 13: Mikroposnetek lamelastih kristalov na področju preloma dolomitnega apnenega vzorca z razmerjem vezivo/pesek 1 : 3 (način SE, povečava 2000-kratna)

including those blended with supplementary cementing materials, such as blast-furnace slag or pulverized fly. In such cements, the precipitation of brucite is believed to be one of the causes of enhanced strength development.

Acknowledgments

The authors wish to thank the DC Mat (Delft Center of Materials) for financing this research project

5 REFERENCES

[1] T. G. Nijland, J. A. Larbi, R. P. J. van Hees, B. Lubelli, M. R. de Rooij, Self healing phenomena in concretes and mortars: A microscopic study, Proc. of the 1st Int. Conf. on Self Healing Materials, Noordwijk, 2007, 1–9

[2] B. Lubelli, T. G. Nijland, R. P. J. van Hees, Self-healing of lime based mortars: microscopy observations on case studies, Heron, 56 (**2011**), 81–97

[3] S. van der Zwaag, Routes and mechanisms towards self-healing behaviour in engineering materials, Bulletin of the Polish Academy of Science, Technological Sciences, 58 (**2010**), 227–236

[4] S. Granger, A. Loukili, G. Pijaudier-Cabot, M. Behloul, Self healing of cracks in concrete: From a model material to usual concretes, Proc. of the 2nd Int. RILEM Symposium on Advances in Concrete through Science and Engineering, France, RILEM pro051, 2006, 207–224

[5] N. ter Heide, E. Schlangen, Selfhealing of early age cracks in concrete Proc. of the 1st Int. Conf. on Self-Healing Materials, Noordwijk aan Zee, 2007, 1–12

[6] R. Polder, J. Larbi, Investigation of concrete exposed to North Sea water submersion for 16 years, Heron, 40 (**1995**), 31–56

[7] G. A. Leegwater, R. B. Polder, J. H. M. Visser, T. G. Nijland, Durability study High Filler concrete, TNO-report 2006-D-R0912, Delft, 2007, 95

[8] T. Mannoni, G. Pesce, R. Vecchiattini, Mortiers de chaux dolomitique avec adjonction de kaolin cuit: L'expérience génoise, ArchéoSciences, 30 (**2006**), 67–79

[9] A. Diekamp, J. Konzett, P. W. Mirwald, Magnesian lime mortars – Identification of magnesium phases in medieval mortars and plasters with imaging techniques, Proc. of the 12th EMABM, Dortmund, 2009, 309–317

[10] F. O. Anderegg, Autogeneous healing in mortars containing lime, ASTM Bulletin, 116 (**1942**), 22

[11] K. van Balen, B. van Bommel, R. van Hees, M. van Hunen, J. van Rhijn, M. van Rooden, Kalkboek - Het gebruik van kalk als bindmiddel voor metsel- en voegmortels in verleden en heden, Rijksdienst voor de Monumentenzorg, Zeist, (**2003**), 296

[12] R. S. Boynton, Chemistry and technology of lime and limestone, 2nd edition, J. Wiley and Sons, Inc., New York, 1980, 592

[13] C. Blaeuer, A. Kueng, Examples of microscopic analysis of historic mortars by mean of polarizing light microscopy of dispersion and thin sections, Materials Characterization, 58 (**2007**), 1199–1207

[14] J. Harrison, Tec-cement update, Concrete 05, Melbourne, 2005

[15] L. J. Vandeperre, M. Liska, A. Al-Tabbaa, Microstructures of reactive magnesia cement blends, Cement & Concrete Composites, 30 (**2008**), 706–714

UDK 669.18(437.3)
Professional article/Strokovni članek

ISSN 1580-2949
MTAEC9, 46(3)297(2012)

DESULPHURIZATION OF THE HIGH-ALLOY AND MIDDLE-ALLOY STEELS UNDER THE CONDITIONS OF AN EAF BY MEANS OF SYNTHETIC SLAG BASED ON $CaO\text{-}Al_2O_3$

RAZŽVEPLJANJE MOČNO IN SREDNJE LEGIRANIH JEKEL V ELEKTROOBLOČNI PEČI S SINTETIČNO ŽLINDRO NA OSNOVI $CaO\text{-}Al_2O_3$

Karel Michalek[1], Libor Čamek[1], Karel Gryc[1], Markéta Tkadlečková[1], Tomáš Huczala[2], Vladimír Troszok[2]

[1]VŠB – Technical University of Ostrava, FMME, Department of Metallurgy and Foundry, 17. listopadu 15/2172, 708 33 Ostrava, Czech Republic
[2]TŘINECKÉ ŽELEZÁRNY, a.s., 739 70 Třinec-Staré Město, Průmyslová 1000, Czech Republic
karel.michalek@vsb.cz

Prejem rokopisa – received: 2011-10-18; sprejem za objavo – accepted for publication: 2012-02-22

The article deals with the results of the experimental heats performed in the electric steel plant of TŘINECKÉ ŽELEZÁRNY, a. s. (TŽ, a. s.). The aim was to verify the possibility of deep desulphurization of steel in the basic 10-t electric arc furnace. Experimental procedures making use of the industrially produced synthetic slag were applied in the production of the high-alloy chrome steels and the middle-alloy tool steels, where the desulphurization, in terms of thermodynamics, is a more demanding process than the chrome-nickel steel desulphurization. With the use of the technological processes it is possible to achieve low contents of sulphur in steel, below mass fraction 0.003 %. Achieving these contents depends on a suitable slag basicity, and, in particular, on the ratio of CaO/Al_2O_3. Based on the analysis of the results, a critical factor significantly affecting the final content of the sulphur and thus the efficiency of the desulphurization of steel, the content of FeO in the reduction slag, is carefully considered. A higher MgO content in slag (up to w = 25 %) had no significant influence on the results of the steel desulphurization.

Keywords: steel, desulphurization, synthetic slag, basicity of slag

Članek predstavlja rezultate eksperimentalnih talin, izdelanih v TŘINECKÉ ŽELEZÁRNY, a. s. (TŽ, a. s.). Namen raziskav je bil preveriti možnost močnega razžvepljanja jekla v bazični 10-tonski elektropeči. Izvršena je bila raziskava z uporabo industrijsko proizvedene sintetične žlindre pri proizvodnji močno legiranega kromovega jekla in srednje legiranega orodnega jekla, pri katerih je termodinamika razžvepljanja bolj zapletena kot pri razžvepljanju krom-nikljevih jekel. S primernimi tehnološkimi ukrepi je mogoče doseči v jeklu majhno vsebnost žvepla, nižjo od masnega deleža 0,003 %. Doseganje teh vsebnosti je odvisno od primerne bazičnosti žlindre in posebno še od razmerja CaO/Al_2O_3. Na osnovi analize rezultatov je bil določen kritični faktor, vsebnost FeO v redukcijski žlindri, ki močno vpliva na končno vsebnost žvepla in s tem na učinkovitost razžvepljanja. Večja vsebnost MgO (do masnega deleža 25 %) v žlindri nima večjega vpliva na razžvepljanje jekla.

Ključne besede: jeklo, razžvepljanje, sintetična žlindra, bazičnost žlindre

1 INTRODUCTION

Options for steel desulphurization primarily depend on managing the technology itself, as well as on the metallurgical processes of desulphurization. In particular, the optimization of the slag regime, and the compliance with the basic thermodynamic and kinetic parameters of slag and metal have to be considered.

The possibility of using a high-quality, industrially produced synthetic slag[1,2] is a significant advantage, which guarantees balanced and high-quality results, and brings a number of metallurgical, and, subsequently, economic benefits. These can be seen not only in achieving the desired cleanliness of steel, but also in compensating for the lack of modern and also expensive technological equipment for the production and secondary metallurgy. Using the production technology with synthetic slag, the high parameters of desulphurization with the final sulphur content in mass fractions being as high as 0.002 % in an electric arc furnace (EAF), and the subsequent tapping of the steel in the ladle can be achieved.

2 BASIC FACTORS INFLUENCING THE DESIRED DEGREE OF STEEL DESULPHURIZATION

In the steel production in an EAF, one of the limiting factors for achieving the desired degree of desulphurization is the sulphur contained in the basic composition of the metal-bearing batch of an external steel waste, or of an internally occurring metal (alloying additives, solid pig iron, slag-forming substances, etc.). Unlike the pure-oxygen production processes, where, in terms of desulphurization, inappropriate oxidation conditions dominate, the process of melting in an EAF is much

more variable, with a choice of heat-melting conditions and the associated slag regime. An EAF can create the standard oxidation conditions that are necessary for the decarburization process, the oxidation of the accompanying elements, the dephosphorization process, and also the reduction conditions that, in turn, provide the possibility of a successful desulphurization of steel.

The thermodynamics of desulphurization shows that, in order to achieve a low sulphur content in the metal, it is necessary to achieve, in particular, the following[3]:

- a high level of activity of free oxygen anions in the slag, i.e., a high alkalinity of the slag with a high proportion of alkaline oxides and a low proportion of acidic oxides;
- a low activity of the oxygen a_o in the steel, i.e., a low content of the dissolved oxygen and a low value of an activity coefficient f_o.

Another negative factor affecting the degree of steel desulphurization is the presence of the "easily reducible" oxides in the refining slag - in addition to FeO there are also MnO, P_2O_5 and Cr_2O_3. The sum percentage content of the aforementioned elements for a well-working refining slag is usually recommended to be up to the mass fraction 3 %.

From the kinetic point of view, an increased temperature has a positive effect on the steel desulphurization. Increasing the temperature helps decrease the viscosity of the slag and metal; it also increases the sulphur-diffusion coefficient and reduces the surface tension, so that the chemical reaction more quickly reaches a state of equilibrium. However, the effect of the appropriate kinetics of the ongoing processes is closely connected with meeting the basic thermodynamic conditions.

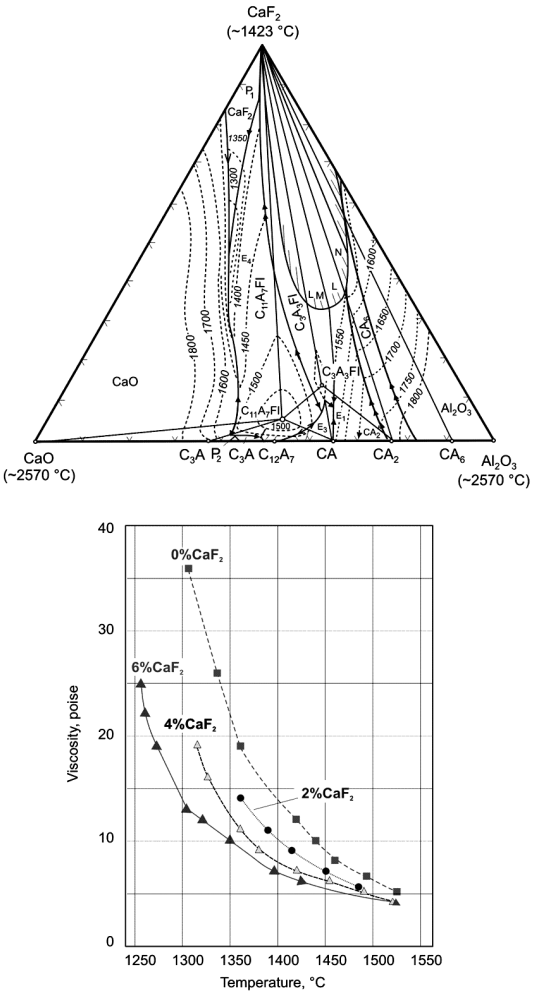

Figure 1: Influence of CaF_2 on liquidus temperature and slag viscosity[4]

Slika 1: Vpliv CaF_2 na temperature likvidusa in viskoznost žlindre[4]

3 CURRENT TECHNOLOGICAL AND METALLURGICAL PROCESSES IN THE PRODUCTION OF THE LOW-SULPHUR STEEL IN THE CONDITIONS OF THE ELECTRIC STEEL PLANT TRINECKE ZELEZARNY, a. s.

The production technology of steel with a low sulphur content, below 0.005 %, is, in terms of the electric steel plant of the TŽ, a. s. EAF, is currently based on the use of the calcium slag containing CaF_2 (calcium fluoride - fluorspar).

In the slag with a low silica content a positive effect of CaF_2 can be explained with a lowered melting point of the slag resulting from the formation of the eutectic, easily meltable phases CaO–CaF_2, or CaO–Al_2O_3–CaF_2 with a low liquidus temperature and a low viscosity, which are shown in **Figure 1**[4]. CaF_2 also affects the reduction of the sulphur activity in the slag, leading to an increased ability of the slag to bind sulphur.

Disadvantages of using technologies with fluorspar can be seen in two major aspects:

In the contact of fluorspar with the liquid metal or liquid slag, environmentally harmful fluorides are released, which worsen the working and living environment. Fluorides concentrate in the bone tissue in a bond with Ca and Mg, thereby preventing these elements from performing their biochemical function.

Fluorspar in the slag causes an increased wear of the furnace lining and casting ladles, particularly in the slag lines, thus significantly reducing the overall durability of the furnace linings.

The use of fluorspar as a slag-forming additive is currently undergoing significant restrictions in many foreign and domestic metallurgical plants, and some economically acceptable replacements in the form of industrially produced homogeneous synthetic slag is being sought.

Currently, reputable companies provide high-quality industrially produced synthetic slag with different Al_2O_3/CaO proportions and in the form of, e.g., granules, pellets, little briquettes, crushed pieces, etc. The primary advantage is the guarantee of the exact required chemical composition with a high homogeneity.

Another group of slag-forming materials are the mixtures prepared from differently treated waste materials or

other technological products. Mixtures of this type can also be named "dilutants" or "flux" for liquefaction of the ladle slag; however, they cannot themselves significantly activate the conditions for deep desulphurization.

4 SELECTION OF SUITABLE, INDUSTRIALLY PRODUCED SYNTHETIC SLAG FOR OPERATIONAL TESTING

The synthetic slag manufactured by the REFRATECHNIK company under the name REFRAFLUX 4842 was purposefully selected for the operational testing in the electric steel plant at TŽ, a.s.

The material in the form of pellets and their fragments with a granulometry from 5 mm to 15 mm is shown in **Figure 2**. Although it is part of the 2008 supply, the granulometry has remained unchanged and with no dust proportion.

The basis for the chemical composition of the synthetic slag was based on a mixture of two oxides (in mass fractions) – 41.1 % Al_2O_3, and 46.2 % CaO, including 4.9 % SiO_2, 1.2 % MgO, 0.2 % FeO and 1.9 % TiO_2.

Figure 3 shows the chemical composition of the tested, industrially produced synthetic slag in a ternary chart Al_2O_3–CaO–SiO_2.[5] It is a synthetic slag designed to be used with lime, for which it provides a high rate of assimilation and a subsequent liquefaction of the entire slag system.

Figure 2: Granulometry of the synthetic slag REFRAFLUX 4842 S
Slika 2: Zrnatost sintetične žlindre REFRAFLUX 4842 S

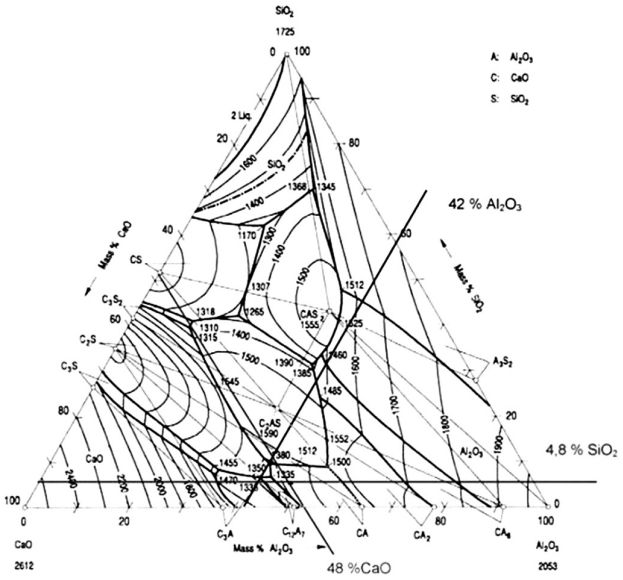

Figure 3: Area of the chemical composition of the tested synthetic slag REFRAFLUX 4842 S in the ternary chart Al_2O_3–CaO–SiO_2
Slika 3: Področje kemijske sestave preizkušene sintetične žlindre REFRAFLUX 4842 S v ternarnem diagramu Al_2O_3-CaO-SiO_2

5 PRODUCTION CONDITIONS OF EXPERIMENTAL HEATS

The production processes of desulphurization have been tested on the 10-ton-EAF when manufacturing the heat-resisting, high-alloyed steel of P91-grade (X10CrMoVNb9-1) and also the medium-alloyed tool steel of 19569-grade (X63CrMoV5.1). **Table 1** shows the internal-release chemical composition of both steels.

The production technology for reduction slag with a high refining effect was based on the use of a mixture of burnt lime and synthetic slag REFRAFLUX, where both components were added into the EAF using an alternating dosing on the bath surface. The proportion of both components was chosen in such a way that the composition of the slag, after the melting, ranged in optimal amounts suitable for the desulphurization of the steel in the values of 50 % to 55 % CaO, 18 % to 25 % Al_2O_3, ≤ 10 % SiO_2, and ≤ 12 % MgO. In terms of good fluidity of the slag and its sulphidic capacity, the task was to maintain an optimal proportion of CaO/Al_2O_3 and its basicity.

Table 1: Internal-release chemical composition of P91 steel and 19569 in mass fractions, *w*/%
Tabela 1: Interna kemijska sestava jekel P91 in 19569 v masnih deležih, *w*/%

Composition *w*/%	C	Si	Mn	P	S	Cr	Ni	Mo	Nb	V	W	N	Al
P91 X10CrMoV Nb9-1 1.4903	0.06–0.12	max. 0.50	0.30–0.60	max. 0.020	max. 0.010	8.00–9.50	max. 0.40	0.85–1.05	0.06–0.10	0.18–0.25		0.030–0.070	max. 0.040
19569 X63CrMoV5.1	0.58–0.68	0.7–1.1	0.25–0.55	max. 0.015	max. 0.010	4.5–5.5		0.8–1.2		0.2–0.4	max. 0.6		

In terms of the composition of the metal bath it was very important to maintain, in compliance with the theory of steel desulphurization, a low activity of the oxygen in the metal. In the EAF, this requirement was ensured with the higher levels of deoxidising elements in the liquid metal (especially Al) during the entire desulphurization process.

For a successful completion of the required chemical reactions, it is necessary, in addition to ensuring the thermodynamic conditions, to provide appropriate kinetic conditions. Mutual mixing of the slag and metal was carried out in the EAF by blowing the argon through the porous block in the furnace bottom, with the 15–50 l.min^{-1} volumetric flows according to the individual production stages. The subsequent thermal and chemical homogenization was performed by argon blowing through the porous block at the bottom of the ladle.

6 RESULTS

It should be noted that the course of each experimental heat was, to some extent, unique. A total of 14 heats were carried out in order to achieve the desired composition of the reduction slag and the other metallurgical and technological parameters, thus achieving the desired desulphurization of steel. Comparisons of the basic chemical analyses of the slag and the steel from the selected tested P91- and 19569-grade heats are shown in **Table 2** and in **Table 3**.

From both tables it is evident that in the composition of the reduction slag, even with the same dosage of REFRAFLUX, the synthetic slag and the burnt lime showed differences. The CaO/Al_2O_3 ratio in most heats ranged from 1.8 to 2.1, while the basicity (CaO/SiO_2) ranged from 5 to 8.

6.1 Effect of the MgO content in the reduction slag on the parameters of steel desulphurization

Some heats showed a higher MgO content in the reduction slag (in some cases up to w = 25 %), whose source can be seen in the wear of the furnace lining, and, especially, in the lower-quality repairing material used for the patch-type repairs of the lining. The slag with this

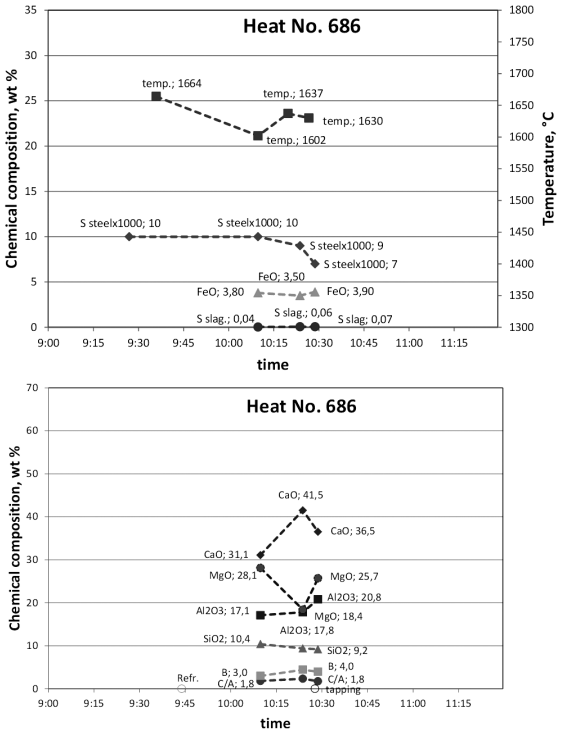

Figure 4: Development of the chemical composition of steel and slag during the reduction period for the heat No. 686 (19569, X63CrMoV5.1)
Slika 4: Razvoj kemijske sestave jekla in žlindre med trajanjem redukcije v talini št. 686 (19569, X63CrMoV5.1)

MgO content showed a higher viscosity, which complicated the course of desulphurization. However, it should be stated that even with these higher MgO contents, the final sulphur content in steel has been, in some cases, up to w = 0.002 %. A comparison of the effect of the increased MgO in the reduction slag is shown in the following charts.

Figure 4 and **Figure 5** show the development of the chemical composition of steel and slag during the reduction period for the heat No. 686 and No. 731.

If we disregard different contents of chromium in individual steel grades and focus only on the MgO content in the reduction slag, we can state that, under the conditions of very different MgO contents in both heats

Table 2: Selected chemical analyses of the final reduction slag and steel of the heats No. 716 and 731 (P91), *w*/%
Tabela 2: Izbrani kemijski analizi končnih redukcijskih žlinder talin št. 716 in 731 (P91) v *w*/%

Heat No.	CaO	Al_2O_3	MgO	SiO_2	FeO	Cr_2O_3	MnO	S_{steel}	Tap temperature
716	47.8	25.5	11.5	8.5	0.5	0.47	0.36	0.0020	1642 °C
731	43.1	21.2	12.6	7.2	5.57	5.70	1.35	0.0110	1688 °C

Table 3: Selected chemical analyses of the final reduction slag and steel of the heats No. 649 and 686 (19569), *w*/%
Tabela 3: Izbrani kemijski analizi končnih redukcijskih žlinder talin št. 649 in 686 (19569) v *w*/%

Heat No.	CaO	Al_2O_3	MgO	SiO_2	FeO	Cr_2O_3	MnO	S_{steel}	Tap temperature
649	45.6	23.0	19.4	6.0	1.5	0.71	0.45	0.0020	1653 °C
686	36.5	20.8	25.7	9.2	3.0	1.13	0.72	0.0070	1630 °C

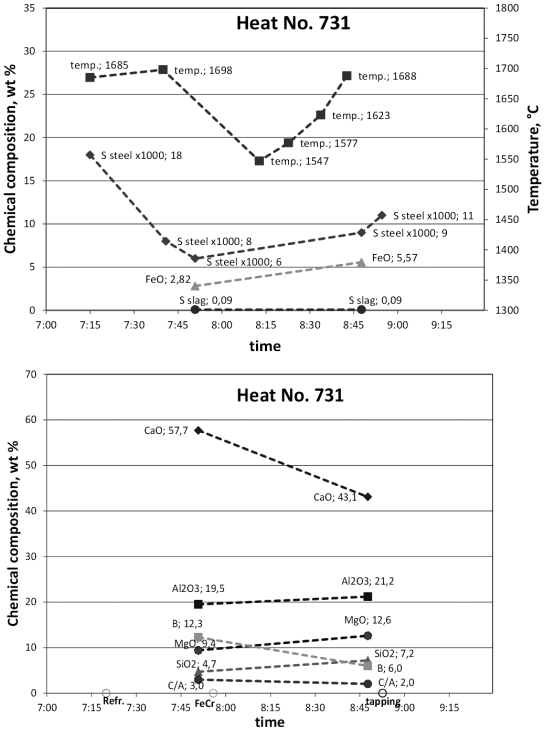

Figure 5: Development of the chemical composition of steel and slag during the reduction period for the heat No. 731 (P91, X10CrMoVNb9-1)

Slika 5: Razvoj kemijske sestave jekla in žlindre med trajanjem redukcije v talini št. 731 (P91, X10CrMoVNb9-1)

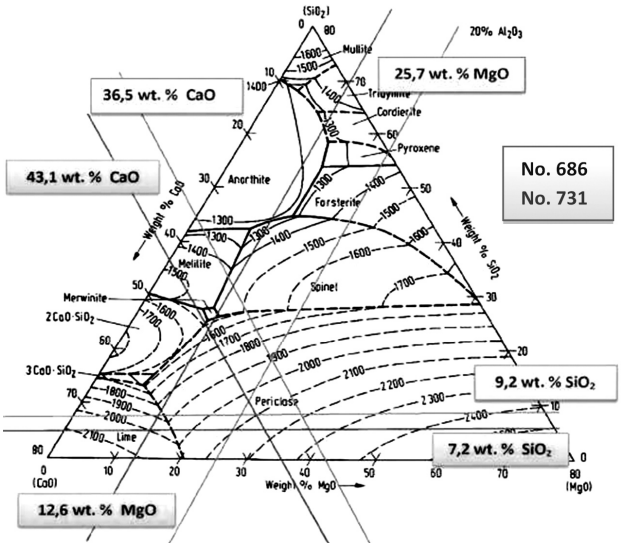

Figure 6: Areas of the chemical composition of the final reduction slag of the tested steel grades for the heats No. 686 (19569, X63CrMoV5.1) and No. 731 (P91, X10CrMoVNb9-1) in the quaternary chart Al_2O_3-CaO-MgO-SiO_2 at w = 20 % Al_2O_3 [5]

Slika 6: Področja kemijske sestave končne redukcijske žlindre preizkušenih jekel, talina št. 686 (19569, X63CrMoV5.1) in št. 731 (P91, X10CrMoVNb9-1) v kvaternarnem diagramu Al_2O_3-CaO-MgO-SiO_2 pri w = 20 % Al_2O_3 [5]

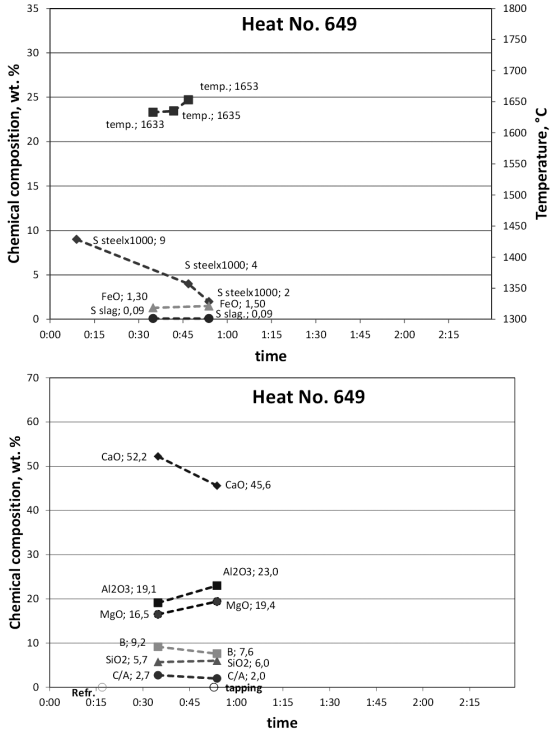

Figure 7: Development of the chemical composition of steel and slag during the reduction period for the heat No. 649 (19569, X63CrMoV5.1)

Slika 7: Razvoj kemijske sestave jekla in žlindre med trajanjem redukcije taline št. 649 (19569, X63CrMoV5.1)

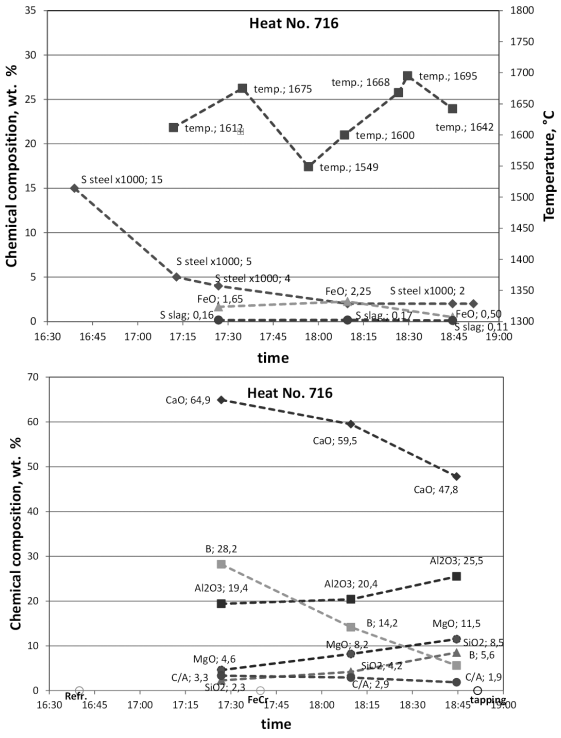

Figure 8: Development of the chemical composition of steel and slag during the reduction period for the heat No. 716 (P91, X10CrMoVNb9-1)

Slika 8: Razvoj kemijske sestave jekla in žlindre med trajanjem redukcije taline št. 716 (P91, X10CrMoVNb9-1)

(w = 26 % and w = 12 %), at comparable temperatures and ratios of CaO/Al_2O_3, a similar, though a low-grade, steel desulphurization (30 % to 40 %) was achieved, together with the final sulphur contents of w = 0.007 % and w = 0.011 %.

The areas of the chemical composition of the final reduction slag No. 686 and No. 731 are shown in **Figure 6** in the quaternary diagram Al_2O_3–CaO–MgO–SiO_2 at 20 % Al_2O_3.

Similarly, **Figure 7** and **Figure 8** show a development of the chemical composition of steel and slag during the reduction period for the heats No. 649 and No. 716.

Again, if we disregard different levels of chromium in the steel, at different steel grades, and focus solely on the MgO content in the slag, it can be stated that under the conditions of the very different MgO contents in the reduction slag in both heats (w = 19 % and 11 %), at comparable temperatures and ratios of CaO/Al_2O_3, a similar, but high, degree of steel desulphurization (from w = 78 % to 87 %) was achieved, which corresponds to very low final sulphur contents, i.e., w = 0.002 %.

The areas of the chemical composition of the final reduction slag in the heats No. 649 and No.716 are shown in **Figure 9** in the quaternary diagram Al_2O_3–CaO–MgO–SiO_2 at w = 20 % Al_2O_3.

When comparing the areas shown in **Figure 6** and **Figure 9**, it is possible to conclude that the negative effect of the increased content of MgO in the reduction slag on the degree of desulphurization was not always associated with a higher content in the given areas

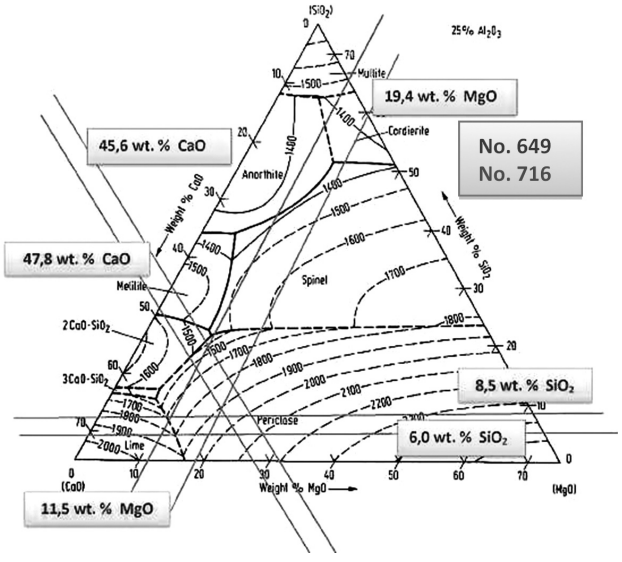

Figure 9: The area of the chemical composition of the final reduction slag of the tested steel grades for the heats No. 649 (19569, X63CrMoV5.1) and No. 716 (P-91, X10CrMoVNb9-1) in the quaternary chart Al_2O_3–CaO–MgO–SiO_2 at w = 25 % Al_2O_3 [5]

Slika 9: Področje kemijske sestave končne redukcijske žlindre preizkušenih jekel, talina št. 649 (19569, X63CrMoV5.1), in št. 716 (P-91, X10CrMoVNb9-1) v kvaternarnem diagramu Al_2O_3–CaO–MgO–SiO_2 pri w = 25 % Al_2O_3 [5]

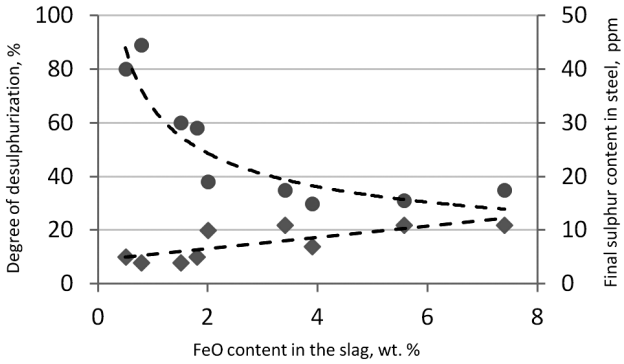

Figure 10: Effect of the FeO content in the slag on the degree of desulphurization and the final sulphur contents

Slika 10: Vpliv vsebnosti FeO v žlindri na stopnjo razžvepljanja in končno vsebnost žvepla

proven in the experimental heats. The deterioration of the kinetic conditions in the case of a higher MgO content due to an increase in the viscosity of the reduction slag was not significant enough to substantially affect the thermodynamics of the chemical reactions observed.

6.2 Effect of the FeO content in the reduction slag on the parameters of steel desulphurization

Of all the monitored parameters, which influenced the desulphurization process and the overall degree of desulphurization, a very negative impact was shown by the content of FeO in the reduction slag. An example of this is the course of sulphur behaviour in the reduction period for the heat No. 731 (steel P91) – see **Figure 5**.

At the beginning of the reduction period the sulphur content in the bath was w = 0.018 %. Upon the reduction refining it was w = 0.006 %. However, at the end of the reduction period the sulphur content in steel was re-increased to w = 0.009 % (before tapping), and to w = 0.011 % (analysis of steel in the ladle).

The cause for this behaviour can be derived from the courses of the slag and metal compositions. As shown in **Figure 5**, the reoxidation and the increase in the FeO content in the slag to the values of approximately up to w

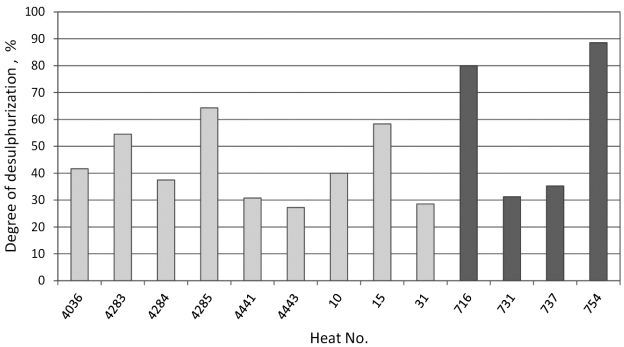

Figure 11: Degree of desulphurization of steel P91 for the experimental heats using synthetic slag REFRAFLUX (dark columns)

Slika 11: Stopnja razžvepljanja jekla P91 pri eksperimentalnih talinah z uporabo sintetične žlindre REFRAFLUX (temni stolpci)

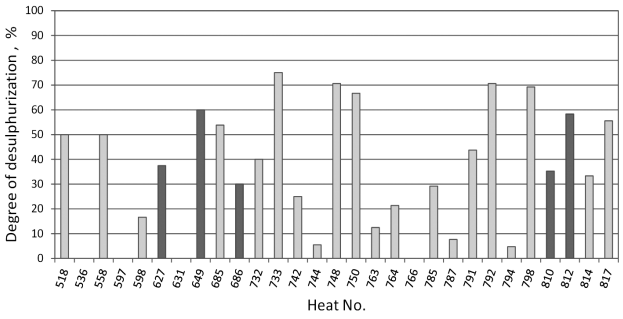

Figure 12: Degree of desulphurization of steel 19569 for the experimental heats using synthetic slag REFRAFLUX (dark columns)
Slika 12: Stopnja razžvepljanja jekla 19569 pri eksperimetalnih talinah z uporabo sintetične žlindre REFRAFLUX (temni stolpci)

= 5.5 % took place in the final phase of the melting process and during the final heating of the melt to the tap temperature using arches. Simultaneously, the content of CaO significantly decreased (down to w = 43 %), and, at the same time, the content of MgO increased, probably from wear or the lining, or from the loose repair material. The main cause for the sulphur-content increase can be considered the "reverse" transition from slag into the metal at an increased temperature, and with an increasing content of FeO in the slag. The mechanism of the reverse transition of sulphur from the slag to the metal is confirmed even by the simultaneous reduction of the sulphur content in the slag.

The behaviour of sulphur in steel during the reduction period is common for all heats, in which the content of FeO was increased. As shown in **Figure 10**, more significant degrees of desulphurization can only be achieved in the cases of very low contents of FeO in the slag (below w = 1 %). The degree of desulphurization is significantly reduced in relative terms when these values are exceeded. Furthermore, if they increase to w = 3 % or 4 %, the FeO content only reaches values of approximately 30 to 40 wt. %. This observation is entirely consistent with the theory and practice of desulphurization by the reduction slag.

6.3 Achieved degree of desulphurization in the EAF

As shown in **Figure 11** and **Figure 12** the achieved degrees of desulphurization, when using the Refraflux-lime mixture, are totally comparable with the heats that use classic technology (lime + fluorspar), and in some cases significantly better results were achieved.

7 CONCLUSION

The steel desulphurization process involving the use of synthetic slag REFRAFLUX 4842 S with the final sulphur-content requirement below w = 0.005 % was optimized for the heats in the EAF at the electric steel plant of TŽ, a. s.

The technology of the operational experimental heats was focused on the desulphurization of the two main steel brands, the high-alloy steel P91 (X10CrMoVNb9-1), and the medium-alloy steel 19569 (X63CrMoV5.1) with a chromium content of w = 9.5 % and 4.5 %.

It was found that even with a deterioration of the kinetic conditions in the cases of higher contents of MgO in the reduction slag (up to w = 26 %), due to a higher slag viscosity, very low sulphur contents, i.e., up to w = 0.002 % in the steel produced can be achieved.

The results of the experimental heats confirmed that a higher degree of desulphurization can be achieved only with a very low FeO content in the slag, preferably below w = 1 %.

Based on the results achieved, the changes in the EAF production technology were recommended, which enabled the final sulphur content in steel to be below w = 0.005 %. The basis for the technology recommended includes not only an application of the new synthetic slag, but also the provision of the necessary thermodynamic and kinetic conditions so that the melted slag showed the declared desulphurization efficiency.

Acknowledgements

The work was funded by the Ministry of Industry and Trade of the Czech Republic within Project No. FR-TI3/374.

8 REFERENCES

[1] L. Socha, J. Bažan, K. Gryc, P. Styrnal, V. Pilka, Z. Piegza, Assessment of Briquetting Fluxing Agent Influence on Refining Effects of Slag during Steel Processing at the Secondary Metallurgy Unit. In 20th Anniversary International Conference on Metallurgy and Materials: METAL, 2011, 163–169

[2] K. Michalek, L. Čamek, Z. Piegza, V. Pilka, J. Morávka, Use of Industrially Produced Synthetic Slag at Trinecke Zelezarny, a.s., Archives of Metallurgy and Materials, Poland, 55 (**2010**) 4, 1159–1165

[3] J. Kalousek, L. Dobrovský, Teorie hutních pochodů. Učební texty VŠB–TU, Ostrava, 2004

[4] A. K. Chatterjee, G. I. Zhmodin, The Phase Equilibrium Diagram of the System CaO-$A1_2O_3$-CaF_2, Journal of Materials Science, 7 (**1972**), 93–97

[5] M. Allibert, H. Gaye, J. Geiseler et al., Slag atlas, 1995

UDK 537.622:549.73
Professional article/Strokovni članek

ISSN 1580-2949
MTAEC9, 46(3)305(2012)

STRUCTURAL, THERMAL AND MAGNETIC PROPERTIES OF BARIUM-FERRITE POWDERS SUBSTITUTED WITH Mn, Cu OR Co AND X (X = Sr AND Ni) PREPARED BY THE SOL-GEL METHOD

STRUKTURNE, TERMIČNE IN MAGNETNE LASTNOSTI PRAHOV BARIJEVEGA FERITA, NADOMEŠČENIH Z Mn, Cu ALI Co IN X (X = Sr IN Ni), PRIPRAVLJENIH PO SOL-GEL METODI

Aylin Gurbuz[1], Nurhan Onar[2], Ismail Ozdemir[3], Abdullah Cahit Karaoglanli[3], Erdal Celik[1]

[1]Metallurgical and Materials Engineering Department, Dokuz Eylul University, 35160 Izmir, Turkey
[2]Textile Engineering Department, Pamukkale University, 20020 Denizli, Turkey
[3]Metallurgical and Materials Engineering Department, Bartin University, 74100 Bartin, Turkey
aylingurbuzeng@gmail.com

Prejem rokopisa – received: 2011-10-20; sprejem za objavo – accepted for publication: 2012-02-13

In this study, Ferrite A (undoped barium hexaferrite), Ferrite B (MnCuNi-doped barium hexaferrite), Ferrite C (MnCuSr-doped barium hexaferrite), Ferrite D (MnCoNi-doped barium hexaferrite) and Ferrite E (MnCoSr-doped barium hexaferrite) powders were prepared by sol-gel processing. The produced powders were calcined at 550 °C for 6 h and sintered at 1000 °C for 5 h to obtain the required phases. The powders were characterized by differential thermal analysis/thermogravimetric analysis (DTA/TG), X-ray diffractometry (XRD) and scanning electron microscopy (SEM), and vibrating-sample magnetometry (VSM). The XRD patterns indicated that the pure barium ferrite phase was not obtained. The presence of M-type $BaFe_{11.6}Mn_{0.4}O_{19}$ was confirmed in the Ferrite B and Ferrite D patterns. In the Ferrite C pattern, there were the phases of $BaFe_{12}O_{19}$, $Ba_2Cu_2Fe_{12}O_{22}$ (X or Z-type) and $Sr_3Fe_2O_{6.16}$. The $Ba_{0.5}Sr_{0.5}Fe_{12}$ phase was easily observed in the Ferrite E pattern. The results showed that the dopant materials significantly change the particle shape of Ferrite A powders, but also lower the value of the coercivity. A higher saturation magnetization was observed for the Ferrite D powder.

Keywords: sol-gel, copper-manganese substitution, barium ferrite

V tej raziskavi so prahovi ferita A (nedopiran barijev heksaferit), ferita B (MnCuNi, dopiran barijev heksaferit), ferita C (MnCuSr, dopiran barijev heksaferit), ferita D (MnCoNI, dopiran barijev heksaferit) in ferita E (MnCoSr, dopiran barijev heksaferit) pripravljeni po sol-gel metodi. Prahovi so bili kalcinirani pri 550 °C 6 ur in sintrani pri 1000 °C 5 ur, da so nastale zahtevane faze. Prahovi so bili karakterizirani z diferenčno termično analizo/termogravimetrijsko analizo (DTA/TG), difraktometrijo rentgenskih žarkov (XRD), z vrstičnim elektronskim mikroskopom in z vibracijskih magnetometrom (VSM). XRD-spektri so pokazali, da ni bila dosežena faza čisti barijev ferit. Prisotnost M-tipa $BaFe_{11.6}Mn_{0.4}O_{19}$ je bila potrjena v feritih B in D. V feritu C so bile tudi faze $BaFe_{12}O_{19}$, $Ba_2Cu_2Fe_{12}O_{22}$ (tip X ali Z) in $Sr_3Fe_2O_{6.16}$. Faza $Ba_{0.5}Sr_{0.5}Fe_{12}$ je bila opažena v feritu E. Rezultati so pokazali, da dopanti pomebno spremenijo obliko prahov ferita A in znižajo koercitivnost. Višja magnetna nasičenost je bila opažena pri prahu ferita D.

Ključne besede: sol-gel, substitucija bakra z manganom, barijev ferit

1 INTRODUCTION

Barium hexaferrite powders have been investigated as a material for permanent magnets, microwave absorber devices and recording media[1–7]. Barium hexaferrite is widely used due to its high stability, excellent high-frequency response, narrow switching-field distribution and its temperature coefficient of coercivity in various applications[1,6]. Barium ferrite with a hexagonal molecular structure has a fairly large magnetocrystalline anisotropy, a high Curie temperature and a relatively large magnetization, as well as chemical and corrosion stability[7]. The conventional ceramic methods, i.e., high-energy ball milling and chemical processes such as chemical coprecipitation, the hydrothermal process, the sol-gel process, etc.[8], were employed to obtain high-quality barium ferrite. Wei et al.[9], Wartewig et al.[10], Singh et al.[11], Yadong et al.[12] and Darokar et al.[13] researched the modification of the magnetic parameters of barium ferrite by substitutions[3]. The magnetic properties of barium ferrite could be changed by the substitution of Fe^{+3} with some divalent-tetravalent (Co^{2+}, Ni^{2+}, Ti^{4+}, etc.) metal ions or their combinations, such as Co-Ti, Zn-Ti, Ni-Zr etc[3,14]. Different cation combinations and their different production methods generate different cation distributions and produce different magnetic properties[9]. For example, the saturation magnetization values of Co-Ti-doped barium ferrites slightly decreased with substitutions and their coercivity values rapidly decreased[14–16]. The preparation methods of barium ferrites affect their magnetic and structural properties. The sol-gel method has emerged as a new method for synthesizing barium ferrite for these applications. This method to a large extent determines their homogeneity, particle size, shape and magnetic characteristics[2,17]. In this study, Mn-, Cu- or Co- and Sr, Ni-doped and undoped barium

ferrite nanopowders were produced using sol-gel processing. The thermal, structural, morphological and magnetic properties of the powders were characterized by DTA-TG, XRD, SEM-EDS and VSM, respectively. In addition, the effects of the doping agents on these properties of the barium ferrite powders were investigated.

2 EXPERIMENTAL

2.1 Material and methods

Barium nitrate ($Ba(NO_3)_2$, 99.999 %, Aldrich), ferric citrate mono hydrate ($C_6H_5FeO_7 \cdot H_2O$, 18–20 %, Fluka), manganese (II) nitrate tetrahydrate ($Mn(NO_3)_2 \cdot 4H_2O$, 98.5 %, Merck), copper (II) nitrate trihydrate ($Cu(NO_3)_2 \cdot 3H_2O$, 99–104 %, Fluka), strontium nitrate ($Sr(NO_3)_2$) and nickel(II) nitrate hexahydrate ($Ni(NO_3)_2 \cdot 6H_2O$, 99.999 %, Aldrich), cobalt(II) chloride hexahydrate ($CoCl_2 \cdot 6H_2O$, Sigma-Aldrich) were used as the precursors, citric acid monohydrate ($C_6H_8O_7 \cdot H_2O$, 99.5–100.5 %, Riedel-de Haen) was used as the chelating agent, and ammonium hydroxide (26 %, NH_4OH, Riedel-de Haen) was used as the pH regulator in the production of barium hexaferrite powders. Barium ferrite powders on the atomic scale were prepared by using the citrate sol-gel process. Ferrite A (undoped barium hexaferrite), Ferrite B (MnCuNi-doped barium hexaferrite), Ferrite C (MnCuSr-doped barium hexaferrite), Ferrite D (MnCoNi-doped barium hexaferrite) and Ferrite E (MnCoSr-doped barium hexaferrite) powders were synthesized[3,4]. Stoichiometric amounts of barium nitrate, ferric citrate, manganese nitrate tetrahydrate, citric acid, copper (II) nitrate trihydrate or cobalt(II) chloride hexahydrate were used to produce the main phase including MnCu- (Ferrite B and Ferrite C) or MnCo- (Ferrite D and E) doped barium ferrites. The barium nitrate and ferric citrate were dissolved in the citric acid solution. The ratios of citric acid: metal = 3 and Fe:Ba = 11 were used from Ref. 1 and 10. Both solutions were mixed. The manganese nitrate, copper (II) nitrate trihydrate, cobalt (II) chloride hexahydrate, strontium nitrate and nickel(II) nitrate hexahydrate were subsequently added to the solution as doping agents in stoichiometric ratios. These solutions were vigorously mixed with a magnetic stirrer until a transparent solution was obtained. Ammonium hydroxide was added to the solution until a pH value of 7.0 was attained at room temperature and then the solution was stirred with a magnetic stirrer. Thus, it was designed to acquire homogeneity in the suspension and stability of pH in the solution during whole solution-preparation process[1,18]. The solution was kept in a water bath at 80 °C for 15 h. The water in the solution was then gradually removed and a wet gel with high viscosity was obtained.

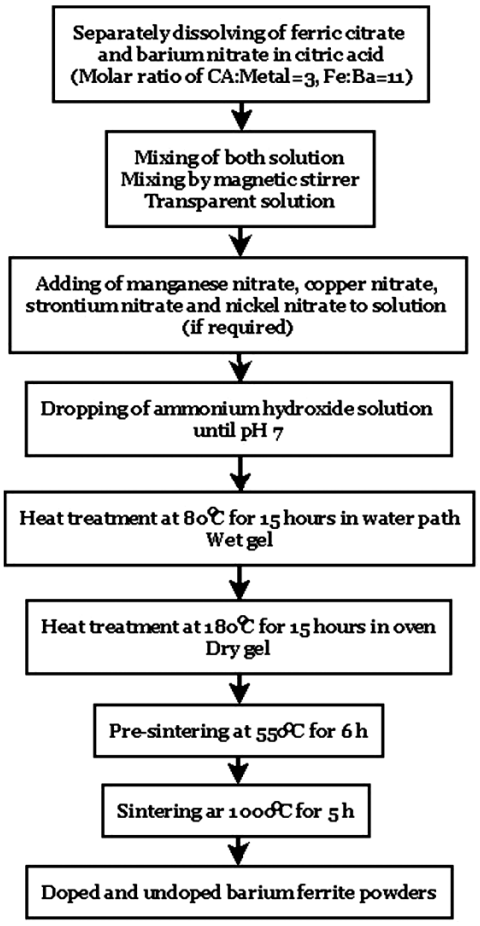

Figure 1: The flow chart of sol-gel citrate process to produce barium ferrite powders

Slika 1: Shema sol-gel citratnega procesa za izdelavo prahov barijevega ferita

The wet gel was treated at 180 °C for 15 h in a Nüve KD400 oven (Nüve, Inc., Ankara, Turkey) to prepare a dry gel. The dry gel was exposed to a pre-sintering process at 550 °C for 6 h to evaporate any impurities and then sintered at 1000 °C for 5 h in ash oven in air[19,2]. The produced powders were characterized by using DTA-TG, XRD, SEM and VSM. The flow chart of the sol-gel citrate process to produce the barium ferrite powders is shown in **Figure 1**.

2.2 Characterization

To determine the decomposition and phase formation of barium ferrite powders, which were dried at 180 °C for 15 h in air, their thermal behavior was evaluated with a DTA–TG device (DTG-60H, Shimadzu, Kyoto, Japan) at a heating rate of 10 °C/min at a temperature range of 0–1200 °C under an oxygen atmosphere.

In order to identify the phase structure, XRD patterns of the barium ferrite powders were determined by means of a Rigaku D Max-2200/PC X-ray diffractometer (Rigaku Corp., Tokyo, Japan) with CuK_α irradiation (wavelength, $\lambda = 0.15418$ nm) using both the θ–2θ mode and the 2θ scan mode. The diffracted X-ray beam was collected by scanning the detector between $2\theta = 3°$ and 90°. The surface morphologies of the barium ferrite powders were examined with a JEOL JJM 6060 scanning electron microscope attached to an energy-dispersive spectroscopy apparatus (JEOL Ltd., Tokyo, Japan). The

magnetic properties of the barium ferrite powders were measured at room temperature on a vibrating-sample magnetometer (VSM, Lakeshore 736, 7400 Series) in a maximum applied field of 15,000 Gauss. From the obtained hysteresis loops, the saturation magnetization (M_s) and coercivity (H_c) were determined.

3 RESULTS AND DISCUSSION

3.1 DTA-TG-analysis

The thermal behavior of the Ba- and Fe-based xerogel powder samples, which were dried at 180 °C for 6 h in air, was evaluated at a heating rate of 10 °C/min in an oxygen atmosphere by DTA/TG analysis in order to determine the temperature of the decomposition and phase formation, and to obtain an optimum heat-treatment regime. **Figure 2** and **3** demonstrate the DTA and TG curves of Ferrite A ($BaFe_{12}O_{19}$), Ferrite B ($BaFe_{12-x}$ $(Mn_{0.5}Cu_{0.5}Ni)_{x/2}O_{19}$)), Ferrite C ($BaFe_{12-x}(Mn_{0.5}Cu_{0.5}Sr)_{x/2}O_{19}$)), Ferrite D ($BaFe_{12-x}(Mn_{0.5}Co_{0.5}Ni)_{x/2}O_{19}$)) and Ferrite E ($BaFe_{12-x}(Mn_{0.5}Co_{0.5}Sr)_{x/2}O_{19}$)) powders for x = 2. In **Figure 2**, the endothermic peaks between 70 °C and 100 °C were due to the removal of solvents in their nature and the endothermic peaks between 200 °C and 300 °C were the result of the degradation of carbon-based organic matter due to the precursors materials, chelating agents and solvents. The exothermic peak between 600 °C and 700 °C resulted from a pure, barium ferrite phase transformation[20].

Moreover, the TG analysis gives the results of the weight loss of the powder samples in the temperature range 0–1200 °C in **Figure 3**. As seen in **Figure 3**, the weight losses of Ferrite A ($BaFe_{12}O_{19}$), Ferrite B ($BaFe_{12-x}(Mn_{0.5}Cu_{0.5}Ni)_{x/2}O_{19}$)), Ferrite C ($BaFe_{12-x}(Mn_{0.5}$

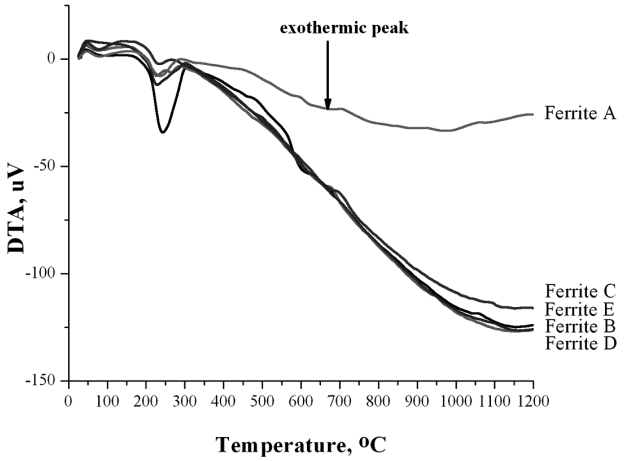

Figure 2: The DTA curves of the Ferrite A ($BaFe_{12}O_{19}$), Ferrite B ($BaFe_{12-x}(Mn_{0.5}Cu_{0.5}Ni)_{x/2}O_{19}$)), Ferrite C ($BaFe_{12-x}(Mn_{0.5}Cu_{0.5}Sr)_{x/2}O_{19}$)), Ferrite D ($BaFe_{12-x}(Mn_{0.5}Co_{0.5}Ni)_{x/2}O_{19}$)) and Ferrite E ($BaFe_{12-x}(Mn_{0.5}Co_{0.5}Sr)_{x/2}O_{19}$)) powders

Slika 2: DTA-krivulje prahov ferita A ($BaFe_{12}O_{19}$), ferita B ($BaFe_{12-x}(Mn_{0,5}Cu_{0,5}Ni)_{x/2}O_{19}$)), ferita C ($BaFe_{12-x}(Mn_{0,5}Cu_{0,5}Sr)_{x/2}O_{19}$)), ferita D ($BaFe_{12-x}(Mn_{0,5}Co_{0,5}Ni)_{x/2}O_{19}$)) in ferita E ($BaFe_{12-x}(Mn_{0,5}Co_{0,5}Sr)_{x/2}O_{19}$))

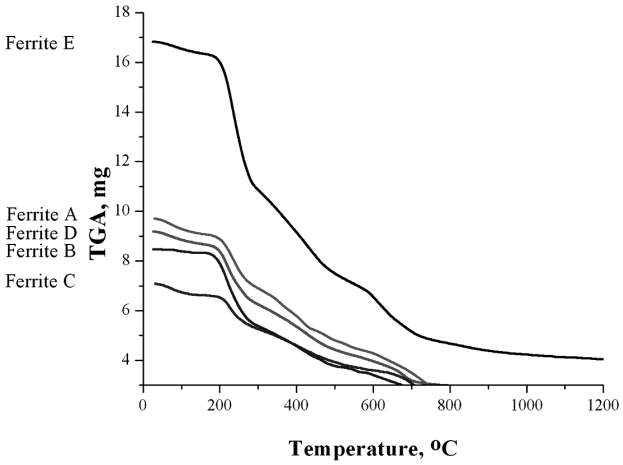

Figure 3: The TG curves of the Ferrite A ($BaFe_{12}O_{19}$), Ferrite B ($BaFe_{12-x}(Mn_{0.5}Cu_{0.5}Ni)_{x/2}O_{19}$)), Ferrite C ($BaFe_{12-x}(Mn_{0.5}Cu_{0.5}Sr)_{x/2}O_{19}$)), Ferrite D ($BaFe_{12-x}(Mn_{0.5}Co_{0.5}Ni)_{x/2}O_{19}$)) and Ferrite E ($BaFe_{12-x}(Mn_{0.5}Co_{0.5}Sr)_{x/2}O_{19}$)) powders

Slika 3: TG-krivulje prahov ferita A ($BaFe_{12}O_{19}$), ferita B ($BaFe_{12-x}(Mn_{0.5}Cu_{0.5}Ni)_{x/2}O_{19}$)), ferita C ($BaFe_{12-x}(Mn_{0.5}Cu_{0.5}Sr)_{x/2}O_{19}$)), ferita D ($BaFe_{12-x}(Mn_{0,5}Co_{0,5}Ni)_{x/2}O_{19}$)) in ferita E ($BaFe_{12-x}(Mn_{0,5}Co_{0,5}Sr)_{x/2}O_{19}$))

$Cu_{0.5}Sr)_{x/2}O_{19}$)), Ferrite D ($BaFe_{12-x}(Mn_{0.5}Co_{0.5}Ni)_{x/2}O_{19}$)) and Ferrite E ($BaFe_{12-x}(Mn_{0.5}Co_{0.5}Sr)_{x/2}O_{19}$)) powders were, respectively, 76 %, 42 %, 33 %, 30 % and 28 %, for temperatures ranging from 0 °C to 1200 °C. In this range of thermal treatment, the weight loss was a result of the solvent removal and the combustion of carbon-based materials. The weight loss up to 200 °C was a small amount since that loss was due to solvent removal. The removal of organic materials up to 300 °C resulted in larger weight loss. The weight loss observed between 600 °C and 800 °C could be the result of Mn or Cu evaporation[21,22].

The exothermic and endothermic reactions occur in the temperature range of about 70 °C to 1200 °C. There are four different steps, including the removal of solvent-based materials, the combustion of carbon-based content, the formation of oxides and barium hexaferrite. The procedure of heat treatment to produce barium ferrite powder was determined according to the DTA-TG results. As a result of that, the xerogel was treated at 80 °C for 15 h to remove water and then treated to produce a dry gel at 180 °C for 15 h in an oven. Subsequently, the powders were sintered at 550 °C for 6 h and at 1000 °C for 5 h for transforming the oxide form and then the ferrite form, respectively. It was reported that the high values of coercivity and magnetic saturation are linked to the annealing temperature. Annealing at higher temperatures led to an increase in the crystallite size and resulted in a decrease of the coercivity[23].

3.2 XRD-analysis

Figure 4 shows XRD patterns of the Ferrite A ($BaFe_{12}O_{19}$), Ferrite B ($BaFe_{12-x}(Mn_{0.5}Cu_{0.5}Ni)_{x/2}O_{19}$)), Ferrite C ($BaFe_{12-x}(Mn_{0.5}Cu_{0.5}Sr)_{x/2}O_{19}$)), Ferrite D

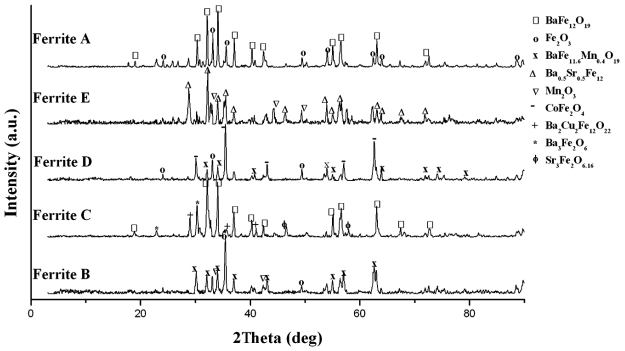

Figure 4: XRD patterns of the Ferrite A ($BaFe_{12}O_{19}$), Ferrite B ($BaFe_{12-x}(Mn_{0.5}Cu_{0.5}Ni)_{x/2}O_{19}$)), Ferrite C ($BaFe_{12-x}(Mn_{0.5}Cu_{0.5}Sr)_{x/2}O_{19}$)), Ferrite D ($BaFe_{12-x}(Mn_{0.5}Co_{0.5}Ni)_{x/2}O_{19}$)) and Ferrite E ($BaFe_{12-x}(Mn_{0.5}Co_{0.5}Sr)_{x/2}O_{19}$)) powders

Slika 4: XRD-spektri prahov ferita A ($BaFe_{12}O_{19}$), ferita B ($BaFe_{12-x}(Mn_{0,5}Cu_{0,5}Ni)_{x/2}O_{19}$)), ferita C ($BaFe_{12-x}(Mn_{0,5}Cu_{0,5}Sr)_{x/2}O_{19}$)), ferita D ($BaFe_{12-x}(Mn_{0,5}Co_{0,5}Ni)_{x/2}O_{19}$)) in ferita E ($BaFe_{12-x}(Mn_{0,5}Co_{0,5}Sr)_{x/2}O_{19}$))

($BaFe_{12-x}(Mn_{0.5}Co_{0.5}Ni)_{x/2}O_{19}$)) and Ferrite E ($BaFe_{12-x}(Mn_{0.5}Co_{0.5}Sr)_{x/2}O_{19}$)) powders produced by the sol-gel citrate process.

The pure barium ferrite phase was not obtained. The presence of the barium ferrite phase and also the small amount of iron oxide (Fe_2O_3) phase in the pattern can be observed in the powders in **Figure 4**. Zhong et al.[24] reported that preheating the gel, which is prepared by sol-gel process, to 400–500 °C prevented any α-Fe_2O_3 phases from forming in the barium ferrite structure. In this study, the presence of the Fe_2O_3 phase was observed in the structure, despite the preheating process, which was conducted at 500 °C for 6 h. The presence of the M-type of $BaFe_{11.6}Mn_{0.4}O_{19}$ was confirmed in the Ferrite B and Ferrite D patterns. In these patterns, the dominant crystalline phase was $BaFe_{11.6}Mn_{0.4}O_{19}$. Thus, we observed the presence of Mn in the barium ferrite structure. This means that the manganese dissolved in the barium ferrite structure and the solid reaction was heterogeneous[20]. It was also determined that the iron substituted with the Mn and the element was embedded in the barium ferrite structure in the $BaFe_{11.6}Mn_{0.4}O_{19}$ form. The existence of phases other than those mentioned above was also observed in the structure. The sol-gel method is an appropriate process for the preparation of multicomponent oxides at relatively low temperatures. The sol-gel process aids not only in reducing the application temperature of the heat treatment but also in controlling the homogeneity and the microstructure. In this study, the XRD patterns obtained were generally complicated and have indicated various phases in the structures. This means the XRD patterns were in agreement with the literature[25]. The Ferrite C pattern indicated phases of $BaFe_{12}O_{19}$, $Ba_2Cu_2Fe_{12}O_{22}$ (X or Z- type) and $Sr_3Fe_2O_{6.16}$. In the pattern the Sr was replaced with Ba and Mn, and the Cu was replaced with Fe, in accordance with Ref. [26]. In the Ferrite D pattern, it was observed that the $CoFe_2O_4$ phase was the dominant phase. In the material, Co was completely substituted by barium. $CoFe_2O_4$ is one of the well-known hard magnetic materials with a very high cubic magnetocrystalline anisotropy, high coercivity, average magnetic saturation[27]. As a result of that, the iron was substituted with manganese and copper in M-type hexagonal ferrites, such as $BaFe_{12}O_{19}$ [28]. Hexagonal ferrites produced have different types, such as the M-, W-, Z- and Y-types, which have complex crystal and magnetic structures. It was also reported in the literature that the magnetic ions can be removed by replacing them with divalent ions[29,30]. It was also reported that magnetic ions can be removed by replacing them with divalent ions[29,30].

3.3 SEM-analysis

The average grain size and the shape of Ferrite A (undoped barium hexaferrite), Ferrite B (MnCuNi-doped barium hexaferrite), Ferrite C (MnCuSr-doped barium hexaferrite), Ferrite D (MnCoNi-doped barium hexaferrite) and Ferrite E (MnCoSr-doped barium hexaferrite) powders are shown in **Figures 5a, 5b, 5c, 5d** and **5e**, respectively. The Ferrite A powders with a platelet microstructure can be seen in **Figure 5a**. This indicates that the M-type ferrite grains are hexagonal-shaped crys-

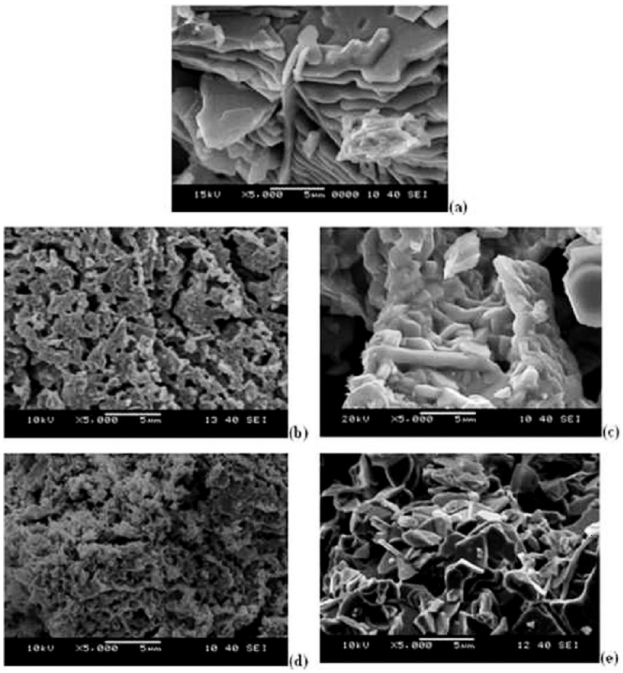

Figure 5: The SEM images of: a) Ferrite A (undoped barium hexaferrite), b) Ferrite B (MnCuNi-doped barium hexaferrite), c) Ferrite C (MnCuSr-doped barium hexaferrite), d) Ferrite D (MnCoNi-doped barium hexaferrite) and e) Ferrite E (MnCoSr-doped barium hexaferrite) powders

Slika 5: SEM-posnetki: a) ferit A (nedopiran barijev heksaferit), b) ferit B (MnCuNi, dopiran barijev heksaferit), c) ferit C (MnCuSr, dopiran barijev heksaferit), d) ferit D (MnCoNi, dopiran barijev heksaferit) in e) ferit E (MnCoS, dopiran barijev heksaferit)

tals. The critical diameter of the spherical barium ferrite with a single magnetic domain is reported to be 460 nm.

Since the produced powders were sintered at 1000 °C, single barium hexaferrite particles were observed in this study. This is why grain growth occurs during the sintering process as well as agglomeration during the preparation of the powders. Similar behavior has been observed previously[2]. **Figure 5d** shows a typical morphology of Ferrite D powders. The major microstructure of Ferrite D powders resembles sponge. The microstructures of the Ferrite C powders were commonly hexagonal shaped (**Figure 5c**). The Ferrite B powders seem to mostly agglomerate, but also the microstructure seems to have a hexagonal shape, as seen in **Figure 5b**. In the microstructure of the Ferrite E powder, the hexagonal shape is the major structure (see **Figure 5e**).

3.4 VSM-analysis

Figure 6 shows the hysteresis curves of $BaFe_{12}O_{19}$ provided by the Aldrich company, Ferrite A (undoped barium hexaferrite), Ferrite B (MnCuNi-doped barium hexaferrite), Ferrite C (MnCuSr-doped barium hexaferrite), Ferrite D (MnCoNi-doped barium hexaferrite) and Ferrite E (MnCoSr-doped barium hexaferrite) powders. Moreover, the magnetic saturation and coercivity values of these powders are given in Table 1. The coercivity value of the Ferrite A powder was 214.859 kA/m (2700 Oe). This value was lower than the value of the $BaFe_{12}O_{19}$ powder provided by the Aldrich company, which was 294.436 kA/m (3700 Oe). It was determined that the magnetic saturation values of the Ferrite A and the $BaFe_{12}O_{19}$, which was provided by Aldrich company, were 55.64 and 34.38 emu/g, respectively. As a result of that, the materials have ferromagnetic properties. It is possible that the higher magnetic saturation values of the Ferrite A powder resulted from agglomerated particles.

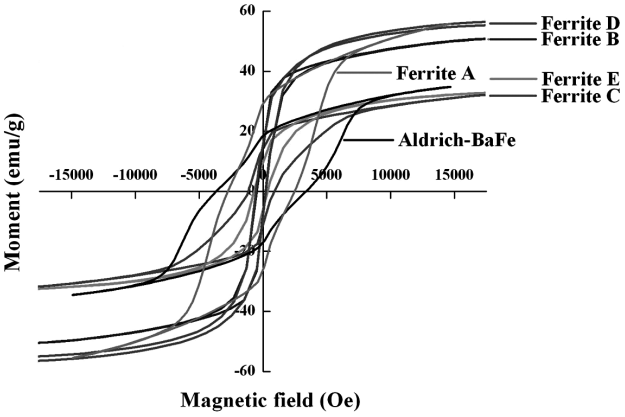

Figure 6: The hysteresis curves of $BaFe_{12}O_{19}$ provided by the Aldrich Company: Ferrite A (undoped barium hexaferrite), Ferrite B (MnCuNi-doped barium hexaferrite), Ferrite C (MnCuSr-doped barium hexaferrite), Ferrite D (MnCoNi-doped barium hexaferrite) and Ferrite E (MnCoSr-doped barium hexaferrite) powders

Slika 6: Histerezne krivulje prahov $BaFe_{12}O_{19}$ od družbe Aldrich: ferit A (nedopiran barijev heksaferrit), ferit B (MnCuBNi, dopiran barijev heksaferit), ferit C (MnCuSr, dopiran barijev heksaferit), ferit D (MnCoNi, dopiran barijev heksaferit) in ferit E (MnCoSr, dopiran barijev heksaferit)

Table 1: The magnetic saturation and coercivity values of $BaFe_{12}O_{19}$ provided by the Aldrich Company: Ferrite A (undoped barium hexaferrite), Ferrite B (MnCuNi-doped barium hexaferrite), Ferrite C (MnCuSr-doped barium hexaferrite), Ferrite D (MnCoNi-doped barium hexaferrite) and Ferrite E (MnCoSr-doped barium hexaferrite) powders.

Tabela 1: Magnetna nasičenost in koercitivna sila $BaFe_{12}O_{19}$ iz družbe Aldrich: ferit A (nedopiran barijev heksaferrit), ferit B (MnCuBNi, dopiran barijev heksaferit), ferit C (MnCuSr, dopiran barijev heksaferit), ferit D (MnCoNi, dopiran barijev heksaferit) in ferit E (MnCoSr, dopiran barijev heksaferit)

Materials	Magnetic Saturation (emu/g)	Coercivity (kA/m)
Purchased nanopowder (Aldrich)	34.38	294.436
Ferrite A powder	55.64	214.859
Ferrite B powder	50.68	27.836
Ferrite C powder	32.07	82.466
Ferrite D powder	55.16	30.304
Ferrite E powder	32.66	42.472

As seen in **Table 1**, the coercivity values of the barium ferrite powders doped with different divalent metals decreased and the magnetic properties approached superparamagnetic properties. In particular, the magnetic saturation values with nickel doping to barium ferrite powders were high, while the magnetic saturation values with strontium doping were low.It is reported that undoped hexaferrite possesses a very high coercive force, which is due to its uniaxial anisotropy along the c-axis of the M-type hexaferrite. In our study, Mn-Cu-Co-Ni-Sr substitution led to a significant decrease of H_c compared to the reported Hc value for the undoped hexaferrite, owing to a reduction of the magnetocrystalline anisotropy. Similar results were also reported for Mn-Co-Ti-substituted barium ferrites by Ghasemi et al.[2] and for Mg-Ti-substituted barium ferrite by Shams et al.[31]. It is believed that the coercivity of the doped hexaferrite was low compared to the coercivity of the undoped barium hexaferrite powders because of the change in the easy axis of magnetization from the c-axis to the basal plane[31]. Ghasemi et al.[2] advocated the results that were indicated by Shams et al.[31]. Tech et al.[26] pointed out that Co(II) substitution in $BaFe_{12}O_{19}$ reduced the coercivity from 1082 G mg^{-1} to 275.8 G mg^{-1}. The hysteresis loss area in the cobalt (II)-substituted barium hexaferrite is smaller than the undoped one.

4 CONCLUSIONS

Ferrite A (undoped barium hexaferrite), Ferrite B (MnCuNi-doped barium hexaferrite), Ferrite C (MnCuSr-doped barium hexaferrite), Ferrite D (MnCoNi-doped barium hexaferrite) and Ferrite E (MnCoSr-doped barium hexaferrite) powders were prepared by using a citrate sol-gel process. The heat-treat-

ment regimes of the powders were determined according to the DTA-TG results. The dopant materials significantly influenced the microstructure of the Ferrite A powder. In particular, the addition of the Sr dopant to barium ferrite powders had a significant role in the production of powders with a hexagonal microstructure. The VSM results are in reasonable agreement with the literature. The doping elements decreased the coercivity of these powders. As the coercivity values of Ferrite A powders were larger than the doped powders, the coercivity value was found about 214.859 kA/m (2700 Oe) for Ferrite A powders and was changed from about 27.285 kA/m (349.8 Oe) and 82.466 kA/m (1036.3 Oe) for the doped barium hexaferrite powders. The XRD results showed that the Ferrite powders produced by the sol-gel process contained a small amount of iron oxide (Fe_2O_3) in their structure in addition to the barium ferrite phase. For doped barium ferrite powders, the iron was substituted with manganese and copper in M-type hexagonal ferrites, such as Ferrite A, while the Sr element was replaced by the Ba element. In conclusion, the dissolution of the Mn, Cu and Sr elements in the Ferrite A structure at the atomic level was successfully accomplished by the sol-gel process.

Acknowledgements

The study has been supported by The Scientific and Technological Research Council of Turkey (TUBITAK, 106M391).

5 REFERENCES

[1] Z. Haijun, L. Zhichao, M. Chengliang, Y. Xi, Z. Liangying, W. Mingzhong, Mater. Sci. Eng. B, 96 (**2002**), 289–295
[2] A. Ghasemi, A. Saatchi, M. Salehi, A. Hossienpour, A. Morisako, X. Liu, Phys Status Solidi A, 10 (**2006**), 2513–2521
[3] Z. Haijun, L. Zhichao, M. Chengliang, Y. Xi, Z. Liangying, W. Mingzhong, Mater Chem Phys., 80 (**2003**), 129–134
[4] G. Mendoza-Suarez, L. P. Rivas- Vazquez, J. C. Corral-Huacuz, A. F. Fuantes, J. I. Escalante-Garcia, Physica B, 339 (**2003**), 110–118
[5] H. Hua, S. Z. Li, Z. D. Han, D. H. Wang, M. Lu, W. Zhong, B. X. Gu, Y. W. Du, Mat. Sci. Eng A-Struct, 448 (**2007**), 326–329
[6] G. Mendoza-Suarez, L. P. Rivas- Vazquez, A. F. Fuantes, J. I. Escalante-Garcia, O. E. Ayala-Valenzuela, E. Valdez, Mater. Lett., 57 (**2002**), 868–872
[7] J. Zhou, H. Ma, M. Zhong, G. Xu, Z. Yue, Z. He, J Magn Magn Mater., 305 (**2006**), 467–469
[8] P. Sharma, R. A. Rocha, S. N. de Medeiros, A. Paesano Jr, J Alloy Compds., 443 (**2007**), 37–42
[9] F. L. Wei, H. C. Fang, C. K. Ong, et al., J. Appl. Phys., 87 (**2000**), 8636–8639
[10] P. Wartewig, M. K. Krause, P. Esquinazi et al., J. Magn. Magn. Mater., 192 (**1999**), 83–99
[11] P. Singh, V. K. Babbar, A. Razdan et al., Mater. Sci. Eng. B, 67 (**1999**), 132–138
[12] L. Yadong, L. Renmao, Z. Zude et al., Mater. Chem. Phys., 64 (**2000**), 256–259
[13] S. S. Darokar, K. G. Rewatkar, D. K. Kulkarni, Mater. Chem. Phys., 56 (**1998**), 84–86
[14] Z. W. Li, C. K. Ong, Z. Yang, F. W. Wei, X. Z. Zhou, J. H. Zhao, A. H. Morrish, Phys. Rev. B, 62 (**2000**), 6530–6537
[15] O. Kubo, T. Ido, and H. Yakoyama, IEEE Trans. Magn. 18 (**1982**), 1122
[16] Z. Yang, J. H. Zhao, H. X. Zeng, G. Yan, Int. J. Soc. Mater. Eng. Resour., 3 (**1995**), 203
[17] A. Mali, A. Ataie, Ceram Int., 30 (**2004**), 1979–1983
[18] L. Dong, Z. Han, Y. Zhang, Z. Wu, Z. Zhang, Rare Metals, 25 (**2006**), 605–608
[19] A. Ghasemi, X. Liu, A. Morisako, J Magn Magn Mater., 316 (**2007**), e105–e108
[20] O. Carp, R. Barjega, E. Segal, M. Brezeanu, Thermochim Acta, 318 (**1998**), 57–62
[21] A. Hakola, O. Heczko, A. Jaakkola, T. Kajava, K. Ullakko, Appl Phys A, 79 (**2004**), 1505–1508
[22] S. T. Park, W. Kang, H. T. Kim, S. J. Yun, B Korean Chem Soc., 293 (**2008**), 685–688
[23] J. Ding, W. F. Miao, P. G. McCormick, R. Street, J Alloy Compd., 281 (**1998**), 32–36
[24] W. Zhong, W. Ding, N. Zhang, J. Hong, Q. Yan, Y. Du, J Magn Magn Mater., 168 (**1997**), 196–202
[25] N. C. Pramanik, T. Fujii, M. Nakanishi, J. Takada, S. I. Seok, Mater Lett., 60 (**2006**), 2718–2722
[26] G. B. The, S. Nagalingam, D. A. Jefferson, Mater Chem Phys., 101 (**2007**), 158–162
[27] X. H. Huang, Z. H. Chen, Scripta Mater., 54 (**2006**), 169–173
[28] H. Fujiki, K. Tomaru, I. Sakurai, A. Suzuki, K. Mita, US 2004/0054029 A1 (2006).
[29] Y. Mizuno, S. Taruta, K. Kitajima, J Mater Sci., 40 (**2005**) 1, 165–170
[30] M. R. Meshrama, N. K. Agrawala, B. Sinhaa, P. S. Misrab, J Magn Magn Mater., 271 (**2004**), 207–214
[31] M. H. Shams, S. M. A. Salehi, A. Ghasemi, Mater Lett., 62 (**2008**), 1731–1733

UDK 621.74.047:536.2
Professional article/Strokovni članek

ISSN 1580-2949
MTAEC9, 46(3)311(2012)

INFLUENCE OF THE WATER TEMPERATURE ON THE COOLING INTENSITY OF MIST NOZZLES IN CONTINUOUS CASTING

VPLIV TEMPERATURE VODE NA INTENZITETO OHLAJANJA Z MEGLIČNIMI ŠOBAMI PRI KONTINUIRNEM ULIVANJU

Miroslav Raudensky[1], Milan Hnizdil[1], Jong Yeon Hwang[2], Sang Hyeon Lee[2], Seong Yeon Kim[2]

[1]Brno University of Technology, Czech Republic
[2]POSCO, Korea
raudensky@fme.vutbr.cz

Prejem rokopisa – received: 2011-10-20; sprejem za objavo – accepted for publication: 2012-02-15

Small mist nozzles used in continuous casting were tested for heat-transfer intensity. These nozzles are used in the secondary cooling area of a steel slab casting machine. The impact pressure distribution was measured first. The laboratory measurements of the cooling intensity (the HTC distribution) were performed with a variable water temperature. A temperature range from 20 °C to 80 °C was used in the tests.

Surprisingly, the water temperature was found to have a strong influence. The most noticeable effect is a shift in the Leidenfrost temperature to low temperatures. Changing the water temperature from 20 °C to 80 °C caused a change in the Leidenfrost temperature of 130 °C. This can be significant and can change the cooling character of the continuous casting machine. It is interesting that with an increase in the cooling intensity, following an increase in the water temperature in a high-temperature region (above the Leidenfrost temperature), there is a small difference of about 30 W/(m^2 K).

Surprisingly, high differences in the Leidenfrost temperature were found for an intensive cooling, where a difference of only 20 °C in the coolant temperature makes a difference of about 100 °C in the Leidenfrost temperature.

The results of the experiments performed with an elevated water temperature showed a high sensitivity of the cooling intensity to this parameter. The decreasing effect of the cooling intensity related to the water temperature is more important for the spray cooling of high intensities.

Keywords: water temperature, cooling intensity, mist nozzles, continuous casting

Majhne meglične šobe, ki se uporabljajo pri kontiuirnem ulivanju jekla, so bile preizkušene na intenziteto prenosa toplote. Te šobe se uporabljajo v območju sekundarnega hlajenja kontinuirne naprave za ulivanje jekla. Najprej je bila izmerjena razporeditev tlaka pri njegovem udarcu. Laboratorijske meritve intenzitete ohlajanja (razporeditev koeficienta prenosa toplote) so bile izvršene s spreminjanjem temperature vode. Pri preizkusih je bila uporabljena voda s temperaturo od 20 °C do 80 °C. Presenetljivo je, da se je izkazalo, da ima temperatura vode močan vpliv. Najbolj opazen učinek je bil premik Leidenfrostove temperature k nižjim vrednostim. Sprememba temperature vode iz 20 °C na 80 °C je povzročila spremembo Leidenfrostove temperature za 130 °C. To je pomembno in lahko močno vpliva na ohlajevalne značilnosti naprave za kontinuirno ulivanje. Zanimivo je, da se z naraščanjem intenzitete ohlajanja z višanjem temperature vode v visokotemperaturnem režimu (nad Leidenfrostovo temperaturo) opazi le majhna sprememba HTC za okrog 30 W/(m^2 K).

Presenetljivo velike razlike v Leidenfrostovi temperaturi so bile dobljene pri intenzivnem ohlajanju, kjer je razlika v temperaturi vode 20 °C povzročila razliko v Leidenfrostovi temperaturi za okrog 100 °C.

Rezultati eksperimentov, izvršeni s povišano temperaturo vode, so pokazali veliko občutljivost intenzitete ohlajanja za temperaturo vode. Padajoči učinek intenzitete ohlajanja z naraščanjem temperature vode je bolj pomemben pri bolj intenzivnem ohlajanju z meglo.

Ključne besede: temperatura vode, intenziteta hlajenja, meglične šobe, kontinuirno ulivanje

1 INTRODUCTION

The heat flux extracted from a cooled surface can be expressed as a product of the heat-transfer coefficient (HTC) and a difference between the surface temperature and the coolant temperature. This paper discusses the question whether the HTC is influenced by the coolant temperature. The cooling-water temperature changes during the year in the steel plants and can be considered to be in the range from 10 °C to 45 °C. Can this change in the coolant temperature influence the cooling characteristics of the mist nozzles typically used in the secondary area of the continuous-casting machines.

A typical dependence of the HTC on the surface temperature is shown in **Figure 1**. The HTC is strongly variable with respect to the surface temperature. The border between the high intensity cooling for low surface temperatures and the low intensity cooling for high surface temperatures is the Leidenfrost temperature[1,2]. The measurements performed with the mist nozzles showed a strong dependence of the Leidenfrost temperature on the kinetic energy of the droplets and of the water impingement density[3,4].

The influence of the cooling medium on the cooling intensity is rarely described in the literature. The research of the University of British Columbia in Canada[5] showed interesting dependences of an increasing temper-

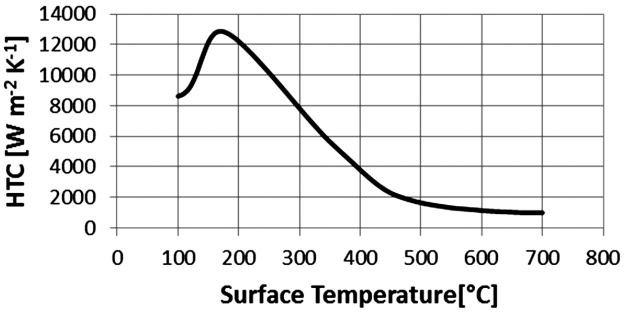

Figure 1: Typical dependence of the HTC on the surface temperature
Slika 1: Značilna odvisnost HTC od temperature površine

ature of the cooling medium. For the measurements, 7 mm thin carbon plates embedded by 16 thermocouples were used. One half of the thermocouples was positioned 1 mm under the surface. The second half was welded to the surface. The test plate was heated to the initial temperature between 700–900 °C, and then positioned under a full cone nozzle. A comparison of the results (**Figure 2**) showed that in the area between 50 °C and 70 °C, where the cooling is effective, the HTC reaches higher values for the water temperature T_w = 50 °C than for the water temperature T_w = 70 °C. On the other hand, the HTC difference between the water temperatures of 50 °C and 40 °C is not significant. The results described in[5] are very interesting showing a substantial dependence of the cooling-medium temperature on the spray cooling efficiency.

2 HTC-MEASUREMENT

2.1 Testing equipment

A laboratory stand (**Figure 4**) developed for testing the nozzles applied for continuous casting was used to test the cooling intensity with the water at elevated temperatures. The tested mist nozzles are located under a test plate. The steel frame holds three major parts of the stand: a test plate, a driving mechanism with a nozzle(s) and a heater.

The test plate is made of austenitic steel to prevent the surface from a significant oxidation. There are holes

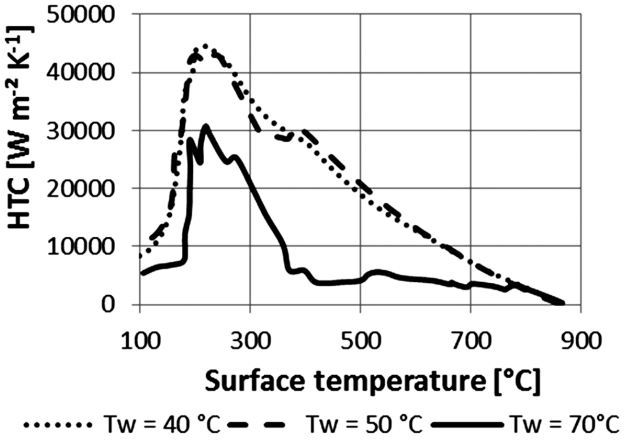

Figure 2: Influence of the water temperature on the HTC, a graph adapted from the paper[5]
Slika 2: Vpliv temperature vode na koeficient prenosa toplote; graf je povzet po viru[5]

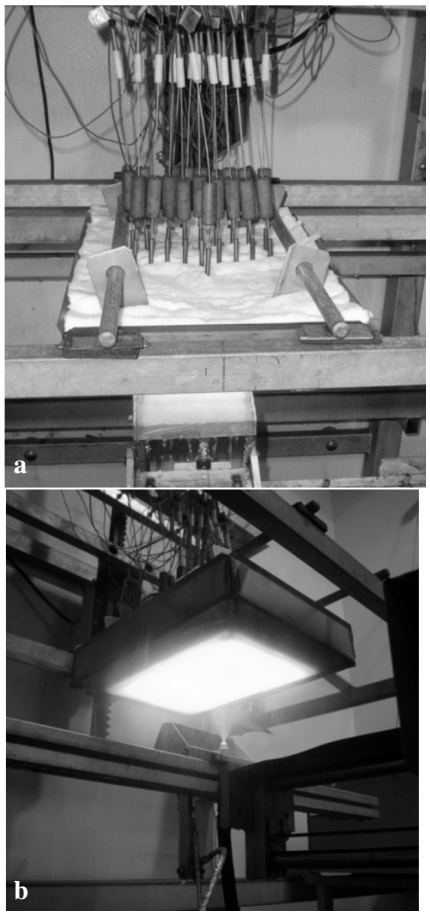

Figure 3: a) Insulated test plate and two rows of thermocouples, b) the test plate sprayed with nozzles
Slika 3: a) Izolirana preizkusna plošča in dve vrsti termoelementov, b) preizkusna plošča, brizgana s šobami

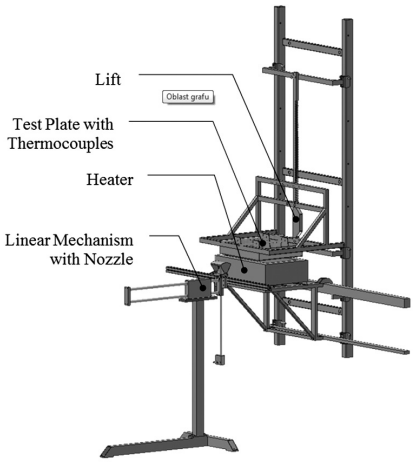

Figure 4: Basic parts of the experimental testing bench
Slika 4: Osnovni deli eksperimentalne klopi za preizkušanje

Figure 5: Initial stage of an experiment – the furnace is moving to the right, the pressure was set
Slika 5: Začetno stanje preizkusa – peč se odmakne na desno, vzpostavi se tlak

drilled into the plate, where the thermocouples are placed. Shielded thermocouples of type K with a diameter of 1.5 mm are used for temperature monitoring. The shape of the plate and the distribution of the thermocouples used in these tests can be seen in **Figure 3**. All of the 18 thermocouples in two rows and nine columns were used.

The driving mechanism moves the spraying nozzle(s) under the plate. The speed of the nozzle motion is controlled by a computer. A pneumatically driven deflector is placed between the nozzle and the cooled plate. The deflector opening and closing when the nozzle is spraying is controlled by the computer. The deflector is closed on the way back to its initial position.

The third major part of the test bench is an electric furnace used for the initial heating of the plate. The furnace moves on rails. It is placed under the test plate when the experiment is prepared and the gap between the furnace edges and the plate is filled with insulation. At the beginning of the experiment the plate is heated up to an initial temperature. The temperature of 1250 °C was set as the initial temperature. The test plate is placed into a jig. This allows the plate to move up, removing the furnace back and positioning the nozzle with the driving mechanism to the space under the plate. This stage of the experiment is shown in **Figure 5**.

A computer with a data-acquisition system is located outside the spray box in a control room. It monitors the heating process, controls the experiment and records the data from thermocouples and the position sensor.

2.2 Experimental process

The test plate is cleaned up, the holes for the thermocouples are cleaned and the thermocouples are tested before each experiment. The plate is positioned into the jig in the stand frame and the thermocouples are embedded. The data-acquisition system, the driving

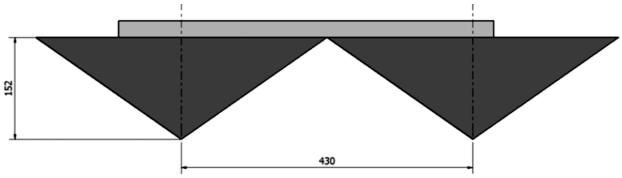

Figure 6: Scheme of a configuration of the air-mist nozzles
Slika 6: Shematičen prikaz razporeditve šob za ustvarjanje megle

mechanism and the deflector go through a cold preliminary test. The furnace is positioned under the plate. The heating control system is set up and the heating of the plate starts. After the plate reaches the initial temperature needed for the experiment, the control system keeps the adjusted temperature in the furnace and the temperature in the plate is homogenized.

The deflector on the driving mechanism is closed and a required pressure of the coolant is set up. The pressure of the coolant is measured in a manifold where the nozzles are mounted. The flow rate of the water is measured by an induction flow meter. The plate is moved up in the jig to adjust the cooling position and the furnace on rails is moved out. The driving mechanism with the spraying nozzle and the closed deflector are moved to a defined position under the hot plate. The data-acquisition system records the temperatures of all the thermocouples, the temperature of the coolant and the position of the nozzle. The nozzle moves in one direction with the open deflector and returns with the closed deflector. The experiment is finished when the temperature in all the measured points is below 500 °C. An inverse task is used to re-compute the internal temperatures to the surface temperatures in order to obtain the HTC[6].

2.3 Test configuration

Commercially available small mist nozzles used for cooling in continuous casting were used for the tests. The nozzles have a spray angle of 110°. A couple of nozzles with parallel main axes were used – see **Figure 6**.

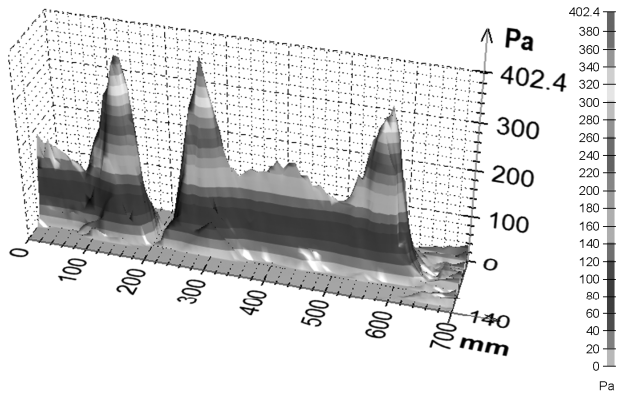

Figure 7: Impact pressure distribution, an example for the water pressure of 2.1 bar and the air pressure of 1.6 bar
Slika 7: Razporeditev udarnih tlakov – primer za tlak vode 2,1 bar in tlak zraka 1,6 bar

Table 1: Nozzle parameters
Tabela 1: Pregled parametrov šob

Experiment	Water Pressure (bar)	Air Pressure (bar)	Water Flow Rate (L/min)	Water Temperature (°C)	Air Flow Rate (m^3/h)	Spray Height (mm)	Pitch (mm)	Casting Velocity (m/min)
T35–41	2.1	1.6	4.5	20–80	8.1	239	430	1
T43	3.6	1.9	8	40 °C	6.3	239	430	1

The nozzles were tested for spray homogeneity prior to the heat-transfer tests. The result of the impact pressure measurement is shown in **Figure 7** (one complete footprint and one half of a footprint of the impacting jets is shown in the Figure). It is obvious that the tested nozzle is far from being ideal. The results published in this paper refer to the impacting area in the nozzle axis. The flow rate and the pressure conditions are described in **Table 1**. All the tests were carried out with a constant velocity of the sample: 1 m/min.

3 RESULTS

The results shown in this part are the average values of the heat-transfer coefficient in the impact area in the direction of the nozzle axis. The impacting area for –150 mm to +150 mm is considered both in longitudinal and transversal directions.

Figure 8 shows the results for seven experiments where the only variable parameter was the water temperature.

The experiments shown in **Figure 8** demonstrate a significant shift in the Leidenfrost temperature. Changing the water temperature from 20 °C to 80 °C causes a change in the Leidenfrost temperature of 130 °C. This

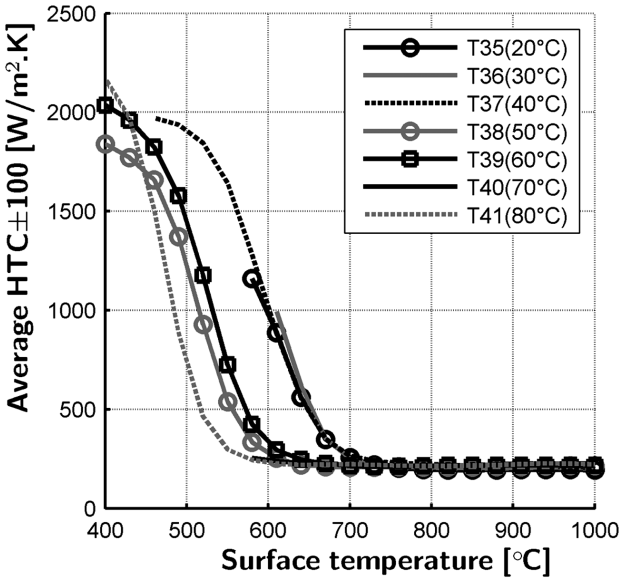

Figure 8: Seven experiments show an increase in the water temperature from 20 °C to 80 °C
Slika 8: Sedem preizkusov, ki kažejo povečanje temperature vode od 20 °C do 80 °C

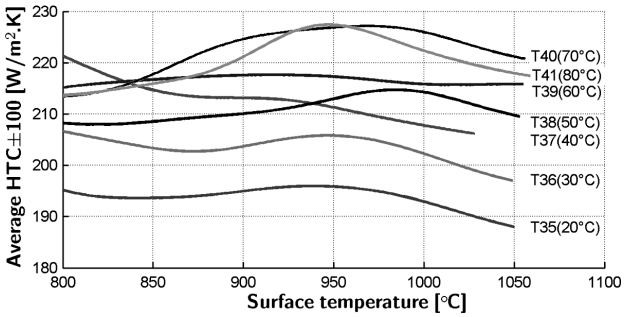

Figure 9: Influence of the water temperature in the high temperature region – a close-up of the right-hand part of **Figure 8**
Slika 9: Vpliv temperature vode v visokotemperaturnem področju – povečan desni del **slike 8**

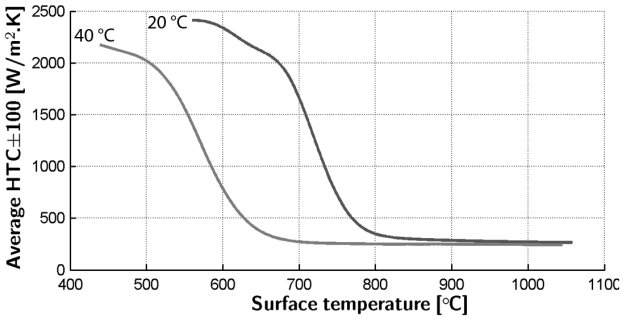

Figure 10: Changes in the cooling intensity for the experiment with a bigger flow rate, the water temperature of 20 °C and the experiment T43 with 40 °C
Slika 10: Sprememba intenzitete hlajenja pri preizkusu z večjim pretokom vode: voda s temperaturo 20 °C in preizkus T43 s 40 °C

can be significant and can change the character of the cooling in the continuous casting machine. It is interesting that there is an increase in the cooling intensity following the increase in the water temperature in the high-temperature region as shown in **Figure 9**. The difference is about 30 W/(m^2 K) (see the scale of the graph). **Figure 9** shows that hot water provides a higher cooling intensity above the Leidenfrost temperature. This finding can be explained with the positive effect between the water temperature and the boiling point that allows a faster setting of the boiling regime with high heat-transfer rates.

Surprisingly, high differences in the Leidenfrost temperature were found for the intensive cooling (**Figure 10**) where a difference of only 20 °C in the coolant temperature makes a difference of about 120 °C in the Leidenfrost temperature.

4 CONCLUSION

A high influence of the water temperature on the cooling intensity of the mist nozzles was found. The major effect is the shift in the Leidenfrost temperature to low temperatures. The effect is more significant in the case of intensive cooling. Even a temperature difference of 20 K (between 20 °C and 40 °C) makes a significant change in the Leidenfrost temperature. This finding can explain some of the problems of the continuous casting machines used in winter and summer when the temperature of the cooling water varies significantly.

Acknowledgement

The paper presented has been supported by an internal grant of the Brno University of Technology focused on specific research and development, No. FSI-S-11-20 - Heat Transfer Intensification.

5 REFERENCES

[1] M. Raudensky, J. Bohacek, Leidenfrost Phenomena at Hot Sprayed Surface, In the 7th ECI International Conference on Boiling Heat Transfer Boiling 2009, 3–7 May 2009, Florianopolis, Brazil

[2] M. Raudensky, J. Horsky, Secondary Cooling in Continuous Casting and Leidenfrost Temperature, Ironmaking and Steelmaking, 32 (**2005**) 2, 159–164

[3] M. Raudensky, A. Horak, P. Kotrbacek, Optimisation Of Controlled Cooling in Continuous Casting, 1st International Conference on Simulation and Modelling of Metalurgical Processes in Steelmaking, 25–27 October 2005, Brno, Czech Republic

[4] J. Horsky, M. Raudensky, A. A. Tseng, Heat Transfer Study of secondary cooling in Continuous Casting, AISTech 2005, Iron & Steel technology Conference and exposition, May 9–12, 2005, Charlotte, USA

[5] F. Xu, M. S. Gadala, Heat Transfer Behaviour in the Impingement Zone under Circular Water Jet, International Journal of Heat and Mass transfer, 49 (**2006**), 3785–3799

[6] M. Pohanka, H. Bellerova, M. Raudensky, Experimental Technique for Heat Transfer Measurements on Fast moving Sprayed Surfaces, Journal of ASTM International, 6 (**2009**) 4, 1–9